Université catholique de Louvain

.

Faculté des Sciences

Institute of Condensed Matter and Nanosciences

Division of Molecular Chemistry, Materials, and Catalysis

Thesis submitted in the fulfilment of Doctorate degree in Science

Role of structural properties of Ni-based catalysts towards aqueous glucose hydrogenation

Yang Fu

Supervisors:

Prof. S. Hermans and Prof. M. Singleton

February 2022

Jury members

Prof. Sophie Hermans (UCLouvain), Promoter

Prof. Michael Singleton (UCLouvain), Promoter

Prof. Yann Garcia (UCLouvain), President

Prof. Eric Gaigneaux (UCLouvain)

Prof. Yaroslav Filinchuk (UCLouvain)

Prof. Vincent Dubois (LABIRIS, Belgium)

Prof. Sébastien Paul (Centrale Lille, France)

"It is never too late to be what you might have been."

-George Eliot

Acknowledgements

I have always refused to put pen to paper on the acknowledgements because it means that I am nearing the end of my PhD in Belgium. Since the first day I left my home country on September 14, 2017, I have been here for 4 years, 2 months and 25 days. I have gone from being curious about everything abroad to being integrated into the local culture; from speaking only a few words to communicating without any barriers; from knowing nothing about catalysis to completing my PhD thesis on this topic and from being alone to being a family of three. The simplicity, purity, tranquillity, freedom and human touch of life in Louvain-la-Neuve are burnt into my memory. With a grateful heart, I would like to thank all the people who have helped me.

First of all, I would like to thank my supervisors Sophie and Michael. I clearly remember that Michael forwarded my PhD application to Sophie on the eve of Chinese New Year 2017 and Sophie replied me the next day and agreed to discuss the possibility for hosting me. I would like to thank Sophie and Michael for offering me the opportunity to study in Belgium. During this time, Sophie scheduled the meeting with me at least once a month to talk about my progress and whether I was having difficulties in my daily life. With Sophie's help, I was able to move into a schoolhouse. Michael never refused my requests to meet with him and always invited me to group meetings and discussions, he was not only a mentor but also a good friend. His pursuit of fundamental study has deeply influenced me and will

continue to guide me in my future research career. Sophie also provided me with a variety of professional training opportunities, including the operation of various instruments and attending international conferences. No matter what problems I encountered, she was always proactive in helping me. I am especially grateful to have such a completely supportive supervisor with me for more than four years. Her optimism, self-discipline, sense of teamwork and efficiency have deeply influenced me. Thanks to Sophie for the team building every Christmas and spring, and to Michael for the team activities at Thanksgiving Day and Christmas, which I will remember fondly. I am fortunate and grateful to have met these two intelligent, supportive and friendly mentors.

Secondly, I would like to thank Prof. Xianbao Wang, my supervisor during my master's study. Without his help, guidance, and persistence in my research area, I would not have been able to get the opportunity to apply for the China Scholarship. Special thanks also to the scholarship support from the China Scholarship Council and UCLouvain, which has enabled me to study and live here. I would like to thank Mr. Yantao Su, Ms. Lihong Liu and Mr. Baoguo Zheng from the Education department in the Embassy of China in Brussels for their support in making our study abroad a success.

I would like to thank all the professors and technicians who trained me in the operation of the instruments and helped me with measurements, especially Jean-François Statsyns and Jacqueline Boniver for their support and help in my

daily experiments; Pierre Eloy for training me in the use of XPS and helping me with data treatment; François Devred for the training in the operation of XRD, TPD, etc. Thanks to Anne Iserentant and our collaborators Prof. Benoit Pichon, Prof. Dario Duca. I would like to also acknowledge 'FNRS' for its financial support during the course of the thesis.

Next, I would like to offer special gratitude towards all the jury members (Prof. Yann Garcia, Prof. Eric Gaigneaux, Prof. Yaroslav Filinchuk, Prof. Vincent Dubois, Prof. Sébastien Paul) for accepting to review this thesis. I believe the constructive feedback and insightful discussions have helped me to improve the manuscript significantly.

I am very thankful to have spent my doctoral studies in such a wonderful place as LLN and to have met many kind friends. It is not possible to mention everyone but to mention a few Shouhe Yan, Yazhou Liu, Lei Hu, Weiyang Li, Xiao Li, Hui Yang, Junjie Lan, Lu bai, Cuilian Liu, Li Sun, He Jia, Lixing Song, Hui Wang, Ran Ye, Jian Wang, Pengcheng Xu, Nathalie, Deb, Varun, Maïté, Samuel, Tommy, Nadzeya, Akin. Thank you to all my friends who have helped me in my life and studies. I spent most of my free time with those Chinese friends, which made me feel that life here is warm and beautiful. Those European friends have helped me a lot in being able to live a richer life in Belgium, especially Nathalie, who has made countless phone calls for me in French and provided me a lot of useful local information.

Finally, I would like to thank my parents for their unconditional support and help, as well as their silent dedication to me. I am grateful to my grandfather and my

uncle for their constant support. Thanks to my wife Jing, who has been with me and supporting me for a long time, and to our lovely son Yiren, who has brought me a lot of growth, happiness and love.

May all the people around me have a healthy, wonderful and happy journey in life.

Thank you

Yang

09.12.2021

Abstract

The demand for a sustainable society and the increase in global warming are driving us to develop sustainable and clean energy sources to reduce and further replace our dependence on traditional fossil fuels. Biomass is currently the only sustainable resource for the production of sustainable organic carbon and biofuels. Sorbitol has been recognized as one of the 12 most important platform chemicals obtainable from biomass, widely applied in food industry, medical applications, cosmetic industry and miscellaneous use. Sorbitol is usually produced by glucose hydrogenation in the presence of Ni, Ru, Pt, Co, or other metal-based catalysts. Ru/Pt catalysts demonstrate dominant catalytic performance, however, considering the industrial costs, non-noble metals are always more preferable. Optimizing non-noble catalyst systems to enhance their properties is also crucial for gaining better understanding on the nature of non-noble metal formulations.

With this aim in mind, first we designed bare Ni nanoparticles with different shapes, and analysed their morphologies, crystallinities and compositions. Amorphous structures and P-doping were found to be critical factors in enhancing catalytic performance of Ni, which leads to Ni nanosphere catalysts being a very active catalyst with a reaction barrier of only 22.45 kJ/mol for glucose hydrogenation. Then, Carbon black (CB) and graphite nanoplatelets (GNPs) carbons were introduced to prepare supported catalysts and further make comparisons between supports. By controlling the synthesis temperatures, Ni nanoparticles with different sizes (7 nm to 24 nm) were obtained on both supports. Ni catalysts with CB support always show higher reactivities than with GNPs support when they were prepared in a same condition. And Ni particles supported by CB with a size average of 17 nm exhibit the highest catalytic performance compared with catalysts with other sizes. Furthermore, we introduced Fe into the Ni catalysts to form Fe-Ni alloy catalysts with CB support, which achieves more than twice the glucose conversion of a monometallic Ni catalyst. The Fe:Ni ratio 1:1 was identified as the best compromise to achieve a high catalytic activity as well as high sorbitol selectivity. Finally, we investigated the morphology, crystallinity and composition of the catalysts before and after use, and found that sintering, surface oxidation and leaching were the main causes of deactivation, and we eventually achieved the mitigation of leaching by changing the catalyst composition and reaction conditions.

Table of Contents

List of abbreviations

AAAS: American Association for the Advancement of Science

ATR: Attenuated Total Reflectance

BET: Brunauer - Emmett - Teller

CB: Carbon black

CNT: Carbon nanotube

CPME: Cyclopentyl methyl ether

CT: Charge transfer

DF image: Dark-field image

DFT: Density functional theory

DI water: Deionized water

DMF: Dimethylformamide

E_a: Activation energy

EDX: Energy-dispersive X-ray spectroscopy

EMSI: Electronic metal-support interaction

FTIR: Fourier-transform infrared spectroscopy

FT: Fischer-Tropsch

FWHM: Full width at half-maximum

GNPs: Graphite nanoplatelets

HAADF: High-angle annular dark-field

HDA: Hexamethylenediamine

HOMO: Highest occupied molecular orbital

HMF: 5-hydroxymethyl furfural

HYZ: HY Zeolite

HR- TEM: high resolution TEM

ICP-OES: Inductively coupled plasma optical emission spectrometry

IUPAC: International union of pure and applied chemistry

LUMO: Lowest unoccupied molecular orbital

MWNTs: Multi-walled carbon nanotubes

ML: Megalangmuir

NP: Nanoparticle

NMR: Nuclear magnetic resonance spectroscopy

ORP: Oxidation-reduction potential

PBE: Perdew - Burke - Ernzerhof

PVP: Polyvinylpyrrolidone

r.h.p.: Reversible hydrogen potential

SAED: Selected area electron diffraction

SMSI: Strong metal-support interaction

TGA: Thermogravimetric analyses

TOF: Turnover Frequency

TOP: Trioctylphosphine

TPD: Temperature-programmed desorption

TEM: Transmission electron microscopy

WGS: water-gas-shift

XPS: X-ray photoelectron spectroscopy

XRD: X-ray diffraction

YSZ: Yttria-stabilized zirconia

Chapter 1

Introduction

1. Introduction: theoretical background and objectives of the thesis

1.1. Biomass

Biomass is plant or animal material used as source to produce electricity, heat, fuel or chemicals. It includes lignocellulose (wood blocks, chips, sawdust, branches, etc.), agricultural waste, aquatic plants, oily plants, organic matter, industrial waste, livestock manure, etc (Figure 1.1). [1, 2] Biomass resources are extremely rich, and the world's annual biomass production is about 146 billion tons. [1] The United Nations Conference on Environment and Development (UNCED) predicts that by 2050 biomass energy utilization will account for about half of global energy consumption.[1, 3]. And production of chemicals from biomass also offers a promising opportunity to improve the overall economics and sustainability of an integrated biorefinery while reducing dependence on oil. And the annual growth rate of the potential of bio-based chemicals in EU markets was estimated to be at about 3.6% per year from 2018 to 2025 in a new Joint Research Centre (JRC) study.[4]

Figure 1.1. The sources of biomass fuels. Copyright from Elsevier B. V. 2016. [1]

1.1.1. Typical biomass

1.1.1.1. Lignocellulosic biomass

Lignocellulosic biomass refers to plant biomass like trees, grass, corn stover, *etc*.which are composed of cellulose, hemicellulose and lignin.

Cellulose accounts for 40 – 50% of the total lignocellulose. It is currently the most abundant biopolymer material known in nature, and it is also an important component in the process of biomass conversion and utilization.[5] Cellulose is consisting of a linear chain of several hundred to many thousands of β D glucose units linked by 1, 4-β glycosidic bonds, with a highly ordered crystalline structure and intramolecular hydrogen bonds. Therefore, cellulose is insoluble and difficult to be degraded. The platform molecule of cellulose hydrolysate glucose allows converting cellulose into many other high value-added downstream products.

Hemicellulose accounts for 25-35% of lignocellulose, of which polyxylose is the most abundant. Unlike cellulose, which only contains a single component of glucose, hemicellulose is formed by the polymerization of multiple sugars, including xylose, arabinose, mannose, glucose, galactose, and other sugar acids.[6]

Lignin accounts for 18-25% of the total lignocellulose. It is mainly composed of phenylpropyl units and contains carboxyl, hydroxyl and other functional groups also polymerized in complex networks.[7] Lignin contains rich aromatic compounds. However, the complex and uncertain composition of lignin limits its efficient use.

1.1.1.2. Oil and algae

Animal fats and vegetable oil are also important raw materials in industrial production. Oleochemicals mainly contain about 52% oleic acid, 11% methyl esters, 9% amines, and 25% alcohols.[8] The transformation of animal and vegetable oils can give surfactants, lubricants, coatings, etc.

Algal biomass is a type of eukaryotic organisms in the Protist Kingdom, including macroalgae and microalgae. Microalgae usually contains oils with carbon chain length of C14~ C26 and a certain content of free fatty acids (20% - 50%).[9]

1.1.2. Biomass conversion

Most of the biomass energy needs to go through a transformation process before use, except for the anaerobic treatment of human and animal manure and the direct extraction of oil and sugar-containing crops. Due to the differences in physical and chemical aspects of biomass resources, the conversion methods mainly include physics, chemistry and biology

technologies, through which the renewable biomass energy are converted into heat, electricity, clean high value-added gas or liquid products. (Scheme 1.1)

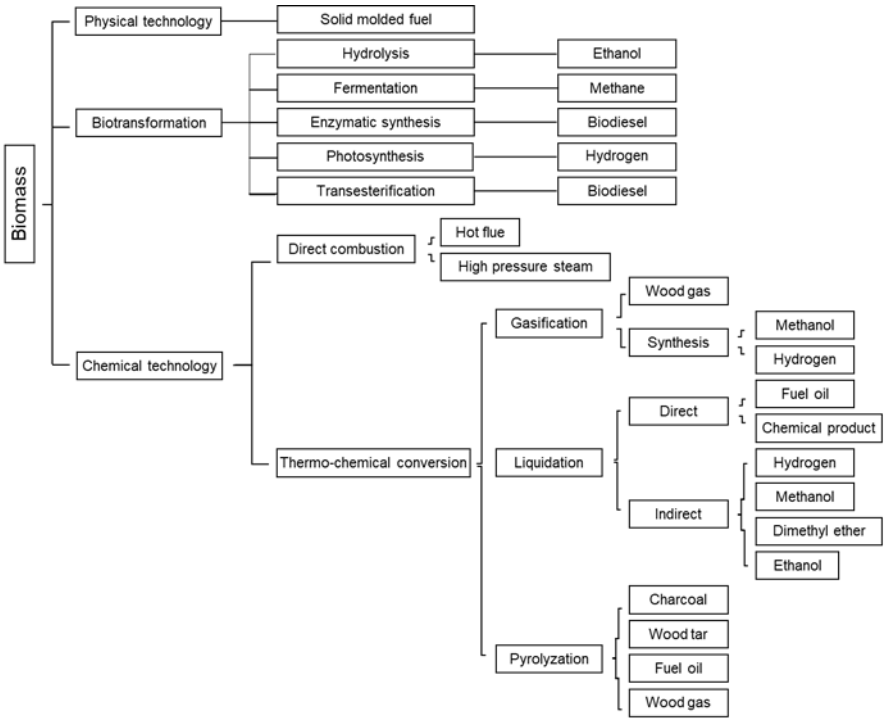

Scheme 1.1 Biomass energy conversion technology and products.

1.1.2.1. Physical and biological conversion technology

Physical conversion is essentially a process of mechanical pressing of crops with high oil content to produce oil and protein panels. The obtained oil, a mixture of methyl esters of fatty acids, can be used directly as fuel for diesel engines (modified) or chemically treated to make diesel fuel (biodiesel).

Biotransformation is the technology that uses microbial fermentation to convert biomass into fuel products like alcohol, acid, H_2 etc. Hydrolysis, anaerobic fermentation and hydrogen production are three main technologies used in this process. Ethanol is the main product from the fermentation of the hydrolysis materials obtained from sugar solution, starch, lignocellulose, etc. Anaerobic fermentation refers to the decomposition of biomass with bacteria in the absence of oxygen, producing organic acids, alcohols, H_2, CO_2, CH_4, etc. Hydrogen production by photosynthetic microorganisms (bacteria) is

mainly used with algae, which decomposes substrates through photosynthesis to produce hydrogen.

1.1.2.2. Chemical conversion technology

High valued-added charcoal, tar and combustible gas can be produced through biomass chemical conversion technology. This technology can be roughly divided into: direct combustion to produce heat and electricity, thermochemical conversion to produce outputs of heat, or gaseous or liquid precursors for upgrading to liquid fuels or chemical feedstocks. Thermochemical conversion covers a range of technologies including gasification, liquidation and pyrolyzation, and catalysts are widely applied in this technology.

In this chemical conversion technology, comprehensive research has been carried out worldwide in the last decades to study the efficient conversion of biomass resources into valuable biofuels and high value-added products with the presence of catalysts. Among those investigations, one attractive route is the preparation and utilization of sorbitol, which has been recognized as one of the 12 important platform chemicals obtainable from biomass.[10] Sorbitol is usually produced by glucose hydrogenation in the presence of Ni, Ru, Pt, Co or other metal-based catalysts.[11-13]

1.1.3. Glucose and Sorbitol

1.1.3.1. Glucose and its transformation

Glucose is a polyhydroxy aldehyde with molecular formula $C_6H_{12}O_6$, (Figure 1.2). D-glucose is one of the sixteen aldohexose stereoisomers. The D-isomers are widespread in nature, while L-isomers are rare and less important. D-glucose is one of the most significant monosaccharides in nature. Pure glucose is colourless and crystalline, easily soluble in water, slightly soluble in ethanol, and insoluble in ether. The natural glucose aqueous solution rotates polarized light to the right. The glucose molecule can exist in an open-chain (acyclic) as well as ring (cyclic) form. It is usually present as a closed pyran ring in the solid form and as a monohydrate. In aqueous solution, less than 0.02% of glucose molecules are open-chain and the furanose forms exist in negligible amounts, while α- or β-pyranose forms are predominant. Three known forms of glucose can be crystallized from aqueous solutions: α -glucopyranose, β-glucopyranose and β-glucopyranose hydrate.[14]

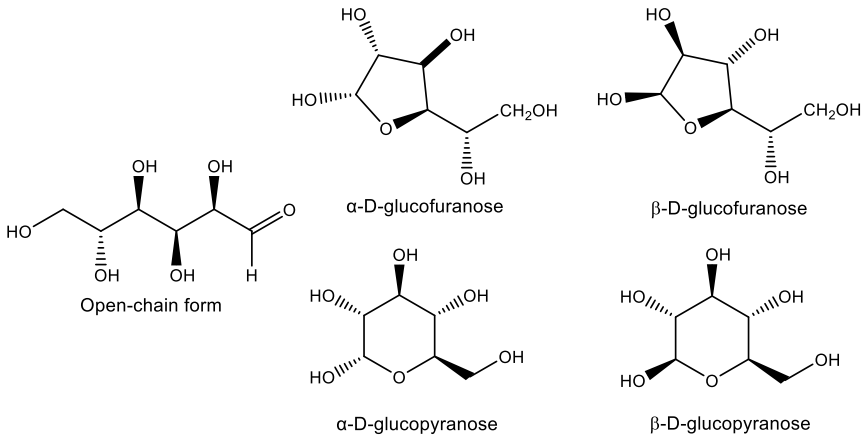

Figure 1.2. The structure of glucose.

Since glucose has five hydroxyl groups and one aldehyde group or pyranose ring, it can undergo isomerization, dehydration, hydrogenation, oxidation and other reactions (Scheme 1.2). Glucose isomerization produces fructose through proton transfer (base catalysis) or intermediate hydrogen species transfer (acid catalysis).[15] This isomerization reaction is also called Lobry de Bruyn–Alberda–Van Ekenstein transformation.[16] Glucose undergoes dehydration under acidic conditions to produce 5-hydroxymethyl furfural (HMF). HMF is an important intermediate, which can be used to prepare

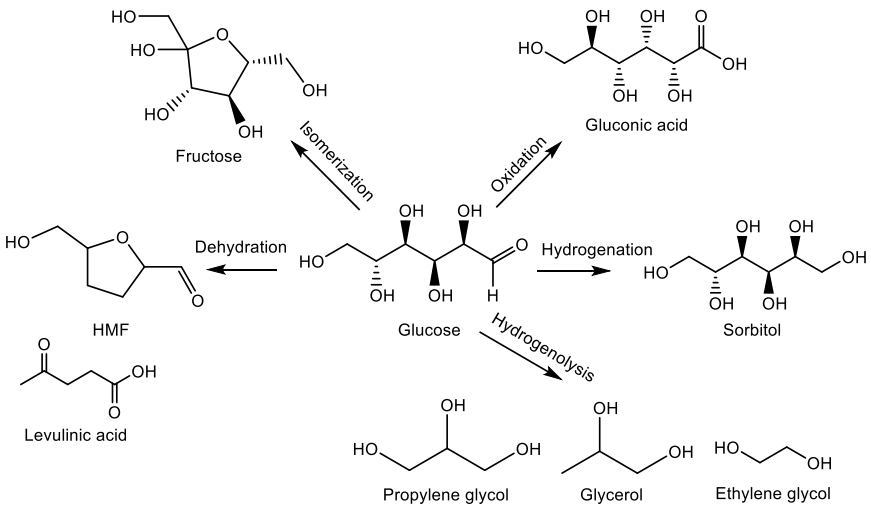

Scheme 1.2. A reaction scheme for glucose transformation into products.

furandial, furandicarboxylic acid, furandiol, levulinic acid, etc.[17] Glucose can be oxidized by bromine or by O_2 in presence of Pd, Au, Pt catalysts to produce gluconic acid or diacids, which are mainly used as a protein coagulant, food preservative and food acidity regulator.[18-22] Glucose can be hydrogenated by Raney Ni, Ru/C, Pt catalysts to produce sorbitol.[12, 23]. Glucose hydrogenolysis reaction can be used to produce glycerol, propylene glycol, and ethylene glycol.[24, 25]

1.1.3.2. Sorbitol

Sorbitol, with a molecular formula $C_6H_{14}O_6$, is the main photosynthesis product of Rosaceae plants and is mainly produced industrially by hydrogenation of glucose. Sorbitol is a white hygroscopic powder or appears as a crystalline powder, flakes or granules, easily soluble in water, slightly soluble in ethanol and acetic acid. Sorbitol has a cool and sweet taste, is commonly used as food sweetener, as well as for improving food moisture retention. It is the raw material of choice for the production of vitamin C and surfactants. It can also be used to synthesize resin plastics, separate and analyse low boiling point oxygen-containing compounds, etc.

Chemical technology provides the possibility to convert biomass into usable high value-added products and biofuels, and catalysts play a crucial role in this process. Therefore, the continuous design of state-in-art and more effective catalysts to accelerate biomass conversion production can not only meet material and fuel needs, but also is the key to the green and sustainable development. We will introduce the broad concept of catalysis in the next section.

1.2. Catalysis

The term *catalysis*, first proposed in 1835 by Swedish scientist Jöns Jakob Berzelius comes from the Greek words *kata* meaning down and *lyein* meaning loosen. In 1901, the German physical chemist W. Ostwald articulated the definition of catalyst, that is, “a catalyst is a substance that accelerates the rate of a chemical reaction without being a part of either the reactants or the products”.

This reaction acceleration can be explained by Figure 1.3 [26] The non-catalytic and catalytic reaction processes are both shown in an energy diagram. The product P only can be obtained when substrate A and B collide

with sufficient energy to overcome the activation barrier. In a catalytic system, the reactants absorb onto the surface of the catalyst, activate, and then the product P desorbs, while in a non-catalytic system, A and B directly react with each other without any assistance. Therefore, the activation energy in a non-catalytic system (E_{a1}) is obviously much higher than it is in a catalytic system (E_{a2}), but the overall change in free energy (ΔG) in each system is the same. Hence, the catalyst does not affect the equilibrium constant of the reaction, only its speed.

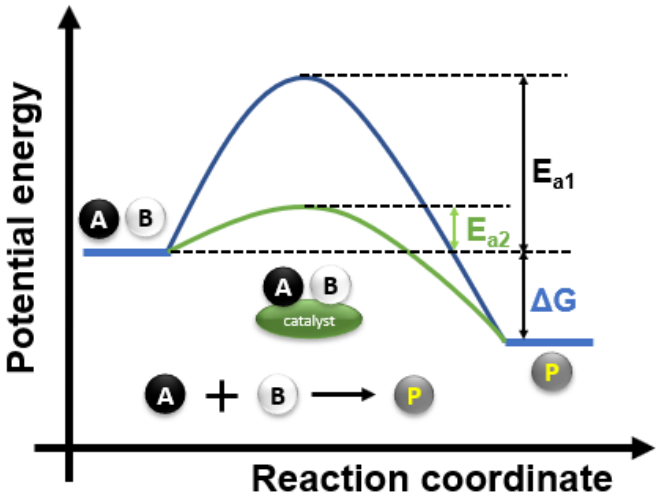

Figure 1.3. Potential energy diagram of a heterogeneous catalysed reaction, with gaseous reactants and product and a solid catalyst.

1.2.1. Homogeneous catalysts, enzymes, and heterogeneous catalysts

The chemical industry cannot exist without catalysts. Approximately, 85-90% of industrial processes use catalysts, for the production of bulk chemicals, biochemicals, fuels, plastics, pharmaceutical ingredients etc. Homogeneous catalysis, enzymatic and heterogeneous catalysis are the main three subdisciplines in catalysis (Figure 1.4).

If the catalyst and the reactants are in the same phase, then the catalyst is a homogeneous catalyst, which includes liquid acid/base catalysts, soluble transition metal compounds (salts and complexes), etc. Homogeneous catalysts act independently as molecules or ions, with uniform active centres,

high activity and selectivity. The major disadvantages are low stability and difficulty to separate from the reactants and products.

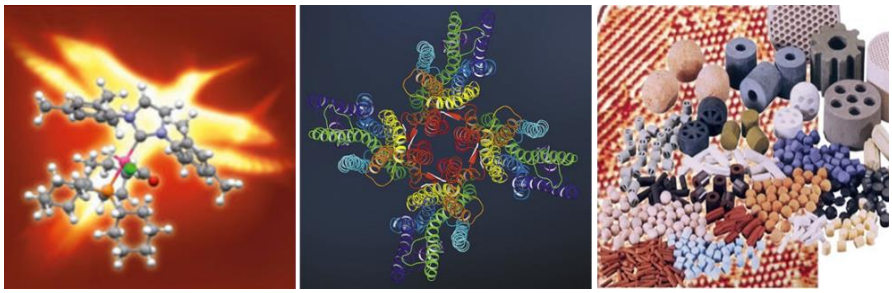

Figure 1.4. Homogeneous catalyst (left),[27] enzyme (middle),[28] heterogeneous catalysts (right) [29].

Enzymes are catalysts from nature, which actually are proteins comprising very often a prosthetic group. Due to the specific structure of the protein, the enzyme exhibits a particularly active catalytic site. Thus, enzymes are highly specific and efficient catalysts. Enzymes have been widely used in chemical and other industries because they can efficiently catalyze specific reactions. In general, the application of enzymes is limited due to the small number of reactions they can catalyze, and their instability in organic solvents and high-temperature environments.

Heterogeneous catalysts are in different phases from the reactants and products, thus it solves the problem of separation, which is considered as the most important feature of heterogeneous catalysts, and so is the case for the reaction of aqueous glucose hydrogenation that we are focusing on in this thesis. Heterogeneous solid catalysts are currently the most used catalysts in the chemical and petrochemical industry, including applications in gas phase and liquid phase transformations. Zeolites, alumina, higher-order oxides, graphitic carbon, transition metal oxides, metals such as Raney nickel for hydrogenation, and vanadium oxide for oxidation of sulfur dioxide into sulfur trioxide are the most important heterogeneous catalysts.[30] We will now delve more into this fascinating topic.

1.2.2. Modification of catalysts

Heterogeneous catalysts can be divided into bulk catalysts and supported catalysts. Bulk catalysts comprise mainly active substances, while supported catalysts are the catalysts that are made by supporting the active components

and promoters on a carrier. This carrier is introduced to potentially reduce the amount of needed metal and improve the catalytic activity and stability. Understanding the components of supported catalysts could help to find ways to modify and optimize its properties.

There are usually two to three main components in the supported catalyst: active phase, eventual promoter, and carrier. (Figure 1.5)

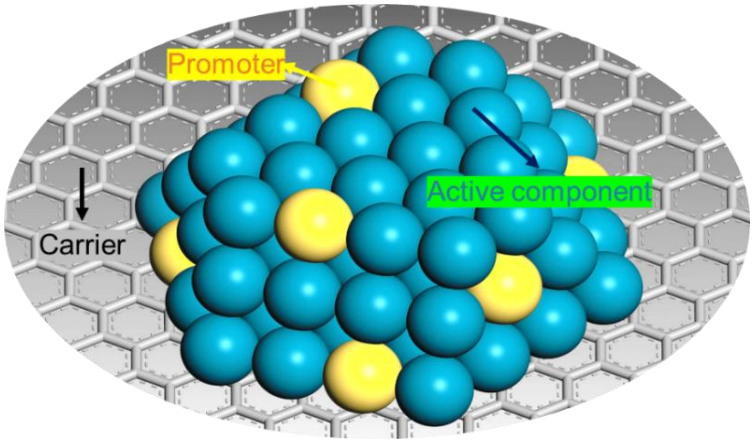

Figure 1.5. Carrier, promoter and active components of a supported catalyst (Modified from Britannica).[31]

The active component is the fundamental substance that plays a catalytic role. For example, in the synthesis of ammonia with Fe / K_2O or Al_2O_3, iron metal is always active, independently from K_2O and Al_2O_3, but the activity is slightly lower, and the life span is slightly shorter without K_2O and Al_2O_3. On the contrary, if there is no iron in the catalyst, the catalyst has no activity at all, so iron is the active component in the ammonia synthesis catalyst.

The promoter is a small amount of substance added to the catalyst, which is an auxiliary component of the catalyst. It has no activity or low activity. However, the promoter can change the chemical composition, chemical structure, ionic valence, acid-base, lattice structure, surface structure, pore structure, dispersion state, mechanical strength, etc., so as to improve the activity, selectivity, stability or lifetime of the catalyst. Generally, there exists an optimal content of promoter to get these improvements.

The physical structure and physical properties of the carrier also have a vital influence on the properties of the catalyst.

Thus, based on the structure of supported catalyst, extensive efforts have been put on particular aspects such as changing supports, manipulating size, shape, composition of the catalytic active particles to design and optimize supported catalyst systems. These will now be discussed in more details with illustrative examples from the literature.

1.2.2.1. Support effect

Dispersing metal species on an appropriate substrate (like carbon, oxides, etc.) enables to significantly change the electronic structure and geometric configuration of metal species via the interaction between metal species and supports. Early empirical research concerning surface characteristics and associated density functional theory calculations show that, for unsupported Au, dissociative adsorption of H_2 and O_2 does not take place at temperatures lower than 473 K, and so it would not be expected to exhibit catalytic activity in respect of hydrogenation and oxidation reactions.[32] However, in the late 1970s, alkene and alkyne hydrogenation were achieved by means of an Au/SiO_2 catalyst.[33] So, supported gold catalysts exhibit unique catalytic performances different from unsupported gold.[34] Further research by Valden et al. concerned that the supported gold nanoparticles exhibiting enhanced activity in low-temperature CO oxidation conditions. [35] J.A. Rodrigueza et al. studied the importance of O vacancies in the activation of gold using a series of gold/ceria systems for destruction of SO_2 and water-gas shift (WGS) reactions. They found the full decomposition of SO_2 was only observed in Au/CeO_2 with O vacancies in the ceria support, and Au NPs in contact with O vacancies of the oxide are the active sites being responsible for the WGS activity at high temperature.[36, 37]

Charge transfer (CT) effects were found existing in the catalysts of nanoparticles (NP) supported on metal oxides. Hakkinen et al. demonstrated that remarkable nanocatalytic properties are due to the charge transfer from the support to the metal clusters. [38] This effect was examined when Au_n particles grow on a rutile TiO_2 (110) surface using gradient density functional theory (DFT) slab calculations, which demonstrated that the delocalization of electrons from oxygen vacancies of the TiO_2 surface change the adsorption and diffusion of Au adatoms due to the difference of potential energy of the surfaces (Figure 1.6).[39] Similar calculations were also done by Siris and Suljo. They suggested that the electronic charge accommodated in the Ti 3d

states of TiO_2 is readily transferred to Au, which account for the fact that oxide-supported Au are promising low-temperature oxidation catalysts.[40] Indubitably, the electronic structure of Au NPs is affected by this charge transfer.[41, 42] Sanchez et al. further highlighted the significant role that electronic effects (charge transfer in metal-support and metal-adsorbate interactions) play in mediating the structural dynamics of supported metallic nanoparticles. Particularly, they revealed that adsorption of hydrogen or oxidation of the Pt particles on γ-Al_2O_3 support reduces or increases the cluster-support interaction, while this effect is much weaker when Pt nanoclusters are supported on a carbon black support.[43]

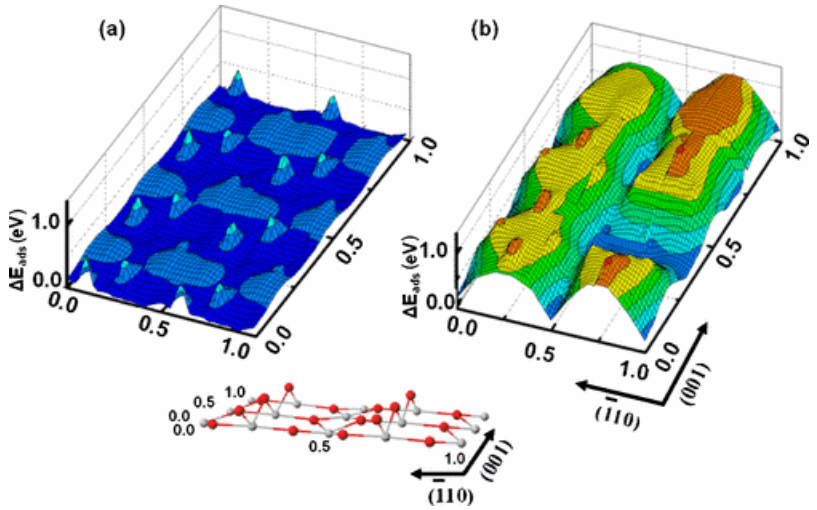

Figure 1.6. Potential energy maps for a single Au on (a) stoichiometric and (b) reduced TiO_2 (110) surfaces. The relative adsorption energies (ΔE_{ads}) in eV are calculated with respect to the lowest adsorption energy on each (2 × 3) surface cell considered. Bottom-middle is stoichiometric surface and reduced surface is prepared by removing a bridging O from a given surface. [39] Copyright from APS physics 2005.

Not only does the chemical composition of the support affect the reactivity of the catalyst, but also does the crystal structure of the support. Yan et al. revealed that Au supported by brookite TiO_2 has a better activity and stability than an anatase support.[44] Li et al. also found that Pt supported by carbon nanotubes produced better performance for cathode catalysts in a direct methanol single cell compared to commercial XC-72 carbon, which may be attributed to the unique structure and better electric properties of the CNTs.[45]

Dispersed nanoparticles can be easily agglomerated with each other to reduce their surface energy, inducing a decrease in catalytic performance. In most of the cases, solid supports play an essential role in stabilizing the NPs.[46] Croy et al. observed the difference in catalytic performance and stability of metallic Pt NPs by studying the decomposition of methanol with reducible (CeO_2, TiO_2) and non-reducible supports (SiO_2, ZrO_2, Al_2O_3). The smallest Pt particles (~ 8 nm) on ZrO_2 were found to be cationic and the most active for methanol decomposition at low temperature and H_2 selectivity compared to other supported Pt NPs (Figure 1.7). Besides, Pt NPs on CeO_2 supports underwent a significant coarsening after catalyst pretreatment, while Pt NPs on ZrO_2 didn't.[47]

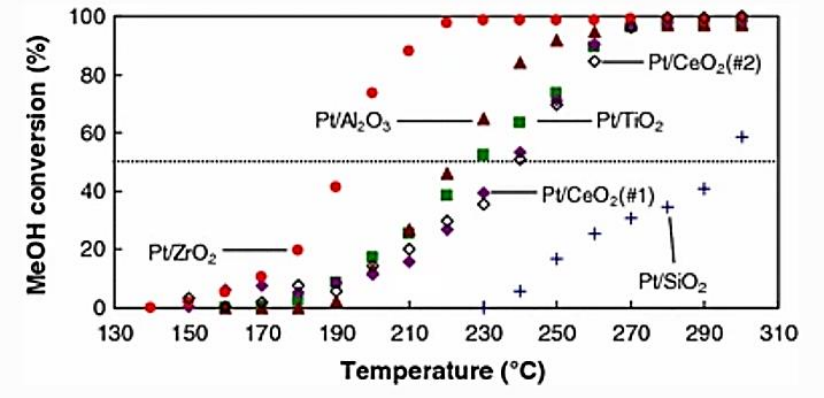

Figure 1.7. MeOH decomposition over Pt nanoparticles supported on nanocrystalline oxide powders: Pt/ZrO_2 (●), Pt/Al_2O_3 (▲), Pt/TiO_2 (■), Pt/CeO_2(#1) (◆), Pt/CeO_2(#2) (◊), Pt/SiO_2 (+). All samples have been calcined at 500 °C for 2.5 h before the reaction. [47] Copyright from Springer Link 2007.

All in all, supports possess several ways of affecting the reactivity of the overlying NPs: (i) in the way of charge transfer from or to the NPs, (ii) by changing the structure and shape of the NPs, (iii) by restraining the coarsening of NPs thus enhancing the stability, (iv) by providing additional reaction sites, (v) by encapsulating the NPs at high temperatures, (vi) by stabilizing intermediate reaction species. [42] Thus, support effects are a nonnegligible factor when considering designing new catalysts and understanding the origin of the catalytic reactivity of supported NPs.

1.2.2.2. Size effect

It is well known that metal species with different sizes exhibit different catalytic behaviours for many types of heterogeneous catalytic reactions. Haruta Masatake et al. prepared gold catalysts (~5 nm) with one of the oxides of 3d transition metals of group VIII, namely, Fe_2O_3, Co_3O_4, NiO by coprecipitation, which were found to be not only much more active but also much more stable than the conventional hopcalite catalysts for CO oxidation reaction in 1987.[49] Ono et al. also revealed an improvement of the catalytic activity with decreasing particle size of Au NPs supported on TiC for CO oxidation reaction.[50] Reske et al. observed the particle size effects during catalytic CO_2 electroreduction on Cu nanoparticles. 2-15 nm Cu NP catalysts were prepared to compare their catalytic activity and selectivity. A dramatic increase in the catalytic activity and selectivity for H_2 and CO was observed with decreasing Cu particle size, especially for NPs below 5 nm. Higher population of low-coordinated surface sites in smaller particles were linked to their higher catalytic activity compared to bigger ones.[51] Particle size effect studies on cobalt NPs performance in Fischer-Tropsch (FT) synthesis found

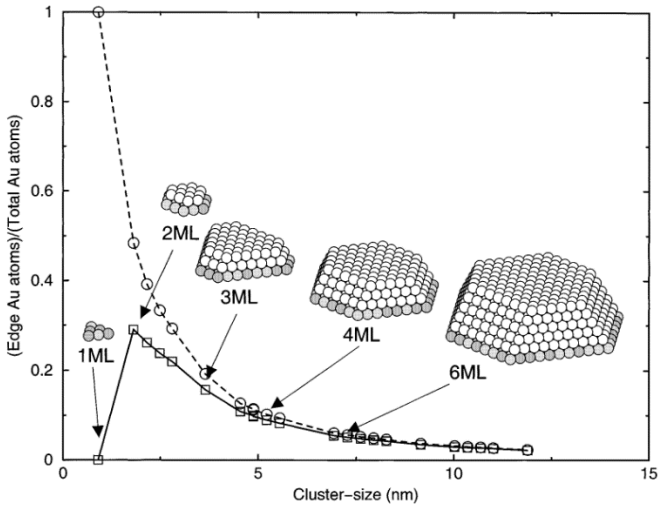

Figure 1.8. Calculated step density for Au particles on TiO_2 as a function of particle size. (○) and (□) correspond to the total and "free" step sites on the Au particles. "Free" are the step sites not in direct contact with the support. Insets illustrate the corresponding Wulff constructions for selected particle sizes. [48] Copyright from Springer Link 2000.

that lower TOF were obtained when Co particles are below 6 nm, which is due to both blocking of edge / corner sites and a lower intrinsic activity at the small terraces.[52] [53] Based on DFT calculations, those high stepped surfaces were shown to be preferentially chemisorbed with substrates like CO, O and O_2, as a consequence of enhanced reactivity of the small particles. (Figure 1.8).[48]

DFT calculations showed that the electronic structures change along with the particle in different size ranges (nanoparticles, cluster, single atom), and electronic properties of metal particles seriously change when going below 1 nm.(Figure 1.9) [54] These electronic property changes with particle size can be measured by detecting binding energy shifts by X-ray photoelectron spectroscopy (XPS).[50]

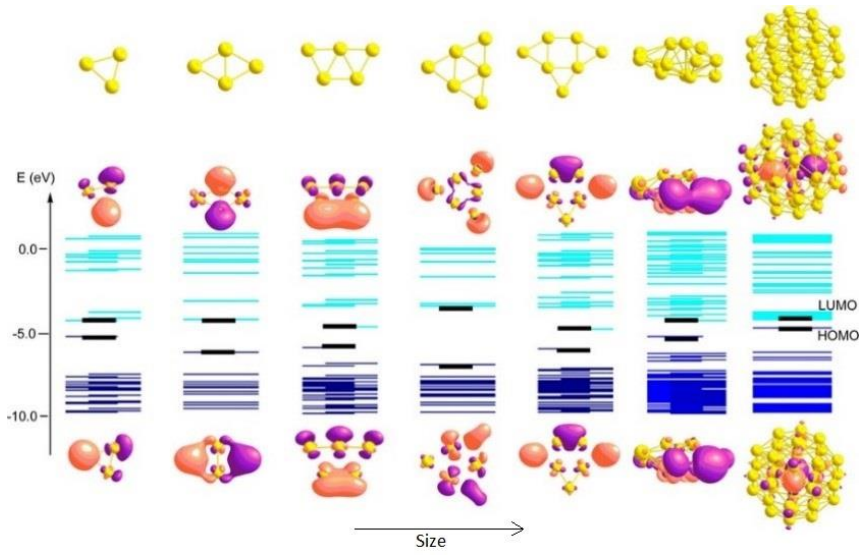

Figure 1.9. Electronic structures of Au clusters according to theoretical calculations. Optimized structure (top) and calculated isosurfaces of the lowest unoccupied molecular orbital (LUMO, center) and highest occupied molecular orbital (HOMO, bottom) of Au_3, Au_4, Au_5, Au_6, Au_7, Au_{13}, and Au_{38} clusters, together with molecular orbital energy levels in blue. Obtained at the B3LYP/LANL2DZ level using the Gaussian 09 program. [54] Copyright from American Chemical Society 2014.

This different electronic structure with different sizes of particles further affects charge transfers with the support, especially for Pt/CeO_2 catalyst with the electronic metal-support interaction (EMSI). Lykhach et al. measured the CT

as a function of particle size from very small aggregates to particles of 3.6 nm for Pt particles supported on cerium oxide, a versatile heterogeneous catalyst with applications in hydrogen production, reforming, environmental catalysis, and electrocatalysis.[55, 56] As shown in Figure 1.10, electrons transferred to support per particle increases with the size. The partial charge per Pt atom shows a linear increase with the size when the particle is below 70 Pt atoms, but the charge transfer is suppressed for larger particles. Thus, when the particle size is around 30-70 atoms (particle diameters approximately 1-1.5 nm), this charge per Pt atom shows a maximum, reaching 0.11 ± 0.025 electrons per atom. Those charges will be mainly localized at metal atoms in the vicinity of the interface for large particles, therefore small clusters consisting of a few atomic layers are close to the CT maximum. This CTaltering by adjusting the particle size should markedly change the catalytic properties of the metal particles.

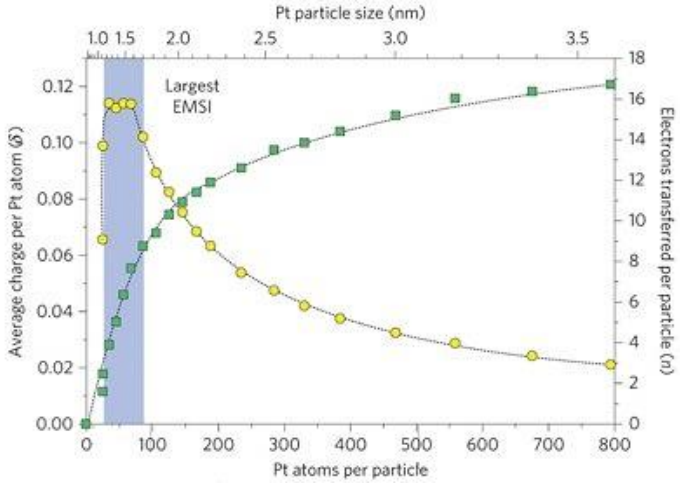

Figure 1.10. The number of electrons transferred per Pt particle to the ceria support increases with increasing particle size (green squares). The partial charge per Pt atom reaches a maximum for particles with 30 to 70 atoms (yellow circles).[56] Copyright from Springer Nature Limited 2016.

The particle size also has a high influence on the stability of supported metal species. Campbell et al. have specified the thermal stability of Ag particles as a function of particle size using adsorption heat of metal atoms onto a metal particle as an indicator.[57, 58] According to their work, when the particle size is in the range of 1-6 nm, their thermal stability strongly increases with the size,

and a particle will stay relatively stable towards sintering when it is as large as 6 nm. Haasterecht et al. investigated the nickel particle growth with supported Ni NPs in the aqueous phase reforming of ethylene glycol. They observed that initially smaller Ni particles (~12 nm) supported on Al_2O_3 outgrew Ni particles with initially larger particles (~20 nm), which was attributed to the higher susceptibility to oxidation of the smaller Ni nanoparticles and differences in initial particle size distribution.[59]

In summary, several causes lead to distinct changes in the catalytic reactivity of NPs as a function of NP size, just like the support effect discussed in the previous section. For the smallest NPs, the surface to volume ratio is higher, generating a larger number of low-coordinated atoms available for interaction with chemical adsorbates. The electronic properties of metal NPs changing, distinct effects including CT effects at the vicinity of NP / support interface play vital roles in chemical reactivity and stability of NPs. Those factors mentioned above accounting for the size effect could take place in parallel, and the underlying origin of this effect is still an open question.

1.2.2.3. Shape effect

Since platinum NPs with different shapes were prepared for the first time in 1996,[61] a lot of attention has been drawn into the synthesis of metal nanoparticles with specific shapes, like tetrahedral,[62] cubic,[63] nanowire,[64] tetrapods,[65] *etc*. to explore their reactivity in different reactions. Metal nanoparticles with different shapes present different crystallographic faces to the surrounding medium, and crystal faces of NPs play an essential role in catalytic properties. For example, Xu et al. have found that the rate of oxidation of styrene over silver nanocubes was more than 14 times higher than that on nanoplates and 4 times higher than that on near-spherical nanoparticles (Figure 1.11).[60]

Those distinct differences in activities were attributed to the presence of different crystalline planes on each of these three shapes, with most reactive (100) facets on the nanocubes, in contrast to the (111) facets present on the nanoplates, and the mixture of (100) and (111) facets on the nanospheres. (Figure 1.11a) Komanicky et al. deployed nanofabrication techniques to generate nearly perfect platinum NPs with controlled particle numbers, shapes,

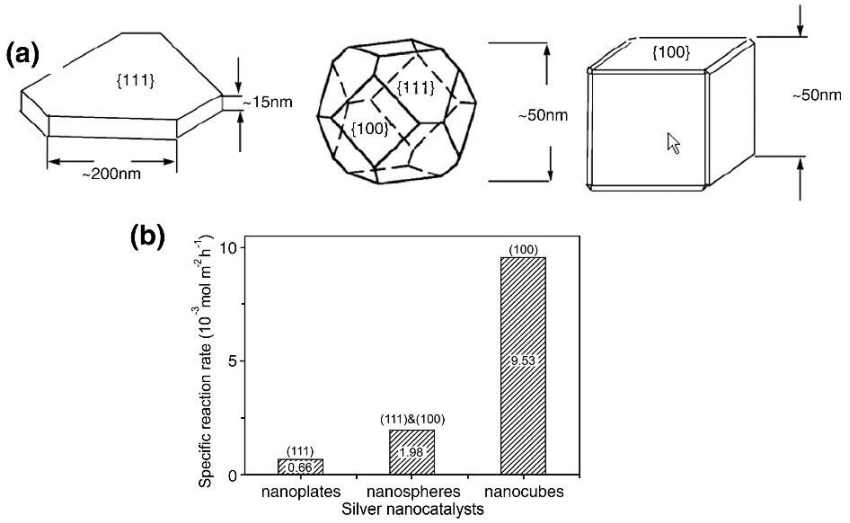

Figure 1.11. (a) The structural models of triangular Ag nanoplates (left), near-spherical (middle), and cubic (right) (b) Specific reaction rate of styrene conversion over Ag NPs with different shapes. Reaction time: 3 h. [60] Copyright from John Wiley & Sons 2006.

orientations, and positions and studied the macroscopic catalytic reactivities related to those morphologies. They observed that the surface area developed by (100) facets is one of the key factors governing the catalytic performance of oxygen electrochemical reduction.[66] One reason for the different activity on different facets is related to surface energies. Pt surface energies of (100), (111) and (110) faces has been calculated by Iddir et al. using the Perdew−Burke−Ernzerhof (PBE) functional, the result is shown in Table 1.1. It is obvious that the surface energies are different on each specific surface of Pt NPs.[67] A compiled list of experimental and calculated surface energies of some transition metals was done by Cabeza et al.[68]

Table 1.1 Calculated Pt surface energies with six layers of Pt.[67] Copyright from American Chemical Society 2007.

	Surface energy		
Surface	**eV/atom**	**J/m2**	**Ratio to (111)**
111	0.660	1.535	1.000
110	1.308	1.863	1.982
100	0.915	1.843	1.386

This difference in the surface energies of different facets in NPs naturally induces different interactions with adsorbed substrates. For example, Porwal et al. have studied the binding configurations of phenol on the (111) and (100) facets using DFT calculations. Two different binding configurations of phenol on the Pd (111) and (100) facets were found, as shown in Figure 1.12. Based on those configurations, a binding energy of -102 kJ / mol of phenol on Pd (111) surface was calculated, while this binding energy of the absorbed state of phenol on Pd (100) was -135 kJ / mol, which consequently affects the activation barriers involved in cyclohexanone hydrogenation on those two Pd facets.[69] Hydrogen adsorption on different facets of seventeen transition metals were also calculated using self-consistent DFT-GGA (PW91) by Ferrin et al. on the (100) and (111) facets of face-centered cubic (fcc) metals. On every facet studied, the existence of subsurface hydrogen is not expected, due to the relative instability of subsurface hydrogen with respect to surface hydrogen. The exothermic occupation of subsurface hydrogen occurs in few metals (Pd, Ta, V), but occupation of the surface is energetically favoured.[70]

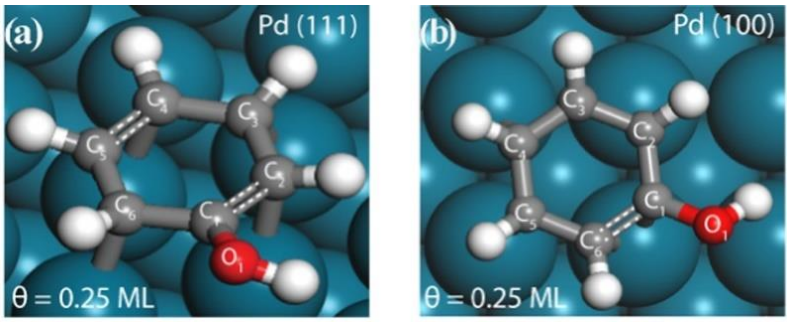

Figure 1.12 Adsorbed states of phenol on (a) Pd (111) and (b) Pd (100) surfaces at coverage (θ) = 0.25 MegaLangmuir.[69] Copyright from American Chemical Society 2019.

Those variation in surface energies and adsorption energies of molecules on different facets of metal NPs result in the shape effect on catalytic activity. A single-crystal of unusual tetrahexahedral shape of platinum nanocrystals was prepared by Tian et al, which is enclosed by 24 high-index facets such as (730), (210), and or (520) surfaces possessing a high density of atomic steps and dangling bonds. The electro-oxidation of small organic fuels such as formic acid and ethanol was largely enhanced by those high-energy surfaces as compared to equivalent Pt surface areas of NPs with different shapes.[71]

Octahedral Pd NPs with both (111) and (100) facets and tetrahedral Pd NPs with mainly (111) facets with a high amount of corners, edges and faces were very active in acetylene hydrogenation, thus they displayed the highest TOF compared to spherical Pd NPs with a mixture of different Pd facets.[72] DFT calculations showed that the barrier for ethylene hydrogenation was lower over Pd (100) surface than over Pd (111) surface, indicating that the latter is more selective towards ethylene.[73, 74]

Thus, different shapes of NPs also have an influence on the product selectivity. Jewell et al. found that the selectivity to ethylene in acetylene semihydrogenation with spherical Pd NPs supported by carbon decreased with increasing hydrogen pressure, while for large octahedral Pd particles comprising mainly Pd (111) only a minor drop in selectivity with pressure increase was observed. As well established, Pd can form α and β phases (Pd_4H_3) of Pd-H hydride at H / Pd ratio of 0.03 and 0.6, respectively.[75] Ethene prefers to absorb on the Pd_4H_3 (100) surface than (111) facets on spherical Pd NPs, but there is a phase change occurring on Pd_4H_3 phase at 0.1 bar of hydrogen pressure, so octahedral Pd NPs with mainly (111) facets has a higher selectivity than spherical Pd NPs with different facets.[73] However, for the selective hydrogenation of acetylene over Pd / Al_2O_3 catalyst, Kim et al. observed a lower acetylene conversion and ethylene selectivity over spherical NPs with a significant amount of (111) facets than cubic Pd NPs with (100) facets. The easier decomposition of subsurface H in Pd (100) contributed to its higher activity , and stronger adsorption of reactants on Pd (111) decreased ethylene selectivity.[76] Shape selective hydrogenation of ethylenic double bonds has also been demonstrated in furan,[77] phenol,[69] cyclohexene,[78] 1-hexene, [78] trans-stilbene[79] and buta-1,3-diene[80] hydrogenation. Besides, selective hydrogenation of a carbonyl bond especially for those compounds with high electron density in the carbonyl group was also highly affected by the NPs shapes.[81-87]

The above examples illustrate the need for having a thorough knowledge of the most stable NPs shapes to have a better understanding of the reactivity of catalysts and being able to optimize it effectively.

1.2.2.4. Composition effect

Since the Bronze Age, humans have discovered that simply mixing two metals to form an alloy would result in a hybrid material, which is stronger than each one of the separated metals involved.[88] It has been more than 4000 years since this discovery, and now we still manufacture multimetallic materials in this similar way to improve the mechanical properties for bulk metals. Apart from that, multimetallic materials also present distinct chemical properties. A well-known example is the creation of stainless steel. It is formed by simply alloying iron with small amounts of Cr and C to protect the bulk from oxidation, unlike pure iron, which is prone to rust when placed in an environment containing water, oxygen and/or salt. Thus, upgrading the simplest monometallic nanocrystals to bimetallic or more complex compositions would greatly enhance their properties, usually better than monometallic counterparts. For example, Ba-promoted Ru catalysts (made of two-dimensional barium-oxygen overlayer on Ru crystals) have been identified as the most active catalysts for ammonia synthesis.[89] Besides, economical aspects (when alloying with a cheaper metal) and long-term stability (because multimetallic systems are usually less easily deactivated) are also factors that have driven rapid development of multimetallic catalytic systems.

Several reasons have been put forward accounting for the enhanced catalytic performance of multimetallic systems. One is that changes of electronic structure of metal surfaces by charge-transfer phenomena between different metals in a multimetallic system induce changes in adsorption energy of adsorbates, and that affects activation barriers for specific chemical reactions. For example, Carlsson et al. found that the binding energy of CO to both Pd and Co sites in Co-Pd alloys is lower in the presence of the other metal. XPS study showed a larger shift of binding energy in the Pd 3d level and a lower binding energy shift in the Co 2p level, which suggests a redistribution of d-band states in the bimetallic systems, or a net polarization induced by the alloy. Interestingly, Co-atop sites are better preserved at bimetallic compositions, which is the favourable adsorption site for CO.[90] Liu et al used DFT calculations to analyse the adsorption of CO on Pd (111) and several Au/Pd (111) surfaces. They found CO was more favourably absorbed on the Pd adsorption sites surrounded by Au atoms, and there are ensemble effects and ligand effects emerging in the alloy. The former being a geometrical argument

regarding the surface structure while the latter is connected to electronic effects. Regarding the ensemble effect, Au weakens the interaction between CO and Au/Pd (111) surface when Au is at the adsorption site (Figure 1.13). For the ligand effect, Au changes the electronic structure of the surface metal atom by shifting of the d band centre away from the Fermi level, which results in a weaker interaction between the adsorbates and the metals. For adsorption on alloy surface, the predominant effect is the ensemble effect.[91]

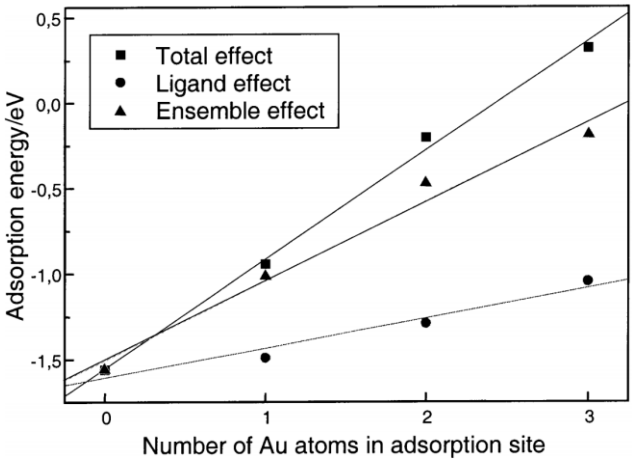

Figure 1.13. Separation of the ligand and ensemble effects from the total effect in the case of CO adsorption on hollow sites of Au / Pd (111) bimetallic surfaces. The number along the horizontal axis corresponds to the number of Au atoms at the hollow site. The squares, circles and triangles correspond to total effect, ligand effect and ensemble effect, respectively.[91] Copyright from Royal Society of Chemistry 2001.

Alloying Pt with less expensive metals in fuel cells has been studied by Hamnett, Demirci, et al.,[92-94] which is also a way to make direct methanol fuel cells more economically viable. Choi et al. prepared Pt-based binary or ternary catalysts systems as anodes for methanol fuel cells to compare the catalytic activities. They found the Pt / Rh (2:1) and Pt / Ru / Rh (5:4:1) alloy catalysts had better catalytic performance than Pt or Pt / Ru (1:1), respectively.[95] Ross et al. used Pt-Rh alloy system to understand the nature of the enhanced activity of the alloy for electrochemical hydrogen molecule oxidation in CO / H_2 gas mixture. They found CO coverage is almost the same with several alloys of different compositions, and the enhanced activity of Pt-

Rh alloys is related to the catalytic properties of a metal alloy with just one unpaired electron per atom, rather than 0.4 (0.6 hole) as in pure Pt.[96]

Multimetallic system can also improve resistance against poisoning and subsequent deactivation. Hamnett et al. found adding other metals to Pt not only enhanced the activity at the electrode, but also improved the resistance to poisoning in methanol oxidation reaction.[92] Igarashi studied the electrocatalytic activity for H_2 oxidation and also the CO tolerance in H_2 oxidation using binary Pt alloy electrocatalysts with non-noble metals in different compositions. They observed that the electronic structure of all the metal alloys composed of a thin Pt layer was different from pure Pt, suggesting an increased 5d vacancy of Pt in the layers of the CO-tolerant alloys. The CO was less covered in the alloy due to less electron donation from the Pt band to the $2\pi^*$ CO orbital. A "Detoxification mechanism" was proposed to explain the CO tolerance in the alloys.[97] Another example is Au-Ni surface alloy catalysts from steam reforming. There, Au in the Ni surfaces does reduce the barrier for hydrocarbon activation, giving therefore higher reactivity, but it decreases the stability of adsorbed C on Ni (Figure 1.14). Thus, the Au minimizes the formation of graphite, protecting the Ni catalyst from deactivation. Naitabdi et al. also demonstrated the high thermal stability of Au in Au-Fe NPs compared to pure Au.[98] A γ-Al_2O_3 supported Pd−Au bimetallic catalyst showed better resistance against carbon deposition than a Pd only catalyst in the hydrogenation of triacetic acid lactone to 5,6-dihydro-4-hydroxy-6-methyl-2H-pyran-2-one in a 1-butanol solvent during 60 h of reaction.[99] Recently, Ru–Sn on carbon gave stable activity and no apparent sintering and leaching compared to other monometallic (Pd, Pt, Ru) catalysts during continuous flow aqueous-phase reduction of succinic acid.[100]

However, multimetallic systems do not always show a positive effect on the catalytic performance. For example, Pt-M (M = Au, Pd, Ru and Fe) alloy catalysts showed lower reactivity than pure Pt NPs in the reaction of methanol decomposition, because the surface sites of Pt were occupied by less reactive metal M atoms.[101]

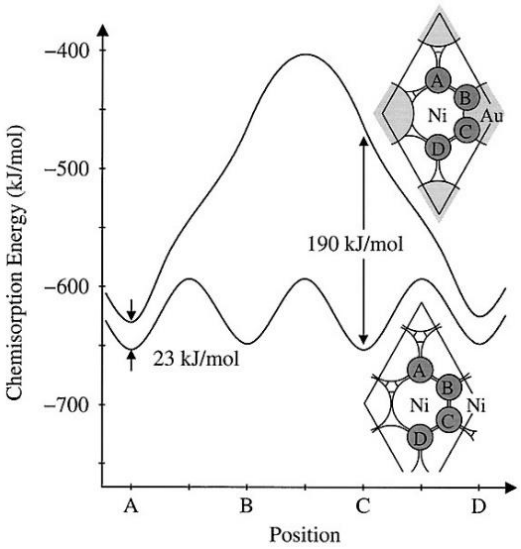

Figure 1.14. (Bottom curve) The calculated adsorption energy of a C atom on a Ni (111) surface as a function of position along the surface. (Top curve) The same energy function is shown when one of the surface Ni atoms has been exchanged for a Au atom. The insets show the geometry in each of the two cases.[98] Copyright from AAAS 1998.

Thus, using mutimetallic catalyst leads to several advantages: changing the electronic properties of NPs; enhancing the catalytic activity; altering the reaction pathway; preventing deactivation effects; definitely reducing the cost of the catalytically active noble elements. Those effects are significantly influenced by the surface properties of the multimetallic system, and the nature of the secondary metal, as well as the preparation and pretreatment conditions.

1.2.3. Catalysts deactivation

Catalyst stability is a significant factor to be considered for designing new catalytic systems, especially for industrial applications. Understanding the origin of catalyst deactivation is the only way to improve the lifetime of catalysts. Normally, several reasons are attributed to the catalyst deactivation: poisoning - active sites deactivated by strong chemisorption of molecular species; fouling deposit - active sites blocked by inert ingredients impacting the physical contact with the reactants; structure change - high temperature causing structural and surface properties change; loss of catalyst – leaching in liquid phase and evaporation with reactants in gas phase, etc. Thus,

catalysts can be deactivated in both gas and liquid phases. Here, we are focusing on liquid phase because most biomass transformations are performed in aqueous solution. Sintering, leaching, poisoning, carbon deposition and support hydrolysis or collapse are the main factors accounting for the deactivation of supported metal NPs catalysts in aqueous-phase reactions (Figure 1.15).[102]

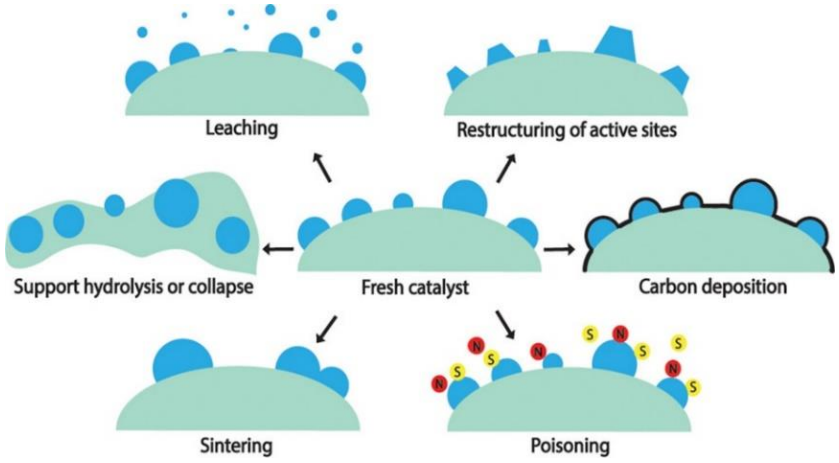

Figure 1.15. Schematic of supported metal catalyst deactivation modes during aqueous-phase reactions. Blue represents metal particles, while green represents the catalyst support.[102] Copyright from American Chemical Society 2021.

Water is able to react with various metal oxide chemical bonds and also metal NPs, especially under high temperature and high-pressure conditions.[103-108] Thus, support hydrolysis or collapse due to dissolution or structural changes happens under hydrothermal conditions. For example, γ - Al_2O_3 changes its phase to boehmite, and hydrolysis of zeolites and silica can also take place.[109] As a consequence, those collapsed supports significantly lose specific surface area, which further leads to active metal particles sintering or being buried inside the support. MgO partially dissolved has been reported during aqueous phase hydrogenation of furfural.[110] And HZSM-5 support was observed to lose its crystallinity in water when the temperature increased from 50 to 200 ^oC under N_2 pressure.[111] Kim et al. studied the hydrothermal stability over two catalysts systems: Pt/Zr-P and Pt-ReO_x/C in the aqueous-phase hydrodeoxygenation of sorbitol reaction. They found phase transformations in the Zr-P support during the reaction results in the

loss of 97% of surface area, 86% of Pt surface sites, and 95% of surface acid sites, but only 17% of surface area was lost in Pt - ReO_x / C, which showed a higher hydrothermal stability. Thus, carbon materials are typically selected for those processes as they usually show better stability under acidic or corrosive conditions than metal oxides supports.[112]

Leaching is the dissolution of active sites (metal or acid) into the reaction medium, which is usually sensitive to several parameters including temperature, pH, solvent, and presence of ions.[113] Metal complexation caused by the reaction between the supported metal and reaction species or solvent induces leaching.[114] Most of the metal oxides, hydroxides and carbonates utilized in catalysts can be slightly soluble in water.[115] Low leaching, even at ppm levels, can raise a lot of issues for both catalyst durability and products separation and purification as well as giving side reactions. Leaching can occur for either noble metals or base metals, but base metals are generally more prone to leaching. For example, Ni leaching was found in various supported Ni catalysts for aqueous phase glucose hydrogenation, but Ru catalysts are rarely leached away in the same conditions.[116] Jocz et al. used revised Helgeson-Kirkham-Flowers thermodynamic equation of state to determine the oxidation states and compositions of metals and oxides in water at 150-550 ^oC and 22-50 MPa. They found noble metals such as Ru, Au, Pd have much lower solubility compared to base metals such as Co, Ni, Cu and Fe.[117] Bimetallic systems also have the leaching issue, like Re leaching from Re-Pd/TiO_2, and this leaching behaviour is largely influenced by catalyst preparation, reaction conditions like solvent polarity and concentration of reactants or products.[118, 119] Complexation can enhance the leaching of metal. Settle et al. found by DFT calculations that the degree of Pd leaching from Pd/TiO_2 is correlated with the binding energies of Pd and adsorbates. The lower the binding energy, the more Pd leached (Table 1.2).[120]

Sintering generally can be described by the Ostwald ripening and particle migration and coalescence modes, which is often observed in gas-phase reactions at high temperature. But for aqueous-phase reactions, sintering can happen even at relatively low temperature. Three stages can be used to describe the sintering process of small metal nanoparticles (Figure 1.16).[121]

Table 1.2 Pd leaching from uncoated 0.5 wt% Pd/TiO_2 upon exposure to various oxygenates and corresponding substrate binding energy to an undercoordinated Pd site calculated using DFT.[120] Copyright from Elsevier B.V. 2019.

Oxygenate	Concentration %	Temperature °C	Pd Leaching ppm	Binding energy (Calculated) kJ/mol
Furfural	1	24	0.31± 0.01	
Hexanoic acid	1	24	1.20±0.70	-58
Adipic acid	1	24	3.39±1.05	-72
Muconic acid	1	24	6.09±0.10	-217

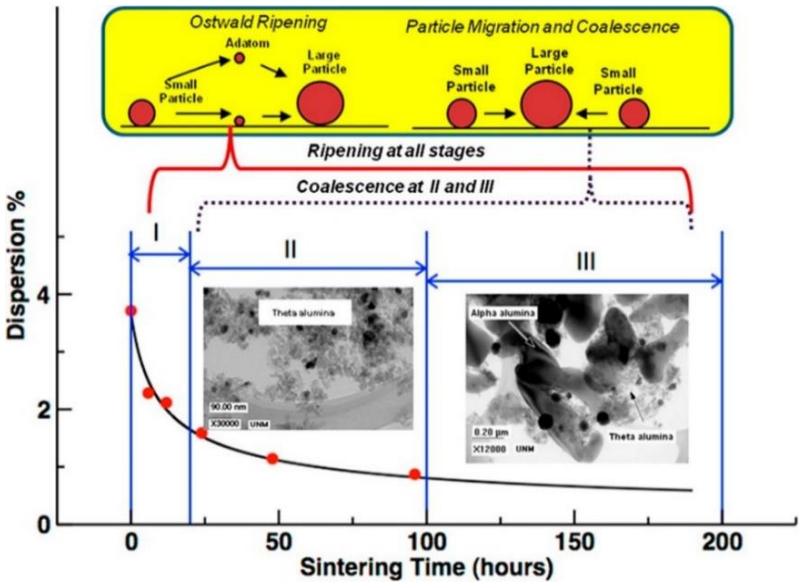

Figure 1.16. Schematic illustration of Ostwald ripening and particle migration and coalescence during the sintering process.[121] Copyright from American Chemical Society 2013.

In the first stage, activity is rapidly lost and small metal particles will agglomerate with adatom to large ones, which can be explained by Ostwald

ripening mechanism.[122, 123] The driving force is the different surface diffusion energy of metal particles with different sizes, which therefore can be controlled by optimizing the particle size in a narrow range. Phase II is where sintering slows down, and phase III is where the catalyst may reach a stable performance. In aqueous-phase reactions, since the temperature is usually below 250 ^{o}C, particle migration and coalescence are less likely. Sintering of supported metal NPs such as Ru, Pd, and Pt has been found on TiO_2, active carbon, carbon nanotubes, graphite, SiO_2 and Al_2O_3 in aqueous-phase reactions below 100 ^{o}C.[124-129] During the hydrogenation of levulinic acid, CuO NPs were found to sinter from 5.4 nm to 38 nm on the fresh Cu/ZrO_2 catalyst at 200 ^{o}C for 6h.[130] In fact, CeO_2 supported Au NPs with larger interparticle distance were found to have less sintering effects than Au NPs with smaller interparticle distance in aqueous-phase base-free oxidation of glucose to gluconic acid.[131] Techniques like liquid-phase TEM technologies have been used to study metal particle growth and dissolution in the condensed phase.[132-134] And operando X-ray absorbance spectroscopy was also used to monitor particle sintering.[135]

Fouling is a common phenomenon for deactivation in gas-phase reactions, especially at high temperature, which includes carbon deposition and coke formation, but it is also observed in some biomass conversion reactions in liquid phase because of those highly reactive oxygen functional groups in biomass-derived molecules. For example, formation of humins from carbohydrates species over HY zeolite can lead to carbon deposition.[136] Carbonaceous moieties can also cover the surface or block pores due to low solubility and strong adsorption.[137] In glycerol oxidation over Pt-B catalysts, active sites were blocked by adsorption of glycerol acid.[138] As a result, carbon deposition can lead to a significant decrease in surface area and pore volume of the support, then exacerbating the mass transfer limitations. For example, after 52 h of hydrogenation of levulinic acid continuous reaction, the surface area of Ru/C dropped from 1110 to 390 m^2 / g.[139] This carbon deposition such as coke or carbon fibres formation can further plug reactors in gas-phase reactions but not under hydrothermal conditions. Diluting reactants could reduce carbon deposition.

Poisoning is a phenomenon occurring when active sites are strongly chemisorbed with some reaction species including reactants or impurities like

N, S, P-containing species, organic acids, amino acids, inorganic salts, etc.[140] Different impurities affect catalysts differently. For example, in the levulinic acid hydrogenation reaction over Ru/TiO_2 and Ru/ZrO_2 catalysts, formic acid led to reversible deactivation, while furfural, HMF, and humins caused a gradual drop in activity, but H_2SO_4 resulted in irreversible deactivation. (Figure 1.17) [141] Gupta et al. used DFT calculations to understand the bonding interactions of biogenic impurities with the Ni (111) catalyst surface. They showed that amino acids containing S (methionine and cysteine) and heterocyclic N (tryptophan and histidine) interacted with Ni surface through nonbonding and bonding interactions.[142] Poison species can also come from the reactor, for example, Fe leached form the stainless reactor was found to poison a supported Ru metal catalyst.[143]

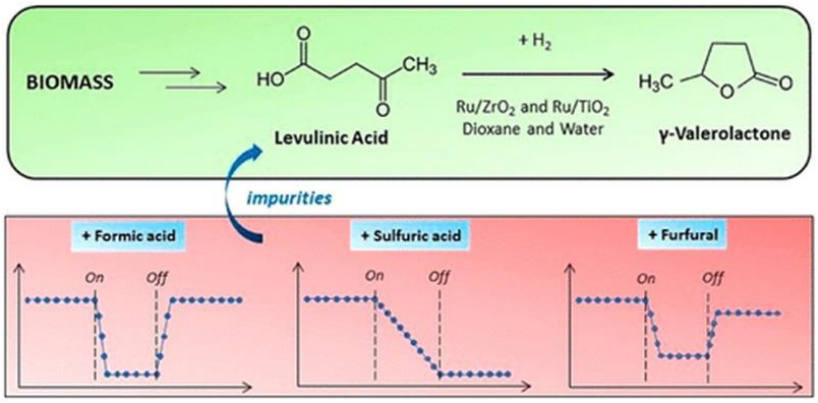

Figure 1.17. Different catalyst deactivation behaviours of Ru/TiO_2 and Ru/ZrO_2 catalysts in dioxane and water in the presence of different impurities such as formic acid, sulfuric acid, and furfural.[141] Copyright from American Chemical Society 2020.

Supported Metal NPs potentially react with the reaction medium such as water, and are sensitive to reaction conditions like temperature, pH, etc. inducing changes in particle shape, structure, composition and oxidation state. Therefore, the active metal sites are restructured. It can happen with monometallic and multimetallic systems. For example, in the aqueous nitrobenzene hydrogenation, metallic Ni active sites can change into inactive $Ni(OH)_2$.[144] 30% activity loss was observed when Ru NPs on Ru/TiO_2 were oxidized on oxidation of succinic acid and p-hydroxybenzoic acid.[145, 146] The distortion of crystalline structure on surface Pt NPs was also observed

during the Suzuki-Miyura reaction in water and DMF.[126] Bimetallic catalysts can be particularly prone to restructuration. In the aqueous-phase reforming of ethylene glycol, Ni was found to segregate to the surface of Ni-Pt bimetallic catalysts leading to a Ni-enrichment of the primarily Pt-terminated surface accounting for higher activity than monometallic Pt catalysts.[147] The Ni leached from the stainless steel reactor creating new Ni-Sn sites on Ru-Sn catalysts was found to be responsible for deceasing activity during aqueous-phase succinic acid reduction.[100]

In all, catalysts deactivation can come down to three aspects: number of active sites, accessibility to active sites, and intrinsic activity. Several parameters can be manipulated when designing a new catalyst to modify the stability of the catalyst. The same strategies (shape, composition, size, etc.) discussed above for improving the reactivity of a catalyst is also applicable here, and understanding the mechanism of deactivation in a specific reaction system is the first thing to do in order to mitigate it.

1.3. Glucose hydrogenation reaction

As it has already been mentioned before, sorbitol is one of the 12 important target chemicals in the biomass valorization program.[10] It is an important precursor for the manufacture of L-ascorbic acid (Vitamin C), which consumes almost 15% of the world sorbitol production. Sorbitol itself is the least costly sugar alcohol, being the most commonly used sugar alcohol, and occupies the biggest market share compared to other similar polyols, widely applied in food, drugs, cosmetics, and so on.

Sorbitol is usually produced by hydrogenation, the substrate of which can be monosaccharide glucose or direct biomass materials such as starch and cellulose.[11, 116, 148-153] A hydrolysis process is involved in the latter substrates. In this production process of sorbitol under the conditions of high pressure of H_2 and high temperature, unavoidable side reactions happen inducing sorbitol degradation into lower alcohols, such as glycol, 1,2-propylene glycol, and methanol.[154, 155] In addition, the yield of mannitol is non-negligible during sorbitol production, which is a result of epimerization of glucose in the case of alkaline medium. In order to concentrate on the metal NPs active sites for direct sorbitol production, here, we are focusing on the one-step reaction of hydrogenation of glucose into sorbitol, avoiding the

process of hydrolysis of polysaccharides, which usually implies completely different active sites, namely strong Brönsted acid sites. The mechanism, kinetics and applied catalysts in this reaction will be discussed below.

1.3.1. Reaction mechanism

Hydrogenation of glucose into sorbitol in the aqueous phase in the presence of a catalyst under H_2 atmosphere is simply shown in Scheme 1.3.

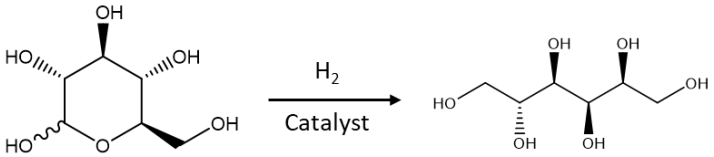

Scheme 1.3. Glucose hydrogenation to sorbitol.

In the very beginning, Bizhanov et al. believed that hydroxide ions catalyse a dismutation reaction to form gluconic acid and sorbitol as well as fructose and mannose due to a tautomeric transformation, as is illustrated in Figure 1.18. Both reactions start with a nucleophilic attack by the OH^- ion at the hydrocarbon carbonyl group. If there is a catalyst (K), the reaction can be represented as: [156]

$$C_6H_{12}O_6 + K \leftrightharpoons C_6H_{12}O_6 \blacksquare K \quad (1)$$

$$H_2\ (gas) \leftrightharpoons H_2\ (sol) \leftrightharpoons H_2 \times K \leftrightharpoons 2H \blacksquare K \quad (2)$$

$$C_6H_{12}O_6 \blacksquare K + 2H \blacksquare K \leftrightharpoons C_6H_{14}O_6 + 3K \quad (3)$$

'×' and '▪' represent sites for physisorption and chemisorption, respectively. The details for the interactions between glucose, H_2 and catalysts were not discussed. Three years later, Makkee from the Netherlands explained the mechanism for the copper-catalysed glucose hydrogenation reaction. They found D-glucose is present as α- and β-pyranose forms in solution, and β-pyranose form is more favourably adsorbed on the copper surface through the coordination of O-1, O-5, and O-6. (Figure 1.19). Ketoses interacting with copper could generate such ionised species. Then the hydride like species (Cu-H) favour an S_N2 type of reaction. Thus, one ^2H was introduced at position 1 for D-glucose during deuterogenation over Cu/silica catalyst.[157]

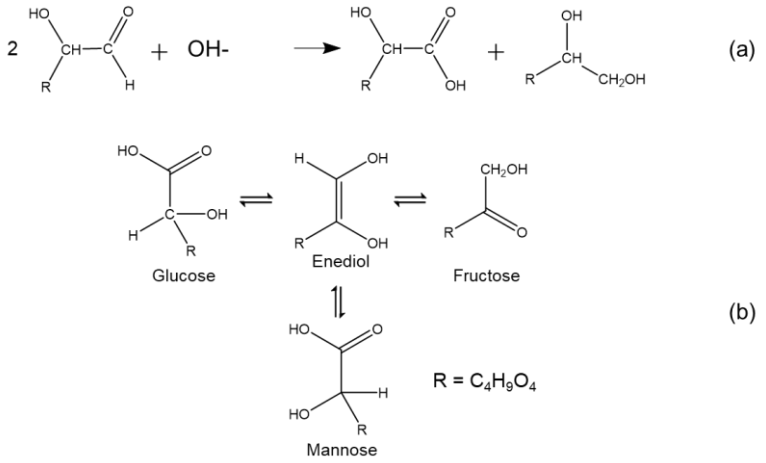

Figure 1.18. Dismutation (a) and tautomeric transformation of glucose (b).[156] Copyright from Springer Nature 1982.

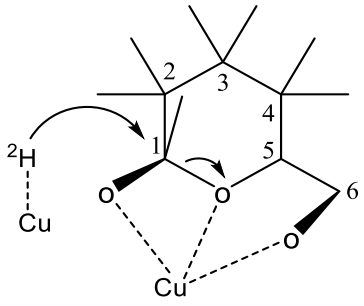

Figure 1.19. β-pyranose interacting with Cu and H adatom attacking C1 position.[157] Copyright from ScienceDirect 1985.

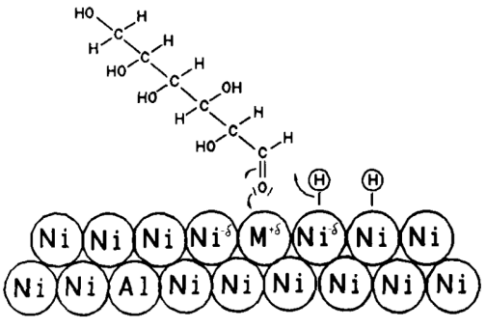

Figure 1.20. Nucleophilic attack of the carbon by hydrogen adatom on Ni surface.[158] Copyright from Elsevier Science Publishers 1991.

These authors thus explained the hydrogenation of glucose in ring form. Cerino et al. proposed alternatively a mechanism based on an open-chain form of glucose with Raney-nickel catalysts. They believed that promoters like Fe, Cr maintained in positively charged form under H_2 pressure, act as adsorption sites for the glucose aldehydic form via the oxygen atom of the carbonyl group. The polarization of the C=O bond favours a nucleophilic attack of the carbon atom by hydrogen dissociated on neighbouring nickel atoms.(Figure 1.20)[158]

Then, Zhang et al. integrated the mechanism of glucose hydrogenation in both the cyclic from and open chain form of glucose with a Ru/C catalyst (Scheme 1.4).[159] They also believed that H_2 was first adsorbed on the active centres of the catalyst, producing activated H. Then glucose reacts with the activated H on the surface of the catalyst. Afterwards, the product desorbs from the catalyst.

Recently, Zhang et al. explained that sorbitol is only produced from the aldose form (Scheme 1.5). As described before, the aldose or ketose open chain forms of glucose only represent 0.0026 mol% in water. Thus, they believe ring-opening of glucose is the rate-limiting step for glucose hydrogenation. Proton is first transferred to the ether-O of the glucopyranose ring inducing subsequent C(1)-O(5) bond scission.[12, 160] The aldehyde function of the aldose conformer may adsorb on metal surfaces via either the oxygen lone pair η_1(O) or η_2 (C,O) configurations.

DFT calculations also help to predict the reaction mechanism. First, the Mushrif group determined the most stable configuration of adsorbed aldoses on transition metal surfaces by using the Perdew, Burke, and Ernzerhof (PBE) functional. Calculation results showed that η_2 (C, O) is the most stable structure because of lower entropy of the η_2 (C, O) configuration (Figure 1.21 a & b), but experiments could only detect the η_1 (O) configuration. Only the formyl oxygen is bound to the metal surface in the η_1 (O) configuration, whereas both C and O in the carbonyl group and the hydroxyl group in the η_2 (C, O) configuration are attached to the carbon bound to the metal surface, thus the latter forms a more constrained structure.[161] Additionally, they

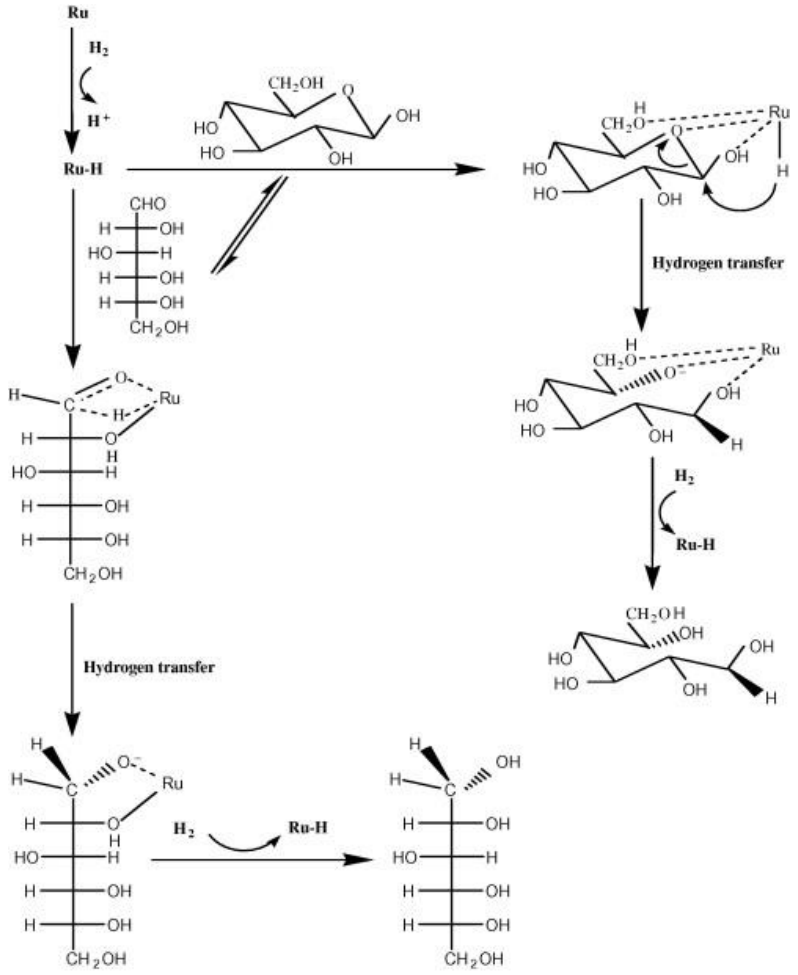

Scheme 1.4. The mechanism of reducing glucose with H_2 over Ru/C catalyst.[159] Copyright from Elsevier B.V. 2011.

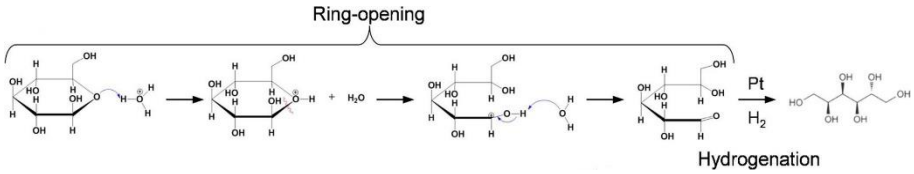

Scheme 1.5. Ring opening and hydrogenation of D-glucose.[12] Copyright from American Chemical Society 2016.

found the open-chain form of glucose could be due to a transition-metal-catalyzed ring-opening process, in which the open-chain adsorption configuration is formed after deprotonation and ring opening. This open-chain

configuration closely resembles the η_1 (O) configuration and the transformation from η_1 (O) to η_2 (C, O) is calculated to be thermodynamically not favourable even at higher temperatures. Thus η_1(O) configuration is visible in experiments. Finally, they calculated the activation barrier at carbon and oxygen atoms of the carbonyl group on Pt (111) and Pd (111) faces (Figure 1.21 c & d), which showed lower barrier on the oxygen atom compared to on the carbon atom. Thus, hydrogenation at the oxygen atom is more preferred. Furthermore, glucose acting as an electron donor was found more inclined to absorb close to the electron-poor metal / support interface.[162] Even though the glucose hydrogenation reaction has been studied for a long time, the precise mechanism of glucose hydrogenation into sorbitol is still debatable. Reaction kinetic studies can indirectly reveal the nature of the glucose hydrogenation details, which will be discussed in the following section.

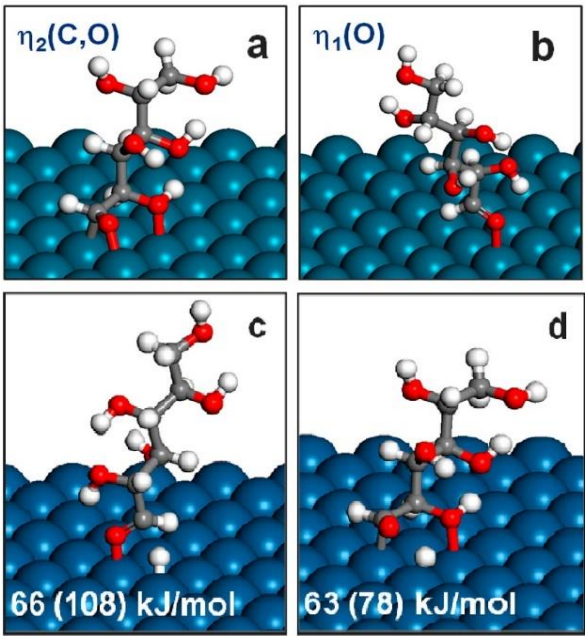

Figure 1.21. η_2 (C,O) configuration (a) and η_1(O) configuration (b) adsorption configurations on Pd surfaces for glucose. Transition states and activation barriers for reactions on Pt (111) surface: (c) addition of H onto carbonyl C atom, and (d) addition of H onto carbonyl O atom. The values in parentheses are the activation energies for similar reactions on Pd (111) surface.[161] Copyright from American Chemical Society 2015.

1.3.2. Reaction kinetics

First, reaction kinetics of the high-pressure hydrogenation was investigated by Hoffman and Bill. They found that transport of reaction medium between gas-liquid-solid phases and their interfaces was the slowest process. Therefore, they believed the diffusion of the dissolved glucose to the surface of the catalyst is the rate-determining step.[163] Then, one equation for measuring the initial rate of the reaction was established (equation 1).

$$-R_0 = K\, C_{0G}^{l}\, C_k^m pH_2^n \qquad \text{Equation 1}$$

Where R_0 = initial rate of reaction, (Gram-molecules of transformed glucose) / (liter × hour); K = reaction rate constant (in h^{-1} for a first order reaction); C_{oG} = initial concentration of glucose; C_k = concentration of catalyst; pH_2 = actual pressure of hydrogen, atm; l, m, n = order of reaction. Experimental results showed the order of reaction relative to hydrogen was 0.5, while reaction order to catalyst concentration was 1. In process technology, both batch and continuous processes and, in the latter case, fixed and suspended catalysts, are known.[164] Akher et al. discussed the factors affecting the catalytic hydrogenation of glucose. They also observed a first order reaction with respect to the catalyst concentration (4%, 8% and 12%) in the first three hours of reaction with Raney nickel catalysts at 100 and 130 ^oC.(Figure 1.22) And a significant deviation from linearity after initial period of the reaction was observed, which was explained due to the decrease of pH value and increase in sorbitol content.[165] Bizhanov and Drozdova studied the kinetics of the reaction in alcohol media with Ru/Al_2O_3 catalyst. A catalyst potential shift from the value of reversible hydrogen potential (r.h.p.) was observed both in water and in 50% ethanol, which was due to the formation of the weak acid sorbitol and gluconic acid.[156]

In order to show the applicability of reaction kinetics of glucose hydrogenation and the effective diffusivities under various operating conditions, Turek et al. studied the kinetics and pore diffusion in four kinds of reactors. Pellets and powdered nickel-silica catalysts were applied in their study at 80 to 150 ^oC and 1.6 to 10 MPa. They found that the reaction rate increased with the increase of pH-value of the reaction solution and the diffusion resistance for small particle size (d_p = 0.3 to 0.5 mm) was negligible. In addition, the conversion increased with the increase of reaction temperature (373-413 K)

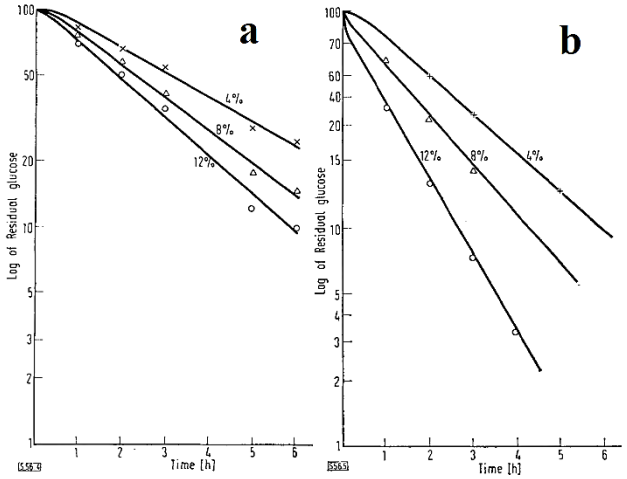

Figure 1.22. Catalyst concentration at 100 (a) and 130 (b) ^{o}C, log of residual glucose vs. time.[165] Copyright from John Wiley & Sons 1974.

or H_2 pressure (0.59 – 2.06 MPa). The activity factor - calculated mass transfer parameters were determined by the selected model equations, then the conversion data were computed in the laboratory-scale trickle-bed reactor, which showed good agreement with the measured data (Figure 1.23).[166] Thus, the reaction kinetics and effective diffusivities they established can be employed in other operating conditions.

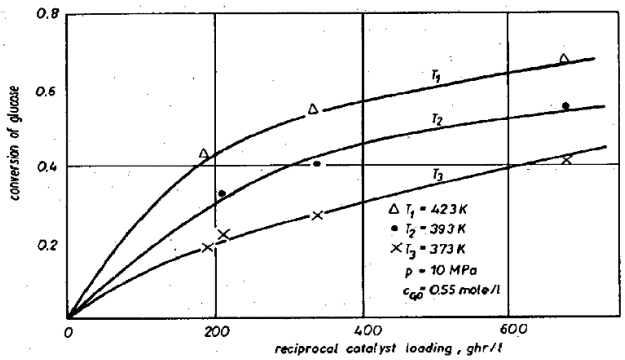

Figure 1.23. Computation of the measured conversion vs reciprocal catalyst loading.[166] Copyright from Elsevier B.V. 1983.

Later on, Wisniak and Simon used the Raney nickel, ruthenium, and rhodium catalysts to study the hydrogenation reaction of glucose, fructose, and their mixtures in the range 85 – 130 ^{o}C, 50 to 1000 psig, and catalyst loading 0.5 to 9% wt.[167] By plotting the logarithm of sugar concentration C vs. the time

of the reaction t, they found that in every case the reaction follows a pseudo-first-order course, which can be represented by the following equation:

$$r = -dC / dt = kC \qquad \text{Equation 2}$$

They stated that the system was probably controlled by the chemical reaction, because in the reaction conditions, mass transfer resistance was negligible (agitation above 900rpm [168] and hydrogen transfer resistances neglected by high pressure). Hydrogen pressure in the gas phase can be assumed to be a proportional measurement of hydrogen concentration at catalyst surface. Adsorption of sugars (substrates and products) and hydrogen were not the controlling step because of the reaction rate was not really proportional to hydrogen pressure (Figure 1.24).

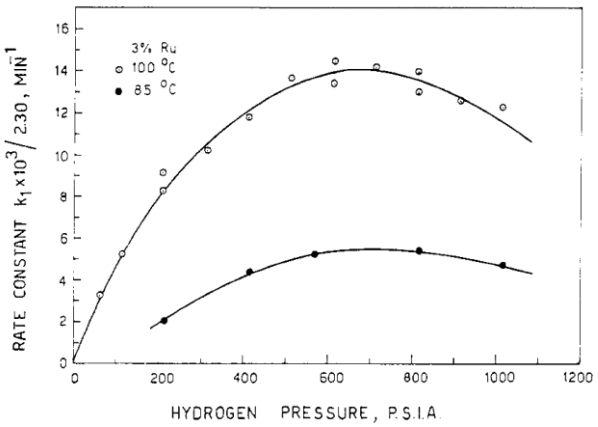

Figure 1.24. Effect of hydrogen pressure. Glucose- Raney ruthenium.[167] Copyright from American Chemical Society 1979.

Recently, first order dependency with respect to D-glucose and hydrogen was testified with various catalyst systems, like 5%Ru/C with E_a of 55kJ/mol,[169] Ru/HYZ with an E_a of 32.9 KJ/mol [170], Pt/silica with an E_a of 47 KJ/mol [12], Ni/NiO with an E_a of 16 kJ/mol [171], etc. Thus, with the development of better catalyst systems, the E_a of glucose hydrogenation into sorbitol decreased. The reactivity and related side reactions, as well as the stability of the applied catalyst are now discussed below.

1.3.3. Applied catalysts, side reactions and catalyst deactivation

In 1912, Ipatieff first reduced glucose to sorbitol in the presence of a Nickel catalyst at 130 ^oC and H_2 pressure of 100 at.[172] After that, numerous studies

were engaged to investigate the mechanism and discover more active catalysts systems. Simply, the existing catalysts can be divided into two families: non-noble catalysts including Raney nickel, [148, 173-176] Co [177, 178] and Ni based catalysts [11, 13, 171, 179-184], and noble metal catalysts including Ru [23, 169, 170, 181, 185-193], Pt, [12, 194] and Pd [195] including their alloys.

Non-noble metal catalysts. Most of the non-noble metal catalysts are based on Ni metal, and Raney nickel is the one of the most investigated since the beginning. Briefly, Raney nickel is a fine-grain solid of Nickel-aluminium alloy, which is prepared by dissolving nickel in molten aluminium followed by quenching and activation in concentrated sodium hydroxide. During the quenching step, small amounts of a third metal are added to enhance the activity and stability. During the activation step in NaOH, aluminium is leached and some porosity is created. Just like what has been said in the previous section, kinetic studies have been deeply studied over Raney nickel catalyst. However, due to the high leaching of Al and Ni from Raney nickel, studies were focused on promoted Raney-nickel with some more electron positive metals like Fe, Mo, Cr, etc. [196-198] For example, for Mo-modified Raney nickel, the specific surface area increased from 56 to 77 m^2 / g and the activity also increased from 0.35 to 0.46 kg $^{-1}$s $^{-1}$.[186, 199] Since Mo-Al alloys (Mo_3Al or Mo_3Al_8) formed in Ni_2Al_3 when Mo was added in Raney nickel, the leaching of Al and Ni was effectively restricted, and Mo showed a high stability without leaching. Cr was also reported to efficiently improve the activity of Raney nickel and the activity depended on Cr content.[186, 200]**.** Regarding Fe promoters, addition of Fe into Raney nickel catalysts largely improved the specific surface area and improved the activity from 0.35 to 0.9 kg^{-1} s^{-1}, while more Ni, Al and Fe leached during the reaction. Clearly, Fe is the most efficient promoter in Raney nickel (Figure 1.25).[173] Phosphorus can also act as a promoter for Ni catalysts. Amorphous Ni-P alloy (Raney Ni-P) prepared by Li et al. showed only less than 1.0 ppm Ni leaching and higher glucose conversion than Raney nickel.[179] Adding a promoter into the Raney nickel could cause the synergy effect in the alloy, the promoter may provide a adsorption site for glucose activation – ring-opening process or cyclic ring adsorption. Thus, works should focus more on finding the origin of synergy effects by studying the nature of the catalyst itself or the kinetics of glucose

hydrogenation. One thing that should be noted for Raney nickel is that proper pH in the aqueous solution was required to both reduce leaching and also prevent the isomerization reaction from occurring. The proper pH is usually around 7.5 in industrial production.[159]

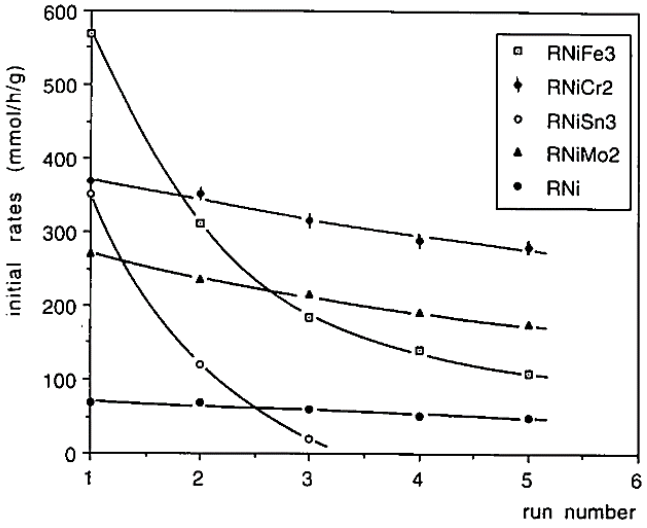

Figure 1.25. Initial rates of glucose hydrogenation for different catalysts as a function of number of recycling (1 corresponds to hydrogenation on the fresh catalyst).[173] Copyright from Elsevier B.V. 1993.

Instead of using a pure bulk metal catalyst such as Raney nickel, introducing a support is a way to reduce the utilization of metal and improve the activity at the same time, as well as enhancing the stability of the active phase through metal-support interaction. As we all know, introducing a support can increase metal dispersion. Al_2O_3, TiO_2, SiO_2, or C have been reported to enhance catalyst activity, following the sequence $Al_2O_3 > TiO_2 > SiO_2 > C$, but they all had Ni leaching (Figure 1.26).[116] One Ni /SiO_2 catalyst prepared by Schimpf's team exhibited almost no leaching due to the very small Ni NPs (2-3 nm) but was less active compared to the commercial Ni/SiO_2. The nickel ethylenediamine complex was used for its synthesis.[11] Thus, Ni precursors play also an important role in controlling the performance of prepared catalysts. Besides, the high specific surface area and desirable porosity of MCM-41 and HZSM-5 molecular sieves were also employed in catalyst preparations to improve the metal dispersion.[191] Ni/Cu/Al hydrotalcite precursors were used to prepared multimetallic catalysts. The prepared catalysts had high activity

as well as excellent selectivity to sorbitol due to Al promoter, but Ni still leached into the solution.[201] Referring to the promoter, Co and Fe with magnetic properties showed additional advantages for the catalyst reuse by magnetic separation. Ni-Co catalyst prepared by impregnation method showed superior performance for glucose hydrogenation to sorbitol compared to Ni, Co monometallic catalysts.[184] Detailed works investigating the catalyst performance of Fe promoted supported Ni catalysts as well as the side reactions induced by the promoter are still necessary.

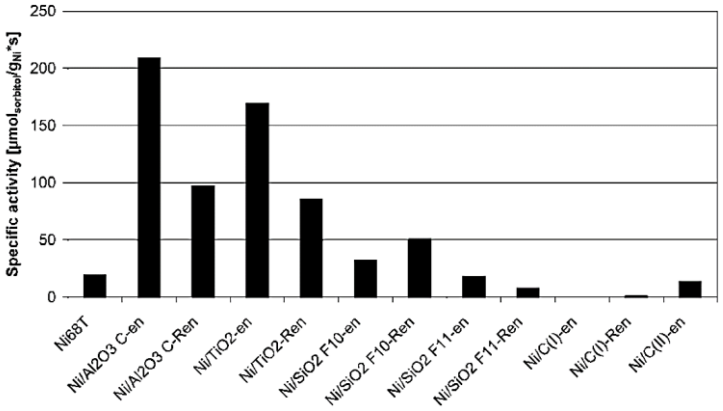

Figure 1.26. Specific activity of the catalysts prepared from ethylenediamine complex, discontinuous (autoclave) hydrogenation.[116] Copyright from John Wiley & Sons 2003.

Noble metal catalysts. Ruthenium was found to be the most effective catalyst for glucose hydrogenation compared to Raney nickel and rhodium catalyst by Wisniak and Simon in 1979.[167] And Ruthenium was resistant to leaching in the aqueous phase. Thus, Ru catalysts were reported to be a promising alternative for Ni based catalysts. Ru/C catalyst showed a nearly 100% selectivity to sorbitol under 4 MPa H_2 with excellent stability.[186, 202] And this high activity of Ru/C catalysts was independent on the preparation methods. A higher dispersion of Ru NPs can potentially lead to higher activity. The influence of preparation methods and supports on catalyst activity of Ru were also studied. [23, 203, 204] For example, glucose conversion increased around 15% when changing the precursors from $RuCl_3$ to ruthenium acetate.[205] And a glucose conversion increased from 34.7% to 72.9% after adding hexamethylene tetramine as ligand when preparing Ru on expanded

graphite.[206] Besides, Ru alloyed with few other elements was also designed to study the catalyst activity and stability. For example, Cr-promoted Ru-B amorphous alloy prevented the coalescence of active Ru.[207] Other noble metals like Pt and Pd also showed a higher activity in general compared with Ni catalysts, but were less active than Ru catalysts.[12, 195]

Table 1.3 shows a series of representative Ni, Ru, Pt catalysts that have been explored in glucose hydrogenation until now. The Ru catalyst series has an absolute advantage in the catalyst activity over Ni based catalysts. The performance of Ni based catalysts can be improved by manipulating the support and also metal active sites. As it has already been elaborated before, several side reactions can occur simultaneously with glucose hydrogenation to sorbitol due to both the structure of glucose and also the harsh reaction conditions. Thus, high sorbitol selectivity is also a significant factor to evaluate when measuring the performance of the catalysts. Apparently, Ru catalysts also prevail in the sorbitol selectivity among other catalyst systems. Catalyst deactivation happened generally among Ni based catalyst systems, but rarely in Ru catalysts. For example, Ni/SiO_2 catalyst activity decreased very strongly during the initial stage of the experiment series, but after a 20 h reaction, the value of activity was almost constant.[166] The disturbance of the catalyst metal-hydrogen structure was put forward to account for catalyst deactivation.[156] And also, poisoning by chemisorption of reaction species, sintering, restructuring of active sites, etc. may be involved in the deactivation. Comprehensive analysis of the fresh and used catalysts are needed to investigate the reasons of deactivation.

Based on the literatures of Hoffer et al. and Sinha et al., the sorbitol productivity with Ru catalysts was calculated approximately to be 6 mol/g_{Ru}, which is 5 times higher than with Ni catalysts.[171, 186] Thus, Ru catalyst demonstrates dominant catalytic performance, however, considering the industrial costs of noble metal catalysts (Ru prices: 16879.14 $/Kg), non-noble metals are always more preferable due to their really low cost (Ni prices: 23.72 $/Kg).[208] Moreover, optimizing non-noble catalyst systems to enhance their performance is also a way to gain better understanding on the mechanism of glucose hydrogenation to sorbitol in general and its requirement in terms of active phase. This brings the main goal of this thesis. The details are expanded in the following section.

Table 1.3 Catalytic hydrogenation of glucose with some representative catalysts. (NR: no data were reported)

Catalyst	Catalyst amount (g)	Metal loading (%wt)	P (bar)	T (ºC)	t (min)	Glucose conversion (%)	Sorbitol selectivity (%)	Ref.
$(RuO_2)_{0.038}\cdot(SiO_2)_{0.962}$	0eq.5	6.3	20	120	60	~97	~100	[193]
Ru/C	>2	3.5-5.6	10-60	100-140	100-140	100	>98	[186]
Ru:Ni/MCM-48	NR	3	30	120	90	70	~100	[191]
Ru/MWNT	0.05	5	40	120	120	62.5	NR	[187]
Pt/SBA-15	0.2	1.5	40	140	120	13	63	[12]
Pt/AC	0.06	1-5	16	180	180	>95	>55	[209]
Raney Ni-P	6	100	40	120	720	55.8	99.5	[179]
Ni/SiO_2	0.4	5-20	120	120	600	19-45	81-92	[11]
Ni/C	0.5	>4.81	120	120	600	7-10.5	0-23	[116]
Ni/NiO	0.05	100	50	100-150	NR	90-95	88-89	[171]
$Ni\text{-}B/SiO_2$	1	6.4	40	120	360	30	NR	[180]
NiCo/HZSM-5	0.1	15	30	120	120	~43	~41	[210]

1.4. Objective and methodology

Sorbitol as one of the derivatives from biomass has been testified as a significant molecule, closely related to our daily life and crucial raw materials in chemical production. In 2020, the global sorbitol market reached a volume of 2.62 Million Tons, and sorbitol is a molecule with approximately 50-60% of the sweetness of sucrose.[211] Therefore, the significance of sorbitol production goes without saying.

It has been more than 100 years since the first report of sorbitol production by Ipatieff. Catalyst design for sorbitol production still prevails today. It has been developed from the first Raney nickel catalyst, then to promoted Raney nickel catalysts, then to supported Ni based catalysts, to current Ru catalysts. The efficiency of sorbitol production from glucose naturally improved with the constantly developing catalysts. Apart from the activity of the catalysts, stability of the catalyst was also enhanced by the addition of precious metals. However, the noble metals (Ru, Os, Rh, Ir, Pd, Pt) suffer from high toxicity and environmental impact in addition to their scarcity and ensuing high cost. First – row metals (Mn, Fe, Co, Ni, Cu) are emerging as environmentally benign alternatives with relatively low price, but the catalytic activity is generally much lower than noble metals. Thus, normally, more contents of base metal catalyst are used in the real-world sorbitol production compared to noble metal catalysts. For example, Raney nickel is a bulk metal catalyst, while commercial Ru catalysts usually are loaded with only 3 wt% of metal on carbon support. When a high metal loading catalyst is applied, purification of the product to remove leached metal species is inevitable, which leads to another factor rising the price of final product. The modern chemical industry also requires alternative and environmentally friendly catalytic processes. Since the industrial production of heterogeneous catalysts is roughly a 13 billion dollar per year business, even small enhancements can result in large economic savings. Thus, from an industrial point of view, the catalyst with low cost metal and minimum metal loading is the most desirable, which is one goal for this thesis – realistic catalysts potentially being alternatives to current Ru catalysts and Raney nickel catalysts.

On the academic side, the reaction kinetics of glucose hydrogenation are clear, but the mechanism of this reaction still remains ambiguous, especially for

recognition of the reaction intermediates. Although different base metals have been tested for this reaction, the actual role of each metal is rarely discussed. In addition, glucose hydrogenation in aqueous solution under harsh conditions leads to other competitive reactions like glucose isomerization, which is less considered in the literature. Furthermore, manipulating noble metal to have particles with different shapes and sizes has been well-developed, but in the base metal part, there are still difficulties to obtain the desired well-defined particles needed for fundamental studies. By controlling the morphology of the particles to have different shapes and sizes of particles of base metals, it can also potentially provide new ideas for the design of catalysts for industrial use. In other words, by altering the structure of the base metal catalysts to investigate their catalytic performance in glucose hydrogenation, we will hit two birds with one stone: on the one side, we can better understand structure-property relationships, and on the other side, we can provide ideas for the design of new industrial catalysts. Meanwhile, analysing competitive reactions during glucose hydrogenation will contribute to uncover the mechanism of this reaction. Besides, understanding the causes of deactivation of the catalysts can help to regenerate the catalysts and also enhance the stability of the catalysts.

As Ni has already been applied in glucose hydrogenation since the beginning, and it has also testified to be the best base metal catalyst with the highest sorbitol selectivity in this reaction, we will here develop base metal catalysts based on Ni metal. First, we will focus on bare Ni catalysts to study important factors affecting their catalytic performance, like doping, shape, crystallinity. Then, supports will be added to reduce the metal loading and also to make the catalyst closer to industrial applications. There, we will only focus on carbon-based supports, since carbon supports have been demonstrated to have less charge transfer (CT) effect and also more stability than oxide supports in aqueous solution (reducing the influence of the support hydrolysis or additional possible reaction occurring over the support). Carbon black and graphite nanoplatelets (GNPs) were chosen to study the support effect, because those two supports exhibit similar specific surface areas but very large differences in structure.

Thus, the **main objective** of our thesis is **the design of nickel-based catalysts and study of active sites for catalysing the hydrogenation of**

glucose, including the investigation of deactivation of those designed catalysts. To achieve this main objective, four sub-goals will be pursued: 1) **design of bare Ni catalysts with different shapes, crystallinities and compositions; 2) preparation of supported Ni nanoparticles with different sizes and supports; 3) design of supported Ni-based bimetallic catalysts; 4) comparative study of the morphology, crystallinity, and composition of the catalysts before and after reaction.**

Staring from the bare Ni catalysts, we will first try to synthesize unsupported Ni particles with different shapes such as cubic, sphere and rod to obtain different surface enrichments. In that case, we could study the effect of different facets on glucose hydrogenation reaction. To do so, solvent thermal synthesis will be applied with the use of capping agents like TOP, HDA, PVP. By exploring different reaction conditions, different shapes of Ni particles should be obtained. Once we acquire the Ni particles with different shapes, surface chemistry analysis will be carefully carried out to determine the surface chemical state including presence of the capping agents on the surface of the particles. Then, morphology study will be carried out to define precisely shape and size of the particles. By means of HR-TEM, external layer facets of the particles could be identified. Besides, XRD, XPS and ICP will be used to probe the crystallinity, surface chemical state and composition, and the bulk composition of the material. This study could give us a general idea about what is the main factor that could affect the catalytic performance of Ni catalysts. This main body of work and results will be discussed in **Chapter 2**.

Then, carbon supports – CB and GNP will be introduced to prepare supported Ni catalysts, in which we will study the size effect of Ni particles on glucose hydrogenation reaction. As we know, the population of low coordinated atoms on the surface of particles normally increases with the decrease of particle size, and those atoms are generally more active, which consequently improves the catalytic performance of the small particles. However, it is not always applicable in every case because catalyst deactivation and competitive reactions are undergoing at the same time. Thus, it is worthy to study this effect with Ni catalysts in glucose hydrogenation reaction. If the size effect exists, it will obviously provide ideas for designing new optimized catalysts. To obtain different sizes of Ni particles, we will prepare the smallest particles first as a growing seed then make the particles grow up at different scales. In other

words, the prepared seeds will be processed under different heat treatment conditions to be controllably sintered. Also, those obtained samples will be investigated by multiple characterization methods, as detailed above, to determine their morphologies, crystallinities, compositions, *etc*. and establish structure/activity relationships. Meanwhile, two carbon supports will also be compared to reveal the support effect. The details of these experiments and presentation of results will be elaborated in **Chapter 3**.

To go one step further than the monometallic Ni catalysts mentioned above, bimetallic catalysts will be designed to study the composition effect of Ni catalysts in glucose hydrogenation. We will add a second metal – Fe as a promoter to see if the catalytic performance including the activity, sorbitol selectivity and stability can be improved or not. Iron has been chosen as a cheap and abundant component. There, monometallic counterpart catalysts, Fe-Ni bimetallic catalysts with different M1/M2 ratios will be prepared by sol-gel method. Since this is a bimetallic catalyst system, the reaction kinetics will be particularly focused on to determine the role of each metal. Similarly, comprehensive characterizations will ensure the understanding of intrinsic properties of the catalysts. All those works will make up the **Chapter 4**.

Another remaining challenge for Ni-based catalysts is maintaining the metal contents of the original catalysts (i.e. reducing leaching) while improving its activity. Thus, the study of Ni leaching will also be addressed for each Ni catalyst system as well as investigating other reasons for Ni catalysts deactivation, like the changes of morphologies, surface chemical states. This will be the work in **Chapter 5**, that will end up with practical suggestions to mitigate deactivation causes.

All in all, several aspects will be studied while designing Ni based catalysts in order to obtain various electronic surface states of Ni NPs and study their activity in glucose hydrogenation reaction, as well as catalyst deactivation. It is worth noting that no specific works have been done so far by other authors on the effect of different carbon supports in glucose hydrogenation. And the size /shape effect has never been discussed in the glucose hydrogenation reaction for non-noble catalysts. Thus, the outcomes of this thesis will definitely bring ideas to guide the design of new highly active and stable base metal catalysts and to better understand the glucose hydrogenation reaction.

Chapter 2

Ni nanospheres, nanorods, nanobead chains catalysts

2. Synthesis of spherical, rod, or chain Ni nanoparticles and their structure-activity relationship in glucose hydrogenation reaction

2.1. Introduction

Biomass is currently the only resource for the production of sustainable organic carbon and biofuels,[212] and it can be used as a substitute for traditional fossil fuels to produce sustainable fuels and chemicals. The utilization of biomass can reduce the dependence on declining petroleum resources and reduce CO_2 emissions.[213] In particular, cellulose accounts for 40% of the biomass obtained through natural photochemical processes yearly.[214] Cellulose derived products have been exploited via degradation processes by enzymes, or under critical conditions like acid or base and heterogeneous catalysis. Catalysis allows to work under softer conditions and increases selectivity. The primary product glucose is produced as a consequence of breakage of β-1,4-glycosidic bonds in cellulose.[214, 215] Sorbitol is the reduction product of glucose, widely used in medical applications and in the food and cosmetic industries, which has been recognized as one of the twelve most important platform chemicals obtainable from biomass.[10, 151]

Sorbitol was first produced by the reduction of glucose in 1912 by Ipatieff in the presence of a nickel catalyst.[172] Since then, plenty of research has been carried out to investigate the mechanism[158, 160, 161], kinetics[156, 166, 169] and mostly the design of new catalysts for this transformation.[12, 191, 193] The applied catalyst has evolved from pure Raney-type nickel catalysts at the beginning to promoted Raney Ni, where a higher electronegativity metal or promoter is used to further enhance catalytic performance of Ni [157, 158, 173]. For example, since Rh has a higher electronegativity than Pt, the activation energy of glucose hydrogenation could be improved from 50-54 kJ/mol (Raney Ni doped with Pt) to 38-42 kJ/mol (Raney Ni doped with Rh).[216] Later, the catalysts were further developed into supported metal nanoparticles, and the noble metals Pt, Pd, and Ru were explored as well.[12, 181, 189, 195]. As a result, Ru is currently the catalyst with best activity, as it is reported by Hoffer for example that 3.5-6.5 wt% of glucose in aqueous

solution was 100% converted into sorbitol with a selectivity >98% over ~ 2g of Ru/C catalyst in ~140 min.[186] Although Ru catalysts demonstrate dominant catalytic activity, considering that the industrial cost of Ru is more than 700 times higher than Ni, non-noble metal catalysts are always preferable for industry.[208] Thus, development of low-cost catalysts has continued to be studied in parallel.[171, 184, 191] In addition to achieving high activity, sorbitol selectivity is also another important criterion of catalyst performance for glucose hydrogenation, since isomerization, as well as other side reactions, take place in aqueous solution under harsh conditions.[11, 217] Among previously developed catalysts, Ni and Ru have the advantage of high sorbitol selectivity, by opposition to Pt, Pd metals that give lower sorbitol yields for the same glucose conversion.[181, 194, 195] Given the high cost of Ru mentioned above, Ni was chosen in this work to construct a more abundant and cheaper metal catalyst with a high activity and sorbitol selectivity for glucose hydrogenation.

Unlike the supported Ni catalysts mentioned above, unsupported Ni particles are favoured in the present study to be able to investigate the structure-activities relationships induced only by the Ni particle itself. Regarding metal particles, the modification of their catalytic performance can be achieved by manipulating the morphologies including regulation of particle sizes and shapes and by tuning the composition and crystallinities.[49, 61] Given that it is easier to obtain metal particles with different sizes, more research has been done on particle sizes than on shapes. Nevertheless, due to the fascination of facet effects caused by different shapes of particles, a great deal of work has been done on shaped controlled nanoparticles applied in catalytic reactions over the last two decades.[42, 66, 218] For example, Xu *et al.* have found that the rate of oxidation of styrene over silver nanocubes was more than 14 times higher than that on nanoplates and 4 times higher than that on near-spherical nanoparticles.[60] The shape of the metal nanoparticle not only has an effect on the activity, but also on product selectivity. For instance, Kim *et al.* observed a lower acetylene conversion and ethylene selectivity over spherical nanoparticles with a significant amount of (111) facets than cubic Pd nanoparticles with (100) facets for the selective hydrogenation of acetylene over Pd / Al_2O_3 catalyst.[76] Apart from the morphology of particles inducing variation of their catalytic performance, altering the crystallinity and

heteroatomic doping also has raised interest since a long time. Heterogenizing metal catalysts with P has been used in electrocatalysis and thermal catalysis due to enhanced catalytic activity.[219, 220] For example, P dopant in Rh catalysts can eliminate the surface hollow sites thus weakening the adsorption strength of CO, leading to a higher hydroformylation activity of Rh-P catalyst compared to Rh catalysts.[220] Ni-P/SiO_2 amorphous catalyst lost its surface active Ni atoms after it was crystallized stepwise from 673 to 873 K, leading to a higher E_a and lower TOF value for the hydrogenation of benzaldehyde.[221] And in particular, amorphous Raney Ni-P alloy catalyst exhibits a superior turnover rate than undoped Raney Ni for the hydrogenation of glucose to sorbitol.[179] Although catalysts that have been tuned by manipulating factors such as morphology, crystallinity and composition have been applied in various catalytic reactions, to the best of our knowledge, for biomass conversion, the influence of metal morphology coupled with crystallinity and composition effect on catalytic performance and product selectivity is rarely studied. In particular, there are no relevant studies for this specific parameter in glucose hydrogenation. Therefore, a fundamental study aiming at understanding structural factors in this reaction can potentially provide implications for the design of novel catalysts for biomass conversion.

Based on this, we prepared Ni nanospheres and Ni nanorods with different crystallinities and compositions by modulating the pressure of hydrogen during the synthesis. This differs from the usual strategies that imply controlling the concentration of the surfactants used as stabilizing agents.[222] Then, a third Ni nanostructured catalyst – namely nanobead chains was synthesized using a well-established method,[223] and was applied to compare the catalytic performance with Ni nanospheres and nanorods in the glucose hydrogenation reaction. The comprehensive surface and bulk analysis of the three different Ni catalysts was carried out to clarify the reasons for their differences in catalytic performance and identify shape, crystallinity and composition factors that are unavoidably intimately entangled.

2.2. Experimental

2.2.1. Chemicals and materials

Nickel(II) acetylacetonate ($Ni(acac)_2$) [$Ni(C_5H_7O_2)_2$, 95%, Sigma-Aldrich], hexadecylamine (HDA) [$CH_3(CH_2)_{15}NH_2$, 90%, Sigma-Aldrich], Nickel chloride

hexahydrate [$NiCl_2$ $6H_2O$, 99.95%, Alfa Aesar], trioctylphosphine (TOP) [$[CH_3(CH_2)_7]_3P$, 97%, Sigma-Aldrich], mesitylene [$C_6H_3(CH_3)_3$, 98%, Sigma-Aldrich], polyvinylpyrrolidone (PVP 40000) [$(CH_6H_9NO)_n$, Sigma-Aldrich], hydrazine hydrate [N_2H_4 H_2O, 99+%, Fisher Chemical], toluene [C_7H_8, 99.85%, Acros Organics], ethylene glycol (EG) [$HOCH_2CH_2OH$, 99%, Alfa Aesar], ethanol absolute [C_2H_5OH, 99.97%, VWR Chemicals] and ethanol [C_2H_5OH, 99%, VWR Chemicals] were used as received.

2.2.2. Catalysts preparation

Synthesis of Ni nanospheres. The reagents used and their relative proportions were referred from the literature [224], but the synthesis conditions and purification steps were designed here. Briefly, 676.9 mg (2.5 mmol) of Ni $(acac)_2$ and 6.69 g (25 mmol) of HDA were dissolved in 42 mL of mesitylene in a 100 mL beaker with an oval stir bar (35 × 16 mm) introduced in advance. After a uniform solution was obtained, 0.62 mL (1.25 mmol) of TOP was added. Then the beaker was immediately placed inside a 300 mL stainless-steel high-pressure reactor. The reactor was degassed under vacuum and put under hydrogen 5 times, and finally filled with hydrogen at a pressure of 2 bar at room temperature. Then the reactor was heated until 180 ^oC and left to react for 19 hours with a stirring speed of 400 rpm. After 19 hours, the beaker was taken out of the reactor at a temperature around 50 ^oC. All the formed particles were attached to the magnetic stirring bar. The particles were transferred from the stirring bar into a clean beaker for further purification, as described below.

Synthesis of Ni nanorods. The same reactants were used as for the nanospheres but different experimental conditions were used: namely 676.9 mg (2.5 mmol) of Ni $(acac)_2$ and 6.69 g (25 mmol) of HDA were dissolved in 42 mL of mesitylene in a 100 mL one-neck round-bottom flask, and an oval stir bar (35 × 16 mm) was introduced in advance. After the flask was degassed and refilled with Argon for 3 times, it was subjected to ultrasounds for 30 min. 0.62 mL (1.25 mmol) of TOP was injected into the flask, then the flask was degassed under vacuum and filled with hydrogen 5 times and kept under hydrogen atmosphere with two individual balloons. Then the flask was heated until 180 ^oC and left to react for 19 hours with a stirring speed of 375 rpm. After 19 hours, all the particles were attached to the magnetic stirring bar. Then the nanoparticles were transferred from the stirring bar into a clean beaker for further purification, as described below.

Synthesis of Ni nanobead chains. The preparation method followed Wen's work.[223] Briefly, 3 g of PVP-40000 was dissolved in 150 mL of EG in a 250 mL round-bottom flask, then 0.75 mL of 1 M aqueous $NiCl_2$ solution was introduced with vigorous stirring using an oval magnetic stirring bar (35 × 16 mm). After the whole mixture was heated to 150 ^oC, 5 mL of N_2H_4 H_2O was added, dropwise with a stirring speed of 500 rpm. The mixture was maintained at this temperature for 12 min. Then a dark grey product was formed. The product was separated by a strong magnet and transferred into a clean beaker for further purification, as described below.

Products purification: For Ni nanospheres and nanorods, the separated products were dispersed into 30 mL of toluene. After 2 min ultrasonication, the particles were separated by a magnet. Then 30 mL of a mixture of toluene and ethanol (1:1) was added to the particles and they were redispersed into the solution using ultrasounds. The particles were again separated by a magnet and the liquid was decanted leaving only the particles. This process was repeated 6 times, then the product was dried in a vacuum oven at room temperature overnight.

For Ni nanobead chains, the product was dispersed into 30 mL of deionized (DI) water by ultrasonication and separated by magnetic decantation, repeating this 3 times. Then it was washed with ethanol another 3 times using the same procedure. After the product was further washed with absolute ethanol, it was dried in a vacuum oven at room temperature overnight. Finally, the catalysts were collected and stored in screw thread vials without any further treatments.

2.2.3. Hydrogenation of D-glucose

Hydrogenation experiments were performed in a stainless-steel high-pressure reactor (Parr autoclave). 12 mg of as-prepared nanoparticles catalyst was added to the aqueous glucose solution of 100 mL with a concentration of 5 g/L, then the reactor was purged with N_2 for 5 min to remove air. The reaction mixture was subsequently heated to the set temperature (within the range 140-160 ^oC) under N_2, then the autoclave was filled to a constant H_2 pressure (30 bar) and the reaction started after turning on the stirring with a speed of 1700 rpm (which was sufficient to eliminate external mass-transport limitations). Samples were periodically withdrawn from the reaction vessel and

filtrated on PVDF membrane (0.2 µm) to evaluate the evolution with time of both glucose conversion and products yields using HPLC. HPLC analysis was performed on filtrates with a Waters system equipped with a refractive index 2414 detector. An HPX-87C carbohydrate column was used, with ultrapure water as mobile phase at a flow rate of 0.5 cm^3 min^{-1}, a column temperature of 358 K and 25 µl of injected volume. Standard alpha-D (+)-glucose ($C_6H_{12}O_6$, ≥ 99%, Acros), D-(-)-fructose ($C_6H_{12}O_6$, ≥ 99%, Sigma), D-(+)-mannose ($C_6H_{12}O_6$, ≥ 99%, Sigma), D-mannitol ($C_6H_{14}O_6$, ≥ 98%, Sigma-aldrich) and D-sorbitol ($C_6H_{14}O_6$, ≥ 99.5%, Sigma) were first analysed by HPLC to determine their retention times separately, which were used as references to identify the products of glucose hydrogenation. The glucose conversion, sorbitol selectivity, product percentage yield, sorbitol productivity and carbon balance were calculated according to equations 3-7:

$$\text{Conversion } (\%) = \frac{\text{moles of glucose (t = 0)} - \text{moles of glucose (t = i)}}{\text{moles of glucose (t = 0)}} \times 100 \quad \text{Equation 3}$$

$$\text{Selectivity } (\%) = \frac{\text{moles of sorbitol (t = i)}}{\text{moles of glucose (t = 0)} - \text{moles of glucose (t = i)}} \times 100 \quad \text{Equation 4}$$

$$\text{Yield } (\%) = \frac{\text{moles of product (t = i)}}{\text{moles of glucose (t = 0)}} \times 100 \quad \text{Equation 5}$$

$$\text{Sorbitol productivity} = \frac{\text{mass}_{\text{sorbitol}}}{\text{time} * \text{mass}_{\text{catalyst}}} \quad \text{Equation 6}$$

$$C_b(\%) = \frac{n_{\text{glucose (t=i)}} + n_{\text{fructose}} + n_{\text{mannose}} + n_{\text{mannitol}} + n_{\text{sorbitol}}}{n_{\text{glucose (t=0)}}} \times 100 \quad \text{Equation 7}$$

2.3. Results and Discussion

2.3.1. Catalysts preparation

Ni nanospheres and nanorods were obtained using the same reactants but different reaction conditions, mainly varying hydrogen pressure. The long chain amine - HDA has been proven a suitable capping agent for nanocrystal synthesis, and TOP was reported as a stabilizing ligand in the formation and stabilization of Ni nanoparticles (Scheme 2.1).[225, 226] Hydrogen pressure is a tuneable factor to affect the kinetic of Ni particle growth, resulting in the production of particles with different morphologies and structures. Under the condition of 2 bars hydrogen pressure, ordered arrays of single dispersed nanospheres were acquired, while Ni nanorod particles were obtained when

the hydrogen pressure was about 1 bar. Thus, two different shapes of Ni nanoparticles were successfully achieved through altering the hydrogen pressure. In addition to hydrogen pressure, it is also significant to emphasize that temperature is a crucial factor to obtain Ni nanoparticles. Several temperatures have been attempted for the preparation of Ni nanoparticles (Table S1) and it was found that with a reaction temperature below 180 ^{o}C, magnetic Ni nanoparticles could not be obtained even when prolonging the reaction time until 46.5 h at 140 ^{o}C. For all failed cases, no particles appeared at the end of the reaction, leaving the reaction medium beige or black in colour, indicating the precursor was not well reduced. Thus, 180 ^{o}C is necessary for the preparation of both Ni nanosphere and nanorod nanoparticles. Ni nanobead chains particles were directly prepared following the reported procedure without any modification.

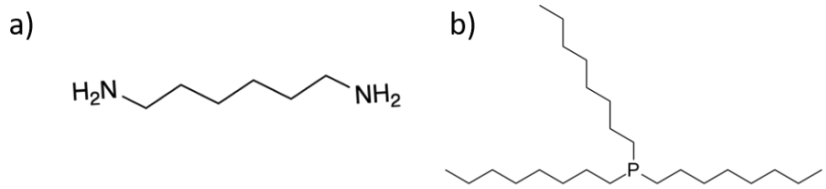

Scheme 2.1 Structures of HDA (a) and TOP (b).

2.3.2. Morphology, surface chemistry and composition of the catalysts

The morphology of different shapes of Ni particles was determined by the comprehensive analysis of SEM and TEM images (Figure 2.1). As shown in Figure 2.1, regular Ni nanospheres were neatly self-assembled, forming three-dimensional stacks. The measured particle size differed in SEM and TEM due to different calibration of magnification and contrast.[227] Due to the TEM images displaying a clearer edge than SEM images, the particle size was measured (more than 10 nanoparticles) on the TEM image in Figure 2.1c, which gave 24.1 ± 0.8 nm with each particle being surrounded with a thin shell, while TEM micrographs show relatively homogeneous structures for nanobead chains and nanorods. Nanorods as shown in Figure 2.1 d and e were organized in a random dispersion, with a 72.3 ± 3.5 nm in length and 15.5 ± 1 nm in width dimension also measured on the TEM image. Nanobead chains do not have a uniform length, but it is greater than 1.5 µm, seeing Figure 2.1g - h, and are formed by stringing together nanospheres with a

diameter of 98.3 ± 9.3 nm. This is consistent with results of the reference.[223] The measured particle sizes differed in SEM and TEM maybe due to combination of inconsistent calibration of magnification and contrast.[227] TEM shows that nanospheres are connected to build anisotropic assemblies probably triggered by dipolar interactions. However, considering the polycrystalline beads, such an anisotropic shape cannot result from oriented crystal growth.

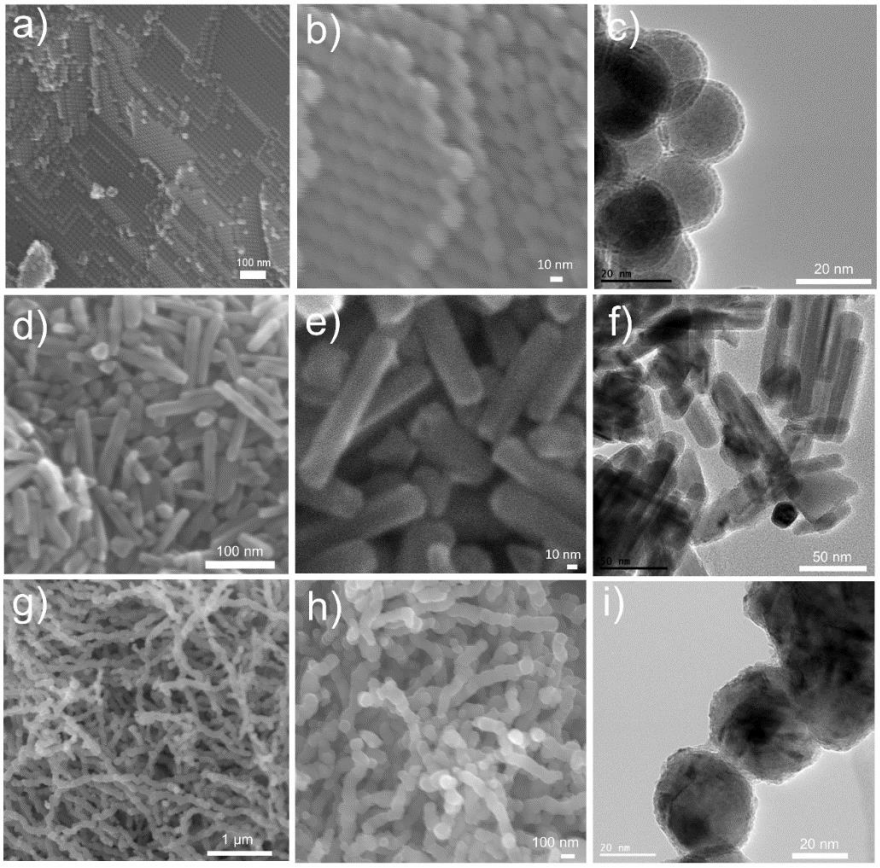

Figure 2.1. SEM (left and center) and TEM (right column) images of Ni nanospheres (a-c), Ni nanorods (d-f) and nanobead chains (g-i).

During the syntheses, large quantities of HDA and TOP were used as stabilizers for Ni nanospheres and nanorods, and surfactant PVP was applied for the preparation of Ni nanobead chains. Even after extensive washings during purification, those reagents could finally stay on the surface of the particles as surface agents, which would affect the catalytic performance by

changing the surface chemical environment.[228] ATR-FTIR, Raman, and XPS were systematically applied to analyse the cleanliness of the surface of the catalysts.

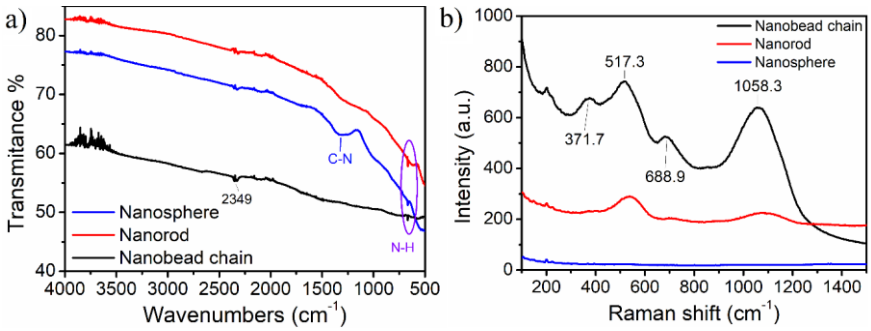

Figure 2.2. ATR-FTIR spectra (a) and Raman spectra (b) of Ni nanospheres (blue), nanorods (red) and nanobead chains (black).

Figure 2.2a shows the ATR-FTIR spectra of prepared catalysts. All the spectra baselines slope down to the right, since all of the three samples in ash black colour display absorption over the entire region from 4000 to 500 cm^{-1} and at low wavenumber this effect grows greater with deeper light penetration.[229] Those "spiky" peaks in the 3800 cm^{-1} region correspond to the active hydrogen bond of the O-H stretching vibration and bending mode of H_2O molecules in the atmosphere. The peak observed at 2349 cm^{-1} was assigned to O=C=O stretching of environmental CO_2. The broad peak around 1313 cm^{-1} in nanosphere sample may correspond to the C-N stretching and a slight sharp peak around 666 cm^{-1} existing in all three samples was ascribed to the N-H wagging mode of amine groups.[230] Both C-P stretching peaks of TOP at 1159, 1070 and 1023 cm^{-1} and N-H stretching and C-H stretching of HDA at 3330 cm^{-1} and 2916 cm^{-1} are absent in the spectra.[231] Moreover, no other vibration peaks appearing in the group frequency and fingerprint region of the three samples suggests that most stabilizing agents were washed away from the products. Similarly, the polarizability of the electrons in those organic molecules were not observed in Raman spectra, for instance, the longitudinal acoustical mode of primary amines around 144 cm^{-1} that would arise from HDA was absent [232] (Figure 2.2b). Nevertheless, phonons within the Brillouin zone are active in Raman spectra. For Ni nanospheres, the approximately flat curve is due to the size of nanospheres being smaller than 30 nm and the loss in long range order.[233] The conservation of phonon momentum $\vec{q}$ in the

oxidation layer of the Ni nanobead chains leaves as Raman active mode the zone centre (q = 0) optical phonon at 1058.3 cm^{-1}, 688.9 cm^{-1}, 517.3 cm^{-1} and 371.7 cm^{-1}, which correspond to $2P_{LO}$, $2P_{TO}$, $1P_{TO}$, $1P_{LO}$ of NiO vibrational modes, respectively.[234] Those phonon frequencies can also be observed in the Ni nanorod sample, but the observation of the narrow or broad humps differentiates between the nanorods and nanobead chain, and can be attributed to different long-range ordered structures within those two.[235, 236] The steeply rising outline below 300 cm^{-1} is the elastically scattered laser radiation.[234]

In addition to IR and Raman acquisitions, XPS was also applied to assess the occurrence of the different elements at the surface of the materials. The atomic % of those elements calculated based on each high-resolution spectra are shown in Table 2.1. N was detected in all three Ni nanoparticles samples, as seen in the N 1s high resolution spectra shown in Figure S1. Peaks at 399.7 eV are corresponding to the amine group in remaining HDA for nanospheres and nanorods and N in PVP for nanobead chains. An additional nitrogen peak observed at 397.9 eV in the nanobead chains sample is associated with electronic donator-acceptor interactions between the chemisorbed PVP and Ni surface.[237] Although the same amount of HDA was used for the preparation of nanospheres and nanorods, the remaining N contents on their surfaces are slightly different, with 1.5 at.% on nanospheres and 0.6 at.% on nanorods. More N content existed in the nanobead chains originating from the usage of PVP during the synthesis. P was detected in nanospheres sample with 1.1 at.% on the surface, which may contribute to different compositions of the external thin layer observed in TEM image. Figure 2.3a shows photoelectron measurement of P 2p core level. The phosphorus core level contains two main components. The lower binding energy peak observed at 130 eV corresponds to elemental phosphorus (P^0), which consists of the characteristic doublet representing the P^0 $2p_{3/2}$ and P^0 $2p_{1/2}$ orbitals with peak positions of 129.9 eV and 130.8 eV respectively.[238] This elemental phosphorus existing in nanospheres catalyst indicates the possible existence of Ni-P alloy, which could be a component positioned at the surface of Ni nanospheres. The peak centred at 133 eV in the spectra represents a pentoxide component such as P_2O_5 (P^{5+}), which also contains two sub-peaks of $P^{\delta+}$ $2p_{3/2}$ at 133.0 eV and $P^{\delta+}$ $2p_{1/2}$ at 134.2 eV.[239, 240] The phosphorous

Table 2.1 Atomic percentages of C, N, Ni, O and P determined by XPS measurement; Binding energy and contents of Ni^0, $Ni^{\delta+}$ in Ni $2p_{3/2}$ level.

Ni particles	C 1s %	N 1s %	Ni 2p3 %	O 1s %	P 2p %	Ni^0 $2p_{3/2}$		$Ni^{\delta+}$ $2p_{3/2}$	
						B.E. (eV)	at.%	B.E. (eV)	at.%
Nanospheres	50.4	1.5	5.1	42.0	1.1	852.5	28.3	856	71.7
Nanorods	61.5	0.6	4.1	33.9	0.0	852.4	28.9	855.1	71.1
Nanobead chains	47.5	2.6	6.8	43.1	0.0	852.1	24.3	855.3	75.7

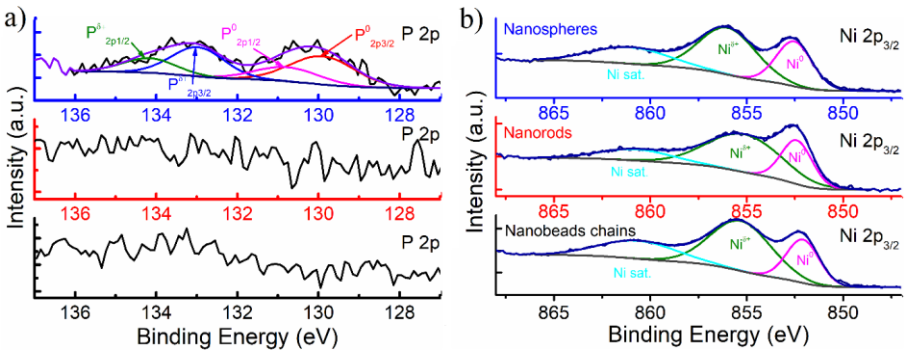

Figure 2.3. High resolution P 2p (a) and Ni $2p_{3/2}$ (b) XPS spectra of nanospheres (blue), nanorods (red) and nanobeads chains (black).

oxide could come from the surface oxidation when phosphorus was exposed to air.[241] Apart from N and P, more than 90 at. % of the elements on the surface were C and O, which may be derived from the remaining organic species, surface oxidation and surface contamination by adventitious carbon.[224, 242] This could affect the chemical state of Ni on the surface. Thus, high resolution XPS of Ni were recorded to identify its chemical state. Those XPS spectra of Ni $2p_{3/2}$ for the three catalysts are shown in Figure 2.3b and the calculated atomic percentage in oxidation and metal states are displayed in Table 2.1. The binding energies around 852 eV and 855 eV are assigned to metallic Ni (Ni^0) and oxidized Ni ($Ni^{\delta+}$), respectively, along with satellite peaks.[243] Since the catalysts were stored without particular precautions, an external Ni oxide layer could be formed due to the contact with air,[224] which explains the presence of oxidized Ni. Similar percentages of

metallic Ni phase were detected on the near surface of nanosphere, nanorod, and nanobead chains catalysts.

Inductively coupled plasma optical emission spectrometry (ICP-OES) analyses were carried out to determine the elemental composition in the bulk material of the three Ni catalysts, and the results are shown in Table 2.2. N was detected in less than 0.1 wt% quantity in all three catalysts while 8.02 wt% of P was present in the bulk of nanosphere catalyst and none in the two others, which is consistent with results of XPS characterization. Since the content of P detected by ICP (*ca.* 9 at. %) is higher than by XPS (1.1 at. %), P should distribute both in the external and internal volumes of the nanosphere particles.

Thus, most of the reactants were well removed from the surfaces of the catalysts after washing, but the adsorption of some species on the surface cannot be totally eliminated even with deliberate washing. Moreover, surface oxidation was found in the three Ni catalysts, and phosphorus as an impurity was only detected in Ni nanospheres catalysts. The possible phases identification within the three catalysts will be elaborated below.

Table 2.2 Elemental analysis (wt%) of Ni nanosphere, nanorod, and nanobead chains samples as measured by ICP-OES.

Element	**C %**	**H %**	**N %**	**Ni %**	**P %**
Nanospheres	1.28	1.03	<0.10	82.82	8.02
Nanorods	2.48	0.89	<0.10	86.41	<0.01
Nanobead chains	<0.10	<0.10	<0.10	96.99	<0.01

2.3.3. Crystallinity of the catalysts

The power XRD patterns of three different catalysts are illustrated in Figure 2.4. The diffraction peaks at 2θ = 44.5° in all samples corresponded to the (111) crystal planes of crystalline face centered cubic (fcc) nickel, and the peaks at 2θ values of 51.8° and 76.4° in the nanorod and nanobead chain

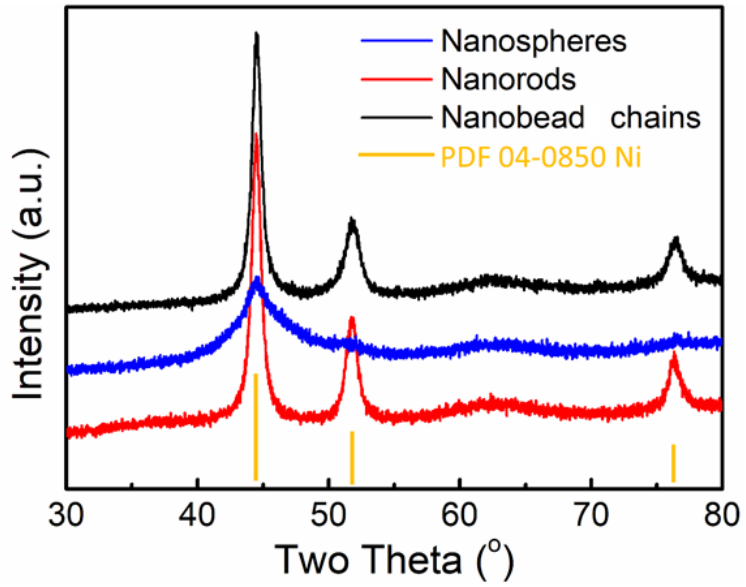

Figure 2.4. XRD patterns of Ni nanospheres (blue), Ni nanorods (red) and Ni nanobead chains (black).

samples were assigned to the (200) and (220) crystal planes of fcc nickel (JCPDS-ICDD card No.04-0850). The low intensity of the broad (111) diffraction peak in the nanospheres indicates small crystal grain size in this catalyst. Particle size calculated using the Debye–Scherrer formula based on the full-width at half-maximum (FWHM) of the (111) diffraction peak in nanospheres catalyst was only 3.4 nm, which is much lower than the value measured by TEM (24 nm), indicating the low crystallinity and / poly-crystalline nature of the Ni nanospheres. Besides, the diffraction of (200) and (220) planes were not distinguished in the nanosphere catalyst. On the contrary, all diffraction peaks can be observed in the nanorod and nanobead chain catalysts, indicating their higher crystallinity compared to nanospheres.

HR-TEM images and SAED patterns of nanospheres, nanorods and nanobead chains catalysts are shown in Figure 2.5. The HR-TEM images (Figure 2.5a-c) of the three catalysts have clear lattice fringes with a spacing of about 0.2 nm corresponding to the Ni (111) face. The SAED patterns of all three samples (Figure 2.5d-f) show concentric circles, which are due to polycrystallinity in the nanostructures. The nanorods (Figure 2.5e) have a relatively more spotty pattern, while there are distinct diffused rings in the

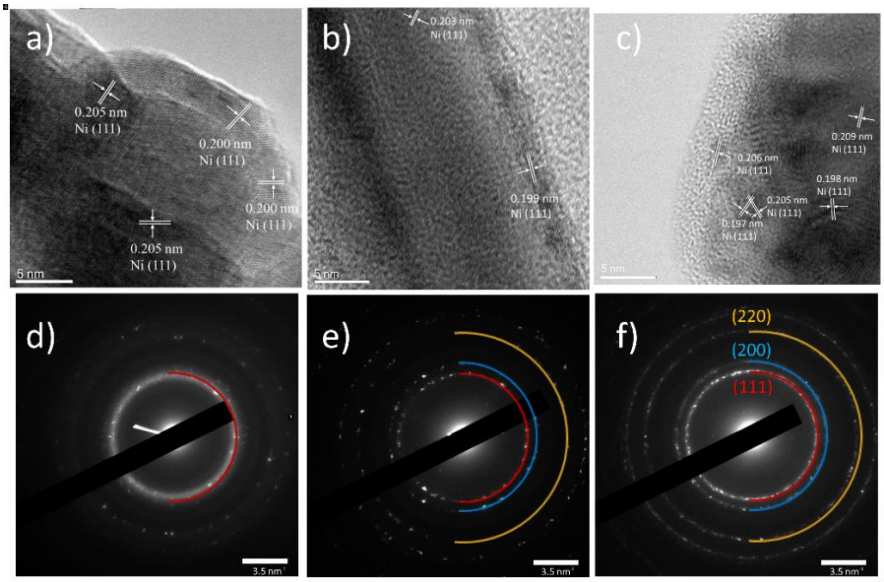

Figure 2.5. HRTEM images and SAED patterns of Ni nanospheres (a, d), nanorods (b, e), nanobead chains catalysts (c, f).

nanospheres and nanobead chains, which implies an amorphous structure with short-range order but with defects. For the nanospheres (Figure 2.5d), one clear and bright diffused ring was observed in the middle, which corresponds to Ni (111) plane. The diffraction rings of Ni (200) and Ni (220) in the nanospheres are not as clear as they are in nanorods and nanobead chains catalysts, which is in complete agreement with the result of p-XRD. The crystallinity was also investigated by dark-field (DF) images. Figure 2.6 illustrates DF images taken in different areas of the samples and at different angular beam tilts. The details of the corresponding bright-field images, SAED images and portions of diffraction ring chosen for DF imaging are illustrated in Figure S2 to S4.

In Figure 2.6a-c, few bright spots with low contrast were observed in the nanospheres catalyst (circled in the images), suggesting low crystallinity for the nanospheres, while the lit up areas in the nanorod sample mostly stretched along the nanorods, forming short light lines rather than light spots as in nanospheres. In addition, the borders of the nanorods, corresponding to Ni (111) facets, were well illuminated (Figure 2.6d-f). This is consistent with the clear presentation of boundary crystal planes on the edges of the nanoparticles as seen in Figure 2.5b. The nanobead chains catalyst has more

and larger bright spot areas than the nanospheres, but those lit up parts are also discrete (Figure 2.6g-i). Thus, the nanorod catalyst presents a more continuous crystalline structure, especially in the outer layers of the particles, compared to the nanospheres and nanobead chains catalysts. This amorphous and low continuous crystalline structure of nanospheres can be further testified by the lowest magnetic moment of the nanospheres, as illustrated in Figure S5. As it is shown in the picture, the three materials in glass vessels were placed in a same site under a permanent magnet. Nanorods and nanobead chains particles were drawn up by the magnet, but the nanospheres particles stayed at the bottom of the vessel.

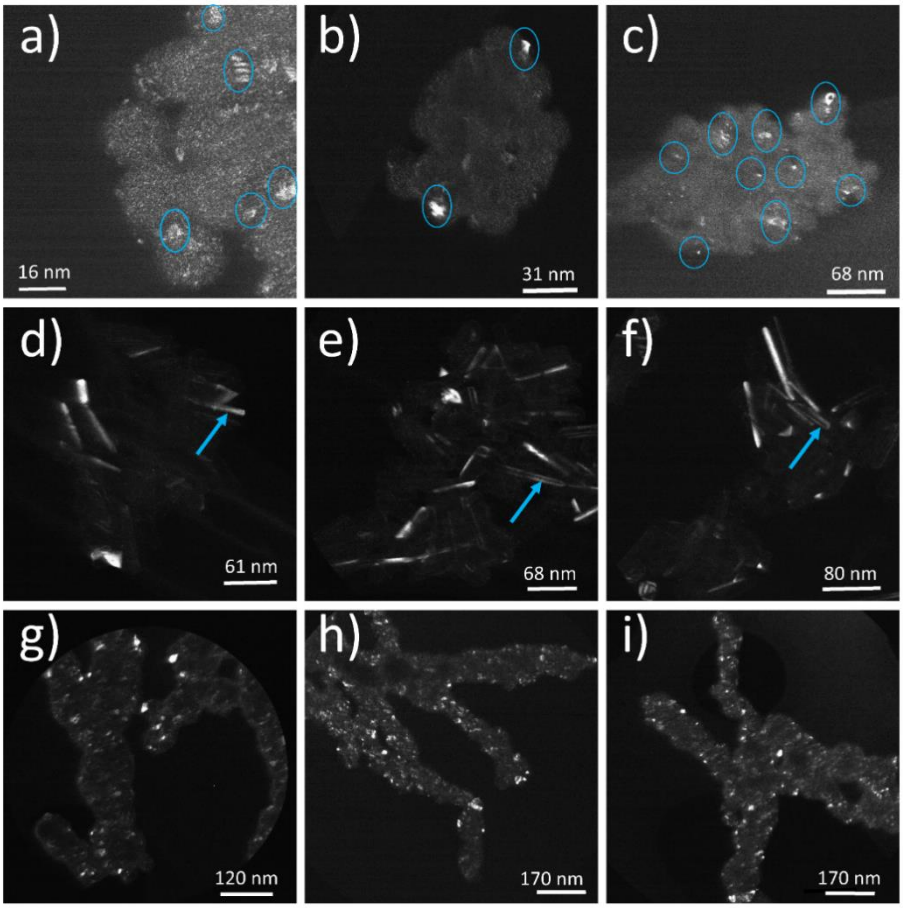

Figure 2.6. Dark field images of nanospheres (a-c), nanorods (d-f), nanobead chains(g-i) catalysts.

The NiO phases on the surface of the three catalysts, detected by Raman and XPS, did not give a clear signal in XRD and SAED analyses. According to XRD patterns, it means that the oxide phase accounts for less than 5 wt%. Thus, Nickel samples were passivated rather than oxidized. Also, the diffraction peaks or patterns of Ni-P alloy phase for nanospheres catalysts were not observed in XRD and SAED. This means that these NiO and Ni-P phases are in an amorphous state or have a low thickness of several angstroms to several nanometres maximum.[224]

The reasons for particles with different components and crystallinities being obtained under different hydrogen pressures can be explained by the particle growth mechanism, involving nucleation and aggregation processes. The nucleation rate relates to the supersaturation of the solution – Lamer mechanism.[244] The $Ni^{(0)}$-TOP mononuclear complexes, such as $[Ni(TOP)_4]$ identified by Ely et al., should act as Ni-atom carriers, promoting the transmission of Ni.[225, 245] Here, hydrogen as a reducing agent can elevate the formation rate of mononuclear complexes thanks to a higher concentration under a higher pressure.[246] Then, the kinetics of aggregation process is promoted with this higher concentration of mononuclear species, inducing that Ni atoms cannot be stabilized under thermodynamic condition. Thus, a hydrogen-undirected controlled aggregation of the nuclei leads to less crystallized particles under a higher pressure. And P is likely introduced into the particles as a dopant during this rapid aggregation process.

2.3.4. Physical adsorption properties of the catalysts

N_2 adsorption/desorption isotherms at -196 ^oC were measured to determine the specific surface area of those prepared catalysts. The isotherms and calculated BET surface areas are shown in Figure S6. The expected Type II adsorption isotherm was obtained for all the samples, which indicates an indefinite multi-layer formation after completion of the monolayer adsorption. Type IV desorption isotherms were observed in nanosphere and nanorod samples, which corresponds to the presence of capillaries (mesopores) created by nanoparticles stacking. Since the length of nanobead chains are in the scale of µm, macropores are more likely formed during the particles stacking, which consequently gives a type II desorption isotherm in this case. The BET surface areas of nanospheres and nanorods are almost the same values (12 m^2 / g), and higher than the surface area of the nanobead chains

(6 m^2 / g). The hysteresis loops in the isotherms of the nanospheres and nanorods indicated the slit holes in the samples formed by uniform particles accumulation (inter-grain voids). The hysteresis loop for nanospheres sample appears at lower relative pressure, which corresponds to the smaller slit pores in the nanospheres compared to nanorods. This is due to the fact that nanospheres are smaller in size than nanorods and therefore present smaller slit pores between the individual particles.

2.3.5. Catalytic performance of the catalysts in glucose hydrogenation reaction

After obtaining different shapes of Ni nanoparticles, we used them to catalyse the reaction of glucose hydrogenation. The catalytic cycle can be simply expressed as in Figure 2.7a. Briefly, hydrogen chemisorbed on the catalyst surface, forms activated H adatoms. The substrate glucose adsorbs on the Ni surface either via O (1), O (5), and O (6) of glucopyranose or oxygen lone pair in the carbonyl group of glucose aldehydic form with η1(O) or η2 (C, O) configurations (Figure 2.7b).[157, 161, 198] The H adatoms can behave as nucleophiles and consequently do a substitution on the C (1) of glucopyranose or an addition onto the carbon atom of the polarized C=O bond of the glucose open-chain form. The resulting alkoxides are then protonated and finally sorbitol is produced after it desorbs from the metal surface.

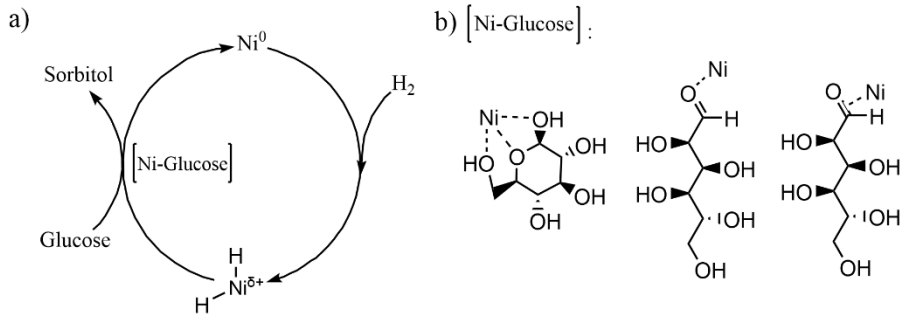

Figure 2.7. a) Catalytic cycle of glucose hydrogenation to sorbitol on Ni; b) Adsorption structures of glucose on Ni [157, 161, 198].

Figure 2.8 shows the evolution trend of glucose conversion with time over the three catalysts, including the results at different reaction temperatures. The experiments at 140 °C were repeated once and the average standard error for glucose conversion is 1.4% and the maximum standard error is 2.0%. The

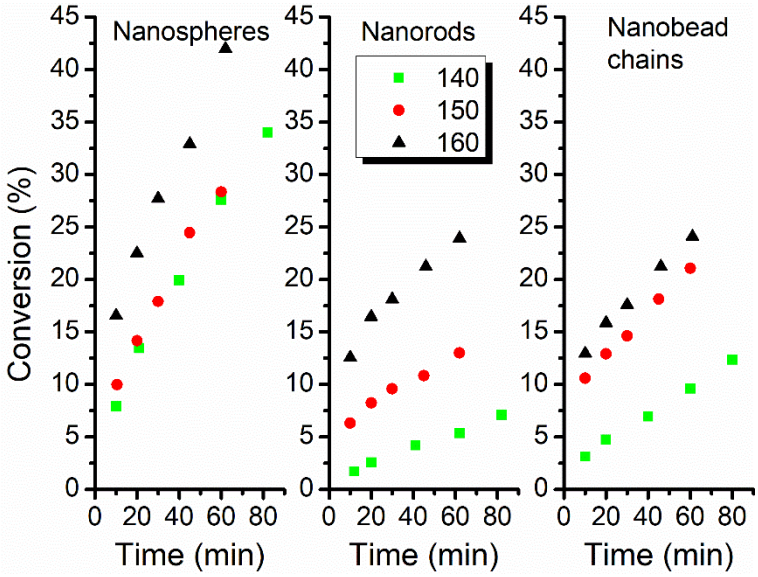

Figure 2.8. Evolution of glucose conversion over time at 140 °C (green), 150 °C (red) and 160 °C (black) over nanospheres (left), nanorods (middle) and nanobead chains catalysts (right) under 30 bar of hydrogen (Error on conversion < 2.1%).

other kinetic curves at the temperature of 150 and 160 °C were only carried out once but we consider an error < 2.1 %. In order to eliminate any decrease in reaction rate due to mass transfer during the reaction, the conversion of the reaction was controlled below 30%. It can be seen that the conversion of glucose increases with increased reaction temperature for the same reaction time, regardless of the type of catalysts used. The conversion of glucose over nanospheres catalysts was the highest at any temperature in the range from 140 to 160 °C, followed by nanobead chains and finally the nanorod catalysts. Similarly, the sorbitol productivity at a same glucose conversion was calculated, and nanospheres catalyst exhibited the highest value compared to other two catalysts at all three temperatures, as can be seen in Table 2.3.

The tendencies for the curves of glucose conversions vs time are consistent with the previously reported first-order reaction.[164, 165] Therefore, the reaction rate constants for the glucose hydrogenation reaction at different reaction temperatures over different catalysts were obtained by plotting ln (1-x) versus reaction time through a linear fit to the equation below (equation 8), where *x* represents the glucose conversion and *k* represents reaction rate

Table 2.3 Sorbitol productivities under different reaction conditions.

Temperature / °C	Catalyst	Glucose conversion / %	Catalyst content / mg	Time / min	Sorbitol / mg	Productivity / $kg.g_{cat}^{-1}.min^{-1}$
140	Spheres	8	14	10	38.4	274.3
140	Rods	7	14	82	19.5	16.9
140	Bead chains	7	14	40	19.7	35.2
150	Spheres	14	14	20	45.7	163.22
150	Rods	13	14	62	24.6	28.32
150	Bead chains	13	14	20	21.6	77.12
160	Spheres	22	14	20	48.9	174.62
160	Rods	21	14	46	15.6	24.22
160	Bead chains	21	14	46	21.7	33.7

constant. The fitted curves are shown in Figure S7. According to the literature, the apparent activation energy of glucose hydrogenation reaction can be obtained by graphing the natural logarithm of the Arrhenius equation (equation 9), where A is the pre-exponential factor; E_a is the activation energy; R is the universal gas constant and T is the absolute temperature in Kelvins.[12, 247]

$$\ln(1-x) = -kt \qquad \text{Equation 8}$$

$$\ln k = \ln A - \frac{E_a}{RT} \qquad \text{Equation 9}$$

The apparent activation energies of glucose hydrogenation reactions over nanosphere, nanorod, and nanobead chains catalysts were calculated as 22.45 kJ/mol, 89.01 kJ/mol, and 47.66 kJ/mol, respectively (Figure 2.9). Thus, the apparent activation energies calculated for the glucose hydrogenation reaction in the temperature range of 413 – 433 K were significantly different for the three catalysts nanostructures. The nanosphere catalyst has the lowest activation energy, which is in good agreement with that observed for highly performant Ru/HYZ catalysts (32.9 kJ/mol)[248], Pt/SBA-15 catalysts(47 kJ/mol)[12], supported Ni (67 kJ/mol) catalysts[116], and Raney nickel catalysts (6-44 kJ/mol)[148]. The lowest catalytic performance with the highest

activation energy was obtained for the nanorods, and the activity of the nanobeads was intermediate between nanospheres and nanorods catalysts.

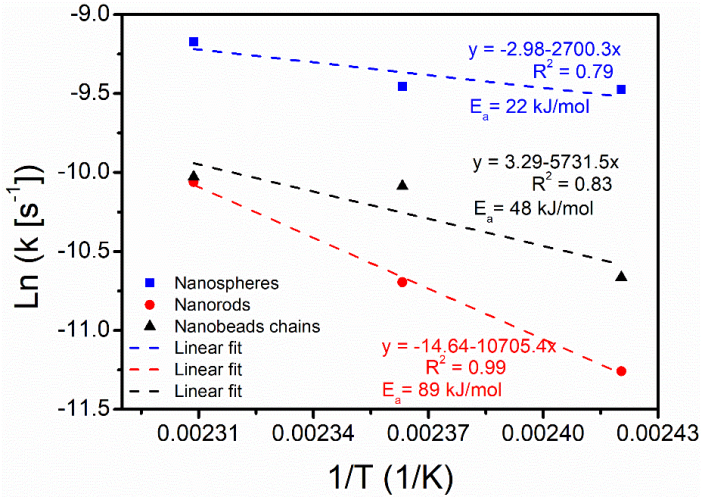

Figure 2.9. Arrhenius plots for determination of the apparent activation energy E_a of glucose hydrogenation over nanospheres (blue), nanorods (red) and nanobead chains (black) from 413 to 443 K under 30 bar of hydrogen.

In the glucose hydrogenation reaction, due to the high temperature of the aqueous solution, other side reactions usually occur, such as isomerization of glucose to fructose or mannose, and further formation of other by-products, like mannitol from the hydrogenation of those isomers, which was illustrated in Scheme S1. Therefore, the sorbitol selectivity is also an important criterion to evaluate the catalyst performance. The trends of sorbitol selectivity with glucose conversion over the three catalysts at different temperatures are compared in Figure 2.10. A selectivity increase with glucose conversion was observed in all cases except nanospheres and nanorods at 140°C. Glucose isomerization to fructose or mannose more easily reach their equilibrium compared to glucose hydrogenation to sorbitol in the initial stage of the reaction. Thus, more sorbitol was produced with longer reaction time along with a relative constant production of fructose / mannose, which leads to the increased of selectivity of sorbitol with the time. As side-reactions mentioned above are promoted along with the increase of temperature, consequently more fructose and mannitol are produced at higher temperature. Thus, higher sorbitol selectivity was obtained at lower reaction temperature in all three

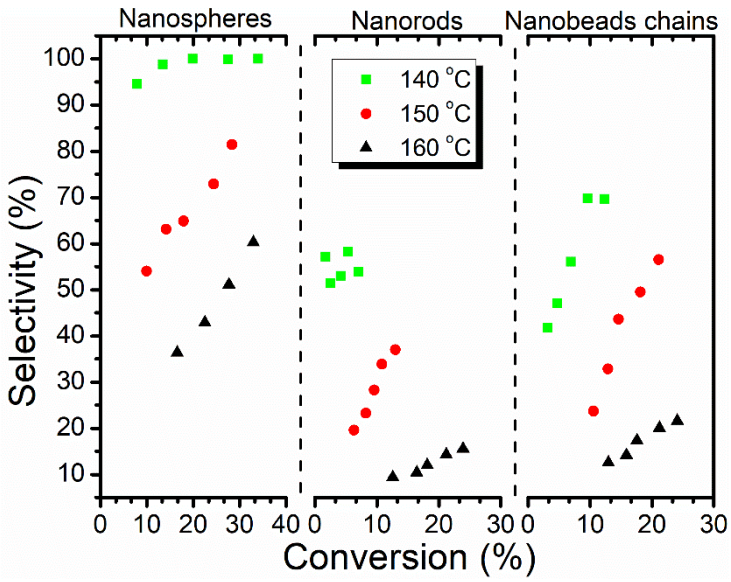

Figure 2.10. Plots of sorbitol selectivity versus glucose conversion during glucose hydrogenation reaction over Ni nanospheres (left), Ni nanorods (middle), and Ni nanobead chains (right) at 140 °C (green), 150 °C (red) and 160 °C (black).

catalysts conditions. At a reaction temperature of 140 °C, the sorbitol selectivity remained essentially at 100% for 1h when using the nanospheres catalysts, while it was only about 55% for the nanorods catalysts and 70% for the nanobead chains catalysts. There is an increasing trend of the selectivity with glucose conversion at temperatures of 150 and 160 °C, which is due to the fact that the glucose isomerization reaction reaches an equilibrium at the beginning, producing a relatively stable amount of fructose. Regardless of the temperature conditions, the nanospheres catalyst exhibited the highest sorbitol selectivity, compared to the other nanorods and nanobead chains catalysts. The carbon balances (C_b) were calculated by equation 7. At the reaction temperature of 140 °C, all the C_b values were 100% with the three catalysts over the whole time range. At 150 °C, there is only 1% difference of the C_b values among three catalysts with time and all those C_b are above 98%. By opposition, all the C_b decreased from 100% to around 91% when the reactions were carried out at 160 °C (Figure 2.11), and the rest are unknown by-products possibly coming from glucose hydrolysis or dehydration reactions.

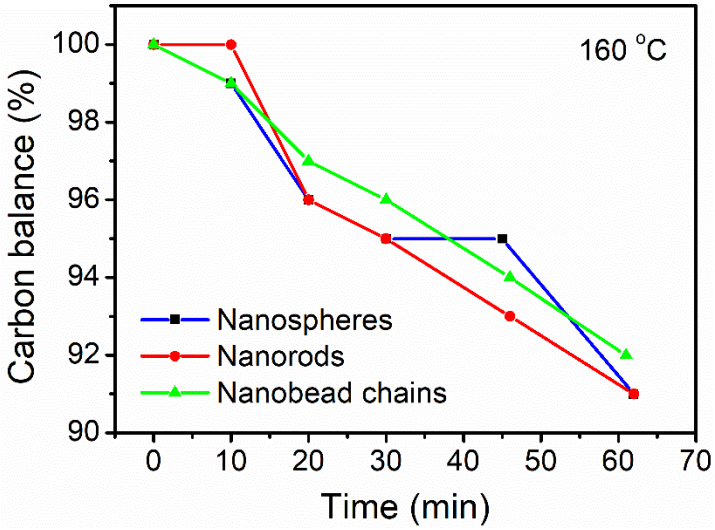

Figure 2.11 Real-time carbon balance monitoring during glucose hydrogenation reaction over nanospheres (blue), nanorods (red) and nanobead chains (green) catalysts at 160 °C, 30 bar H_2, 1700 rpm and 360 min.

Nanospheres catalyst not only has highest catalytic activity, but also a definite advantage of highest sorbitol selectivity. The possible reasons for the best catalytic performance observed with Ni nanospheres catalyst will be discussed now.

First, regarding the morphologies of nanospheres, nanorods and nanobead chains observed by SEM and TEM, surface crystalline facets distributions should vary among particles with different morphologies if they are monocrystalline.[69, 84, 249] However, polycrystalline structures were detected, especially in nanospheres and nanobead chains catalysts, which makes the surface facet enrichment indeterminable. While nanorods catalyst appear with a continuous crystalline structure - fcc Ni (111) in the external layers, it shows the lowest catalytic activity compared to nanosphere and nanobead chains catalysts, implying that the particles with polycrystalline nature are more active. In addition to the polycrystalline nature, amorphous Ni structures are coexisting in both nanosphere and nanobead chains catalysts. It has been studied that amorphous composition of the catalysts with abundant defects and coordination-unsaturated sites on the metal surface can potentially lead to higher catalytic performance than crystalline

counterparts.[250-252] Therefore, the nanospheres with lowest crystallinity (highest content of amorphous nickel) has the best reactivity, followed by the nanobead chains and finally nanorods.

Although both nanospheres and nanobead chains contain amorphous fractions in their structures, the catalytic activity of spheres is significantly superior to that of nanobead chains, which should be mainly due to P doping. As charge-transfer process is commonly occurring at the interface of a hybrid catalyst, this P dopant in the nanospheres catalysts can induce the electron transfer from Ni atom to P atom at the heterointerface of Ni-P phase, leading to positively charged Ni atoms, which has been demonstrated by density functional theory (DFT) calculations.[253] This can probably facilitate the glucose adsorption step with η1(O) or η2 (C, O) configurations. An hydrogen uptake rate was enhanced as well with P doping according to the reported Ni-P alloy catalyst study, from which the order of hydrogen uptake rate per gram Ni is Raney Ni-P > Raney Ni.[179] Furthermore, the doping P atoms can separate the surface Ni atoms and potentially create more amorphous structure. Therefore, P dopant in nanosphere catalyst has a contribution to its catalytic activity both in tuning the electron distribution among adjacent atoms and crystallinity of the material.

Besides, the organic capping agents not being detected by IR and Raman can be largely ignored for their effect on catalytic activity. The effect of surface chemical state of Ni could be excluded as well because the contents in metallic Ni on the surface of these three catalysts are similar, and NiO overlayer would be reduced in situ during the first stages of the reaction under hydrogen pressure. Moreover, similar specific areas and nonporous textures were measured for three catalysts, thus external and internal diffusion of the substrates during the reaction should show no difference among those three samples. Also, the difference in catalytic performance should not be due to a mere particle size effect, because the nanobead chains are much larger and thus display the lowest specific surface area than the nanorods in size, but have a higher catalytic activity than nanorods. Overall, amorphous structure and P dopant make Ni nanospheres an outstanding catalyst that outperforms Ni nanobead chains and nanorods.

2.4. Conclusions

Three different morphologies of Ni nanoparticles, namely nanospheres, nanorods, nanobead chains, were successfully prepared for investigating comparatively their catalytic performance in the glucose hydrogenation reaction. By altering the hydrogen pressure during the synthesis, Ni nanospheres and Ni nanobead chains nanoparticles with different compositions and crystallinities were obtained, together with a temperature of 180 ^{o}C which was demonstrated to be a necessary condition for forming magnetic Ni nanoparticles. Magnetism was taken as a criteria to identify formation of metallic Ni nanoparticles. Decent washing steps were applied to remove the reactants after the synthesis, and as a consequence, HDA and TOP were not detected in the IR and Raman spectra of the final particles. NiO phase was probed by Raman spectra for Ni nanorods and Ni nanobead chains, but it was invisible in XRD pattern and SAED images, attributed to its amorphous structure and thin layers with less than 5 wt % contents. XPS and ICP test indicated the presence of a Ni-P component in Ni nanospheres catalysts, and this component was again not observed by XRD and SAED, suggesting its amorphous structure. These differences in crystallinity and composition ultimately led to significant differences in the catalytic performance of the three catalysts. Thus, activation energies of 22 kJ/mol, 89 kJ/mol, and 48 kJ/mol were attained for the glucose hydrogenation reaction catalysed with Ni nanospheres, Ni nanorods and Ni nanobead chains catalysts, respectively. In addition to the best catalytic activity obtained with Ni nanospheres, the highest selectivity in sorbitol was also achieved with Ni nanospheres, which is around 100% at a typical reaction temperature of 140 ^{o}C. Thus, amorphous P-doped Ni nanospheres has not only superior catalytic activity but also excellent product selectivity contrasting with Ni nanorods and nanobead chains.

Here, bare Ni nanoparticles have been chosen to investigate the effect of P-dopant and crystallinity on the activity of Ni catalysts. Although the designed Ni nanospheres catalyst exhibits a superior catalytic performance, this pure metal catalyst still has an issue of dispersion presenting a low specific surface area, which potentially limits the usage of the active phases. Thus, in the next chapter we will introduce a support to better disperse the Ni particles, which makes the catalysts more viable in industry..

Chapter 3

Ni catalysts with different sizes and supports

3. The effect of Ni particle size and carbon support on catalytic activity for glucose hydrogenation reaction

3.1. Introduction

Sorbitol as a sweetener, moisturizer, texturizer and softener is largely used in the food industry, for medical applications as well as cosmetics. Its global market size was valued at USD 1244.5 million in 2018 and is predicted to rise to 1928.3 million by the end of 2026, showing a compound annual growth rate (CAGR) of 5.54% in the forecast period 2019-2026.[254] Sorbitol is produced mostly by glucose catalytic hydrogenation. Metal catalysts applied in the process have been investigated among Ni, Pt, Co, Ru metals and their multicomponent structures with promoters like P, B, Al, Fe.[12, 13, 23, 171, 173, 177-180, 184, 192-195, 202, 255] Among these catalysts, Raney type Ni was the first to be applied as early as in 1912.[172] For Raney nickel catalysts, a large amount of metal leaching during the reaction is an inevitable issue. It can be diminished by reducing the amount of Ni used and stabilizing small metal particles by supports like SiO_2, C, zeolite.[180, 184] On the contrary, noble metals do not have this leaching problem and usually possess absolute advantages in their catalytic activity compared to base metals. For example, the conversion of glucose and selectivity to sorbitol with a Ru catalyst presenting a 0.6 wt% metal loading were comparable to a Ni catalyst with a 66.78 wt% metal loading and no leaching was detected after 1155 h time in a continuous process.[181] Besides Ru catalysts, other noble metals like Pt also have a higher activity than Ni catalysts but not as good as Ru catalyst.[194] Ruthenium and Nickel catalysts are both used to produce sorbitol from glucose solutions in the industry right now. In comparing further these two catalysts, an obvious cost issue arises, as Ru metal is more expensive than Ni metal by a factor 711.[208] For this reason, there has been a demand for the modification of low-cost Ni catalysts to enhance their catalytic performance as potential alternatives of Ru catalysts.

The modification of supported metal catalysts can be achieved by altering the support and tuning the morphology of the metal particles such as size and shape.[34, 46, 256, 257] Due to the fact that electronic structures of metal particles change along with the size ranges (nanoparticles, cluster, single atom), extensive research has been done by many authors focusing on the

size effect among single atoms, clusters and small nanoparticles. For example, the turnover frequencies for CO oxidation per surface gold atom of Au catalysts supported on TiO_2, α-Fe_2O_3, and Co_3O_4 were found independent of the supports used but increase sharply with a decrease in diameter of gold particles below 4 nm.[258] And Pd particles supported by carbon black with a size centred on 7 nm present an optimal activity in the glucose oxidation reaction.[18] It was also demonstrated that most active Pd/h-BN catalysts must have a particle size distribution between 3-15 nm for lactose oxidation[259]. Charge transfer between the metal particle and support was demonstrated to account for the size effect in the case of a well-defined platinum/ceria catalyst by combing synchrotron radiation photoelectron spectroscopy, scanning tunnelling microscopy and density functional calculations, and Pt with a size around 1-1.5 nm was calculated to have a maximum charge transfer.[56] Thus, most of the size effects were found in nanoparticles smaller than 10 nm, and the catalytic properties remain unchanged as the nanoparticles increase in size.[53]. However, this size effect varies with the reaction considered as well as with the used metal itself. Therefore, it is meaningful to investigate the size effect of Ni nanoparticles larger than 10 nm in glucose hydrogenation. These can be even considered as model structures for local domains in Raney Ni.

Here, we prepared carbon black (CB) and graphene nanoplatelets (GNP) supported Ni catalysts (Ni/CB and Ni/GNP) by sol-gel method, and Ni particles with different sizes were obtained by controlling the temperature during the synthesis. In situ XRD was applied to probe the growth of Ni particles and ex situ XRD was used to analyse the catalysts obtained after each synthesis. The obtained catalysts were used to catalyse the glucose hydrogenation reaction in the liquid phase under high pressure. The conversion of glucose, the yield of sorbitol and other by-products were analysed to reveal the relation between the Ni particle size (over 10 nm) on CB and GNP support and their catalytic performance. N_2 sorption isotherms, XPS, TGA, ICP-OES and H_2-TPD were also applied for a comprehensive analysis of catalysts properties.

3.2. Experimental

3.2.1. Chemicals and materials

Nickel (II) nitrate hexahydrate [Ni $(NO_3)_2 \cdot 6H_2O$, 99.999%, Sigma-Aldrich], carbon black [received as 250G type from IMERYS GRAPHITE & CARBON], graphene nanoplatelets (M15, Sigma-Aldrich), citric acid [$C_6H_8O_7$, 99.5%, Alfa Aesar], and ethanol [C_2H_5OH, 100%, Merck] were used as received.

3.2.2. Catalysts preparation

3.2.2.1. Synthesis of Ni nanoparticles supported on carbon black (Ni/CB):

Pechini-type sol-gel method was used for the preparation of supported catalysts.[260] Typically, 400 mg of CB, 1.6 g of citric acid, 1.7 mmol of the Ni $(NO_3)_2 \cdot 6H_2O$ salt (495.2 mg of Ni $(NO_3)_2 \cdot 6H_2O$) and a stirring bar were introduced into a round-bottom flask, respectively. After 16 mL of ethanol was added, the mixture was stirred for 10 min, then sonicated for another 20 min at the power level of 4 (VWR ultrasound cleaner USC 1200-THD). Then, the suspension was heated at 90 ^oC for 3 h under reflux. Afterwards, the suspension was transferred into a 33 mL ceramic boat and dried under vacuum at 30 oC until a gel formed. Then, the gel was introduced in a tubular furnace and heated to 300 oC for 2 h under Ar/H2 atmosphere. The recovered powder was labelled as CB-300, which was treated as a seed for further particles growth through heat treatment. To do so, CB-300 was reintroduced into the tubular furnace and heated to a set temperature for 1h under Ar/H_2 atmosphere. Afterwards, the final catalyst was obtained and named according to the temperature of heat treatment (CB-xxx). In that way, CB-400, CB-500, CB-550, CB-600 and CB-650 catalysts were prepared at 400, 500, 550, 600 and 650 ^oC, respectively. Those catalysts were used without further precautions.

3.2.2.2. Synthesis of Ni nanoparticles supported by GNP

Ni nanoparticle supported by GNP catalysts were prepared following the same procedure as mentioned above by replacement of the carbon support. Consequently, GNP-350, GNP-450, GNP-550 and GNP-650 were obtained through the heat treatment of GNP-300 at 350, 450, 550 and 650 ^oC.

3.2.3. Hydrogenation of D-glucose

Hydrogenation experiments were performed in a stainless-steel high-pressure reactor (Parr autoclave) under the given conditions, typically, 140 ^{o}C at 30 bar H_2 using a stirring rate of 1700 rpm (which was sufficient to eliminate external mass-transport limitations) using 0.5 g of glucose and 60 mg of catalyst in 100 mL Milli-Q water. In brief, 60 mg of catalyst was added to the aqueous glucose solution, then the reactor was purged with N_2 for 5 min to remove air. The reaction mixture was subsequently heated to 140 ^{o}C under N_2, then the autoclave was filled to a constant H_2 pressure (30 bar) and the reaction started. When the experiment ended, the filtrate of the reaction slurry was analysed by HPLC. HPLC analysis was performed on a Waters system equipped with a refractive index 2414 detector. An HPX-87C carbohydrate column was used, with ultrapure water as mobile phase at a flow rate of 0.5 cm^3 min^{-1}, a column temperature of 358 K and 25 µl of injected volume. Standard alpha-D (+)-glucose ($C_6H_{12}O_6$, ≥ 99%, Acros), D-(-)-fructose ($C_6H_{12}O_6$, ≥ 99%, Sigma), D-(+)-mannose ($C_6H_{12}O_6$, ≥ 99%, Sigma), D-mannitol ($C_6H_{14}O_6$, ≥ 98%, Sigma-aldrich) and D-sorbitol ($C_6H_{14}O_6$, ≥ 99.5%, Sigma) were first analysed by HPLC to determine their retention times separately, which were used as references to identify the products of glucose hydrogenation. The glucose conversion, sorbitol selectivity, and product percentage yield were calculated according to equations 3-5 listed in chapter 2:

3.3. Results and Discussion

3.3.1. Characterization of Ni/CB catalysts.

During the synthesis of our starting carbon-supported Ni catalyst, a gel is formed after the ethanol was evaporated for 2 h under vacuum, which allows a nice distribution of the metal precursors. Thanks to coalescence and Ostwald ripening, it allows us to control the Ni particle size simply by altering subsequent heat treatment temperature and duration under reductive atmosphere.[18, 121, 261-264] Ni nanoparticle growth with temperature was monitored by in situ p-XRD, diffraction patterns of which are shown in Figure 3.1a. The starting CB-300 gave an almost flat curve at the bottom of the diffraction patterns, which is due to the Ni grain size being less than 5 nm as well possibly as the amorphous texture of remaining reagents.[265] When the temperature increased to 350 ^{o}C, a diffraction hump at $2\theta \approx 44^{o}$ becomes

visible, which corresponds to the diffraction by Ni face centered cubic (fcc) (111) planes (JCPDS-ICDD card No.40-0850). As the temperature continued to rise, this hump became sharper and sharper and a diffraction peak at 2θ ≈ 51° assigned to the (200) crystal plane of fcc nickel, appeared. This latter turns to be more visible after the temperature reached 450°C. Since the grain increased with the temperature increment, the full width at half maximum (FWHM) decreased, inducing a shaper peak after a higher temperature treatment. Due to the thermal expansion of the crystalline unit cells, the diffraction peaks shifted to the left as the temperature increased. Once the final sample was cooled down to 35°C (yellow curve on the top in Figure 3.1a), the peaks restored to their original positions. Based on the diffraction patterns collected at different temperatures, we calculated the grain sizes of Ni particles from the FWHMs of (111) diffraction peaks using Scherrer equation, and the results are illustrated in Figure S8. The Ni grain grows from ~3.78 nm

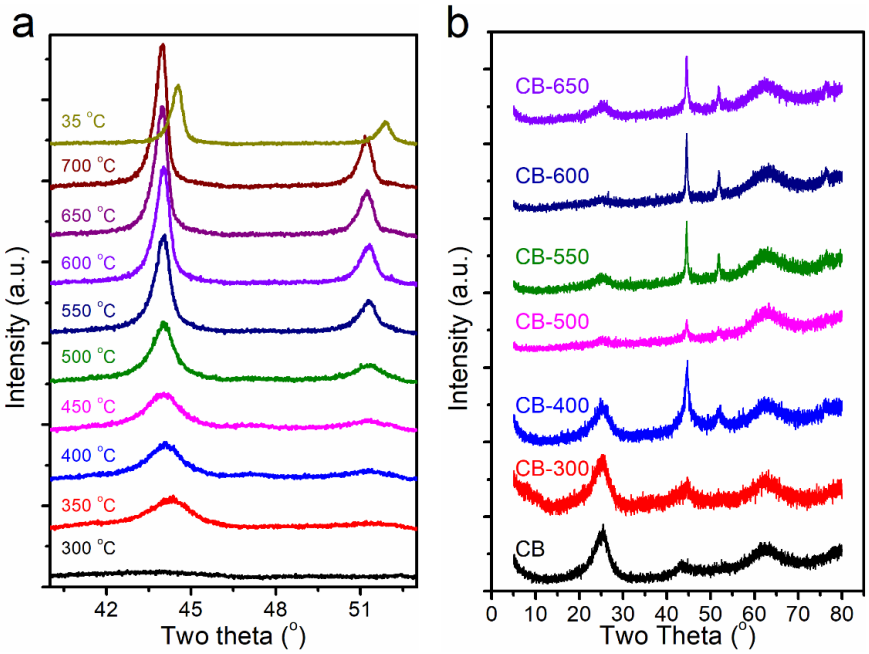

Figure 3.1. a) In situ XRD patterns of CB-300 recorded every 50 °C from 300 °C to 700 °C. b) ex situ XRD patterns of prepared Ni nanoparticles supported by CB at the corresponding temperatures of heat treatment marked in the names of the samples. The XRD pattern of pure CB is shown at the bottom as a blank reference.

at 300 °C to ~13.37 nm at 700 °C, and in the temperature ranges of 300-450 °C and 600-700 °C, the grain sizes changed the least. Given this result, temperatures at 400, 500, 550, 600 and 650 °C were chosen to prepare the diverse sizes of Ni nanoparticles supported on CB. The XRD patterns of obtained catalysts are shown in Figure 3.1b. The XRD pattern of pure CB support (black curve) is given as a reference. One main broad peak at 2θ = 25.4° attributed to the (002) plane of graphite (JCPDS-ICDD card No.41–1487) is visible for the support. This broad peak reveals the disordered graphitic nature of CB. For the catalysts, the peak at 2θ = 44.7° attributable to the Ni fcc (111) plane started appearing in CB-400 and grow with the temperature increase, and the same happened with the peak at 2θ = 51.9°. The Ni grain sizes of all the prepared catalysts were also calculated with the Scherrer equation based on FWHMs of the Ni (111) diffraction peaks and the results are displayed in Table 3.1. It was observed that the grain size exhibits a distinct variation in different catalysts, with a size growth with temperature, except for CB-550, CB-600 and CB-650, which is consistent with the above in situ XRD outcome. Smaller sizes were obtained in the in situ XRD experiments than with ex situ XRD, due to the heat duration in the former that is shorter than the latter (1 h) where it allows the particles to grow more with time.

The particles morphology identified by TEM imaging and the related statistics histograms are illustrated in Figure 3.2 & 3. Diverse Ni nanoparticles profiles were obtained along with different synthesis temperature conditions. The Ni particles synthesized at a temperature of 400 °C display more homogeneous size range than others, and as the temperature increased, more and more particles with larger sizes appeared. To further illustrate the size distribution in the different samples, 100 particles in the TEM images of each sample were selected for statistical analysis, and the resulting histograms are shown next to the TEM images of each sample (Figure 3.2 & 3). Statistical values of average particle sizes are displayed in Table 3.1. For the CB-400 catalyst, its average size is around 6.86 nm, and when the synthesis temperature increases, the size of the obtained particles increases accordingly, which is consistent with the XRD results. At the same time, higher temperature induces larger variation of particle size distributions, which standard deviation increases from 1.25 nm at 400 °C to 11.6 nm at 650 °C. Besides, regardless

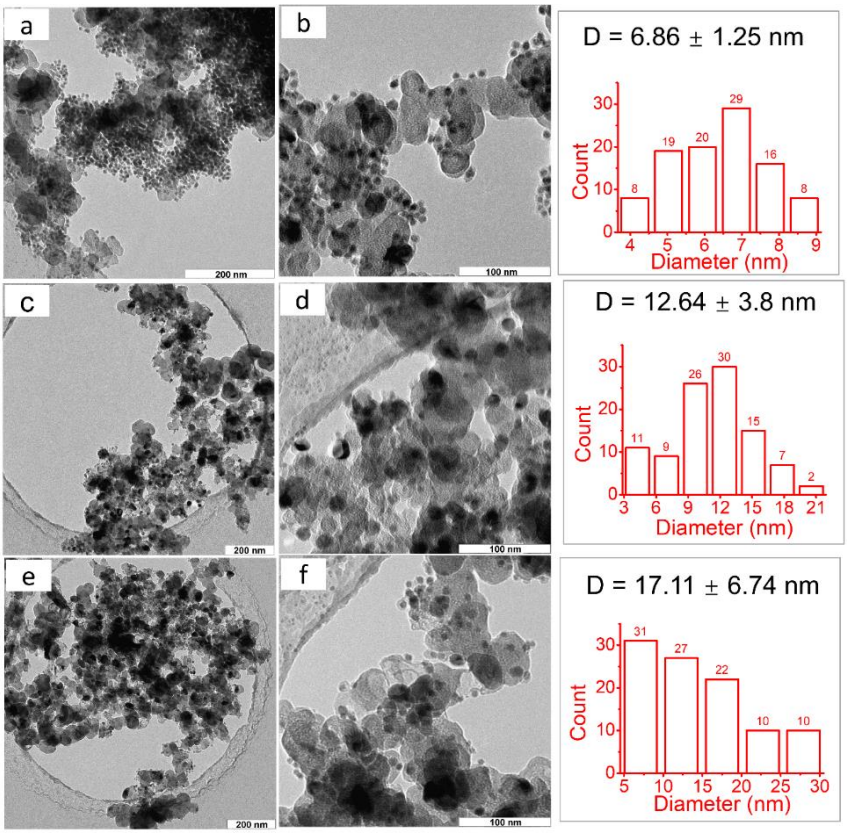

Figure 3.2. TEM images of CB-400 (a, b), CB-500 (c, d), CB-550 (e, f) samples. The corresponding statistical histograms of particle sizes are shown at the right of each two images and the average diameter (D) is written in the histograms.

of the temperature condition, there are always Ni particles around 7 nm present in all the samples, which is due to the fact that Ni particles were prepared by heat treatment of identical starting CB-300 material and that the heat-treatment was not prolonged.

The Ni metal loading of CB-series catalysts was analysed using ICP-OES and the results are also shown in Table 3.1. For CB-300 sample, the loading of Ni is 11.8 wt%, while Ni loading increased with the synthesis temperature, at 400, 500 and 550 ^{o}C, and it is independent of the temperature increase after 550 ^{o}C. The lowest Ni loading for CB-300 is due to the incomplete decomposition and reduction of the reactants, which can be further reduced at high temperature, inducing a higher Ni loading for the next samples that have been

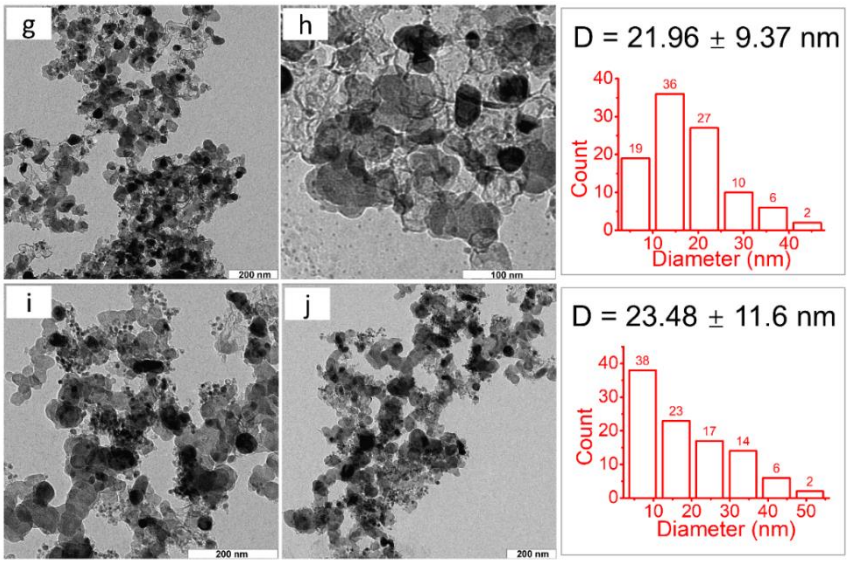

Figure 3.3. TEM images of CB-600 (g, h) and CB-650 (i, j) samples. The corresponding statistical histograms of particle sizes are shown at the right of each two images and the average diameter (D) is written in the histograms.

Table 3.1 Nickel particle sizes in Ni/CB catalysts calculated from XRD patterns and TEM images; Ni weight percentages in the prepared catalysts determined by ICP-OES.

Entry	Size / nm		Ni wt%
	XRD	TEM	
CB-300	4.9	-	11.8
CB-400	8.3	6.86 ± 1.25	16.54
CB-500	13.4	12.64 ± 3.8	18.28
CB-550	19.1	17.11 ± 6.74	20.7
CB-600	21.1	21.96 ± 9.37	21.18
CB-650	20.4	23.48 ± 11.6	19.27

further heated. The similar Ni loading for CB-550, CB-600 and CB-650 suggests that all the reactants were well decomposed leaving only Ni particles and CB support in the samples from a reduction temperature of 550°C. This result can also be demonstrated by TGA analysis (Figure 3.4). 28.5% of

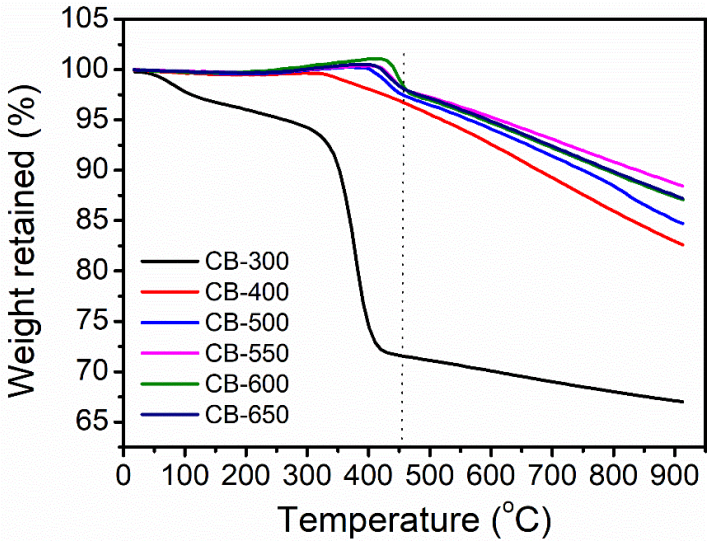

Figure 3.4. TGA curves of CB-300 (black), CB-400 (red), CB-500 (blue), CB-550 (pink), CB-600 (green) and CB-650 (dark blue) recorded under N_2 atmosphere from 25 to 900 °C with a heat rate of 10 °C / min.

weight lost in CB-300 when it was heated until 450 °C is observed, implying the gel texture formed by citric acid and metal precursor were remaining in CB-300 sample. There is less than 3.4 % of weight loss for other samples before 450 °C, and after 450 °C the trend of the curves is almost the same.

XPS analysis was applied to determine the surface chemical composition and metal oxidation states within the catalysts. Figure 3.5 illustrates the high resolution XPS Ni $2p_{3/2}$ spectra of those obtained catalysts. The peak with binding energy around 853 eV is ascribed to metallic Ni (Ni^0). The peaks (red components) around 855 eV are assigned to oxidized Ni ($Ni^{\delta+}$), along with satellite peaks (blue components).[243] In the CB-300 sample, there is no metallic Ni present, while in the CB-550, more than half of the Ni state detected is Ni^0. The binding energy and contents of Ni^0 and $Ni^{\delta+}$ as well as elemental analysis result of the Ni/C ratio are listed in Table 3.2. A similar Ni/C mass ratio was present on the surface of CB-400, CB-500, CB-550, CB-600 and CB-650 catalyst, as determined by XPS. For CB-300 catalyst, it has a Ni/C mass ratio of 6.17%, higher than other catalysts, which means that CB-300 contains the highest amount of Ni. But by analysing by ICP, a lowest Ni weight

Table 3.2 Binding energy and contents of Ni^0, $Ni^{\delta+}$ in Ni 2p3/2 level; atomic ratios of Ni and carbon obtained by XPS and corresponding calculated weight ratios.

Catalyst	Ni^o		$N^{\delta+}$		Ni/C	
	B.E. (eV)	at.%	B.E. (eV)	at.%	at.%	wt%
CB-300	-	0	857.5	100	1.26	6.17
CB-400	852.6	30.9	855.3	69.1	0.63	3.08
CB-500	852.5	11.5	854.9	88.5	0.73	3.57
CB-550	852.8	60.8	856.3	39.2	0.67	3.26
CB-600	852.6	41.2	854.8	58.8	0.56	2.76
CB-650	852.6	13.8	854.9	86.2	0.47	2.32

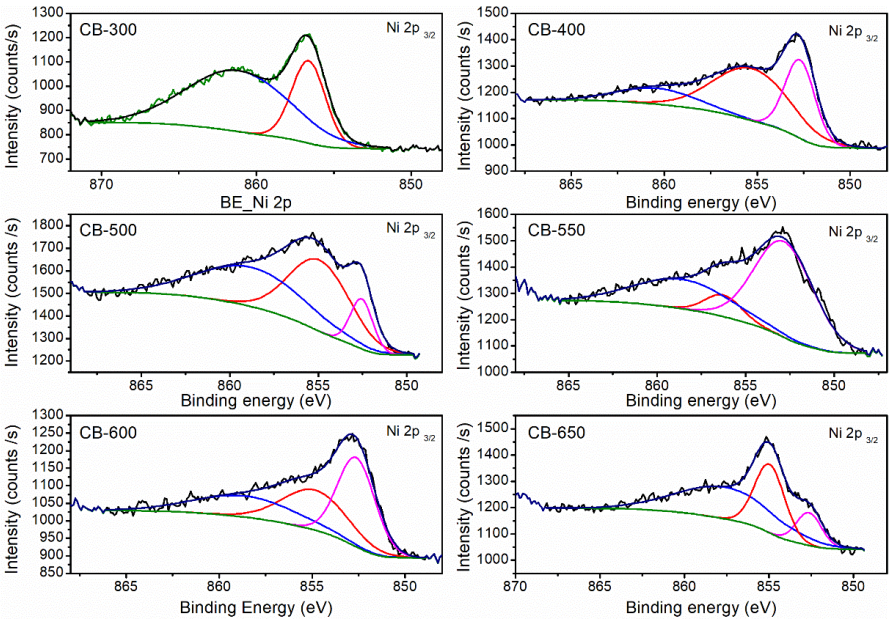

Figure 3.5. Fitted Ni 2p $_{3/2}$ XPS spectra of CB-300, CB-400, CB-500, CB-550, CB-600, CB-650 catalysts. Ni (^{0}) = pink component, $Ni^{\delta+}$ =red component, Ni $_{sat.}$ = blue component.

percentage was detected in CB-300. As demonstrated before, there are remaining unreduced reactants in CB-300, which makes Ni dispersed more homogenously than the well reduced Ni particles anchored on the surface of the support after higher temperatures treatments. Thus, the Ni/C ratio of CB-300 (6.17%) is closer to both the initial value - 10% and the ratio evaluated by

ICP (11.8%), compared to other samples. And it should be noted that during the synthesis of CB-300, the initial Ni/C ratio engaged in the sol-gel synthesis is calculated to be around 10%. Once the Ni is well reduced and formed particles with a size larger than 5 nm, not all Ni can be analysed anymore due to the limitation of the XPS detection depth. In addition to the adsorption of carbon on the surface of Ni particles, it leads to lower Ni/C ratios in CB-400 to CB-650 samples compared to CB-300.

3.3.2. N_2 physical adsorption properties and H_2 TPD analysis of CB-500, CB-550 and CB-650.

The textural properties of CB-500, CB-550 and CB-650 were studied through adsorption/desorption isotherms of N_2 at -196 ^oC and the results are shown in Figure S9. According to the IUPAC classification [266], Type II isotherms were identified for all the samples, which shows a nonporous or macroporous texture of all the catalysts. The BET surface areas of CB-500, CB-550 and CB-650 are 67, 89, 72 m^2/g, respectively, which is similar to the pure CB support (68 m^2/g). All the BET constant (C) values are around 130, and thedifference in surface area values could be due to the experimental errors induced by the weight of samples or by variations in analysis temperature that may be caused by evaporation of liquid N_2. As the catalysts are nonporous and the Ni particles are anchored on the external surface of the support, active sites remain fully accessible to reactants.

Figure 3.6 displays H_2 – TPD profiles of CB, CB-500, CB-550 and CB-650 catalysts that were recorded to estimate the hydrogen uptake and type of adsorption in each case, and as shown before, each catalyst has a Ni loading of 19.4 ± 1.3%. First the samples were reduced and then maintained under H_2 atmosphere until the samples reached the room temperature. After that, Ar was purged to remove the physically-adsorbed H_2. Then H_2 desorption profiles were recorded by heating the sample in the temperature range of 50 – 800 ^oC. The experimental details are described in the characterization methods part. The H_2 - TPD Three major H_2 desorption peaks are present within the test temperature range of 50 – 800 ^oC and no peak arises in blank CB. A very low temperature desorption peak I observed at around 100^oC could be assigned to the weak type C hydrogen bound to the metal surface in a pre-dissociative form.[267] Another low-temperature peak II at around 400^oC is corresponding to the desorption of the hydrogen atoms bound to the Ni surface in α-state (Ni-

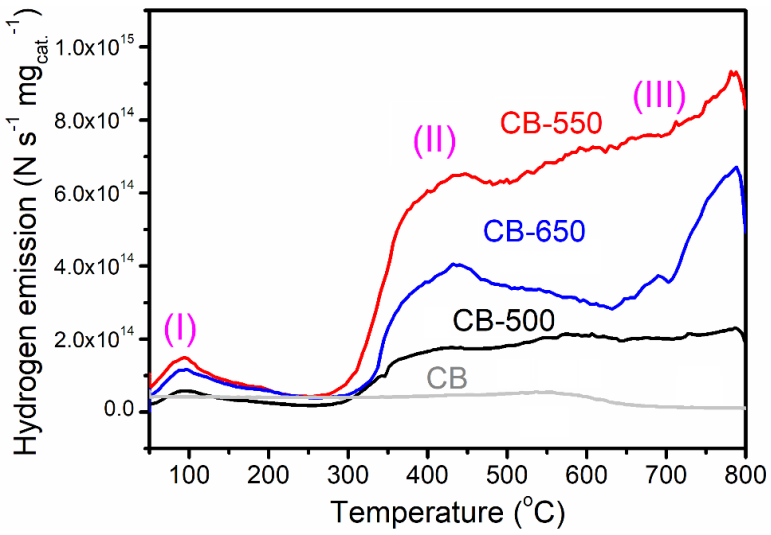

Figure 3.6. H_2 TPD profiles of CB blank, CB-500, CB-550, and CB-650 catalysts.

H) indicating the exposed portion of Ni atoms.[268-272] The very high H_2 desorption peak III at above 500°C originated from strongly adsorbing H_2 on corners, edges and high index planes of Ni and spill over hydrogen.[267, 273] The intensity of all the peaks vary with respect to the nature of the catalysts. In all cases, the intensity of peaks in CB-550 was the highest, followed by CB-650, then CB-500, which is related to the above results obtained with CB-550 for the highest specific surface area and high content of Ni^0. The positions of peak I for all three catalysts exhibit no difference, while the peak II of CB-550 shifted slightly toward lower temperature compared to CB-400 and CB-650, indicating that some weaker hydrogen adsorptions exist in CB-550 catalyst. Besides, CB-550 catalyst possesses the highest hydrogen emission value at any temperature compared to the other two, which implies the strongest H_2 adsorption capacity in this sample.

3.3.3. Catalytic performance of CB-400, CB-500, CB-550, CB-600 and CB-650 catalysts

The catalytic performance of Ni supported by CB catalysts with different morphologies were evaluated in glucose hydrogenation reaction. Since the glucose hydrogenation reaction was carried out in aqueous solution at high temperature and hydrogen pressure, by-products can easily be produced,

through for example the isomerization reaction of glucose under water-catalyzed conditions forming mannose and fructose,[274] and their reduction product – mannitol, as well as other hydrous thermolysis and dehydration products (Scheme S1).[116] Therefore, it is necessary to study the yields of by-products to better understand the product selectivity. Fructose, mannose, and mannitol are main by-products analysed here for yield comparison with sorbitol. The conversion of glucose and yields of products are shown in Figure 3.7. It is clearly seen that there is a trend of increasing and then decreasing conversion of glucose going from CB-400 to CB-650 catalyst, and the glucose conversion has a maximum value over CB-550 catalyst, which is 33.1 % after 2 h reaction, while the yield of sorbitol has a similar pattern (grey portions). For fructose, the yield has an opposite trend to that of sorbitol, decreasing first and then increasing when the catalyst applied is varied from CB-500 to CB-650. The yield of mannitol (hydrogenation product of fructose) was related to fructose, and when the content of fructose was high, the content of mannitol was also relatively high. The yield of mannose was around 0.8% for all applied catalysts. Overall, there is a jump in glucose conversion as well as sorbitol yield for the applied catalysts ranging from CB-500 to CB-550, then a large drop from CB-600 to CB-650. In order to understand the reasons for the

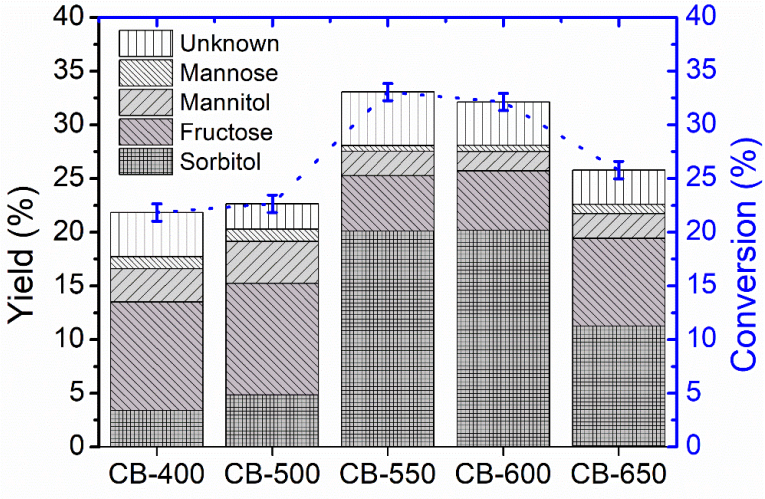

Figure 3.7. The conversion of glucose (blue plot) and yields of different products (stack column) under hydrogenation conditions of 140 ^{o}C for 2 h and 30 bars of hydrogen with catalysts prepared at various temperatures.

different catalyst performance, first, we plotted the graph of glucose conversion versus Ni average particle size in the different catalysts in Figure 3.8a. The glucose conversion increases with the increase of Ni particle size and reaches a maximum at 17.1 ± 6.7 nm, and then it gradually decreases as the size continues to increase. Furthermore, the variation curve of glucose conversion versus metallic Ni content (from XPS) is illustrated in Figure 3.8b.

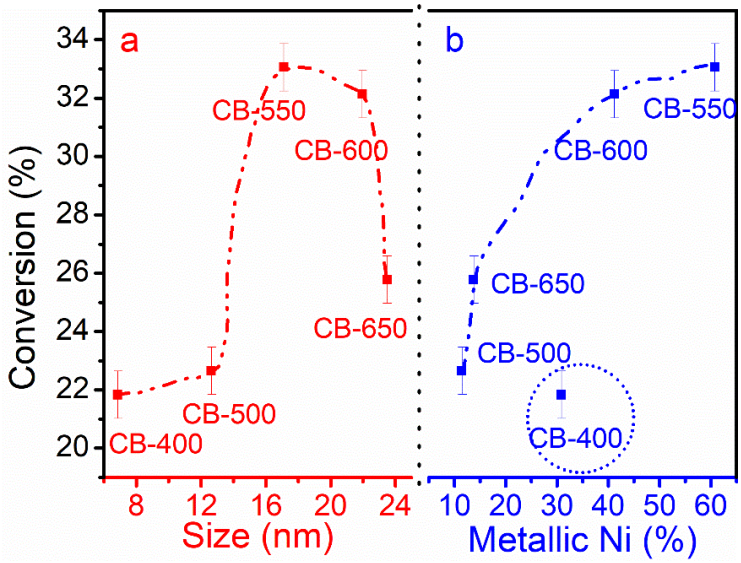

Figure 3.8. Glucose conversion vs Ni particle size in the applied catalysts (a) and metallic Ni content in the applied catalysts (b).

It shows that as the content of metallic Ni increases from one catalyst to another, the glucose conversion increases accordingly, except for the CB-400 catalyst. This is probably because the CB-400 itself contains incompletely reduced reactants that inhibit the metallic Ni for catalysing the reduction of glucose. Thus, in addition to the size affecting the catalytic performance, the content of metallic Ni was linearly correlated to the catalytic activity. Similarly, by graphing sorbitol selectivity versus size as well as versus the content of metallic Ni, a similar conclusion as the conversionwas reached, that is, the sorbitol product selectivity shows a trend of increasing and then decreasing with increasing size and has a maximum at 17.1 nm, and it increases with the increase of metallic Ni content (Figure S10). In addition, sorbitol productivity over CB-550 and CB-600 catalysts showed an absolute superiority compared to other catalysts (Table 3.3). The higher H_2 adsorption ability of CB-550

catalyst highlighted by H_2 – TPD analysis enhances the hydrogenation activity compared to CB-650 and CB-500 catalysts, which has been testified by other authors comparing Co-B and Ni-B catalysts where best performance resulted from the strong hydrogen adsorption ability on the catalyst surface.[178]

Table 3.3 Sorbitol productivities with different catalysts calculated by equation 6. Reaction condition: 60 mg of catalysts, 0.5 g of glucose, 140 ^oC, 30 bar of hydrogen, 2 h.

Catalyst	Glucose conversion / %	Sorbitol / mg	Productivity / $kg.g_{cat.}^{-1}.min^{-1}$
CB-400	21.8	17.6	2.4
CB-500	22.7	24.9	3.5
CB-550	33.1	104.5	14.5
CB-600	32.1	103.9	14.4
CB-650	25.8	57.6	8

3.3.4. Catalytic performance of GNP-450, GNP-550, and GNP-650.

The synthesis method of Ni/CB catalysts was applied for the preparation of graphene nanoplatelets catalysts, named GNP-450, GNP-550 and GNP-650 as function of the heat-treatment applied. The p-XRD patterns of prepared catalysts as well as of the pure GNP support are shown in Figure S11. The diffraction peaks assigned to Ni (111) and Ni (200) at $2\theta = 44.5^o$ and 51.8^o show a similar change as in the Ni/CB series catalysts, which corresponds to the fact that the size of Ni particles increase with increasing reduction temperature on the GNP carrier. Unlike CB support, GNP displays an intense diffraction peak at $2\theta = 26.5^o$, which is corresponding to the characteristic crystalline graphite (002) plane.[275] The grain size of Ni particles over GNP support was also calculated using the Scherrer equation and the result is shown in Table 3.4. The average grain sizes of GNP-450, GNP-550 and GNP-650 were 7.47, 16.6 and 20.6 nm, respectively. TGA profiles of GNP series catalysts (Figure S12) indicate that the GNP-450 catalyst possesses an incompletely decomposed reactant mixture from the preparation process, which is similar to the result with CB-400 catalyst. N_2 adsorption isotherms (Type II) of GNP-450, GNP-550 and GNP-650 samples (Figure S13) indicate a mesoporous texture and the type H4 loops are associated with narrow slit

Table 3.4 Grain sizes of Ni supported by GNP catalysts; Ni weight percentage determined by ICP-OES and XPS elemental analysis; Binding energy and contents of Ni^0, $Ni^{\delta+}$ in Ni $2p_{3/2}$ level of GNP-450, GNP-550 and GNP-650 catalyst determined by High-resolution Ni $2p_{3/2}$ XPS spectrum; BET specific surface area determined by N_2 adsorption at 77K.

	Grain size	**Ni wt%**		**Ni^o**		**$N^{\delta+}$**		**S_{BET}**
	nm	**ICP**	**XPS**	**B.E. (eV)**	**a.t.%**	**B.E. (eV)**	**a.t.%**	**$m^2\ g^{-1}$**
GNP-450	7.47	16.15	3.29	852.78	32.9	854.11	67.1	85[#]
GNP-550	16.6	17.34	3.55	852.92	28.0	855.4	72	89[#]
GNP-650	20.6	17.19	3.81	852.84	13.9	855.77	86.1	92[#]

[#]Those values are not fully reliable because of negative C-values.

pores.[266]. The BET specific areas exhibit similar values around 90 m^2g^{-1}(Table 3.4). Bulk and surface Ni percentages in GNP catalysts were verified using ICP-OES and XPS elemental analysis (Table 3.4), which testifies that GNP-450, GNP-550 and GNP-650 catalysts have similar Ni contents. XPS was also applied to analyse the metallic Ni contents on the surface of GNP samples, the results are shown in Table 3.4. GNP-450 and GNP-550 have a similar Ni^0 content, around 30%, and both are higher than in GNP-650, which is similar to the result of CB series catalysts, where the catalyst prepared at 650^o has less Ni^0 percentage than that heated only at 550^o.

As with the CB series catalysts, the glucose hydrogenation reaction was used to verify the catalytic performance of GNP-450, GNP-550 and GNP-650 catalysts. The glucose conversion after 2 h reaction over those three catalysts is illustrated in Figure S14. The conversion shows the same pattern as before with CB series catalysts, appearing to increase and then decrease as the catalysts change from GNP-450 to GNP-650. The highest glucose conversion was observed over GNP-550 with an average Ni grain size around 16.6 nm, which is similar to the nanoparticle size of CB-550 catalysts. However, the glucose conversion over GNP-550 catalyst (20.9%) is not as high as that over CB-550 (33.1%), which may be due to the lower content of Ni^0 in GNP-550 catalyst or to the different interactions between Ni particles and CB/GNP supports. This lower content of Ni^0 in GNP-550 can be further testified by the

lower atomic Ni/O ratio (0.2581) by comparison with CB-550 catalyst (0.353) calculated by XPS. In general, supported Ni catalysts prepared at 550^{o}C with an average size around 16 nm show the highest catalytic performance regardless of whether CB or GNP supports were used, and catalysts obtained with CB support has a higher catalytic performance than those using GNP support. Similar results were observed in the CO_2 methanation reaction over Ni/YSZ catalysts. Ni particle size with 19 nm has a good performance due to the high Ni^0 dispersion.[276] And Ni nanoparticles in the size range of 10-20 nm were also exhibiting the best catalytic performance for CO methanation reaction compared to smaller (5-10 nm) and bigger (20-35 nm) particle range, because carbon deposits easily onto small Ni particles and carbon nanofibers can grow fast onto big particles.[277] Besides, small particles with more edges and corners favour the adsorption of one reactant versus the other, resulting in less reaction possibilities compared to medium size particles. For instance, based on DFT calculations, stepped surfaces of Au particles with more edges atoms were shown to be preferentially chemisorbed with substrates like CO, O and O_2.[48] By opposition, big particles certainly lose the active metal surface (number of adsorption sites) compared to medium ones. Thus, particles with a medium size can achieve highest activity, as exemplified also with 7 nm nanoparticles in glucose oxidation with a good compromise balance of adsorption of the reactants [18]. Thus, metallic Ni contribution, stable surface and optimal adsorption of reactants could lead here to the best catalytic performance of Ni particles at 16.6 nm compared to other sizes particles.

3.4. Conclusions

In situ XRD was used to study Ni particle growth on a Carbon Black (CB) support with temperature, and it was found that the growth of particles is more obvious in the temperature range of 450 to 550 ^{o}C compared to other temperatures. Thus, CB-400, CB-500, CB-550, CB-600 and CB-650 catalysts were chosen to be prepared at the corresponding temperatures, whose Ni particle size were analysed to be 6.86 ± 1.25, 12.64 ± 3.8, 17.11 ± 6.74, 21.96 ± 9.37 and 23.48 ± 11.6 nm respectively, by the statistical analysis of particles in TEM images. TGA analysis indicated the presence of undecomposed portion of reaction mixture in the CB-400 catalyst. The relative contents of Ni

and C on the catalyst surface obtained by XPS analysis were all in the 2.32 – 3.04 range, while the content in metallic Ni varies considerably from catalyst to catalyst, with CB-550 having the highest Ni^0 content of 60.8%, while this value for CB-650 is only 13.8%. H_2 desorption analysis highlighted that CB-550 exhibits the highest hydrogen uptake and the weakest adsorbed hydrogen, compared to CB-450 and CB-650. Furthermore, glucose hydrogenation reaction with CB-550 catalyst was found to have the highest glucose conversion (33.1%) and sorbitol selectivity (62.8%) within 2 h compared to other catalysts. Combined with the Ni particle size analysis, it was found that glucose conversion increases and then decreases with particle size increase and the maximum is with CB-550 catalyst that displays a Ni particle size of 17.11 ± 6.74 nm. Also, glucose conversion was found to be positively correlated with metallic Ni content, and CB-550 owns again the highest content of metallic Ni, which is one further reason for its high catalytic activity. The same conclusion was reached by replacing CB support with GNP support: GNP-550 has the best catalytic performance relative to GNP-450 and GNP-650, but GNP-550 is not superior to CB-550 catalyst, highlighting a support effect. Moreover, it is interesting to note that Ni on CB or GNP supports appears to have less metallic Ni content at 650 ^oC than at 550 ^oC. The preparation of Ni catalysts presenting different particle sizes by simple control of the temperature of the synthesis conditions to alter their catalytic performance was achieved in this work and size effect was demonstrated to exist in nanoparticles larger than 10 nm.

Since Ni particles supported by GNP showed lower catalytic performance than CB support, we will choose the CB as the catalyst support in the next chapter to elaborate the composition effect of the Ni catalysts.

Chapter 4

Fe-Ni nanoalloy catalysts

4. Synergistic effects altering reaction pathways: the case of glucose hydrogenation over Fe-Ni catalysts

4.1. Introduction

Sorbitol was identified by the U.S. Department of Energy as one of the 12 most important value-added chemicals obtainable from biomass. It can be potentially used as a source of alkanes for liquid biofuels or as an "outstanding building block" for commodity chemicals.[10, 159] Industrially, sorbitol is produced either via biochemical methods, such as conventional fermentation by Zymomonas mobilis [278] or by chemical routes such as catalytic hydrogenation of glucose. Compared with fermentation processes, chemical approaches can be potentially more easily fine-tuned and refined to give higher production at lower costs. Notably, catalytic methods for obtaining sorbitol have attracted substantial attention recently.

The reduction of glucose to sorbitol by hydrogenation was first reported by Ipatieff and co-workers using a nickel catalyst at high temperature and pressure.[165] Based on kinetic studies, the reaction was found to be first order in glucose concentration and catalyst concentration, and half-order with respect to hydrogen pressure when using Raney nickel.[279] Wisnlak et al. also found that this reaction followed a similar pseudo-first-order course when using different catalysts or supported catalysts, such as ruthenium or rhodium supported by active carbon.[167] A challenging aspect of this hydrogenation is that side reactions involving epimerization of the substrate can occur, leading to lower yields or necessitating additional purification steps. While this problem is largely avoided by the use of noble metal catalysts, their cost has still largely limited their applicability for industrial processes. The less expensive nickel has been reported to show minimal epimerization, but generally has lower reactivity than Ru or Pt.[143] For this reason, increased interest has been placed on the development of new catalytic systems for improving the reactivity of base metals for the hydrogenation of glucose.

In the view of creating higher number of catalytic sites with same amount of metal, nanoparticles, especially supported nanoparticles for glucose hydrogenation, have been broadly studied recently.[11, 191, 280] For example, the activity of SiO_2 supported amorphous Ni-B catalysts was reported to be

adjusted by calcination temperature[180]. Schimpf and co-workers confirmed the necessity of complete reduction of precursors within Ni/SiO_2 catalyst to optimize activity and selectivity.[11] Besides SiO_2, other different supports like MWNTs (multi-walled carbon nanotubes), Al_2O_3, or TiO_2 were also applied to investigate the catalytic activities in this reaction, because different metal-support interactions could affect the activity and stability of metal particles.[116, 281, 282] For example, the Ru/MWNTs material showed the highest catalytic activity, compared with Raney Ni and ruthenium supported on Al_2O_3 or SiO_2.[187] Ni catalysts supported on carbon were found to leach less compared with other Al_2O_3, TiO_2 or SiO_2 supports.[116] Additionally, carbon is robust at high pressure and temperature in aqueous solution. Thus, carbon is an ideal material to support metals with desired catalyst activity and stability for glucose hydrogenation.

Regarding to the metal, it is practical to find strategies to improve activity of Ni-based catalysts as most commercial processes are still using Raney nickel.[171] Raney nickel has been reported to be enhanced by promoters like molybdenum, chromium, and iron.[158, 167, 283, 284] Among them, Fe is the most electropositive metal and glucose hydrogenation reaction with Fe promoted Raney- Nickel catalyst exhibits the highest initial rate.[173] So, Fe as a promoter can maximally enhance the activity of Ni catalyst. Also, the magnetic properties of Fe make it easy to separate from the products for successive use when considering recycling. Since most of the previous works on this bimetallic association were focusing on the activity enhancement by an Fe promotor on Raney nickel,[158, 173] to the best of our knowledge, supported Ni-Fe-based catalysts have never been reported in the hydrogenation of glucose, let alone to investigate the reaction pathways. Thus, Ni integrating Fe on carbon support catalysts is worth studying not only for fundamental research but also for industrial applications.

With this aim in mind, we synthesized Fe_xNi_y alloy catalysts, using carbon black (CB) as a support to study both their catalytic performance and the function of Fe and Ni atoms during the hydrogenation reaction. Moreover, the synergy and reaction pathway were also clarified. The catalytic transformation of glucose to sorbitol in the aqueous phase can be described as schematized in Figure 4.1. The open-chain glucose conformer, transformed from the glucopyranose ring, is adsorbed on the FeNi alloy surface via the oxygen lone

pairs. Then the polarization of the C = O bond favours nucleophilic addition of hydrides (H adatoms) present on the metal surface, producing sorbitol.

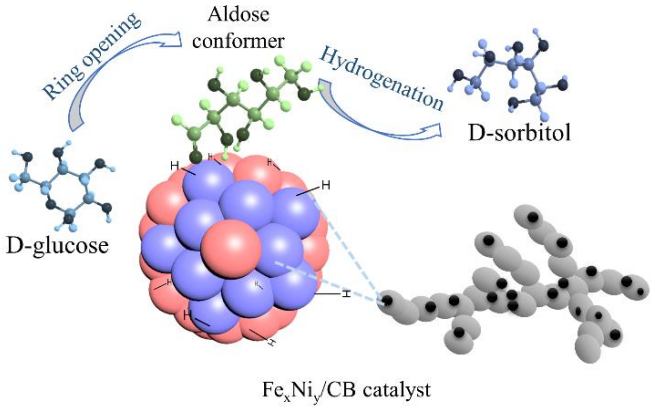

Figure 4.1. Aqueous-phase hydrogenation of glucose to sorbitol on the surface of Fe_xNi_y alloy catalysts supported on carbon black.

4.2. Experimental

4.2.1. Catalysts preparation

Chemicals. Nickel (II) nitrate hexahydrate [$Ni(NO_3)_2 \cdot 6H_2O$, 99.999%, Sigma-Aldrich], iron(III) nitrate nonahydrate [$Fe(NO_3)_3 \cdot 9H_2O$, >98%, Sigma-Aldrich], carbon black support [received as 250G type from IMERYS GRAPHITE & CARBON], citric acid [$C_6H_8O_7$, 99.5%, Alfa Aesar], and ethanol [C_2H_5OH, 100%, Merck] were used as received.

Synthesis of monometallic Fe/CB, Ni/CB catalysts. The synthesis of Fe or Ni nanoparticles supported by carbon black was inspired by a Pechini-type sol-gel method.[285] In a typical procedure, 100 mg of CB, 400 mg of citric acid and 0.34-0.35 moles of the $M(NO_3)_n \cdot XH_2O$ salt (99.1 mg of $Ni(NO_3)_2 \cdot 6H_2O$ or 144.7 mg of $Fe(NO_3)_3 \cdot 9H_2O$) were added into a round-bottom flask equipped with a stir bar. After, 6 mL of ethanol was added, and the mixture was stirred and sonicated until a homogenous suspension was obtained. Then, the suspension was heated at 90 ^oC for 3 h under reflux. Afterwards, the suspension was transferred into a ceramic boat and dried under vacuum at 30 ^oC until a gel formed. Finally, the gel was introduced in a tubular furnace and heated to 750 ^oC for 2 h under Ar/H_2 atmosphere. It should be stated that this temperature is sufficient to reduce nickel and iron

precursors in monometallic and alloy samples.[286-288] The recovered magnetic powder was used as catalyst without further precautions.

Synthesis of Fe_3Ni/CB, FeNi/CB, $FeNi_3$/CB alloy catalysts. The alloy catalysts were prepared following the same procedure as for the synthesis of monometallic Fe/CB (Ni/CB) detailed above, but with simultaneous addition of two metal salts in the following ratios: Briefly, 24.8 mg of Ni $(NO_3)_2 \cdot 6H_2O$ and 108.5 mg of Fe $(NO_3)_3 \cdot 9H_2O$ were used to obtain the Fe_3Ni/CB catalyst. 49.6 mg of Ni $(NO_3)_2 \cdot 6H_2O$ and 72.3 mg of Fe $(NO_3)_3 \cdot 9H_2O$ were used to obtain FeNi/CB catalyst, and 74.3 mg of Ni $(NO_3)_2 \cdot 6H_2O$ and 36.2 mg of $Fe(NO_3)_3 \cdot 9H_2O$ were used to obtain the $FeNi_3$/CB catalyst.

4.2.2. Hydrogenation of D-glucose

Hydrogenation experiments were performed in a stainless-steel high pressure reactor (Parr autoclave) under the given conditions, typically, 140 ^oC at 30 bar H_2 using a stirring rate of 1700 rpm (which was sufficient to eliminate external mass-transport limitations) using 0.5 g of glucose and 60 mg of catalyst in 100 mL Milli-Q water. In brief, 60 mg of catalyst was added to the aqueous glucose solution, then the reactor was purged with N_2 for 5 min to remove air. The reaction mixture was subsequently heated to 140 ^oC under N_2, then the autoclave was filled to a constant H_2 pressure (30 bar) and the reaction started. For the kinetic tests, samples were periodically withdrawn from the reaction vessel to evaluate the evolution with time of both glucose conversion and products yields. When single experiments ended, the filtrate of the reaction slurry was analysed by HPLC. HPLC analysis was performed on a Waters system equipped with a refractive index 2414 detector. An HPX-87C carbohydrate column was used, with ultrapure water as mobile phase at a flow rate of 0.5 $cm^3\ min^{-1}$, a column temperature of 358K and 25 µl of injected volume. Standard alpha-D(+)-glucose ($C_6H_{12}O_6$, ≥ 99%, Acros), D-(-)-fructose ($C_6H_{12}O_6$, ≥ 99%, Sigma), D-(+)-mannose ($C_6H_{12}O_6$, ≥ 99%, Sigma), D-mannitol ($C_6H_{14}O_6$, ≥ 98%, Sigma-aldrich) and D-sorbitol ($C_6H_{14}O_6$, ≥ 99.5%, Sigma) were first analysed by HPLC to determine their retention times separately, which were used as references to identify the products of glucose hydrogenation. The glucose conversion, sorbitol selectivity, product percentage yield, sorbitol productivity, and carbon balance (C_b) were calculated according to equations 3-7 listed in chapter 2.

4.3. Results and Discussion

4.3.1. Characterization of Fe_xNi_y/CB catalysts

Three bimetallic Fe_xNi_y catalysts supported on carbon black, with different ratios between the two metals, were prepared. For comparison, monometallic materials were also synthesized by the same method. P-XRD was applied to determine the crystal phases in the synthesized nanocatalysts, and the patterns of the FeNi/CB catalyst (pink line), Ni/CB, (blue line), Fe/CB (red line), as well as pure CB (black curve) are shown in Figure 4.2. In each curve, one main broad peak at 2θ = 25.31° attributable to the (002) plane of graphite was observed along with a small hump at 2θ = 43.36° corresponding to the (100) plane (JCPDS-ICDD Card No.41–1487), which revealed the disordered graphitic nature of CB. This graphitic carbon in CB lacking long-range order and disorderly distributed potentially makes CB rich in defects, consequently reducing the content of aromatic carbon, which may help to reach a better dispersion of active phase when it is applied as support in catalytic aqueous reactions. The peaks attributable to Fe, Ni, or FeNi phases were much stronger and sharper than those of carbon black, indicating the high crystallinity of the metal nanoparticles. As Fe-Ni catalysts were prepared at

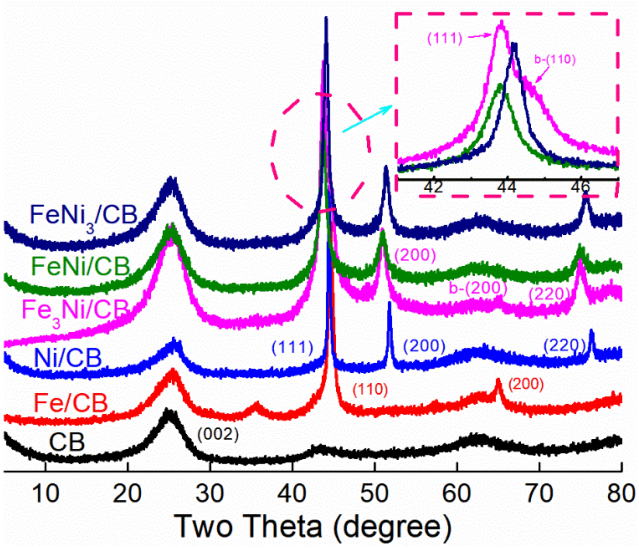

Figure 4.2. Powder X-ray diffraction patterns of CB, Fe/CB, Ni/CB, Fe_3Ni/CB, FeNi/CB, $FeNi_3$/CB. Inserted imaged: the enlarged peaks around 2θ = 44° of Fe_3Ni/CB, FeNi/CB, $FeNi_3$/CB samples.

750 ^{o}C, all the nanoparticles were considered as γ-Fe-Ni magnetic alloys , based on the reported 'metastable' phase diagram of Ni-Fe alloys.[289] The peaks at 2θ = 44.75^{o} and 65.05^{o} for Fe/CB corresponded to the (110) and (200) planes of crystalline body centered cubic (bcc) iron structure, respectively. The peaks at 2θ values of 44.51^{o}, 51.83^{o}, 76.37^{o} corresponded to the (111), (200) and (220) crystal planes of crystalline face centered cubic (fcc) nickel in the Ni/CB catalyst, respectively. For bimetallic FeNi/CB catalyst with atomic ratio 1:1, the peaks at 2θ = 43.79^{o}, 51.01^{o}, 75.05^{o} corresponded to the (111), (200) and (220) crystal planes of crystalline fcc FeNi alloy (JCPDS 12-0736). Each crystalline peak in FeNi/CB has shifted to the left compared to Ni/CB although they are both fcc phases, because the unit cell parameters increased when the larger Fe atoms entered the fcc structure of Ni. The XRD patterns of the two other Fe-Ni alloy catalysts supported on CB, namely Fe_3Ni/CB and $FeNi_3$/CB, with atomic ratios of 3:1 and 1:3, with a total metal loading unchanged around 16 wt% (theoretically), are also illustrated in Figure 4.2. For Fe_3Ni/CB, the bcc and fcc phases coexisted in the alloy particles. The peaks at 2θ = 44.64^{o}, 65.15^{o} corresponded to the (110) and (200) planes of crystalline bcc Fe-Ni alloy structure (JCPDS37-0474), respectively. For $FeNi_3$/CB, the peaks at 2θ values of 44.16^{o}, 51.44^{o}, 75.71^{o} corresponded to the (111), (200) and (220) crystal planes of crystalline fcc Fe-Ni alloy structure (JCPDS38-0419), respectively.[290] The average size of alloy nanoparticles that were calculated using the Debye–Scherrer formula based on the full-width at half-maximum (FWHM) of the (200) diffraction peak were 9.4 nm, 9.0 nm and 11.1 nm for $FeNi_3$/CB, FeNi/CB, and Fe_3Ni/CB materials, respectively.

The STEM-HAADF images in Figure 4.3a-c show that the as-prepared alloy catalysts exhibit mostly spherical morphology with a narrow size distribution (Figure 4.3d-e), which is consistent with P-XRD analysis. Furthermore, the average nanoparticles size in Fe_3Ni/CB, FeNi/CB, $FeNi_3$/CB samples is almost the same, so the effect of particle sizes on catalytic performance can be eliminated. Meanwhile, STEM-EDX analysis (Figure S15 and Table 4.1) illustrated that the composition of the particles was stable from one to another, that is to say no monometallic Fe particles or Ni particles were observed in the bimetallic catalysts.

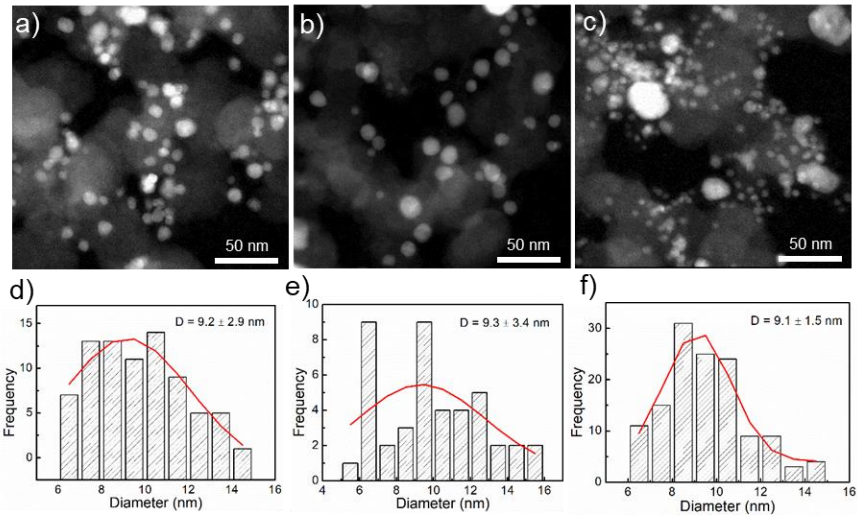

Figure 4.3. STEM-HAADF images and nanoparticle size distribution determined with ImageJ software of Fe_3Ni/CB catalyst (a, d), FeNi/CB catalyst (b, e), and $FeNi_3$/CB catalyst (c, f).

Table 4.1 The average composition of nanoparticles in Fe_3Ni/CB, FeNi/CB, and $FeNi_3$/CB samples. (data acquired by EDX analysis from particle to particle)

	Fe (at.%)	error	Ni (at.%)	error
Fe_3Ni/CB	70.6	14.1	29.4	9.6
FeNi/CB	50.6	8.9	49.4	9.3
$FeNi_3$/CB	20.5	3.7	79.5	9.9

The metal loadings measured by ICP-OES are given in Table 4.2. These are slightly lower than theoretical values (based on engaged amounts). This is due to traces of insoluble ash during the digestion process causing systematic underestimation by ICP. However, those differences do not affect the comparison of the catalyst series with various compositions.

To study the textural properties of catalysts, adsorption/desorption isotherms of N_2 at -196 ^oC were determined and results are illustrated in Figure S16. The expected Type II isotherm was obtained for all the samples, which exhibit nonporous or macroporous texture, but the BET surface area showed differences among parent CB, monometallic catalysts and bimetallic catalysts.

Table 4.2 Metal loading, Fe:Ni ratio, textural properties of Fe/CB, Ni/CB, Fe_3Ni/CB, FeNi/CB, $FeNi_3$/CB catalysts and bare CB support.

Catalyst	Theoretical metal loading (wt%)			Measured metal loading (wt%) – ICP-OES			S_{BET} (m^2g^{-1})
	Fe	Ni	Fe:Ni	Fe	Ni	Fe:Ni	
CB	-	-	-	-	-	-	69
Fe/CB	14.29	-	-	11.1	-	-	141
Ni/CB	-	14.29	-	-	14.0	-	92
Fe_3Ni/CB	12.50	4.17	3.0	12.04	4.12	2.92	111
FeNi/CB	8.33	8.33	1.0	8.2	8.2	1	113
$FeNi_3$/CB	4.17	12.50	0.3	4.12	12.43	0.33	114

The increase in BET surface area after nanoparticle loading is possibly due to nanoparticles anchored on the surface of CB, which creates additional surfaces by both increasing the rugosity with the Ni nanoparticles and the separation of clumped CB support grains induced by Ni particle intervening. It should be noted that those nonporous materials and exposed metal particles remain fully accessible to reactants.

The state and the occurrence of the different elements at the surface of the materials was evaluated through XPS. Figure 4.4 illustrates the XPS spectra of the Ni $2p_{3/2}$ and Fe $2p_{3/2}$ region of Fe/CB, Ni/CB and FeNi/CB catalysts. The binding energies around 707 eV and 852 eV (red components) are ascribed to metallic Fe (Fe^0) and metallic Ni (Ni^0), respectively.[243] The peaks (blue components) around 710 eV and 854 eV are assigned to oxidized Fe ($Fe^{\delta+}$) and oxidized Ni ($Ni^{\delta+}$), along with two satellite peaks (pink peaks).[243] The Ni (δ+) 2p 3/2 peak (856.8 eV) of Ni/CB shifted towards lower binding energies with the introduction of Fe, while the Fe (δ+) 2p 3/2 peak (706.79eV) of Fe/CB moved towards higher binding energies after alloy formation with Ni. This shift of the binding energies may be attributed to partial electronic transfer from Fe to Ni in the FeNi/CB alloy catalysts.[210, 291] Since the catalysts were stored with no particular precautions, an external Ni or Fe oxide layer could be formed

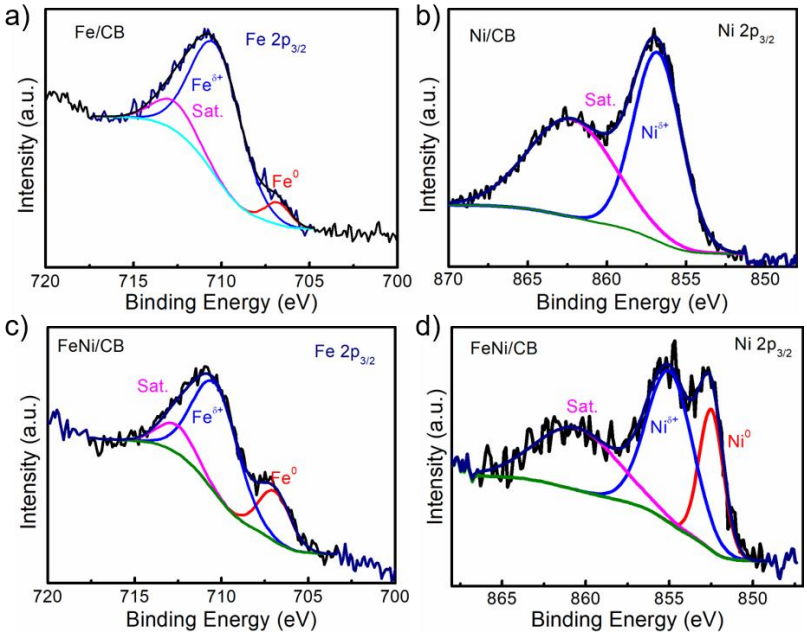

Figure 4.4. Fitted Fe $2p_{3/2}$ and Ni $2p_{3/2}$ XPS spectra of (a) Ni/CB, (b) Fe/CB, (c, d) FeNi/CB catalysts. Fe (0), Ni (0) = red components; Fe (III), Ni (II) = blue components

due to contact with air, which explains the presence of oxidized Ni and Fe. It could be observed that there is no Ni^0 on the surface of the monometallic Ni/CB catalyst (Figure 4.4b), while 22% of Ni^0 exists in the FeNi/CB catalyst, and the metallic portions are even higher in the two other alloys (Table 4.3). As for Fe^0, the proportion in the alloy catalysts is more than 2 times higher than it is in the monometallic Fe/CB catalyst. This suggests that a stabilization effect exists in the alloy catalysts, which could inhibit surface oxidation to some extent. As hydrogen is dissociated by the metallic atoms on the surface of the catalyst during the hydrogenation reaction, this remaining metallic Fe and Ni in the alloy catalysts are active sites, which can allow reaction without prereduction of the oxidation layer.[157] From the comparison of XPS and ICP elemental analysis results (Table 4.3), it can be seen that those Fe:Ni ratios are almost the same, which mirrors the consistent internal and external compositions.

Table 4.3 Binding energy and contents in Fe^0, $Fe^{\delta+}$ in Fe $2p_{3/2}$ level and Ni^0, $Ni^{\delta+}$ in Ni $2p_{3/2}$ level; weight ratio of Fe and Ni obtained by XPS and ICP.

Catalyst	Fe^0 $2p_{3/2}$		$Fe^{\delta+}$ $2p_{3/2}$		Ni^0 $2p_{3/2}$		$Ni^{\delta+}$ $2p_{3/2}$		Fe:Ni (wt%)	
	B.E. (eV)	at. %	B.E. (eV)	at.%	B.E. (eV)	at.%	B.E. (eV)	at.%	XPS*	ICP
Fe/CB	706.79	6.5	710.26	93.5	-	-	-	-	-	-
Ni/CB	-	-	-	-	0	0.00	856.8	100.0	-	-
Fe_3Ni/CB	706.95	51.2	710.67	48.8	852.29	57.4	854.15	42.6	3.02 ± 0.3	2.92
FeNi/CB	706.93	20.8	710.3	79.2	852.49	22.0	854.97	78.0	0.92 ± 0.3	1
$FeNi_3$/CB	706.95	40.4	710.67	59.6	852.29	38.3	854.15	61.7	0.56 ± 0.3	0.33

* Atomic percentages have been converted into mass percentages.

4.3.2. Activity test: Hydrogenation of glucose

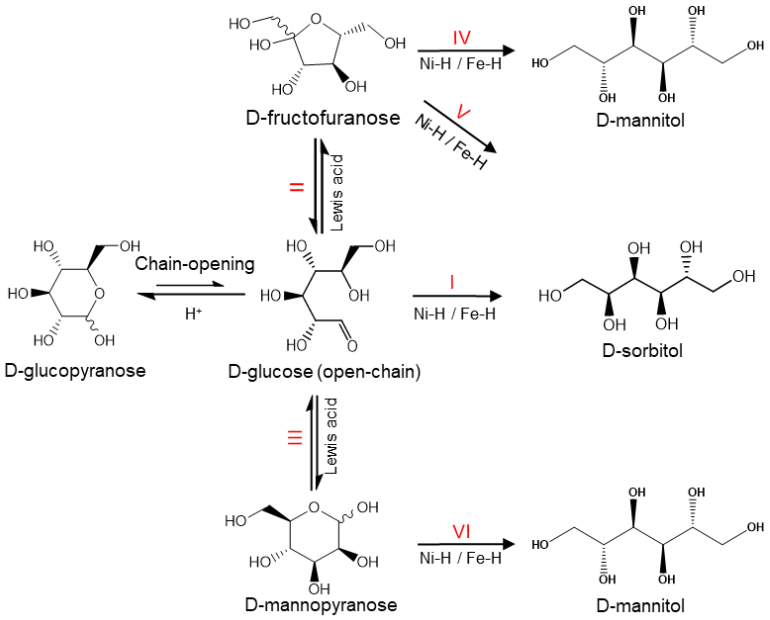

Figure 4.5. Reaction network for D-glucose hydrogenation over Fe/CB, Ni/CB and Fe_xNi_y/CB catalysts at 140 °C, 30 bar H_2 and 1700 rpm stirring speed.

Catalytic hydrogenation of glucose in aqueous solution was employed as a model reaction to evaluate the catalytic performance. The reaction network

and key products are illustrated in Figure 4.5. As it is well known, sorbitol, one of the main hydrogenation products (pathway I), can be obtained from the open chain form of glucose, which only exists at ~0.0026 mol% in solution due to its thermodynamic instability and its spontaneous isomerization to cyclic forms.[274] This open chain form then adsorbs on the metal surface via its O lone pair and subsequently gets reduced by the hydridic adatoms formed on the metal surface by H_2 splitting. Therefore, the formation of the open-chain conformation is generally considered to be the rate-limiting step.[12] Pathway II is glucose conversion to fructose, which involves the isomerization of an α-hydroxy aldehyde to the corresponding α-hydroxy ketone.[292] In the presence of catalytic Lewis acids, this process has been shown to occur via an intramolecular hydride shift. For the Fe/Ni catalysts, the isomerization could be catalysed by leached metal ions like Fe^{3+}, Ni^{2+} which would act as Lewis acids or also simply by metallic Fe.[15] The reversibility of this intramolecular process can also lead to epimerization of the C2 position and formation of mannose. (pathway III).[293, 294] Mannitol in consequence would then be produced through fructose and mannose hydrogenation (IV, V). As sorbitol, fructose, mannose and mannitol are the major products/reactive intermediates found during glucose hydrogenation reaction, the dehydration and other aldose-ketose isomerization processes were not taken into account in this work.[12, 193] The real-time changes in the yield of those products and glucose conversion over 360 min of reaction are shown in Figure 4.6 for the monometallic and bimetallic 1:1 formulations, along with the case of using a mixture of both monometallic catalysts, for comparison. It can be seen that in the first 40 minutes or so, glucose conversion curves with these different catalysts are all linearly correlated with the X axis time. Taking the experimental data of glucose conversion (x) presented in Figure 4.6, and plotting Ln (1-x) over reaction time in the first 50 minutes, a linear fitting was indeed obtained in all cases (Figure S17). It should be noted that conversion (x) was determined at low conversion from the linear portion of reaction profiles, considering no mass-transport limitations and catalysts deactivation. So this pseudo-first-order dependence with respect to glucose was revealed under excess of H_2, which is consistent with previous reports.[167, 191] In addition, the reaction rate constant with various catalysts was compared through the slopes of the profiles in Figure S17, giving the order $k_{Fe/CB}$ >

$k_{FeNi/CB}$ > $k_{Fe/CB+Ni/CB}$ > $k_{Ni/CB,}$ where r is the initial reaction rate of glucose hydrogenation. So, Fe/CB is the most active catalyst in these conditions, followed by FeNi/CB, and the Ni/CB is the least active catalyst. The favoured reaction paths and corresponding product yields with each catalyst are discussed below.

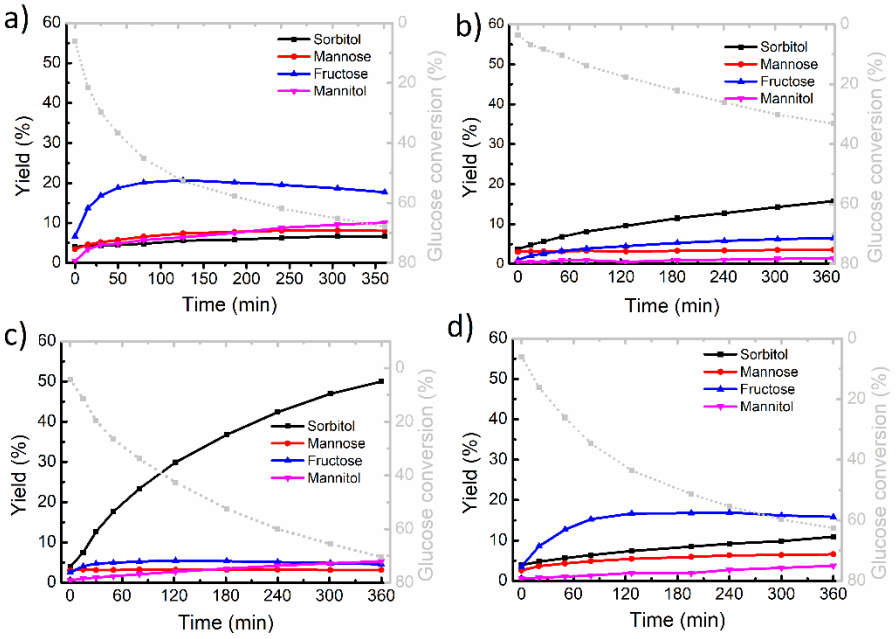

Figure 4.6. Yield (left axis) of sorbitol (black), fructose (blue), mannose (red) and mannitol (pink) vs time and glucose conversion (right axis) vs time over Fe/CB (a), Ni/CB (b), FeNi/CB (c) and mixture of Fe/CB and Ni/CB (d) catalysts at 140 °C, 30 bar H_2, 1700 rpm and 360 min. Yield scales are different in each case to better highlight the differences for each species.

The yield of the four key products and the conversion of glucose *vs* reaction time during glucose hydrogenation in the presence of the monometallic Fe/CB catalyst are illustrated in Figure 4.6a. The conversion and various yields increased with time, while the rate of conversion decreased substantially over time, especially after 40 min, which may be attributed to insufficient amount of glucose remaining (due to one drawback of batch reactor process – a fixed raw materials amount leading to a low productivity compared to a continuous process) or catalyst deactivation. Additionally, a decrease in fructose yield was observed, probably due to its isomerization to glucose and hydrogenation to mannitol. Within 360 min, a total of 68% of the glucose was consumed in

the reaction, giving 17.7% yield in fructose, 10.1% yield in mannose, 8.1% yield in mannose and 6.6 % yield in sorbitol, respectively. Thus, for the Fe/CB catalyst, isomerization of glucose to fructose is the most preferred reaction path, which is consistent with previous reports stating that Fe species are active sites for glucose isomerization.[295] In contrast, Ni/CB catalyst encourages a different reaction pathway (Figure 4.6b). As described above, under the same conditions, the initial reaction rate on Ni/CB is lower than with Fe/CB, thus only 33.1% of glucose was transformed in the reaction, however sorbitol formed with a yield of 15.7%, more than double that of Fe/CB catalyst. Additionally, lower yields of the undesired products were observed, fructose (6.5% yield), mannose (3.5% yield), and mannitol (1.5% yield). The fructose production was not catalysed by Ni/CB catalyst compared to Fe/CB catalyst, which leads to a low yield of fructose, far from equilibrium. Thus, while its activity is not as good as the Fe/CB catalyst, Ni/CB gave the desired sorbitol as the major product.

Interestingly, when Fe and Ni formed an alloy, the two metals promote each other, both driving the reaction via the sorbitol producing pathway and exhibiting higher activity. As a result, sorbitol is the dominating product with a yield of 50 % in 360 min, 3 times higher than that of Ni/CB (Figure 4.6c). Moreover, isomerization of glucose to fructose seems to be depressed by Ni, and consequently, the yield of fructose is much lower than with the monometallic Fe/CB. The yields in mannose and mannitol remain similarly low. Glucose conversion with FeNi/CB also improved from 33.1% to 70.5% in comparison with Ni/CB. Thus, synergistic effects arise from alloying: the conversion of glucose and the yield in sorbitol are both highly improved, and simultaneously the isomerization of glucose is restricted. To further verify the presence of a synergistic effect in the alloy catalyst, a mechanical mixture of both Fe/CB and Ni/CB catalysts was used to catalyse glucose hydrogenation. It should be noted that in this case 30 mg of Fe/CB and 30 mg of Ni/CB were employed, instead of 60 mg in the previous cases, to keep the total metal quantity involved in the reaction constant and corresponding to FeNi/CB (1:1) catalyst. The glucose conversion and product yield results are shown in Figure 4.6d. It is obvious that fructose is a major product with a similar line shape as for pure Fe/CB, which is attributed to the function of Fe/CB catalyst, and the sorbitol yield of 10.9 % is similar to the catalytic reaction with Ni/CB. In 360

min, 62.6 % of glucose was transformed in the reaction, which is also lower than the conversion obtained with the FeNi/CB alloy. The hydrogenation results of the catalyst mixture indicate that its catalytic behaviour comes largely from the simple superposition of the results of the two single catalysts, that is, the mixing of two monometallic catalysts does not generate a synergistic effect like for the alloy. Electron rearrangement in the alloy may contribute to this synergistic effect. Since Fe atoms in FeNi/CB are more electropositive than Ni given their electron affinities, even under H_2 pressure, they can remain positively charged and act as adsorption sites for the open-chain glucose.

The result of real- time carbon balance is shown in Figure 4.7, which was calculated using equation 4. It should be noted that C_b is underestimated when there are products obtained other than sorbitol, mannose, fructose and mannitol, because those unidentified minor by-products were not considered in this equation. All values of C_b with the four different catalysts decreased with prolonged reaction time, which may be attributed to increased by-products formation. As the C_b with Ni/CB and FeNi/CB catalysts were consistently higher than with Fe/CB and mixtures of Fe/CB and Ni/CB

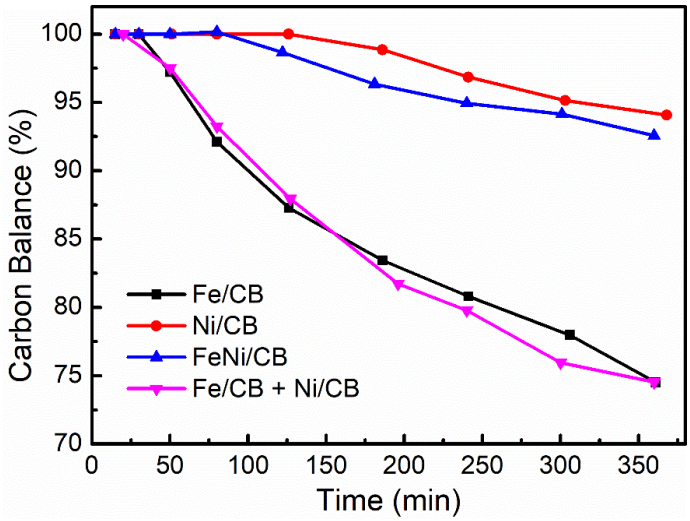

Figure 4.7 Real-time carbon balance monitoring during glucose hydrogenation reaction over Fe/CB (black), Ni/CB (red), FeNi/CB (blue) and mixture of Fe/CB and Ni/CB (pink) catalysts at 140 ^oC, 30 bar H_2, 1700 rpm and 360 min.

catalysts, it means that more side reactions occurred with Fe/CB and mixtures of the Fe/CB and Ni/CB catalysts than with the other two catalysts. These results support that, relative to Fe/CB and mixtures of Fe/CB and Ni/CB, synergistic effects in FeNi/CB reduce the occurrence of other side reactions over Fe metal surface, keeping the C_b above 92.6%.

In order to investigate the principle of synergistic effects in Fe-Ni alloys with different compositions, the two other Fe_3Ni/CB and $FeNi_3$/CB catalysts were used to catalyse the glucose hydrogenation reaction, and their conversion and sorbitol selectivity results at 2 h are illustrated in Figure 4.8. The Fe mass percentage in the alloy (x-axis) was directly correlated with conversion. As %Fe increased from 0 to 100%, (from left to right) the conversion increased from 21.4% to 52.8%. This indicates that the activity of the alloy catalyst increases simply with the increment of Fe. However, the sorbitol selectivity decreases with Fe content, especially after 50% Fe composition, while before it remains approximately unchanged. This is possibly due to the fact that in iron-rich samples (Fe_3Ni/CB), more Fe atoms are clustered within the alloy and do not feel the influence of Ni (Scheme 4.1). Since it is the bcc Fe-Ni alloy structure that is detected in this catalyst by XRD and the main contribution of

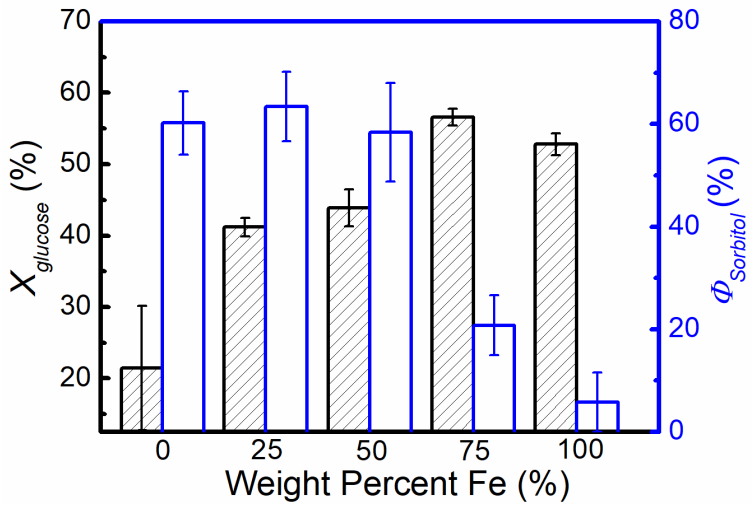

Figure 4.8. Influence of composition of Fe-Ni/CB catalysts on glucose conversion ($X_{glucose}$) and sorbitol selectivity ($\Phi_{sorbitol}$). Reaction conditions: 60 mg catalyst, 0.5 g glucose, 100 mL H_2O, T = 140 °C, p (H_2) = 30 bar, 120 min and stirring speed of 1700 rpm.

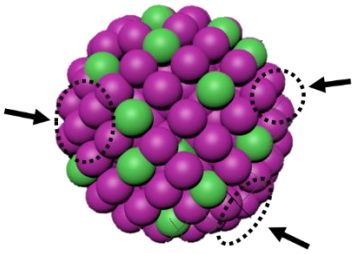

Scheme 4.1 Diagram of Fe_3Ni alloy nanoparticle. Green balls stand for Ni atoms and purple balls stand for Fe atoms. The circled areas indicated by the arrows refer to clustered Fe atoms.

b-(110) diffraction peak is from the clustered Fe atoms. This b-(110) diffraction should not come from isolated pure Fe particles, as isolated pure Fe particles were not observed in EDX mapping images (Figure S15 (3, 6, 9)). Hence, these Fe atoms still exhibit the same electron distribution than in pure Fe samples, which favoured the isomerization reaction. This leads to lower selectivity of sorbitol. In a word, catalytic performance of Ni catalyst was promoted after adding Fe forming an alloy, but selectivity to sorbitol dropped seriously if the composition of iron exceeds 50%. Based on that, FeNi/CB with 1:1 atomic ratio appears to be the best compromise for achieving higher catalytic activity while maintaining high sorbitol selectivity. In this FeNi/CB alloy, the Fe and Ni atoms are supposed to be evenly distributed, which could maximize the activation of Ni, resulting in the optimal synergistic effect versus the other alloys.

4.4. Conclusion

Aiming at investigating the synergistic effect in alloy Fe-Ni catalysts during glucose hydrogenation, monometallic Fe, Ni and Fe-Ni alloy catalysts supported by CB were synthesised through a sol-gel method. XRD results demonstrated that an alloy phase was formed in the bimetallic catalysts. HAADF-TEM images and EDS analysis evidenced that the size distribution and composition of the nanoparticles were uniform. Fe and Ni in the alloy form were found to be less prone to oxidation than monometallic Fe and Ni through XPS analysis, so metallic Fe and Ni sites remain at the surface of the bimetallic catalysts, contributing to the splitting of hydrogen necessary for the catalytic transformation.

By analysing the hydrogenation reaction of glucose over monometallic and alloy catalysts, it was found that Fe and Ni favour different reaction pathways and that synergistic effects were present with the FeNi alloy catalysts. With the Fe/CB catalyst, 68% of glucose was transformed in the reaction, with fructose as the major product, obtained in 17.7% yield, while only 6.6% of sorbitol was produced. For the Ni/CB catalyst, in which glucose to sorbitol is the dominating pathway, a higher percentage of sorbitol (15.7%) was obtained but overall glucose conversion was lower (33.1%). Interestingly, the glucose conversion and sorbitol productivity were enhanced to a great extent when Fe and Ni formed an alloy, with a glucose conversion of 70.4% and sorbitol yield of 50%. This synergistic effect cannot be observed with a simple mixture of Fe/CB and Ni/CB catalysts, as electronic effects only appears in alloys. By comparing catalytic performance using Fe-Ni alloys with different compositions, FeNi/CB with an atomic ratio of 1:1 was identified as the best compromise for efficient hydrogenation of glucose to sorbitol.

Chapter 5

Ni-based catalysts deactivation

5. Deactivation of Ni catalysts in aqueous glucose hydrogenation reaction.

5.1. Introduction

Stability as a critical criterion for heterogeneous catalysts has been studied and enhanced specially for industrial applications. Extensive works have been carried out, targeting the deactivation of catalyst in different phases. Catalyst stability and deactivation in the gas-solid phase has been widely established over the past years.[296] However, less attention has been paid to the liquid phase.

Regarding the nature of deactivation mechanisms that have been proposed, three aspects can be taken into account – physical, thermal and chemical.[114] For instance, physical deactivation occurs with chemical species deposition (fouling), resulting in lack of accessibility to the active sites. Mechanical alterations like crushing, attrition, abrasion, erosion of the catalyst particles can also cause the loss of active phase. Sintering effects are typically caused by thermal processes. And poisoning, new inactive phases formation and leaching can be classified into the chemical deactivation mechanisms.[297-300] Poisoning refers to strong chemical adsorption of reactants or impurities on the active sites, while leaching is the dissolution of active sites into the reaction medium. Usually, catalysts deactivation is caused by more than one factor.

In our case, Ni catalysts were used for glucose hydrogenation in aqueous medium. Thus, the crucial aspects regarding to deactivation of Ni catalysts is leaching of the active sites into the liquid medium. The obtained catalysts described in the previous chapters were studied for their stability. TEM, p-XRD, XPS, and ICP-OES / AAS were applied to study the morphologies, crystallinities, chemical states and compositions of the catalysts before and after catalytic reaction. Trials to mitigate the deactivation of catalysts such as introducing another stable metal into the catalysts formulation, and changing the reaction medium, were also carried out. The specific results and discussions arising from such study are as follows.

5.2. Experimental

Chemicals and materials

The Ni catalysts obtained in chapters 2 - 4 were applied to study the deactivation. First, fresh catalysts catalysed the glucose hydrogenation reaction. Then the spent catalysts were collected from the reaction slurry by filtration and washed using ultrapure water. Finally, spent catalysts were stored for further characterization after drying in vacuum oven overnight at room temperature.

FeNi/N-GNPs catalysts were prepared following the same procedure as FeNi/CB catalysts mentioned in chapter 4 by replacement of the carbon support. Nitrogen-doped N-GNPs support was obtained according to the method reported in the literature by our team.[202]

3%RuFeNi/CB catalyst was synthesized by adding Ru precursor ($RuCl_3$ xH_2O, Sigma-Aldrich, targeting 3 wt% Ru equivalents in the final catalyst) into the mixture of Fe and Ni precursors during the synthesis of FeNi/CB catalysts as described in chapter 4.

5.3. Results and Discussion

5.3.1. Sintering

Sintering is known as particles compacting and forming a solid mass of material by the action of heat or pressure.[121] Thus, it can happen widely in metal catalysts under harsh reaction conditions. Here, TEM-HAADF images of fresh and spent catalysts were collected to analyse the sintering occurring during glucose hydrogenation reaction. Figure 5.1 shows the morphologies of Fe_3Ni/CB, FeNi/CB and $FeNi_3$/CB catalysts before (left column) and after (right column) catalytic test. All the fresh catalysts appear more homogeneous than the used ones. Also, clear aggregations (larger particles) can be observed especially in Fe_3Ni/CB and FeNi/CB spent catalysts.

This sintering effect can also be observed by grain increase detected using p-XRD. Figure 5.2 illustrates the diffraction patterns of fresh and spent bimetallic catalysts Fe_3Ni/CB, FeNi/CB and $FeNi_3$/CB. The peaks at $2\theta = 25.3^o$ are attributed to the (002) plane of graphite (JCPDS-ICDD card No.41–1487). For Fe_3Ni/CB, peaks at 2θ 44.6^o and 65.2^o are corresponding to the (110) and (200) planes of crystalline bcc Fe-Ni alloy structure (JCPDS37-0474). For FeNi/CB sample, peaks at $2\theta = 43^o$, 51^o, 75^o are attributed to the (111), (200) and (220) crystal planes of fcc FeNi alloy (JCPDS 12-0736), respectively. For $FeNi_3$/CB, peaks at $2\theta = 44.2^o$, 51.4^o, 75.7^o are assigned to the (111), (200)

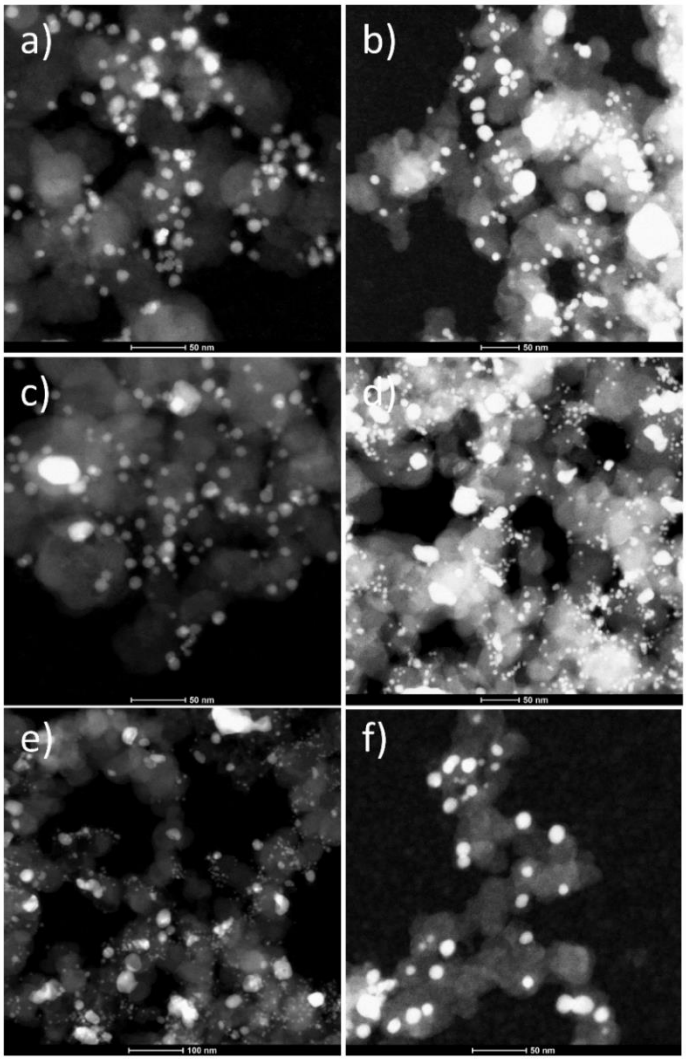

Figure 5.1. TEM-HAADF images of fresh (left column) and spent (right column) catalysts Fe_3Ni/CB (a, b), FeNi/CB (c, d) and $FeNi_3$/CB (e, f).

and (220) crystal planes of fcc Fe-Ni alloy structure (JCPDS38-0419).[290] The average grain sizes of alloy nanoparticles were calculated using Debye-Scherrer formula based on the full width at half-maximum (FWHM) of the (200) diffraction peaks, which are indicated in the graph with black colour for fresh catalysts and red colour for spent ones. For the FeNi/CB and $FeNi_3$/CB catalysts, the grain sizes increase from 9.2 nm to 18.2 nm, and 11.1 nm to 14.1 nm after catalytic test, respectively, induced by coalesce. For Fe_3Ni/CB sample, only 0.5 nm grain size increased after reaction, as measured based

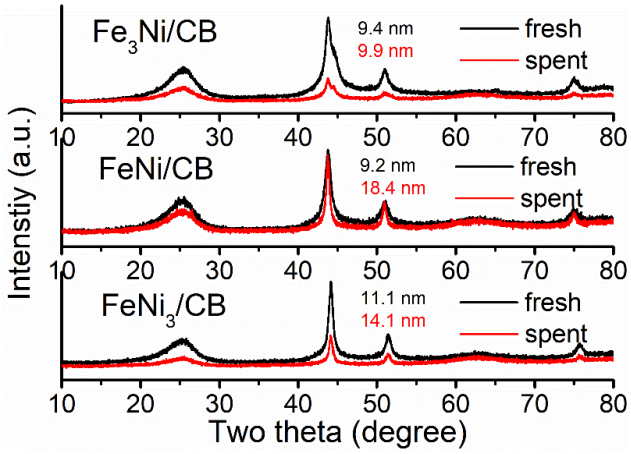

Figure 5.2. p-XRD patterns of fresh and spent catalysts: Fe_3Ni/CB (top), FeNi/CB (middle) and $FeNi_3$/CB (bottom).

on XRD patterns, while distinct increase of particle size was observed in TEM images, which could be due to the fact that particles aggregate but do not coalesce in this sample.

Metal atom dissolution and redeposition to form larger metal particles is usually quoted to explain the sintering effect in aqueous-phase reactions.[122, 123] In other words, small Ni particles are more easily dissolved and then re-deposited on the surface of big Ni particles, forming larger particles. The coalescence by the migration of small particles on the surface of CB could also contribute to the sintering effect here, due to the different surface diffusion energy of particles with different sizes. This sintering effect has been observed with the metals Ru, Pd, and Pt on the supports TiO_2, active carbon, carbon nanotubes, graphite, SiO_2 and Al_2O_3 in aqueous-phase reactions below 100°C [124-129]. However, how the detached metal atoms interact with the reaction medium in the Ostwald ripening process is still unclear.

5.3.2. Surface oxidation of Ni particles

Since Ni^0 is the active phase for glucose hydrogenation, it is essential to study the quantity of Ni^0 phase on the surface of the Ni catalyst before and after catalytic test. Thus, XPS spectra were recorded to probe the Ni^0 phase of fresh and spent catalysts. As is shown in Figure 5.3, the binding energies around 707 eV and 853 eV (red components) are ascribed to metallic Fe and Ni, respectively.[243] The peaks around 711 eV and 856 eV (blue components)

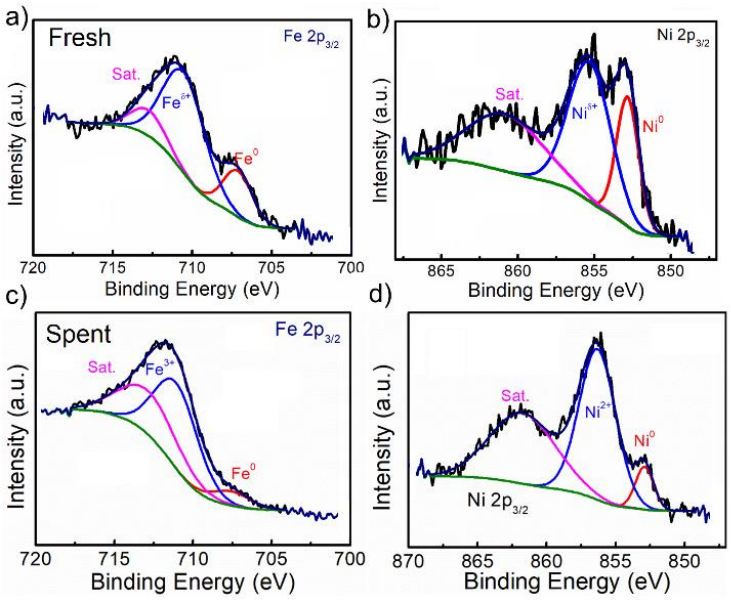

Figure 5.3. Fitted Fe $2p_{3/2}$ and Ni $2p_{3/2}$ XPS spectra of fresh FeNi/CB catalyst (a, b) and spent FeNi/CB catalyst (c, d).

are assigned to oxidized Fe ($Fe^{\delta+}$) and oxidized Ni ($Ni^{\delta+}$), along with satellite peaks (pink components). Apparently, the metallic portions of Ni and Fe decreased in the spent catalysts compared with the fresh one, indicating the metal oxidation occurring during the hydrogenation reaction. Since the FeNi/CB catalyst was used in aqueous solution of sugar alcohol and aldose at a temperature of 140°C (pH<5), Fe or Ni can react with water forming Fe^{2+} and Ni^{2+} species in a form of a complex with sugar alcohol on the surface of the catalysts.[301, 302] This oxidation can be further accelerated by increasing the reaction temperature. For example, when the hydrogenation reaction was carried out at 160°C with monometallic Fe catalysts for 3 h, the reaction medium turns out to be faint yellow in color, which is due to the Fe leaching in an oxidized form. This will be elaborated in the following part. However, this oxidation of Fe and Ni was prohibited in a way by forming FeNi/CB alloy catalyst. In Figure 5.4, red component is standing for the metallic Fe on the surface of the monometallic catalyst. Less percentage of Fe^0 (6.5 at. %) is present on the surface of Fe/CB catalysts compared to FeNi/CB catalyst (20.8 at. %). And even no metallic Ni appears in the fresh Ni/CB monometallic catalyst in contrast to 22% of metallic Ni in FeNi/CB

catalyst. That is to say, when Fe and Ni formed an alloy, the Fe and Ni oxidation was lowered thus metallic part of Fe and Ni remained on the surface. Therefore, alloy structure potentially maintains better the active sites, i.e. metallic Ni.

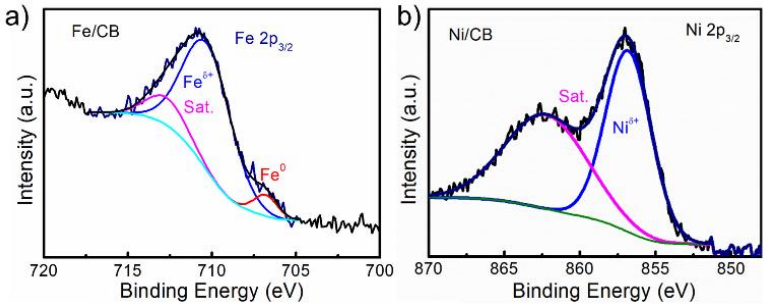

Figure 5.4. Fitted Fe $2p_{3/2}$ spectra of fresh monometallic Fe/CB catalyst (a) and Ni $2p_{3/2}$ spectra of fresh monometallic Ni/CB catalyst (b).

5.3.3. Metal leaching

Leaching is usually affected by temperature, pH, solvent, and the concentration of reactants and products.[113] It happens with either noble or base metals but normally base metals are more prone to leaching because they are more easily oxidised. It is known that Ni leaches seriously in aqueous hydrogenation of glucose especially when using Raney-type Nickel as a catalyst.[114] Analysing the Ni leaching in the reaction slurry during or after hydrogenation reaction helps to understand the leaching principle and potentially ways to eliminate or restrain it. Figure 5.5 shows the Ni leaching percentage of monometallic Fe/CB, Ni/CB, FeNi/CB and a mixed catalyst of Fe/CB and Ni/CB. The Fe or Ni leaching percentage was calculated by using the equation 10 below:

$$\text{Leaching}\ (\%) = \frac{m_{leached\ content}}{m_{initial\ content}} \times 100 \qquad \text{Equation 10}$$

The mass of leached content was calculated by multiplying the concentration of leached element in reaction medium and the volume of the medium. The mass of initial metal content was determined by ICP-OES analysis on the solid catalysts before tests. The error on leaching numbers can be estimated at about 2%, which mostly origins from the experimental operations during the acid digestion process, in which traces of ashes might not be well dissolved. For the monometallic Fe/CB catalyst, around 27 % of Fe leached away after

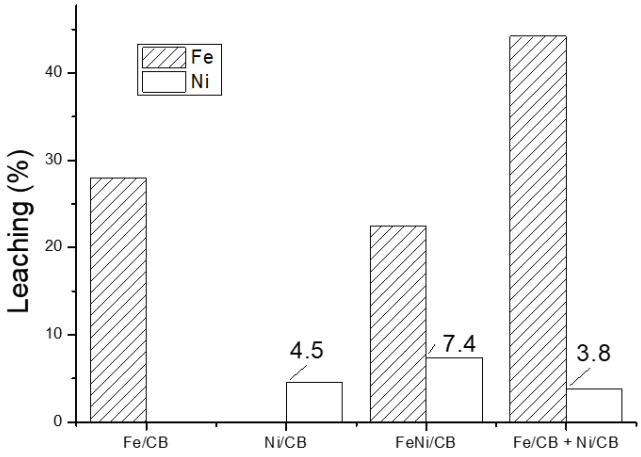

Figure 5.5. Leaching percentages of Fe and Ni from Fe/CB, Ni/CB, FeNi/CB and mixture of Fe/CB and Ni/CB catalysts after catalytic glucose hydrogenation reaction at 140°C with 30 bar of hydrogen for 2h.

one-time reaction, while 4.5 % of Ni leached from the Ni/CB catalyst. The leaching of Fe increased from 27% to 45% when Fe/CB catalyst was mixed with Ni catalyst, while Ni leached a little bit less compared to itself alone. Interestingly, when Fe and Ni formed an alloy, Fe leached less but Ni leached more than their monometallic counterparts, implying that Fe promotes the leaching of Ni while its own leaching was reduced. To further confirm this observation, the leaching behaviours of Fe-Ni alloys with different Fe/Ni ratios were studied. The results are shown in Figure 5.6. Regarding the Ni leaching among $FeNi_3$/CB, FeNi/CB and Fe_3Ni/CB catalysts, it increased from 5% to 21.2% with the Fe/Ni ratio varying from 0.33 to 2.92 in the catalysts. Thus, indeed, Fe promotes Ni leaching. Since the standard reduction potential of Fe is lower than Ni, it is more prone to be oxidized than Ni. Once Fe atoms in the alloy are dissolved into the solution, it creates cavities on the surface of alloy nanoparticles leaving the Ni atoms more exposed to the aqueous solution. Consequently, Ni leaches more. This could be one possible reason to explain the Fe promotion. This Ni leaching could also be partially related to the activity of the catalysts, since more hydrogenation products induce a lower pH measured at the end of the reaction, which is consistent with the trend that as the proportion of Fe in the alloy increases, the catalyst activity increases, while the leaching of Ni also increases. Hence with more active Ni catalysts, Ni will be more likely to be dissolved.

As carbon supports doped with N have been reported to improve the stabilities of Ru, Pd nanoparticles,[303, 304] we tried to synthesise a FeNi alloy catalyst supported onto N-doped GNPs.[202] The Fe and Ni leaching percentages obtained with this new catalyst after hydrogenation reaction are shown in Figure 5.6. 5.1 % of Ni and 11.2% of Fe leached away after reaction, which is less than the same alloy supported on CB, but still introducing N in the support does not prevent the metal leaching completely. In addition, with FeNi alloy on the N-doped GNP support, both the glucose conversion (36.1 %) and sorbitol selectivity (0) in 2 h were lower than with pure GNP support (68% of glucose conversion, 22% of sorbitol selectivity).

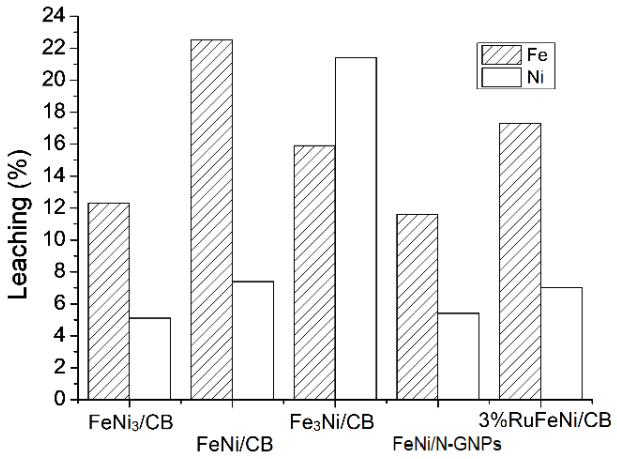

Figure 5.6. Leaching percentages of Fe and Ni from $FeNi_3$/CB, FeNi/CB, Fe_3Ni/CB, FeNi/N-GNPs and 3%RuFeNi/CB catalyst after catalytic glucose hydrogenation reaction at 140°C with 30 bar hydrogen for 2h.

Following another train of thoughts, adding a third stable Ru component into the FeNi alloy has no effect on stopping the leaching of Fe and Ni (see last column in Figure 5.6). Meanwhile, the glucose conversion increased from 45 % to 55.3 % but the sorbitol yield dropped from 55 % to 38.4 % in 2 h after adding 3%Ru to FeNi/CB catalyst. Besides, based on the leaching behaviours of Fe and Ni in FeNi/CB catalysts during three consecutive recycling tests (Figure 5.7), the contents of Fe and Ni in the catalysts is seen as continuously decreasing during each test, which means that the metals are constantly dissolving into the solutions. It should be noted that the leaching of metals in

the first cycle test is the worst compared to the 2nd and 3rd ones, and Fe always leached more seriously than Ni metal. The highest contents of metallic Ni and Fe in the fresh catalyst could also be correlated to the highest leaching in the first catalytic test, then the leaching slows down successively as the contents of metallic Ni and Fe decrease in the spent catalysts.

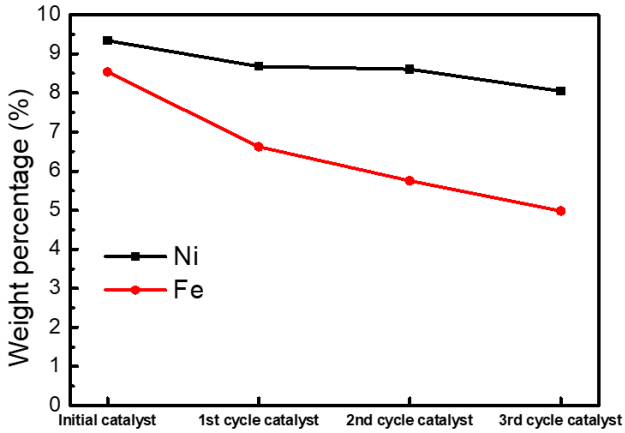

Figure 5.7. Weight percentages of Fe and Ni in fresh FeNi/CB and spent catalysts after each cycle of glucose hydrogenation reaction at 140°C with 30 bar hydrogen for 2h. (Weight percentages of metals in the catalysts were determined by ICP-OES analysis)

In order to find out the critical factors affecting the leaching, hydrogenation tests controlled for a single variable were performed and the leaching results are illustrated in Figure 5.8. In the starting point, FeNi/CB catalyst was added into 100 mL pure water stirring at 140 °C. In that condition, around 1% of Fe and 3.7% of Ni were leached away after 2 h. After adding 30 bars of hydrogen into the previous reaction condition (new batch of reaction), Fe leaching increased from 1% to 2.5%, but it decreased back to 1% when the reaction temperature was decreased to 120 °C. In the meantime, the leaching of Ni also decreased with the decrease of reaction temperature. In the last test, the substrate glucose was added, and the leaching of Fe increased dramatically – from 3.7% to 26%, while the Ni leaching remains almost the same. It was reported that glucose can form complexes with both Fe(III) and Ni(II) in MeOH.[305, 306] Maybe those complexes could be also formed in aqueous solution during hydrogenation reaction. However, there should be a competition of forming two complexes when both Fe (III) and Ni (II) are present

in the liquid. That Fe (III) complexes of glucose are more easily formed than Ni (II) complexes of glucose could be one explanation for the fact that Fe leaching is more sensitive to the substrate. In a word, leaching of Fe in the FeNi alloy is sensitive to the temperature and largely promoted by the glucose, but the leaching of Ni in FeNi alloy catalyst exhibited immunity from the temperature and substrate compared to Fe.

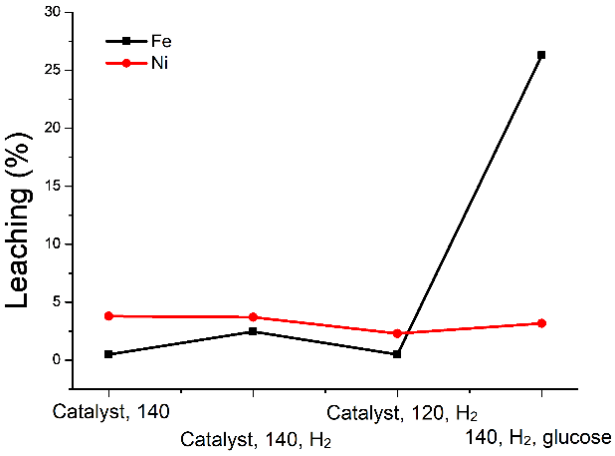

Figure 5.8. Fe and Ni leaching percentages in the corresponding reaction conditions: Catalyst, 140 – FeNi/CB, 100 mL of water, 140°C, 2 h. Catalyst, 140, H_2 – Adding 30 bar of hydrogen to the condition of 'Catalyst, 140'. Catalyst, 120, H_2 – Changing the temperature to 120 °C in condition of 'Catalyst, 140, H_2'. Catalyst, 140, H_2, glucose – Add 0.5 g of glucose to the condition of 'Catalyst, 140, H_2'.

Based on the leaching behaviour of Fe and Ni investigated as described above, several attempts have been implemented to decrease the leaching of Ni and Fe in the catalysts (Figure 5.9). First, the pH of the reaction medium was adjusted from 6 to 10 by adding 1M NaOH solution before the reaction started. The Ni leaching turned out to decrease from 7.6% to 5% while the leaching of Fe increased. As mentioned before, adding 3 wt% of Ru into the FeNi alloy does not prevent the leaching of Ni but Fe leaching can decrease by around 6%. After that, we tested the reaction in a mixture of water and ethanol with a volume ratio of 1:1. The Fe leaching decreased largely from 22.5% to 0.6%, but the Ni leaching remains almost unchanged. At last, we did the reaction in an aprotic solvent – cyclopentyl methyl ether (CPME). Remarkably, no leaching of Ni and Fe were found after two hours reaction.

Thus, the aprotic solvent is the key to solve the leaching problem. It should be mentioned that the glucose conversion (53.3%) and sorbitol selectivity (17.9%) were low with CPME solvent due to the poor solubility of glucose in CPME. Therefore, aprotic solvent with high solubility of glucose such as dimethyl sulfoxide (DMSO) should be the ideal reaction medium for high sorbitol productivity and no leaching of Ni and Fe.

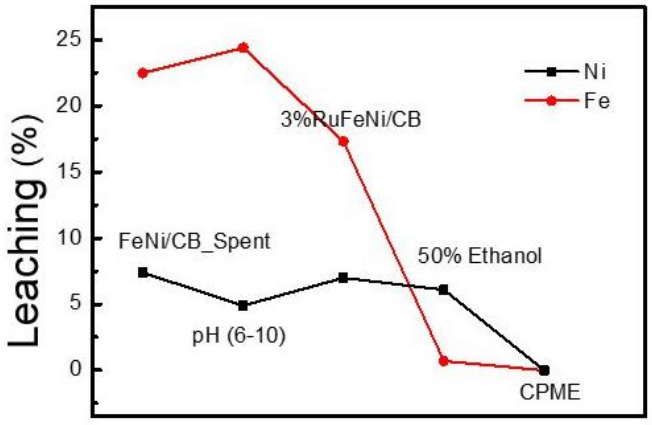

Figure 5.9. Leaching percentages of Fe and Ni from FeNi/CB (RuFeNi/CB) catalyst after glucose hydrogenation reaction at 140 °C and 30 bar of hydrogen for 2h and other specific reaction conditions indicated in the graph.

In addition to the previous leaching study based on FeNi alloy catalysts, we found additional results in the investigation of Ni leaching kinetics using bare Ni catalysts with different structures and morphologies – Ni nanospheres, nanorods, and nanobead chains catalysts. Figure 5.10 shows the Ni leaching percentage changes along with the reaction time. The leaching values were recorded by analysing the Ni concentration in the filtrates of samples taken from the reaction slurry at regular intervals, and the leaching behaviours of Ni nanosphere, nanorods and nanobead chains catalysts were investigated under a temperature of 130, 140, 150 and 160 °C, separately. For all three catalysts, the higher the reaction temperature, the more Ni leaching. In addition, Ni leached less in nanobead chain catalysts as compared to the other two catalysts under the same conditions, which may be due to the fact that some remaining capping agent - polyvinylpyrrolidone (PVP) on the surface of nanobead chains prevents the leaching to some extent. While nanosphere catalysts has the highest leaching compared to nanorod and

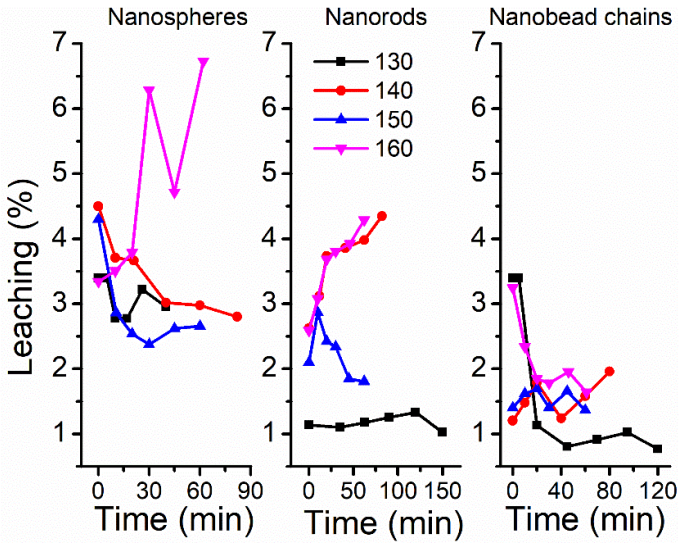

Figure 5.10. Ni leaching kinetics of Ni nanospheres, nanorods and nanobead chains catalysts in glucose hydrogenation under 30 bar of hydrogen, at a temperature of 130, 140, 150, and 160 °C.

nanobead chains catalysts, which could be due to the fact that low crystallinity of Ni nanospheres allows the amorphous Ni to leach more easily. Furthermore, an interesting phenomenon, namely that Ni leaching decreased during the reaction, was observed with all the three catalysts. For instance, at the reaction temperatures of 130, 140 and 150°C with nanospheres, the highest Ni leaching was observed when the reaction medium reached the target temperature before starting the hydrogenation reaction (at 0 min). After hydrogen was added, the reaction started, and the Ni leached decreased and reached a plateau along with the reaction time. However, this Ni leaching continuously increased at a reaction temperature of 160 °C. This leaching decreasing also happens with nanorod catalyst at 150 °C and nanobead chains at 130 and 160 °C. In situ reduction of oxidized Ni could explain the decrease of Ni leaching during the reaction, since 30 bars of hydrogen was added when the reaction started, which could potentially reduce the $Ni^{\delta+}$. And the leaching could show a relatively stable value when the oxidation and reduction of Ni reach an equilibrium under a corresponding reaction condition. Thus, in the cases of FeNi/CB catalyst testing in different conditions by varying parameters such as hydrogen pressure, reaction medium, temperature, etc, the equilibriums of Ni/Fe to oxidized Ni/Fe should be different, resulting in

variations in the leaching percentage (Figure 5.8 and Figure 5.9). Based on this, the adding of Nickel ions to the reaction medium allows the leaching to reach its equilibrium at the start of the reaction and may serve as a method to reduce Ni leaching.

At a high temperature, the oxidation of Ni dominates compared to the reduction, leading to continuous Ni leaching. And the fact that the initially oxidized Ni cannot be totally reduced is due to the oxidation-reduction potential (ORP) of the glucose aqueous solution which is not low enough. Thus, this leaching kinetic study further demonstrates that an oxidation reaction occurred between Ni catalysts and glucose aqueous solution and reduction of oxidized Ni undergoes during the hydrogenation reaction.

5.4. Conclusions

By analysing the morphologies, crystallinities, surface chemical states and the compositions of Fe-Ni alloy catalyst before and after the glucose hydrogenation reaction using TEM, p-XRD, XPS and ICP-OES / AAS, sintering, surface oxidation and leaching were demonstrated to contribute to the deactivation of the FeNi catalysts. This sintering effect is most evident in FeNi/CB catalysts, compared to Fe_3Ni/CB and $FeNi_3$/CB catalysts, the grain size of which increased from 9.2 nm to 18.4 nm after one-time use. Ostwald ripening via metal dissolution and redeposition to from larger metal particles contribute to sintering of Fe-Ni alloy catalysts. XPS analysis indicated that metallic Ni and / or Fe were oxidized during glucose hydrogenation, leading to surface oxidation of the catalysts after use. Fe-Ni alloy catalysts can preserve some metallic portions of Ni and Fe from oxidation in the fresh and spent catalysts rather than all surface metals being oxidized in the monometallic counterparts.

ICP-OES / AAS analysis of the filtrates of the reaction medium shows metal leaching after hydrogenation reaction. For Fe-Ni alloy catalysts, Fe leached less but Ni leached more than their monometallic counterparts, and Fe and Ni continuously leached away in the successive tests. Adding Fe into Ni catalysts was found to promote Ni leaching and Ni leached increased with the Fe contents in the Fe-Ni alloy catalysts. Fe leaching was demonstrated to be more sensitive to the reaction conditions like hydrogen pressure, adding substrate, solvent changing compared to Ni. And at a low reaction

temperature, Fe and Ni leached less in contrast to higher temperature. This Fe and Ni leaching was not prevented either by changing the CB support for N-doped GNP support or adding a third metal Ru into the alloy. However, when the reaction medium was changed from water to a mixture of water and ethanol, the leaching of Fe was largely constrained but Ni leaching remained the same. Finally, with aprotic solvent CPME, the leaching of Fe and Ni was totally blocked with zero leaching after reaction, but the glucose conversion and sorbitol yield were very low due to the poor solubility of glucose in this medium.

Regarding the leaching kinetics studies of Ni nanospheres, nanorods and nanobead chains catalysts during glucose hydrogenation reaction, Ni nanobead chain leached less in the reaction temperature range 130 – 160 ^{o}C compared to nanorods and nanospheres catalysts. Besides, in situ reduction of oxidized Ni was proposed to explain the decrease of Ni leaching during the hydrogenation reaction. And the leaching of Ni can reach a stable value when the reduction and oxidation of Ni reach an equilibrium. Thus, if the reaction was carried out using a Ni^{2+} solution with a proper concentration related to the reaction condition (eg. 5 ppm for Ni/CB catalyst at 140^{o}C for 2 h (the average leaching amount of Ni in this condition)), by adding a compound like $NiNO_3$, it may stop the Ni leaching because the equilibrium of Ni^{0} to Ni^{2+} would be directly reached and not depend on the Ni^{2+} and Ni contents in catalysts. And also, polar aprotic solvents could be a promising solution to both stop the leaching of Ni and improve the solubility of glucose.

Chapter 6

Conclusions and perspectives

6. Conclusions and perspectives

6.1. General conclusions

With the scope of designing Ni based non-noble catalysts for efficient selective hydrogenation of glucose to sorbitol in mind, we have prepared bare Ni catalysts with three different shapes – sphere, rod, bead chains, but also CB/GNPs supported pure Ni nanoparticles with particle sizes from 7 nm to 24 nm, and CB supported Fe-Ni alloy catalysts. Comprehensive investigations have been applied to analyse the structure-reactivity relationships of the catalysts. The significance to the presented work including main developments are concluded in the following paragraphs.

Since many previous works had reported that the particle shapes have a significant influence on their catalytic properties including activity and product selectivity, we tried to obtain three types of particles with different shapes hence enriched in some particular facets to investigate the activity and sorbitol selectivity in glucose hydrogenation. As it is more difficult to control the nucleation and growth of non-noble metal particles than noble metals, we obtained three different shapes of Ni particles but with polycrystalline structures rather than a single crystal, which makes us consider that the kinetic of Ni particle growth changes with the hydrogen pressure. Then, it is inaccurate to determine the exposed facets with polycrystalline structures. However, we indeed observed large differences of the catalytic performance among those three different particles. By further analysing the crystallinities, large amounts of amorphous phases were found in Ni nanosphere catalyst, which turns out to be one key for its high activity. We were not expecting to have different compositions of Ni nanospheres and nanorods, since they are using the same amounts of reactants. However, both surface and bulk analyses provided evidence that P was doped into Ni nanosphere catalysts and not in nanorod catalysts. Finally, the unexpected amorphous P-doped Ni nanospheres exhibit an even lower activation energy than reported Ru catalysts. This is a blessing in disguise.

Then we started investigating the size effect of Ni particles on glucose hydrogenation. Simply changing the temperatures of thermal treatment, Ni particles with different sizes were prepared as described in chapter 3. The particle sizes were determined by statistical analysis of TEM images as well

as XRD with Scherrer equation. The average particle sizes range from 7 nm for CB-400 to 23 nm for CB-650. One starting assumption could have been that the highest reactivity of the catalysts should be given by the lowest average particle size sample, since at a constant metal loading, the smaller the particles, the more active sites. However, a volcano plot behaviour was observed, and the best activity was shown with medium size Ni particles - 17 nm. This CB-550 catalyst was also demonstrated to have the highest portion of metallic Ni on the surface, which obviously can catalyse the reaction more efficiently compared to catalysts with more oxidized metal surface. Considering both the deactivation and substrate adsorption processes in the glucose hydrogenation, the medium size particles could be a result of a compromise. That is to say, although small particles have more active sites (edge and corner atoms), they are also more easily leached away or poisoned, thus small particles have less reaction possibilities compared to medium size particles. By opposition, big particles certainly lose the active metal surfaces compared to medium ones. These similar conclusions were also given by Ni particles with different sizes on GNPs support. Thus, in the real reaction conditions, we have to consider the stability and accessibility of catalysts while increasing the number of active sites.

Fe is known as a promoter for enhancing the activity of Raney-Nickel catalysts, but its catalytic role was not clear at the beginning of this thesis for the target reaction. Meanwhile, Fe is less electronegative than Ni, so it potentially can be used as a protection metal for saving the Ni active sites. Thus, in chapter 4 we designed bimetallic catalysts to investigate the synergistic effect in Fe-Ni alloy catalysts during the glucose hydrogenation. In this goal, monometallic Fe/CB and Ni/CB catalysts, Fe-Ni nanoalloy catalysts with three different compositional ratios were prepared. The bimetallic Fe-Ni particles were confirmed to present small and alloyed structures by XRD and TEM-EDS analysis. As we expected, Fe indeed can protect Ni active sites in both fresh catalysts and spent catalysts. That is, more metallic portions of Ni were present in the Fe-Ni alloy catalysts than in monometallic Ni catalysts. Undoubtedly, FeNi alloy catalysts were much more active than Ni/CB, but less active than Fe/CB. However, Fe/CB was involved in catalysing the glucose isomerization process. When Fe and Ni formed an alloy, this glucose isomerization reaction was suppressed. By comparing the alloy with different

Fe:Ni ratios, the 1:1 formulation was identified as the best compromise to achieve a high catalytic activity while maintaining high sorbitol selectivity.

At the end of this thesis, we studied the deactivation of the catalysts obtained above during aqueous glucose hydrogenation reaction. TEM-HAADF and XRD analysis indicated that sintering occurs during the use of the Fe-Ni alloy catalysts. Surface chemical state analysis by XPS indicated that the partial oxidation of Ni active sites occurs during the hydrogenation reaction. Ni leaching, detected by ICP/AAS, induced the loss of active sites. Different surface energy of particles with different sizes, the formation of Ni/Fe-glucose complexes on the surface of the catalysts and oxidation of active sites could contribute to explain those deactivation phenomena, respectively. Besides, introducing Fe into Ni catalysts has been found to help maintaining the Ni active sites in the normal storage condition and real hydrogenation reaction conditions. Changing the hydrogenation reaction medium from protic to aprotic one, the leaching of Ni can be largely restricted. Furthermore, in situ reduction of oxidized Ni was proposed to explain the decrease of Ni leaching during the hydrogenation reaction in water medium.

To summarize in a few words, we have achieved our objective – design of efficient selective non-noble catalysts for glucose hydrogenation and understanding of fundamental key parameters for their performance. A brief comparison of catalytic performance among those different types of Ni catalysts is illustrated in Figure 6.1. Amorphous P-doped Ni nanosphere catalyst exhibits the highest activity and sorbitol yield. Though FeNi/CB can have similar conversion than the Nanospheres, the sorbitol yield is lower due to the Fe addition that promotes side-reactions. The catalytic activity of Ni/CB, nanobead chain and nanorod catalyst are all relatively lower. A test result with a commercial Ru/C catalyst was also introduced in this graph, but it was obtained under different reaction conditions – namely longer reaction time but lower metal amount compared to other tests. Considering a very low metal loading for the commercial one, it should be feasible to make a preliminary comparison with other results at a longer reaction time. And the test in the same conditions must be done in the future to have a precious conclusion. Based on the current results shown in this figure, the catalyst whose performance is closest to that of commercial Ru/C catalysts is Ni nanosphere, but the activity is still far below the noble metal commercial one.

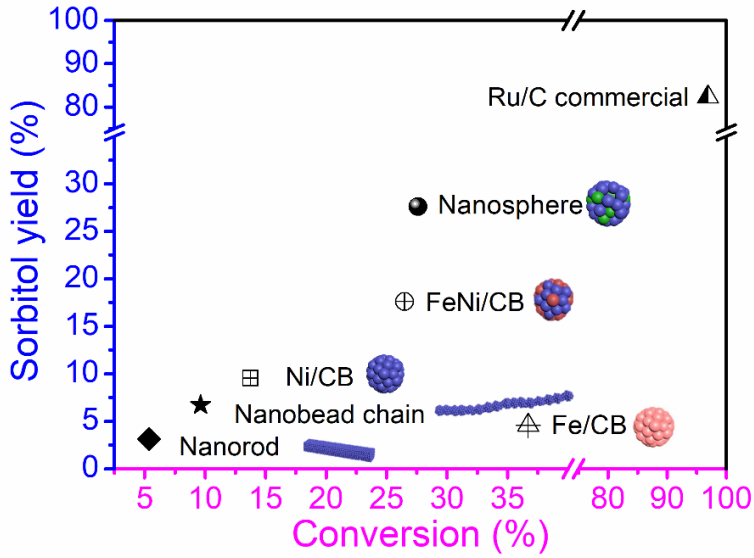

Figure 6.1. Glucose conversion and sorbitol yield comparisons after 1 h reaction when using different catalysts except for Ru/C commercial catalyst. Reaction conditions with catalysts in this thesis: 14 mg of pure metal catalyst or equivalent metal content in supported catalysts, 0.5 g of glucose, 100 mL of Milli-Q water, 140 °C, 1 h, 30 bar hydrogen, 1700 rpm stirring speed. The Reaction conditions with Ru/C catalyst: 60 mg of 5 % Ru/C grade 1 catalyst (60% H_2O, PMPC SP3210 W, EVONIK, Germany), 100 mL of Milli-Q water, 140 °C, 2 h, 30 bar hydrogen, 1700 rpm stirring speed.

Therefore, for Ni metal catalysts, P doping, amorphous phase, sphere NPs with a particle size of 17 nm, CB support, as well as introducing a promoter – such as Fe are the significant factors that enhance the catalytic performance. Those features should be considered when designing a new base metal catalyst. Furthermore, altering the hydrogenation pressure changed the kinetic of formation of Ni NPs, leading to different shapes of Ni particles, which is for the first time proposed in this thesis. This can be applied in preparation of other base metal particles of different shapes. Besides, the equilibrium of reduction and oxidization of Ni or Fe was proposed as a key factor during the investigation of leaching kinetics from FeNi catalysts during glucose hydrogenation. Based on this hypothesis, few attempts can be done to prevent base metal leaching in the future.

Those investigations bring the base metal catalysts closer to noble metal catalysts in terms of activities. But, the deactivation especially the leaching of

base metals remains a problematic issue. Even though we proposed the aprotic solvent to somehow prevent the leaching, it is not as environmentally-friendly as water. Thus, further investigations should be done on solving the deactivation of base metals. And the specific prospects for possible future works are described as follows in the next section.

6.2. Perspectives

We propose perspectives for this thesis in three parts: (i) complete the deactivation study on prepared catalysts; (ii) integrate all the advantages that we have identified in this thesis to form a new optimised catalyst (iii) mechanism study of glucose hydrogenation reaction.

The observation of in situ reduction of leached Ni and leaching behaviours of Ni catalysts with different sizes:

As leaching of Ni nanospheres decreased and reached a relative constant value after about 20 min reaction, we propose that the leaching species were reduced in situ when hydrogen was introduced during glucose hydrogenation. Thus, it would be valuable to testify this hypothesis by characterizations like TEM to visually observe the morphology changes along with the reaction time. In this way, we need to separate and analyse the catalysts intermittently or implement in situ methods. If we cannot have clear observations by using TEM due to the fact that the amount of leaching is too small, high-resolution images could theoretically help to find differences. The leaching kinetics of Ni/CB catalysts with different particle sizes are also worthy to study. It would at least give an idea about the relationship between leaching and Ni particle size as well as the homogeneity of size distribution. This will also tell us if the conclusion about high activity leading to more leaching is applicable to those catalysts. After we pin-point all the issues causing deactivation, we can finally modify the catalysts accordingly to prevent it.

Amorphous Fe-Ni nanoparticles / core-shell Fe/Ni NPs supported by CB catalyst preparation:

We have found several features promoting the reactivity of Ni catalysts in this thesis. Naturally, we could think of designing a Ni catalyst combining all those advanced features to further boost its catalytic performance. In this case, we will first try to synthesize amorphous Fe-Ni bimetallic nanoparticles or Fe/Ni core-shell NPs (Fe as a core and Ni as a shell) by a thermal solvent method

or coprecipitation method. If it succeeds, CB support could be introduced easily by adding it to the suspension of NPs. After ultrasound and filtration, we can analyse the particles immobilized on CB support using ICP-OES and other usual methods such as XPS. Once the metal loading is confirmed, we could evaluate the catalytic performance of this new catalyst. Different parameters could be applied to obtain the amorphous Fe-Ni or Fe/Ni catalysts, such as hydrogen pressure, the amounts of capping agents and reductants. Or we can change the capping agents -TOP to triethylphosphine with short branch chains to spare more accessibilities for metal precursors and reduce the electron density of P. Phosphorous doping is another key point that needs to be integrated in optimized catalysts, through the phosphine capping agents or other P-rich reactants addition.

Mechanism study of glucose hydrogenation reaction

Though few adsorption configurations of glucose on Pt/Pd surface have been proposed by DFT calculations, the reaction intermediates are still unknown. And also, there is still a debate about the idea that glucose can be directly hydrogenated without turning into an open-chain form. Thus, in situ Raman or in situ IR could be used to try to find out the intermediates during the aqueous or non-aqueous reaction. If this reaction still runs under harsh conditions, an inertial catalyst such as Ru/CB with metal loading less than 1% should be used to ensure the reaction proceeds slowly enough to 'see' the intermediates. Or we could try to use a more active catalyst with higher Ru loading to run this reaction in less harsh conditions. Here we want to avoid using Ni metal because we would like to avoid the influence of Ni leaching. In addition, the pH of the reaction solution should also be monitored and further controlled with an automatic regulator equipped on the high-pressure reactor, to better understand the influence of pH value on both glucose isomerization and hydrogenation. These mechanistic studies should be strengthened by theoretical calculations, which we also initiated during the course of this thesis work, in collaboration with the group of Dario Duca, but would require further effort to complete.

Appendix

Characterization methods

Appendix: characterization methods

In order to understand the intrinsic properties of the prepared catalysts in different aspects, multiple characterization techniques were used. For instance, electron microscopy such as TEM and SEM were used to observe the morphology of the nanoparticles, in which HR-TEM, TEM-HAADF and dark field images were also carried out for specific samples. X-ray diffraction was applied to determine the crystal phases present in the samples in powder form. Surface chemistry including vibrations of the surface groups, and elemental valence and contents were detected by ATR-IR or Raman and XPS, respectively. As opposed to surface analysis, bulk elemental analysis was implemented with ICP-OES and TEM-EDS techniques. Besides, the specific surface area and H_2 desorption were analysed by N_2 sorption and H_2-TPD, separately. Apart from that, TGA was specifically used to monitor the thermal stability of the catalysts prepared at different temperatures (in chapter 3). Those equipment descriptions and detailed operation procedures are specified below.

Morphology

Transmission electron microscopy (TEM) and high resolution TEM (HR-TEM) were performed by using JEOL 2100 LaB6 with a 0.2 nm point to point resolution. Dark field images were recorded after selecting parts of diffraction rings in order to observe the corresponding lighted area, i.e. oriented crystals (In chapter 2).

TEM images were obtained on a LEO 922 Omega Energy Filter Transmission Electron Microscope operating at 120 kV. The samples were suspended in ethanol under ultrasonic treatment. Three drops of the suspension were deposited on a holey carbon film supported on a copper grid (Holey Carbon Film 300 Mesh Cu), which was dried before introduction in the microscope for imaging (In chapter 3).

TEM high angle annular dark field (HAADF) images were obtained on a field emission gun (FEI) Osiris TEM operated at 200 kV equipped with a CHEMISTEM detector. The samples were suspended in ethanol under ultrasonic treatment. Three drops of the suspension were deposited on a holey carbon film supported on a copper grid (Holey Carbon Film 300 Mesh Cu) (In chapter 4 and 5).

SEM images were obtained on a field-emission scanning electron microscope JEOL 7600F operating at 15 kV. A small amount of sample was collected with a spatula and deposited on a carbon double-sided sticker bonded on a 26 mm diameter specimen holder, then air spray was used to remove the excess particles.

Crystallography

The powder sample was tiled on a silicon crystal sample holder with a thin layer of cream as an adhesive, and its X-ray diffraction (XRD) analysis were performed using a Bruker D8 advanced diffractometer (Bragg-Brentano geometry) equipped with a LInkeye XE-T detector. The X-ray source (Cu $k_{\alpha 1,2}$, λ = 0.15418 nm) operates at 1200 W (30 mA, 40 kV). Analysis were made within a 2θ range from 5 to 80° using a step size 0f 0.015° and 0.15s per step. For in situ experiments, a Paar Instrument XRK 900 chamber was used to control the reducing atmosphere (30 mL / min of 5% H_2 in argon) and the temperature (from 300 ^{o}C to 650 ^{o}C). Thermal expansion of the chamber is adjusted by correcting the height of the sample at each temperature. Eva software (Bruker) and the PDF-2 database were used for data treatment.

Surface chemistry

The attenuated total reflection (ATR) infrared spectroscopy spectra were recorded on a PerkinElmer Spectrum two instrument in the range of 500 – 4000 cm^{-1} at room temperature. A small amount of sample was placed over the surface of the diamond crystal in the centre of the circular mounting plate in the instrument.

Raman spectra at room temperature were recorded using Thermo Scientific DXR Raman Microscope in the backscattering configuration with a 532 nm green laser. A small amount of sample was placed in the centre of a microslide, then another slide was gently pressed once on top of the sample and removed. Then, the slide with sample was placed on the worktable of the Microscope. The accumulation time and spot size of the laser used were 120 s and 865 nm, respectively, and a 50 × objective was used on an Olympus microscope.

X-ray photoelectron spectroscopy (XPS) analyses were carried out at room temperature with an SSI-X-probe (SSX 100/206) photoelectron spectrometer from Surface Science Instruments (USA), equipped with a monochromatized microfocus Al X-ray source (1486.6 eV). Samples were set on the sample

holders by double face adhesive tape. Charging effect of the samples were eliminated by placing a nickel grid above the samples and using a flood gun set at 8 eV. All the binding energies were calculated according to the C-(C, H) component of the C 1s peak fixed at 284.8 eV. Data analysis was carried out using CasaXPS software, and the peaks were decomposed by Gaussian/Lorentzian product formula GL(15) after a Shirley-type background was subtracted.

Elemental analysis

Elemental analysis was carried out using ICP-OES Varian 720ES by analytical and chemical consultancy services from MEDAC LTD (UK). The samples were digested with 5 mL of nitric acid and 1 mL of hydrogen peroxide, then the solutions were made up to a volume with 18.2 MOhm water and analysed.

The elemental analyses of solid carbon-based materials in chapter 4 were determined by microgravimetry (weight loss associated with carbon calcination), and the elemental analyses of Fe and Ni were carried out by an ICAP 6500 thermoscientific spectrophotometer after acid digestion.

The amount of metal leaching during the catalytic tests in chapter 5 was directly analysed in the products solutions by the same instrument as used in chapter 4.

TEM-EDX elemental maps were obtained on a field emission gun (FEI) Osiris TEM operated at 200 kV equipped with a CHEMISTEM detector (the probed volume is 1 μm^3). The samples were suspended in ethanol under ultrasonic treatment. Three drops of the suspension were deposited on a holey carbon film supported on a copper grid (Holey Carbon Film 300 Mesh Cu).

N_2 sorption and H_2 - TPD analysis

The specific surface area of the catalysts was measured through nitrogen adsorption-desorption isotherms, which was performed in a Micromeritics ASAP 2020 analyser at 77 K. Before analysis, the samples (around 0.2 g) were degassed for 2 h at 473 K with a heating rate of 10 K/min under 0.133 Pa pressure. The specific surface areas were calculated based on the Brunauer-Emmett-Teller (BET) equation by analysis of the isotherms in a relative pressure range of 0.05 to 0.2.

H_2-Temperature-programmed desorption (TPD) experiments were performed on a Catlab equipment from Hiden (UK). Typically, a sample of ca. 60 mg was

treated under a 30 mL / min flow of 5% H_2/Ar at 300 ^oC for 1 h, and subsequently cooled down to 50 ^oC. The same reductive atmosphere was maintained for 1 h. After that, the sample was purged with pure Ar (30 mL / min) for 1 h to eliminate the physical absorbed H_2 and H_2-TPD profiles were recorded in flowing Ar in the temperature range 50 – 800 ^oC with a heating rate of 10 ^oC/min.

TGA analysis

5-10 mg samples were placed in alumina containers and introduced in a Mettler Toledo TGA/SDTA 851e instrument. Thermograms were recorded up to 900 ºC using a 10 °C/min heating rate under a N_2 flux.

Supporting information

Supporting information

Figure S1. High-resolution N 1s XPS spectra for Ni nanospheres (a), nanorods (b) and nanobead chains (c).

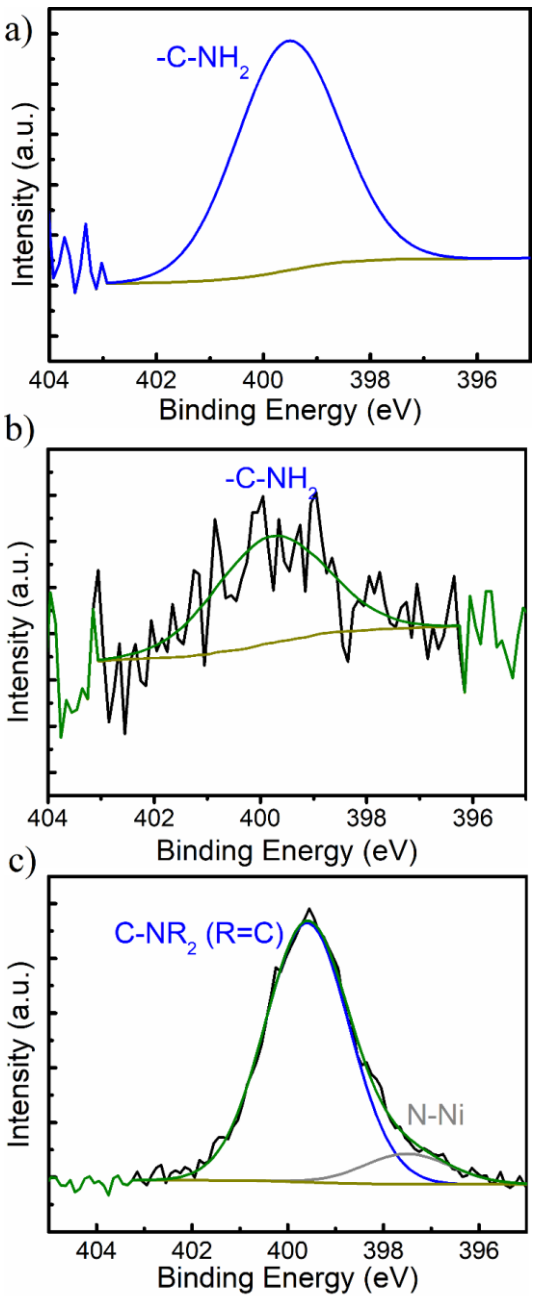

Figure S2. Nanospheres: bright-field images (left), corresponding SAED images (middle), and the aperture rings and covered sections of diffraction rings for DF images (right). The scales for bright-field images are the same as with DF images reported in the main text.

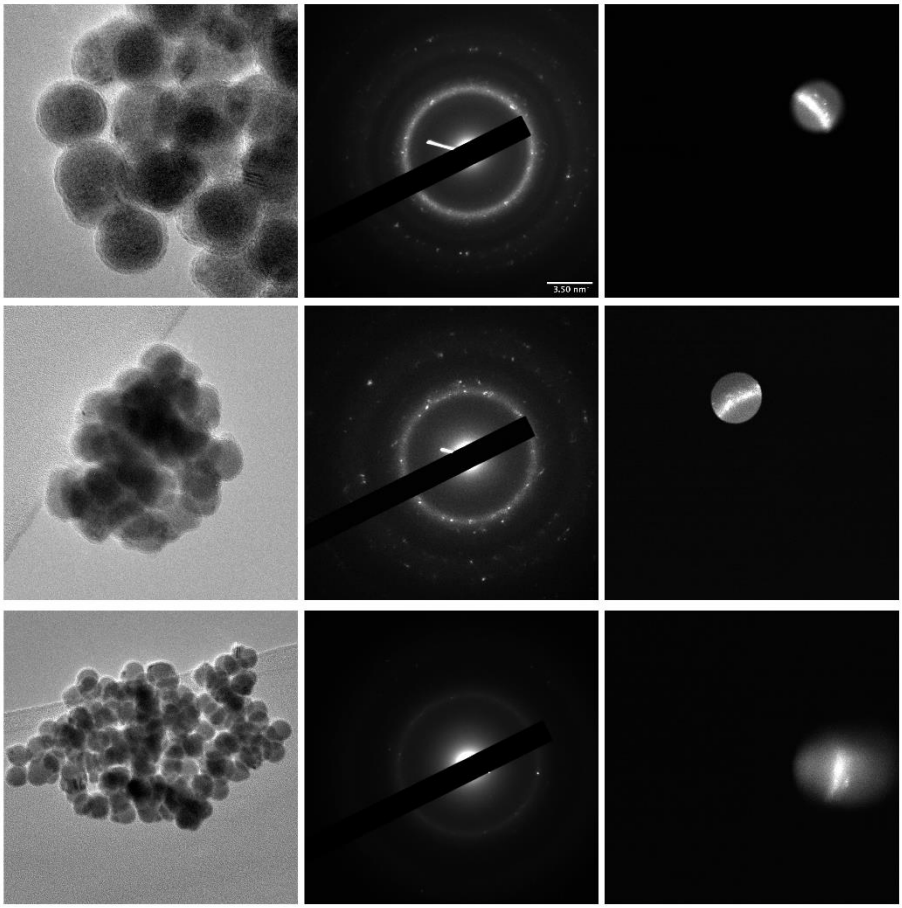

Figure S3. Nanorods: bright-field images (left), corresponding SAED images (middle), and the aperture rings and covered sections of diffraction rings for DF images (right). The scales for bright-field images are the same as with DF images reported in the main text.

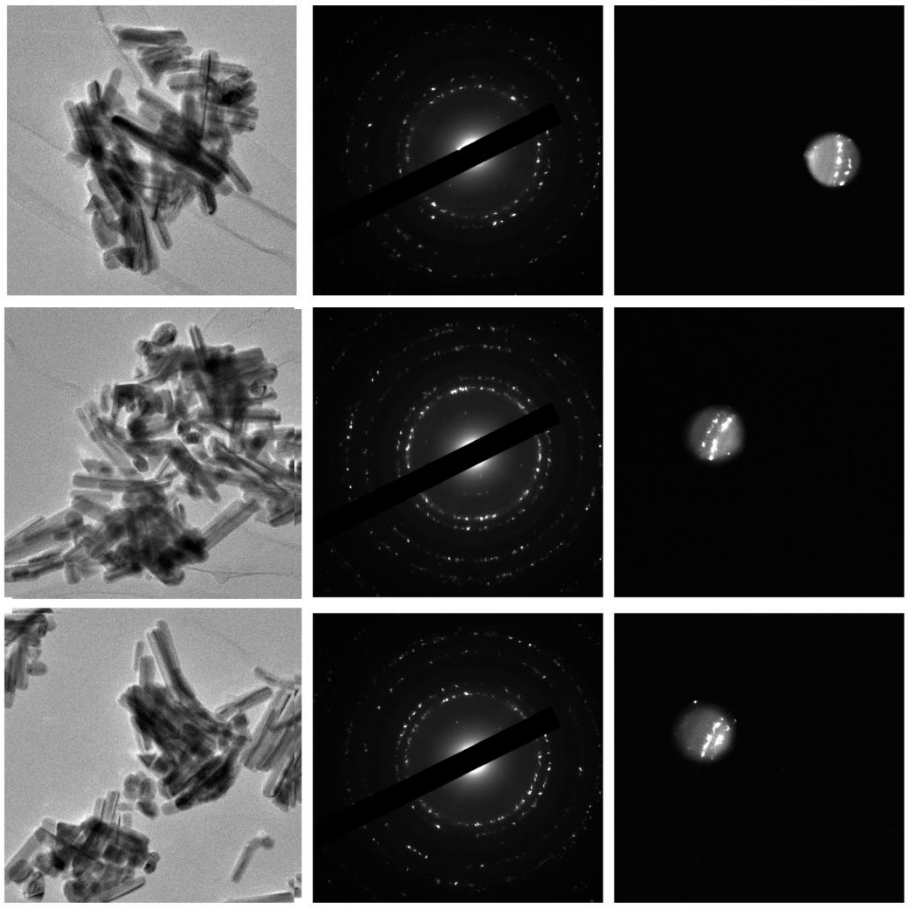

Figure S4. Nanobead chains: bright-field images (left), corresponding SAED images (middle), and the aperture rings and covered sections of diffraction rings for DF images (right). The scales for bright-field images are the same as with DF images reported in the main text.

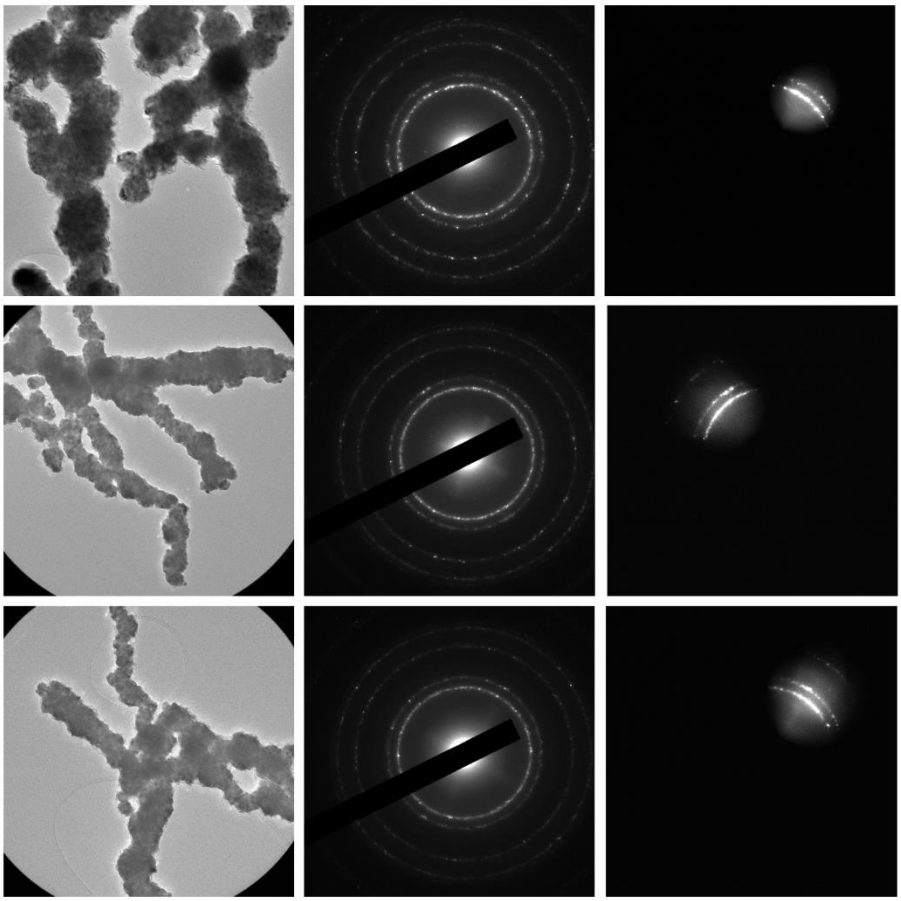

Figure S5. Pictures of the magnet-particles interactions. The dry powders were simply contained in glass vials and were placed in a fixed position under a strong permanent magnet. Patterns marked on the vials indicate the types of samples, i.e., circle is nanospheres sample (left), cylinder is nanorods sample (middle), and chain is nanobead chains (right).

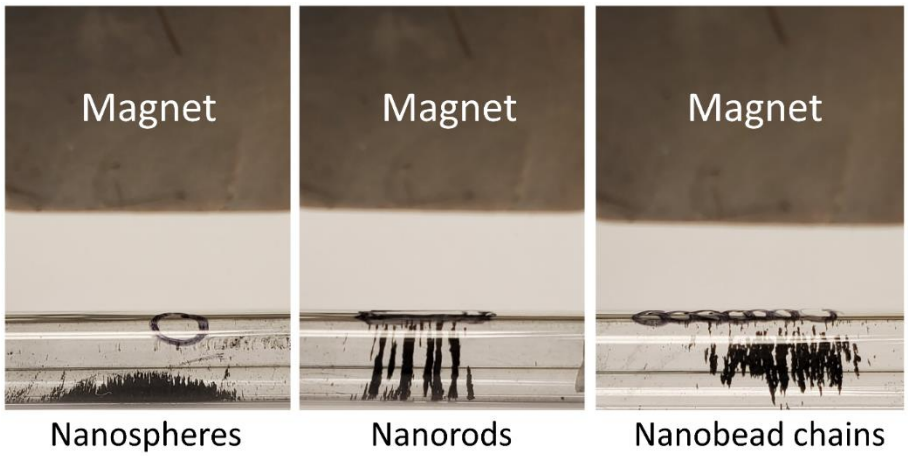

Figure S6. N_2 sorption isotherms for nanospheres (a), nanorods (b), nanobead chains (c). BET surface areas are given in the parentheses.

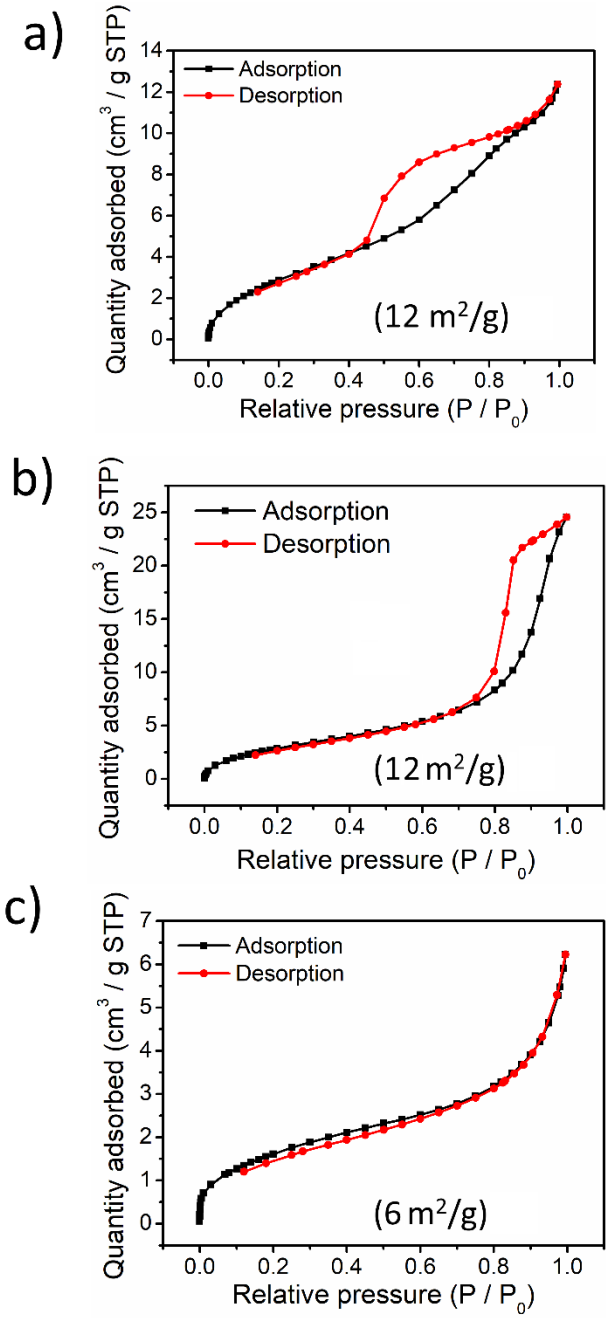

Figure S7. Plots of Ln (1-x) vs t and linear fit curves at 140 ºC (green), 150 ºC (red) and 160 ºC (black) of glucose hydrogenation reaction over nanospheres catalysts (a), nanorods catalysts (b) and nanobead chains catalysts (c).

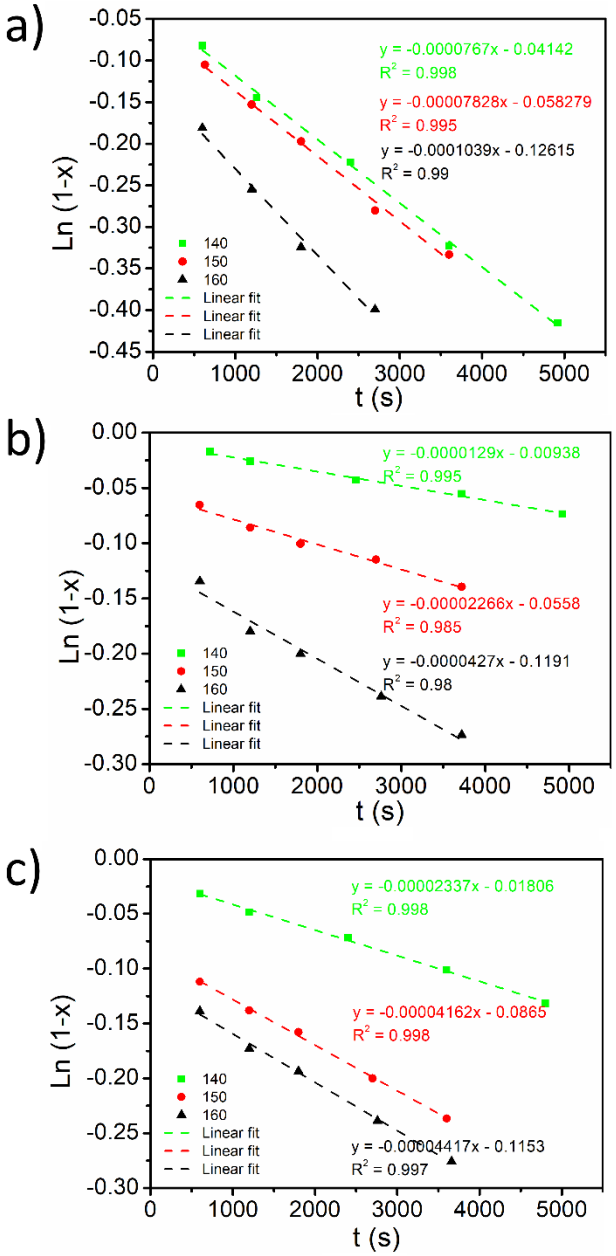

Figure S8. Ni grain size calculated by Scherrer equation growth with reduction temperature.

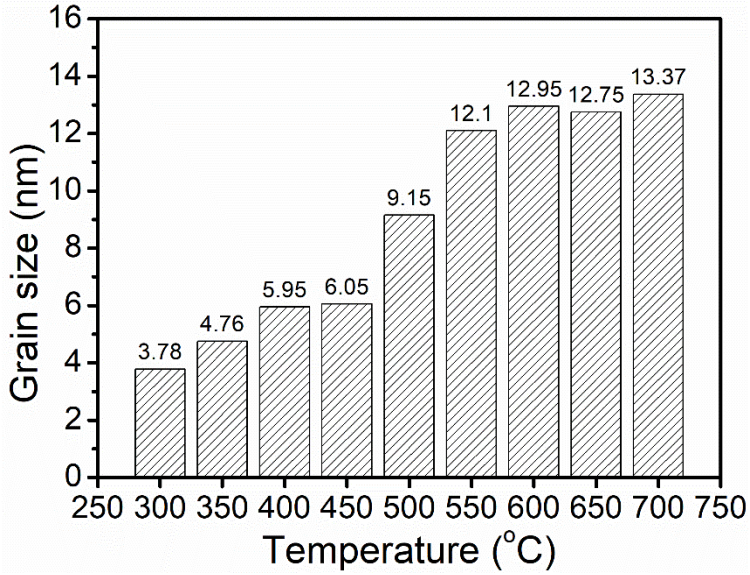

Figure S9. N_2 sorption isotherms for CB-500, CB-550, CB-650 catalysts.

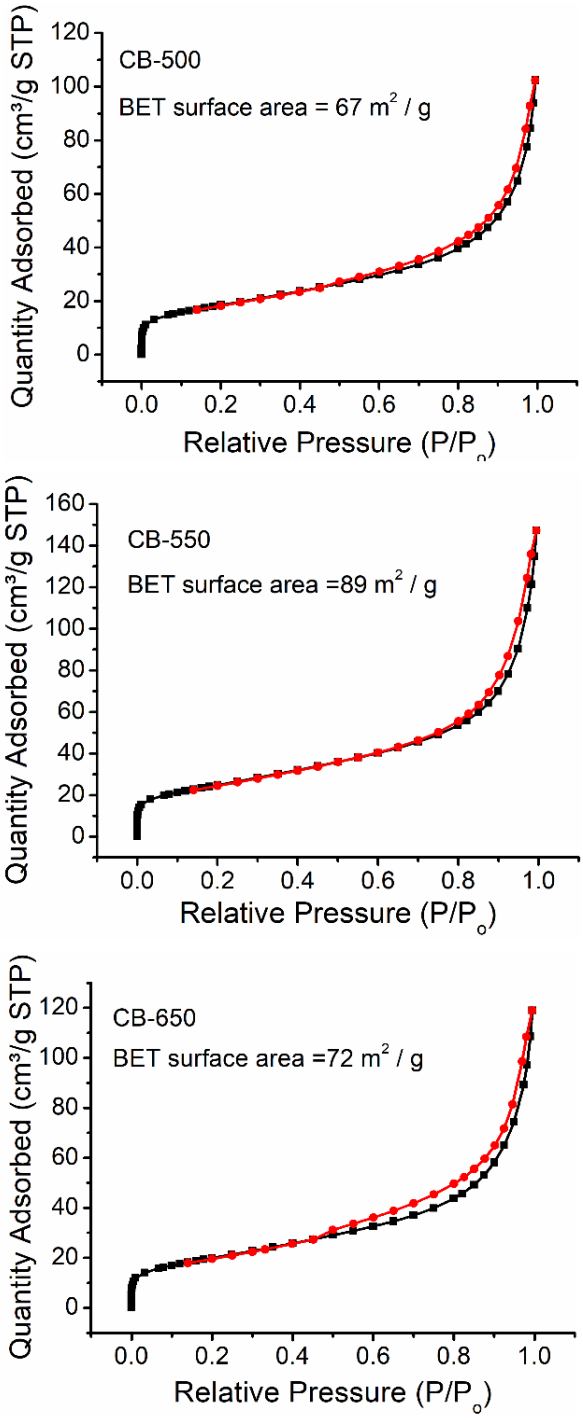

Figure S10. Sorbitol selectivity vs the Ni particle size of the applied catalysts (a) and metallic Ni content in the applied catalysts (b). The glucose conversions are indicated in the brackets.

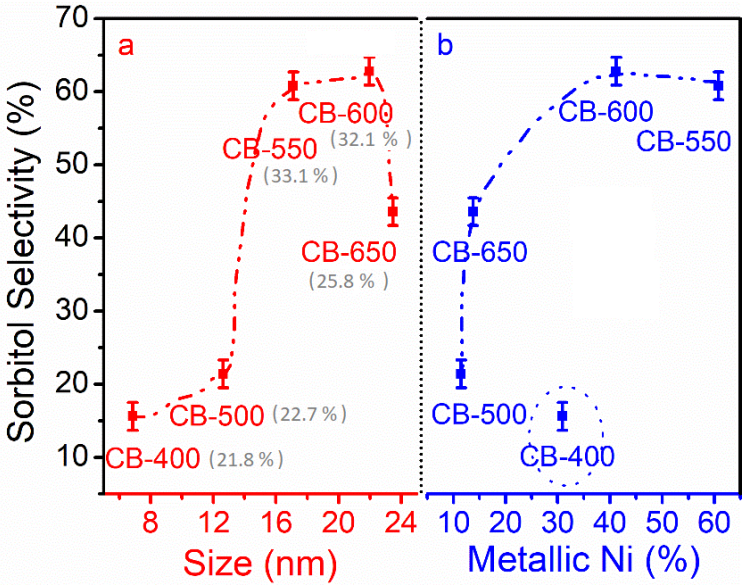

Figure S11. XRD patterns of GNP, GNP-300, GNP-450, GNP-550 and GNP-650 catalysts.

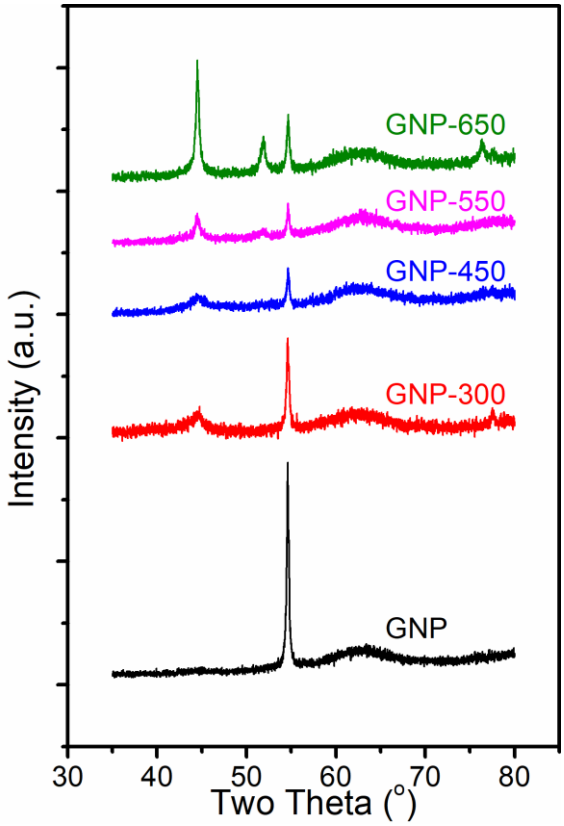

Figure S12. TGA profiles of Ni/GNP-300, Ni/GNP-450, Ni/GNP-550 and Ni/GNP-650 catalysts.

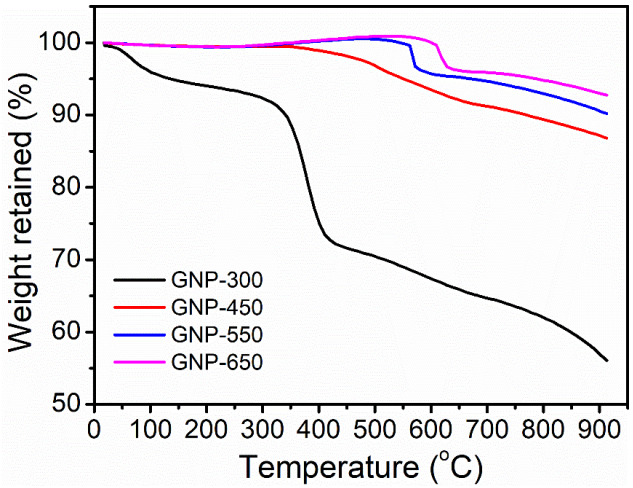

Figure S13. N_2 sorption isotherms for GNP-450, GNP-550 and GNP-650 catalysts.

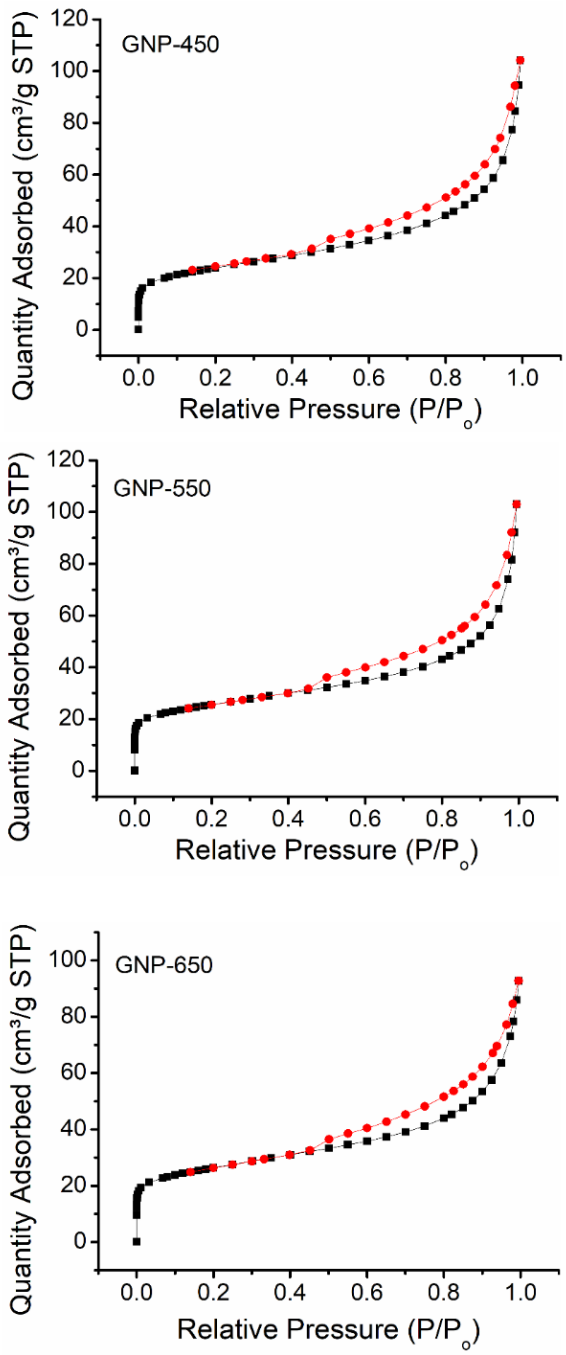

Figure S14. Glucose conversions over GNP-450, GNP-550 and GNP-650 catalysts after 2 h reaction.

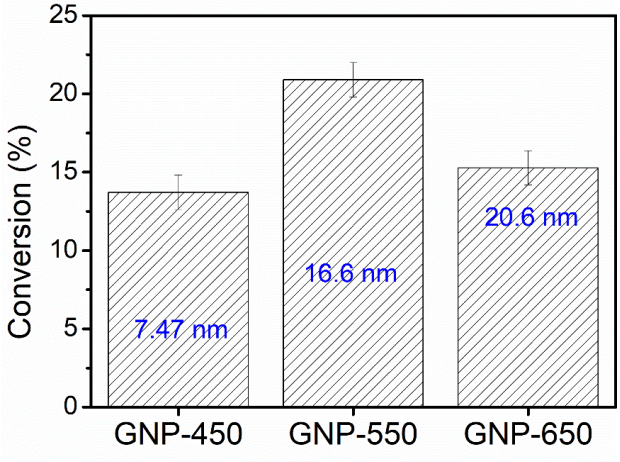

Figure S15. STEM-HAADF images, Fe elemental mapping and Ni elemental mapping of Fe_3Ni/CB (1, 4, 7), FeNi/CB (2, 5, 8), $FeNi_3$/CB (3, 6, 9).

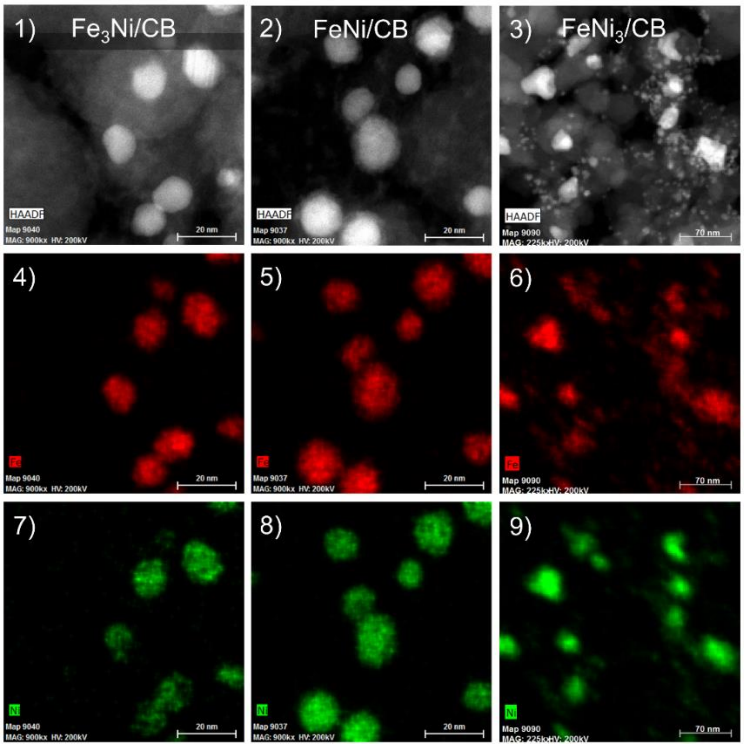

Figure S16. N_2 sorption isotherms for CB (a), Fe/CB (b), Ni/CB (c), Fe_3Ni/CB (d), FeNi/CB (e), $FeNi_3$/CB (f).

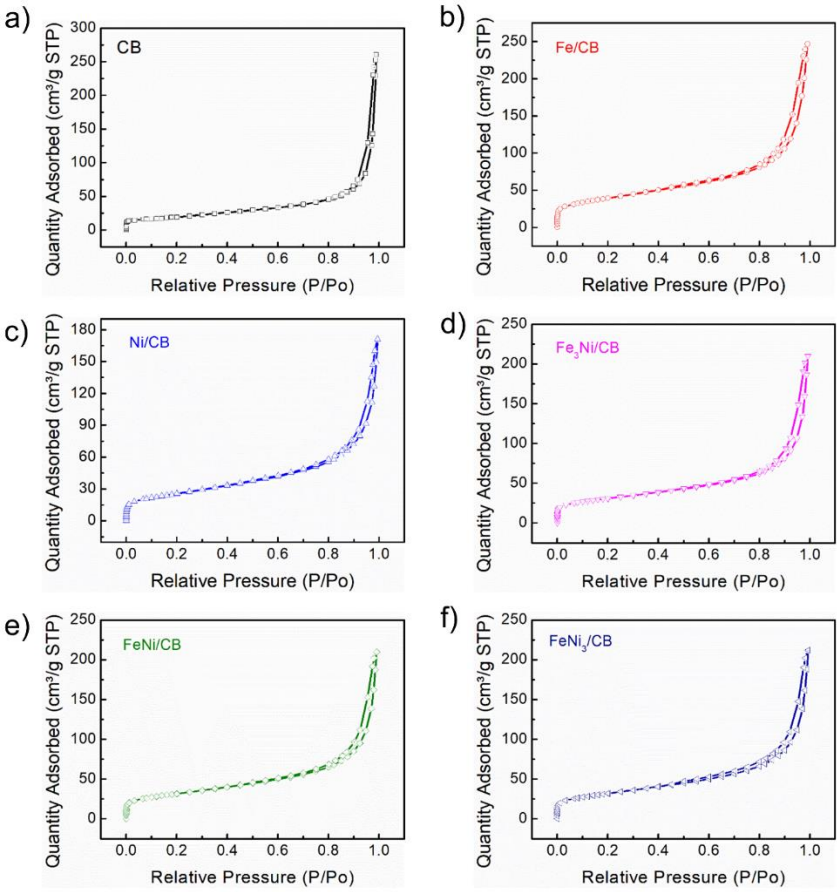

Figure S17. Pseudo-first order fitting of kinetic curves for Fe/CB, Ni/CB, FeNi/CB, Fe/CB+Ni/CB catalysts in glucose hydrogenation at 140 °C, 30 bar H_2, and 1700 rpm reaction conditions.

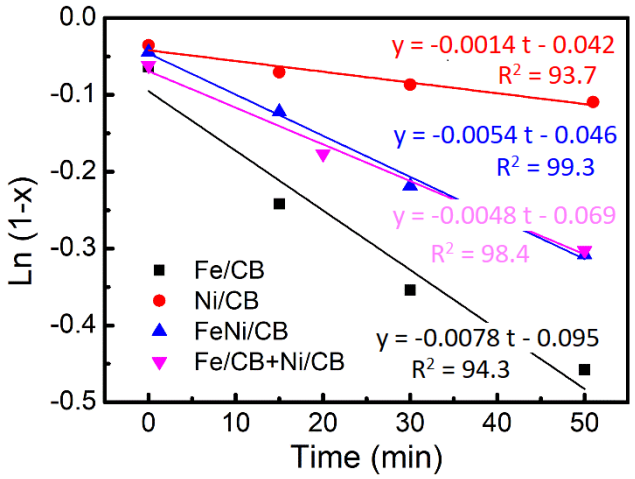

Table S1 Reaction conditions comparison for Ni magnetic particles synthesis (stirring bar with oval shape).

Entry	P (H_2) / bar	Time / h	T / °C	Magnetic particles	Colour of the liquid
1	~ 1	24	140	×	Black
2	~ 1	46.5	140	×	Black
3	~ 1	24	155	×	Beige
4	~ 1	19	180	√	Grey transparent
5	2	24	140	×	Black
6	2	32	140	×	Black
7	2	19	180	√	Transparent

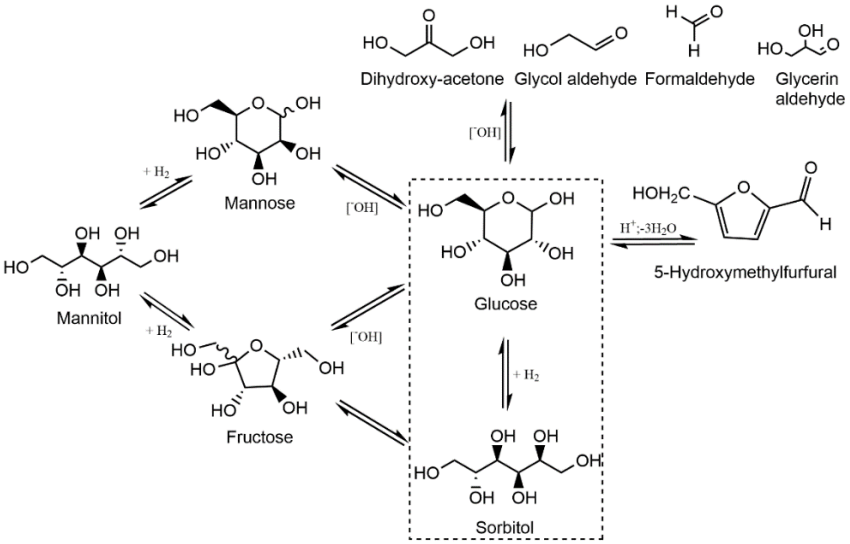

Scheme S1. Reaction network for hydrogenation of glucose.[116]

References

[1] A. Demirbaş, Biomass resource facilities and biomass conversion processing for fuels and chemicals, Energy Convers. Manage., 42 (2001) 1357-1378.
[2] M.Z. Hossain, P.A. Charpentier, Hydrogen production by gasification of biomass and opportunity fuels, in: V. Subramani, A. Basile, T.N. Veziroğlu (Eds.) Compendium of Hydrogen Energy, Woodhead Publishing, Oxford, 2015, pp. 137-175.
[3] M.M. Küçük, A. Demirbaş, Biomass conversion processes, Energy Convers. Manage., 38 (1997) 151-165.
[4] Y. M., Bits, Splits, t4nkyong, dukang, The future of bio-based chemicals in the EU Bioeconomy, in, EU SCIENCE HUB, 2019.
[5] Y. Wang, H. Song, J.-P. Hou, C.-M. Jia, S. Yao, Systematic Isolation and Utilization of Lignocellulosic Components from Sugarcane Bagasse, Separation Science and Technology, 48 (2013) 2217-2224.
[6] B.C. Saha, Hemicellulose bioconversion, Journal of industrial microbiology & biotechnology, 30 (2003) 279-291.
[7] P.R. Lennartsson, C. Niklasson, M.J. Taherzadeh, A pilot study on lignocelluloses to ethanol and fish feed using NMMO pretreatment and cultivation with zygomycetes in an air-lift reactor, Bioresour Technol, 102 (2011) 4425-4432.
[8] J. Salimon, N. Salih, E. Yousif, Industrial development and applications of plant oils and their biobased oleochemicals, Arabian Journal of Chemistry, 5 (2012) 135-145.
[9] G. Andrich, U. Nesti, F. Venturi, A. Zinnai, R. Fiorentini, Supercritical fluid extraction of bioactive lipids from the microalga Nannochloropsis sp, European Journal of Lipid Science and Technology, 107 (2005) 381-386.
[10] T. Werpy, G. Petersen, Top value added chemicals from biomass: volume I--results of screening for potential candidates from sugars and synthesis gas, in, National Renewable Energy Lab., Golden, CO (US), 2004.
[11] S. Schimpf, C. Louis, P. Claus, Ni/SiO2 catalysts prepared with ethylenediamine nickel precursors: Influence of the pretreatment on the catalytic properties in glucose hydrogenation, Appl. Catal., A, 318 (2007) 45-53.
[12] X. Zhang, L.J. Durndell, M.A. Isaacs, C.M.A. Parlett, A.F. Lee, K. Wilson, Platinum-Catalyzed Aqueous-Phase Hydrogenation of d-Glucose to d-Sorbitol, ACS Catal., 6 (2016) 7409-7417.
[13] J. Zhang, S. Wu, Y. Liu, B. Li, Hydrogenation of glucose over reduced Ni/Cu/Al hydrotalcite precursors, Catal. Commun., 35 (2013) 23-26.
[14] F.W. Schenck, Glucose and Glucose-Containing Syrups, in: Ullmann's Encyclopedia of Industrial Chemistry.
[15] Y. Román-Leshkov, M. Moliner, J.A. Labinger, M.E. Davis, Mechanism of Glucose Isomerization Using a Solid Lewis Acid Catalyst in Water, Angew. Chem., Int. Ed., 49 (2010) 8954-8957.
[16] M. Miljkovic, Carbohydrates: Synthesis, Mechanisms, and Stereoelectronic Effects, 1 ed., Springer-Verlag New York, 2009.

[17] B. Cinlar, T. Wang, B.H. Shanks, Kinetics of monosaccharide conversion in the presence of homogeneous Bronsted acids, Appl. Catal., A, 450 (2013) 237-242.
[18] T. Haynes, V. Dubois, S. Hermans, Particle size effect in glucose oxidation with Pd/CB catalysts, Appl. Catal., A, 542 (2017) 47-54.
[19] S. Solmi, C. Morreale, F. Ospitali, S. Agnoli, F. Cavani, Oxidation of d-Glucose to Glucaric Acid Using Au/C Catalysts, ChemCatChem, 9 (2017) 2797-2806.
[20] S. Hermans, A. Deffernez, M. Devillers, Au–Pd/C catalysts for glyoxal and glucose selective oxidations, Appl. Catal., A, 395 (2011) 19-27.
[21] S. Hermans, M. Devillers, On the role of ruthenium associated with Pd and/or Bi in carbon-supported catalysts for the partial oxidation of glucose, Appl. Catal., A, 235 (2002) 253-264.
[22] S. Hermans, A. Deffernez, M. Devillers, Preparation of Au–Pd/C catalysts by adsorption of metallic species in aqueous phase for selective oxidation, Catal. Today, 157 (2010) 77-82.
[23] D.K. Mishra, J.M. Lee, J.S. Chang, J.S. Hwang, Liquid phase hydrogenation of d-glucose to d-sorbitol over the catalyst (Ru/NiO-TiO 2) of ruthenium on a NiO-modified TiO 2 support, Catal. Today, 185 (2012) 104-108.
[24] A.M. Ruppert, K. Weinberg, R. Palkovits, Hydrogenolysis goes bio: from carbohydrates and sugar alcohols to platform chemicals, Angewandte Chemie (International ed. in English), 51 (2012) 2564-2601.
[25] C. Liu, C. Zhang, K. Liu, Y. Wang, G. Fan, S. Sun, J. Xu, Y. Zhu, Y. Li, Aqueous-phase hydrogenolysis of glucose to value-added chemicals and biofuels: A comparative study of active metals, Biomass and Bioenergy, 72 (2015) 189-199.
[26] J.W.N. I. Chorkendorff, Introduction to Catalysis, in: Concepts of Modern Catalysis and Kinetics, Wiley, Weinheim, 2003, pp. 1-21.
[27] R.D. John C. Chadwick, Zoraida Freixa, Piet W. N. M. van Leeuwen, Homogeneous Catalysts: Activity - Stability - Deactivation, WILEY-VCH, 2011.
[28] M. Baker, Cryo-electron microscopy shapes up, Nature, 561 (2018) 565-567.
[29] J.A. Dumesic, G.W. Huber, M. Boudart, Principles of Heterogeneous Catalysis, in: Handbook of Heterogeneous Catalysis.
[30] C.E.S. Housecroft, Alan G., Inorganic Chemistry (2nd ed.), Pearson Prentice-Hall, 2005.
[31] H.S. Taylor, Catalysis, in, Encyclopedia Britannica, 2018.
[32] A. Nouailhat, An introduction to nanoscience and nanotechnology, John Wiley & Sons, 2010.
[33] P.A. Sermon, G.C. Bond, P.B. Wells, Hydrogenation of alkenes over supported gold, Journal of the Chemical Society, Faraday Transactions 1: Physical Chemistry in Condensed Phases, 75 (1979) 385-394.
[34] M. Haruta, Size- and support-dependency in the catalysis of gold, Catal. Today, 36 (1997) 153-166.
[35] M. Valden, X. Lai, D.W. Goodman, Onset of Catalytic Activity of Gold Clusters on Titania with the Appearance of Nonmetallic Properties, Science, 281 (1998) 1647-1650.

[36] J.A. Rodriguez, X. Wang, P. Liu, W. Wen, J.C. Hanson, J. Hrbek, M. Pérez, J. Evans, Gold nanoparticles on ceria: importance of O vacancies in the activation of gold, Topics in Catalysis, 44 (2007) 73-81.
[37] J.A. Rodriguez, P. Liu, J. Hrbek, J. Evans, M. Pérez, Water Gas Shift Reaction on Cu and Au Nanoparticles Supported on CeO2(111) and ZnO(000$\bar 1$): Intrinsic Activity and Importance of Support Interactions, Angew. Chem., Int. Ed., 46 (2007) 1329-1332.
[38] H. Häkkinen, S. Abbet, A. Sanchez, U. Heiz, U. Landman, Structural, Electronic, and Impurity-Doping Effects in Nanoscale Chemistry: Supported Gold Nanoclusters, Angew. Chem., Int. Ed., 42 (2003) 1297-1300.
[39] D. Pillay, G.S. Hwang, Growth and structure of small gold particles on rutile TiO_2 (111), Phys. Rev. B, 72 (2005) 205422.
[40] S. Laursen, S. Linic, Oxidation Catalysis by Oxide-Supported Au Nanostructures: The Role of Supports and the Effect of External Conditions, Phys. Rev. Lett., 97 (2006) 026101.
[41] A. Sanchez, S. Abbet, U. Heiz, W.D. Schneider, H. Häkkinen, R.N. Barnett, U. Landman, When Gold Is Not Noble: Nanoscale Gold Catalysts, The Journal of Physical Chemistry A, 103 (1999) 9573-9578.
[42] B.R. Cuenya, Synthesis and catalytic properties of metal nanoparticles: Size, shape, support, composition, and oxidation state effects, Thin Solid Films, 518 (2010) 3127-3150.
[43] S.I. Sanchez, L.D. Menard, A. Bram, J.H. Kang, M.W. Small, R.G. Nuzzo, A.I. Frenkel, The Emergence of Nonbulk Properties in Supported Metal Clusters: Negative Thermal Expansion and Atomic Disorder in Pt Nanoclusters Supported on γ-Al2O3, J. Am. Chem. Soc., 131 (2009) 7040-7054.
[44] W. Yan, B. Chen, S.M. Mahurin, S. Dai, S.H. Overbury, Brookite-supported highly stable gold catalytic system for CO oxidation, Chem. Commun., (2004) 1918-1919.
[45] W. Li, C. Liang, J. Qiu, W. Zhou, H. Han, Z. Wei, G. Sun, Q. Xin, Carbon nanotubes as support for cathode catalyst of a direct methanol fuel cell, Carbon, 40 (2002) 791-794.
[46] S.K. Shaikhutdinov, R. Meyer, M. Naschitzki, M. Bäumer, H.J. Freund, Size and Support Effects for CO Adsorption on Gold Model Catalysts, Catal. Lett., 86 (2003) 211-219.
[47] J.R. Croy, S. Mostafa, J. Liu, Y. Sohn, H. Heinrich, B.R. Cuenya, Support Dependence of MeOH Decomposition Over Size-Selected Pt Nanoparticles, Catal. Lett., 119 (2007) 209-216.
[48] M. Mavrikakis, P. Stoltze, J.K. Nørskov, Making gold less noble, Catal. Lett., 64 (2000) 101-106.
[49] H. Masatake, K. Tetsuhiko, S. Hiroshi, Y. Nobumasa, Novel Gold Catalysts for the Oxidation of Carbon Monoxide at a Temperature far Below 0 °C, Chem. Lett., 16 (1987) 405-408.
[50] L.K. Ono, D. Sudfeld, B. Roldan Cuenya, In situ gas-phase catalytic properties of TiC-supported size-selected gold nanoparticles synthesized by diblock copolymer encapsulation, Surface Science, 600 (2006) 5041-5050.
[51] R. Reske, H. Mistry, F. Behafarid, B. Roldan Cuenya, P. Strasser, Particle Size Effects in the Catalytic Electroreduction of CO2 on Cu Nanoparticles, J. Am. Chem. Soc., 136 (2014) 6978-6986.

[52] J.P. den Breejen, P.B. Radstake, G.L. Bezemer, J.H. Bitter, V. Frøseth, A. Holmen, K.P. de Jong, On the Origin of the Cobalt Particle Size Effects in Fischer−Tropsch Catalysis, J. Am. Chem. Soc., 131 (2009) 7197-7203.
[53] G.L. Bezemer, J.H. Bitter, H.P.C.E. Kuipers, H. Oosterbeek, J.E. Holewijn, X. Xu, F. Kapteijn, A.J. van Dillen, K.P. de Jong, Cobalt Particle Size Effects in the Fischer−Tropsch Reaction Studied with Carbon Nanofiber Supported Catalysts, J. Am. Chem. Soc., 128 (2006) 3956-3964.
[54] M. Boronat, A. Leyva-Pérez, A. Corma, Theoretical and Experimental Insights into the Origin of the Catalytic Activity of Subnanometric Gold Clusters: Attempts to Predict Reactivity with Clusters and Nanoparticles of Gold, Acc. Chem. Res., 47 (2014) 834-844.
[55] A.F. Trovarelli, P, Catalysis by Ceria and Related Materials, World Scientific, 2002.
[56] Y. Lykhach, S.M. Kozlov, T. Skála, A. Tovt, V. Stetsovych, N. Tsud, F. Dvořák, V. Johánek, A. Neitzel, J. Mysliveček, S. Fabris, V. Matolín, K.M. Neyman, J. Libuda, Counting electrons on supported nanoparticles, Nature Materials, 15 (2016) 284-288.
[57] C.T. Campbell, S.C. Parker, D.E. Starr, The Effect of Size-Dependent Nanoparticle Energetics on Catalyst Sintering, Science, 298 (2002) 811-814.
[58] C.T. Campbell, The Energetics of Supported Metal Nanoparticles: Relationships to Sintering Rates and Catalytic Activity, Acc. Chem. Res., 46 (2013) 1712-1719.
[59] T. van Haasterecht, M. Swart, K.P. de Jong, J.H. Bitter, Effect of initial nickel particle size on stability of nickel catalysts for aqueous phase reforming, J. Energy Chem., 25 (2016) 289-296.
[60] R. Xu, D. Wang, J. Zhang, Y. Li, Shape-Dependent Catalytic Activity of Silver Nanoparticles for the Oxidation of Styrene, Chem. Asian J., 1 (2006) 888-893.
[61] T.S. Ahmadi, Z.L. Wang, T.C. Green, A. Henglein, M.A. El-Sayed, Shape-Controlled Synthesis of Colloidal Platinum Nanoparticles, Science, 272 (1996) 1924-1925.
[62] R. Narayanan, M.A. El-Sayed, Effect of Colloidal Nanocatalysis on the Metallic Nanoparticle Shape: The Suzuki Reaction, Langmuir, 21 (2005) 2027-2033.
[63] R. Narayanan, M.A. El-Sayed, Effect of Nanocatalysis in Colloidal Solution on the Tetrahedral and Cubic Nanoparticle SHAPE: Electron-Transfer Reaction Catalyzed by Platinum Nanoparticles, J. Phys. Chem. B, 108 (2004) 5726-5733.
[64] J. Chen, T. Herricks, M. Geissler, Y. Xia, Single-Crystal Nanowires of Platinum Can Be Synthesized by Controlling the Reaction Rate of a Polyol Process, J. Am. Chem. Soc., 126 (2004) 10854-10855.
[65] T. Herricks, J. Chen, Y. Xia, Polyol Synthesis of Platinum Nanoparticles: Control of Morphology with Sodium Nitrate, Nano Letters, 4 (2004) 2367-2371.
[66] V. Komanicky, H. Iddir, K.-C. Chang, A. Menzel, G. Karapetrov, D. Hennessy, P. Zapol, H. You, Shape-Dependent Activity of Platinum Array Catalyst, J. Am. Chem. Soc., 131 (2009) 5732-5733.
[67] H. Iddir, V. Komanicky, S. Öğüt, H. You, P. Zapol, Shape of Platinum Nanoparticles Supported on SrTiO3: Experiment and Theory, J. Phys. Chem. C, 111 (2007) 14782-14789.

[68] G.F. Cabeza, N.J. Castellani, P. Légaré, Adhesion and bonding of Pt/Ni and Pt/Co overlayers: Density functional calculations, Journal of Physics and Chemistry of Solids, 67 (2006) 690-697.
[69] G. Porwal, S. Gupta, S. Sreedhala, J. Elizabeth, T.S. Khan, M.A. Haider, C.P. Vinod, Mechanistic Insights into the Pathways of Phenol Hydrogenation on Pd Nanostructures, ACS Sustainable Chem. Eng., 7 (2019) 17126-17136.
[70] P. Ferrin, S. Kandoi, A.U. Nilekar, M. Mavrikakis, Hydrogen adsorption, absorption and diffusion on and in transition metal surfaces: A DFT study, Surface Science, 606 (2012) 679-689.
[71] N. Tian, Z.-Y. Zhou, S.-G. Sun, Y. Ding, Z.L. Wang, Synthesis of Tetrahexahedral Platinum Nanocrystals with High-Index Facets and High Electro-Oxidation Activity, Science, 316 (2007) 732-735.
[72] J. Feng, X. Ma, Y. He, D.G. Evans, D. Li, Synthesis of hydrotalcite-supported shape-controlled Pd nanoparticles by a precipitation–reduction method, Appl. Catal., A, 413-414 (2012) 10-20.
[73] X.-T. Li, L. Chen, G.-F. Wei, C. Shang, Z.-P. Liu, Sharp Increase in Catalytic Selectivity in Acetylene Semihydrogenation on Pd Achieved by a Machine Learning Simulation-Guided Experiment, ACS Catal., 10 (2020) 9694-9705.
[74] B. Yang, R. Burch, C. Hardacre, G. Headdock, P. Hu, Influence of surface structures, subsurface carbon and hydrogen, and surface alloying on the activity and selectivity of acetylene hydrogenation on Pd surfaces: A density functional theory study, J. Catal., 305 (2013) 264-276.
[75] L.L. Jewell, B.H. Davis, Review of absorption and adsorption in the hydrogen–palladium system, Appl. Catal., A, 310 (2006) 1-15.
[76] S.K. Kim, C. Kim, J.H. Lee, J. Kim, H. Lee, S.H. Moon, Performance of shape-controlled Pd nanoparticles in the selective hydrogenation of acetylene, J. Catal., 306 (2013) 146-154.
[77] C. Sun, Z. Cao, J. Wang, L. Lin, X. Xie, Shape and ligand effect of palladium nanocrystals on furan hydrogenation, New Journal of Chemistry, 43 (2019) 2567-2574.
[78] M. Cao, K. Miyabayashi, Z. Shen, K. Ebitani, M. Miyake, Olefin hydrogenation catalysis of platinum nanocrystals with different shapes, Journal of Nanoparticle Research, 13 (2011) 5147.
[79] X. Zhao, Y. Zhao, G. Fu, N. Zheng, Origin of the facet dependence in the hydrogenation catalysis of olefins: experiment and theory, Chem. Commun., 51 (2015) 12016-12019.
[80] D. Pham Minh, Y. Oudart, B. Baubet, C. Verdon, C. Thomazeau, Nanostructured Heterogeneous Catalysts: Well Defined Platinum Nanoparticles Supported on Alumina. Preparation, Characterization and Application to the Selective Hydrogenation of Buta-1,3-diene, Oil & Gas Science and Technology - Rev. IFP, 64 (2009) 697-706.
[81] Y. Gou, X. Liang, B. Chen, Catalytic hydrogenation of acetophenone over shape controlled Pd catalysts supported on sheet-like NiO, Catal. Today, 216 (2013) 200-204.
[82] Y. Han, Z. He, S. Wang, W. Li, J. Zhang, Performance of facet-controlled Pd nanocrystals in 2-ethylanthraquinone hydrogenation, Catal. Sci. Technol., 5 (2015) 2630-2639.

[83] K.D. Kim, Z. Wang, Y. Tao, H. Ling, Y. Yuan, C. Zhou, Z. Liu, M. Gaborieau, J. Huang, A. Yu, The Comparative Effect of Particle Size and Support Acidity on Hydrogenation of Aromatic Ketones, ChemCatChem, 11 (2019) 4810-4817.
[84] K. Murata, K. Ogura, J. Ohyama, K. Sawabe, Y. Yamamoto, S. Arai, A. Satsuma, Selective Hydrogenation of Cinnamaldehyde over the Stepped and Plane Surface of Pd Nanoparticles with Controlled Morphologies by CO Chemisorption, ACS Appl. Mater. Interfaces, 12 (2020) 26002-26012.
[85] J. Ohyama, S. Kato, M. Machida, A. Satsuma, Shape Control Preparation of Supported Platinum Nano-octahedra by Ethylene Treatment for Enhancement of Selective Hydrogenation of Cinnamaldehyde, Chem. Lett., 48 (2019) 1203-1205.
[86] J.C. Serrano-Ruiz, A. López-Cudero, J. Solla-Gullón, A. Sepúlveda-Escribano, A. Aldaz, F. Rodríguez-Reinoso, Hydrogenation of α, β unsaturated aldehydes over polycrystalline, (111) and (100) preferentially oriented Pt nanoparticles supported on carbon, J. Catal., 253 (2008) 159-166.
[87] H. Chen, S. Liu, J. Yin, X. Gao, Z. Tao, B. Wu, H. Xiang, Y. Yang, Y. Li, The Influence of Size and Shape of Pd Nanoparticles on the Performances of Pd/Beta Catalysts for n-Heptane Hydroisomerization, ChemCatChem, 11 (2019) 3542-3551.
[88] A.C. Reardon, Metallurgy for the Non-Metallurgist, ASM International, 2011.
[89] T.W. Hansen, J.B. Wagner, P.L. Hansen, S. Dahl, H. Topsøe, C.J.H. Jacobsen, Atomic-Resolution in Situ Transmission Electron Microscopy of a Promoter of a Heterogeneous Catalyst, Science, 294 (2001) 1508-1510.
[90] A.F. Carlsson, M. Naschitzki, M. Bäumer, H.J. Freund, The Structure and Reactivity of Al2O3-Supported Cobalt−Palladium Particles: A CO-TPD, STM, and XPS Study, J. Phys. Chem. B, 107 (2003) 778-785.
[91] P. Liu, J.K. Nørskov, Ligand and ensemble effects in adsorption on alloy surfaces, Phys. Chem. Chem. Phys., 3 (2001) 3814-3818.
[92] A. Hamnett, Mechanism and electrocatalysis in the direct methanol fuel cell, Catal. Today, 38 (1997) 445-457.
[93] U.B. Demirci, Theoretical means for searching bimetallic alloys as anode electrocatalysts for direct liquid-feed fuel cells, J. Power Sources, 173 (2007) 11-18.
[94] E. Antolini, Formation of carbon-supported PtM alloys for low temperature fuel cells: a review, Materials Chemistry and Physics, 78 (2003) 563-573.
[95] J.-H. Choi, K.-W. Park, I.-S. Park, W.-H. Nam, Y.-E. Sung, Methanol electro-oxidation and direct methanol fuel cell using Pt/Rh and Pt/Ru/Rh alloy catalysts, Electrochimica Acta, 50 (2004) 787-790.
[96] P.N. Ross, K. Kinoshita, A.J. Scarpellino, P. Stonehart, Electrocatalysis on binary alloys: I. Oxidation of molecular hydrogen on supported Pt−Rh alloys, Journal of Electroanalytical Chemistry and Interfacial Electrochemistry, 59 (1975) 177-189.
[97] H. Igarashi, T. Fujino, Y. Zhu, H. Uchida, M. Watanabe, CO Tolerance of Pt alloy electrocatalysts for polymer electrolyte fuel cells and the detoxification mechanism, Phys. Chem. Chem. Phys., 3 (2001) 306-314.
[98] A. Naitabdi, L.K. Ono, F. Behafarid, B.R. Cuenya, Thermal Stability and Segregation Processes in Self-Assembled Size-Selected AuxFe1-x

Nanoparticles Deposited on TiO2(110): Composition Effects, J. Phys. Chem. C, 113 (2009) 1433-1446.
[99] T.J. Schwartz, R.L. Johnson, J. Cardenas, A. Okerlund, N.A. Da Silva, K. Schmidt-Rohr, J.A. Dumesic, Engineering Catalyst Microenvironments for Metal-Catalyzed Hydrogenation of Biologically Derived Platform Chemicals, Angew. Chem., Int. Ed., 53 (2014) 12718-12722.
[100] D.R. Vardon, A.E. Settle, V. Vorotnikov, M.J. Menart, T.R. Eaton, K.A. Unocic, K.X. Steirer, K.N. Wood, N.S. Cleveland, K.E. Moyer, W.E. Michener, G.T. Beckham, Ru-Sn/AC for the Aqueous-Phase Reduction of Succinic Acid to 1,4-Butanediol under Continuous Process Conditions, ACS Catal., 7 (2017) 6207-6219.
[101] J.R. Croy, S. Mostafa, L. Hickman, H. Heinrich, B.R. Cuenya, Bimetallic Pt-Metal catalysts for the decomposition of methanol: Effect of secondary metal on the oxidation state, activity, and selectivity of Pt, Appl. Catal., A, 350 (2008) 207-216.
[102] J. Huo, J.-P. Tessonnier, B.H. Shanks, Improving Hydrothermal Stability of Supported Metal Catalysts for Biomass Conversions: A Review, ACS Catal., 11 (2021) 5248-5270.
[103] H. Xiong, H.N. Pham, A.K. Datye, Hydrothermally stable heterogeneous catalysts for conversion of biorenewables, Green Chem., 16 (2014) 4627-4643.
[104] C. Sievers, Y. Noda, L. Qi, E.M. Albuquerque, R.M. Rioux, S.L. Scott, Phenomena Affecting Catalytic Reactions at Solid–Liquid Interfaces, ACS Catal., 6 (2016) 8286-8307.
[105] J. Matthiesen, T. Hoff, C. Liu, C. Pueschel, R. Rao, J.-P. Tessonnier, Functional carbons and carbon nanohybrids for the catalytic conversion of biomass to renewable chemicals in the condensed phase, Chin. J. Catal., 35 (2014) 842-855.
[106] R.M. Ravenelle, J.R. Copeland, W.-G. Kim, J.C. Crittenden, C. Sievers, Structural Changes of γ-Al2O3-Supported Catalysts in Hot Liquid Water, ACS Catal., 1 (2011) 552-561.
[107] H. Li, Y. Zhao, C. Gao, Y. Wang, Z. Sun, X. Liang, Study on deactivation of Ni/Al2O3 catalyst for liquid phase hydrogenation of crude 1,4-butanediol aqueous solution, Chem. Eng. J., 181-182 (2012) 501-507.
[108] R.M. Ravenelle, F. Schüßler, A. D'Amico, N. Danilina, J.A. van Bokhoven, J.A. Lercher, C.W. Jones, C. Sievers, Stability of Zeolites in Hot Liquid Water, J. Phys. Chem. C, 114 (2010) 19582-19595.
[109] H.N. Pham, A.E. Anderson, R.L. Johnson, K. Schmidt-Rohr, A.K. Datye, Improved Hydrothermal Stability of Mesoporous Oxides for Reactions in the Aqueous Phase, Angew. Chem., Int. Ed., 51 (2012) 13163-13167.
[110] K. Fulajtárova, T. Soták, M. Hronec, I. Vávra, E. Dobročka, M. Omastová, Aqueous phase hydrogenation of furfural to furfuryl alcohol over Pd–Cu catalysts, Appl. Catal., A, 502 (2015) 78-85.
[111] S. Salakhum, K. Saenluang, C. Wattanakit, Stability of monometallic Pt and Ru supported on hierarchical HZSM-5 nanosheets for hydrodeoxygenation of lignin-derived compounds in the aqueous phase, Sustainable Energy & Fuels, 4 (2020) 1126-1134.

[112] Y.T. Kim, J.A. Dumesic, G.W. Huber, Aqueous-phase hydrodeoxygenation of sorbitol: A comparative study of Pt/Zr phosphate and PtReOx/C, J. Catal., 304 (2013) 72-85.
[113] M. Besson, P. Gallezot, Deactivation of metal catalysts in liquid phase organic reactions, Catal. Today, 81 (2003) 547-559.
[114] I. Sádaba, M. López Granados, A. Riisager, E. Taarning, Deactivation of solid catalysts in liquid media: the case of leaching of active sites in biomass conversion reactions, Green Chem., 17 (2015) 4133-4145.
[115] T. Okuhara, Water-Tolerant Solid Acid Catalysts, Chem. Rev., 102 (2002) 3641-3666.
[116] B. Kusserow, S. Schimpf, P. Claus, Hydrogenation of Glucose to Sorbitol over Nickel and Ruthenium Catalysts, Adv. Synth. Catal., 345 (2003) 289-299.
[117] J.N. Jocz, P.E. Savage, L.T. Thompson, Thermodynamic Analysis of Catalyst Stability in Hydrothermal Reaction Media, Ind. Eng. Chem. Res., 57 (2018) 8655-8663.
[118] B.K. Ly, B. Tapin, F. Epron, C. Pinel, C. Especel, M. Besson, In situ preparation of bimetallic ReOx-Pd/TiO2 catalysts for selective aqueous-phase hydrogenation of succinic acid to 1,4-butanediol, Catal. Today, 355 (2020) 75-83.
[119] R. Mariscal, P. Maireles-Torres, M. Ojeda, I. Sádaba, M. López Granados, Furfural: a renewable and versatile platform molecule for the synthesis of chemicals and fuels, Energy Environ. Sci., 9 (2016) 1144-1189.
[120] A.E. Settle, N.S. Cleveland, C.A. Farberow, D.R. Conklin, X. Huo, A.A. Dameron, R.W. Tracy, R. Sarkar, E.J. Kautz, A. Devaraj, K.K. Ramasamy, M.J. Watson, A.M. York, R.M. Richards, K.A. Unocic, G.T. Beckham, M.B. Griffin, K.E. Hurst, E.C.D. Tan, S.T. Christensen, D.R. Vardon, Enhanced Catalyst Durability for Bio-Based Adipic Acid Production by Atomic Layer Deposition, Joule, 3 (2019) 2219-2240.
[121] T.W. Hansen, A.T. DeLaRiva, S.R. Challa, A.K. Datye, Sintering of Catalytic Nanoparticles: Particle Migration or Ostwald Ripening?, Acc. Chem. Res., 46 (2013) 1720-1730.
[122] S.B. Simonsen, I. Chorkendorff, S. Dahl, M. Skoglundh, J. Sehested, S. Helveg, Direct Observations of Oxygen-induced Platinum Nanoparticle Ripening Studied by In Situ TEM, J. Am. Chem. Soc., 132 (2010) 7968-7975.
[123] S.B. Simonsen, I. Chorkendorff, S. Dahl, M. Skoglundh, J. Sehested, S. Helveg, Ostwald ripening in a Pt/SiO2 model catalyst studied by in situ TEM, J. Catal., 281 (2011) 147-155.
[124] O.A. Abdelrahman, A. Heyden, J.Q. Bond, Analysis of Kinetics and Reaction Pathways in the Aqueous-Phase Hydrogenation of Levulinic Acid To Form γ-Valerolactone over Ru/C, ACS Catal., 4 (2014) 1171-1181.
[125] O.A. Abdelrahman, H.Y. Luo, A. Heyden, Y. Román-Leshkov, J.Q. Bond, Toward rational design of stable, supported metal catalysts for aqueous-phase processing: Insights from the hydrogenation of levulinic acid, J. Catal., 329 (2015) 10-21.
[126] L. Shao, B. Zhang, W. Zhang, S.Y. Hong, R. Schlögl, D.S. Su, The Role of Palladium Dynamics in the Surface Catalysis of Coupling Reactions, Angew. Chem., Int. Ed., 52 (2013) 2114-2117.

[127] J.H. Vleeming, B.F.M. Kuster, G.B. Marin, F. Oudet, P. Courtine, Graphite-Supported Platinum Catalysts: Effects of Gas and Aqueous Phase Treatments, J. Catal., 166 (1997) 148-159.
[128] M.S. Ide, D.D. Falcone, R.J. Davis, On the deactivation of supported platinum catalysts for selective oxidation of alcohols, J. Catal., 311 (2014) 295-305.
[129] A. Douidah, P. Marécot, S. Labruquère, J. Barbier, Stability of supported platinum catalysts in aqueous phase under hydrogen atmosphere, Appl. Catal., A, 210 (2001) 111-120.
[130] D.R. Jones, S. Iqbal, S. Ishikawa, C. Reece, L.M. Thomas, P.J. Miedziak, D.J. Morgan, J.K. Edwards, J.K. Bartley, D.J. Willock, G.J. Hutchings, The conversion of levulinic acid into γ-valerolactone using Cu–ZrO2 catalysts, Catal. Sci. Technol., 6 (2016) 6022-6030.
[131] Y. Wang, S. Van de Vyver, K.K. Sharma, Y. Román-Leshkov, Insights into the stability of gold nanoparticles supported on metal oxides for the base-free oxidation of glucose to gluconic acid, Green Chem., 16 (2014) 719-726.
[132] N. de Jonge, F.M. Ross, Electron microscopy of specimens in liquid, Nature Nanotechnology, 6 (2011) 695-704.
[133] J. Hermannsdörfer, N. de Jonge, A. Verch, Electron beam induced chemistry of gold nanoparticles in saline solution, Chem. Commun., 51 (2015) 16393-16396.
[134] T. Kraus, N. de Jonge, Dendritic Gold Nanowire Growth Observed in Liquid with Transmission Electron Microscopy, Langmuir, 29 (2013) 8427-8432.
[135] B.J. O'Neill, J.T. Miller, P.J. Dietrich, F.G. Sollberger, F.H. Ribeiro, J.A. Dumesic, Operando X-ray Absorption Spectroscopy Studies of Sintering for Supported Copper Catalysts during Liquid-phase Reaction, ChemCatChem, 6 (2014) 2493-2496.
[136] R. Weingarten, G.A. Tompsett, W.C. Conner, G.W. Huber, Design of solid acid catalysts for aqueous-phase dehydration of carbohydrates: The role of Lewis and Brønsted acid sites, J. Catal., 279 (2011) 174-182.
[137] M. Guisnet, P. Magnoux, Organic chemistry of coke formation, Appl. Catal., A, 212 (2001) 83-96.
[138] N. Worz, A. Brandner, P. Claus, Platinum−Bismuth-Catalyzed Oxidation of Glycerol: Kinetics and the Origin of Selective Deactivation, J. Phys. Chem. C, 114 (2010) 1164-1172.
[139] A.S. Piskun, J.E. de Haan, E. Wilbers, H.H. van de Bovenkamp, Z. Tang, H.J. Heeres, Hydrogenation of Levulinic Acid to γ-Valerolactone in Water Using Millimeter Sized Supported Ru Catalysts in a Packed Bed Reactor, ACS Sustainable Chem. Eng., 4 (2016) 2939-2950.
[140] Z. Zhang, J.E. Jackson, D.J. Miller, Effect of biogenic fermentation impurities on lactic acid hydrogenation to propylene glycol, Bioresour. Technol., 99 (2008) 5873-5880.
[141] H.C. Genuino, H.H. van de Bovenkamp, E. Wilbers, J.G.M. Winkelman, A. Goryachev, J.P. Hofmann, E.J.M. Hensen, B.M. Weckhuysen, P.C.A. Bruijnincx, H.J. Heeres, Catalytic Hydrogenation of Renewable Levulinic Acid to γ-Valerolactone: Insights into the Influence of Feed Impurities on Catalyst Performance in Batch and Flow Reactors, ACS Sustainable Chem. Eng., 8 (2020) 5903-5919.

[142] M. Gupta, T.S. Khan, S. Gupta, M.I. Alam, M. Agarwal, M.A. Haider, Non-bonding and bonding interactions of biogenic impurities with the metal catalyst and the design of bimetallic alloys, J. Catal., 352 (2017) 542-556.
[143] B.J. Arena, Deactivation of ruthenium catalysts in continuous glucose hydrogenation, Appl. Catal., A, 87 (1992) 219-229.
[144] W. Lin, H. Cheng, J. Ming, Y. Yu, F. Zhao, Deactivation of Ni/TiO2 catalyst in the hydrogenation of nitrobenzene in water and improvement in its stability by coating a layer of hydrophobic carbon, J. Catal., 291 (2012) 149-154.
[145] M. Besson, P. Gallezot, Stability of ruthenium catalysts supported on TiO2 or ZrO2 in catalytic wet air oxidation, Top. Catal., 33 (2005) 101-108.
[146] D. Pham Minh, P. Gallezot, M. Besson, Treatment of olive oil mill wastewater by catalytic wet air oxidation: 3. Stability of supported ruthenium catalysts during oxidation of model pollutant p-hydroxybenzoic acid in batch and continuous reactors, Appl. Catal., B, 75 (2007) 71-77.
[147] S.A. Tupy, A.M. Karim, C. Bagia, W. Deng, Y. Huang, D.G. Vlachos, J.G. Chen, Correlating Ethylene Glycol Reforming Activity with In Situ EXAFS Detection of Ni Segregation in Supported NiPt Bimetallic Catalysts, ACS Catal., 2 (2012) 2290-2296.
[148] B.W. Hoffer, E. Crezee, F. Devred, P.R.M. Mooijman, W.G. Sloof, P.J. Kooyman, A.D. Van Langeveld, F. Kapteijn, J.A. Moulijn, The role of the active phase of Raney-type Ni catalysts in the selective hydrogenation of D-glucose to D-sorbitol, Appl. Catal., A, 253 (2003) 437-452.
[149] J. Zhang, L. Lin, J. Zhang, J. Shi, Efficient conversion of d-glucose into d-sorbitol over MCM-41 supported Ru catalyst prepared by a formaldehyde reduction process, Carbohydr. Res., 346 (2011) 1327-1332.
[150] H. Danner, R. Braun, Biotechnology for the production of commodity chemicals from biomass, Chem. Soc. Rev., 28 (1999) 395-405.
[151] A. Fukuoka, P.L. Dhepe, Catalytic Conversion of Cellulose into Sugar Alcohols, Angew. Chem., Int. Ed., 45 (2006) 5161-5163.
[152] W. Deng, X. Tan, W. Fang, Q. Zhang, Y. Wang, Conversion of Cellulose into Sorbitol over Carbon Nanotube-Supported Ruthenium Catalyst, Catal. Lett., 133 (2009) 167.
[153] R. Palkovits, K. Tajvidi, A.M. Ruppert, J. Procelewska, Heteropoly acids as efficient acid catalysts in the one-step conversion of cellulose to sugar alcohols, Chem. Commun., 47 (2011) 576-578.
[154] J.H. Zhou, M.G. Zhang, L. Zhao, P. Li, X.G. Zhou, W.K. Yuan, Carbon nanofiber/graphite-felt composite supported Ru catalysts for hydrogenolysis of sorbitol, Catal. Today, 147 (2009) S225-S229.
[155] M. Banu, S. Sivasanker, T.M. Sankaranarayanan, P. Venuvanalingam, Hydrogenolysis of sorbitol over Ni and Pt loaded on NaY, Catal. Commun., 12 (2011) 673-677.
[156] F.B. Bizhanov, R.B. Drozdova, Studies of the kinetics and mechanism of glucose hydrogenation over ruthenium catalysts, React. Kinet. Catal. Lett., 21 (1982) 35-39.
[157] M. Makkee, A.P.G. Kieboom, H. van Bekkum, Hydrogenation of d-fructose and d-fructose/d-glucose mixtures, Carbohydr. Res., 138 (1985) 225-236.

[158] P.J. Cerino, G. Fleche, P. Gallezot, J.P. Salome, Activity and Stability of Promoted Raney-Nickel Catalysts in Glucose Hydrogenation, in: Studies in Surface Science and Catalysis, 1991, pp. 231-236.
[159] J. Zhang, J.-b. Li, S.-B. Wu, Y. Liu, Advances in the Catalytic Production and Utilization of Sorbitol, Ind. Eng. Chem. Res., 52 (2013) 11799-11815.
[160] W. Plazinski, A. Plazinska, M. Drach, The water-catalyzed mechanism of the ring-opening reaction of glucose, Phys. Chem. Chem. Phys., 17 (2015) 21622-21629.
[161] Q.T. Trinh, B.K. Chethana, S.H. Mushrif, Adsorption and Reactivity of Cellulosic Aldoses on Transition Metals, J. Phys. Chem. C, 119 (2015) 17137-17145.
[162] A. Prestianni, R. Cortese, F. Ferrante, R. Schimmenti, D. Duca, S. Hermans, D.Y. Murzin, α-d-Glucopyranose Adsorption on a Pd30 Cluster Supported on Boron Nitride Nanotube, Top. Catal., 59 (2016) 1178-1184.
[163] H. Hofmann, M.W. Bill, Geschwindigkeitsbestimmende Faktoren bei Reaktionen mit suspendiertem Kontakt, Chemie Ingenieur Technik, 31 (1959) 81-88.
[164] J. Karolyi, Production of Sorbitol by Use of Ammonia Synthesis Gas, Ind. Eng. Chem. Process Des. Dev., 7 (1968) 107-110.
[165] M. Abdel Akher, J. Ghali, M.S. Raouf, M. Roushdi, Factors Affecting the Catalytic Hydrogenation of D-Glucose. Part I. Effect of Type of Catalyst and Concentrations of both Glucose and Catalyst, Starch - Stärke, 26 (1974) 307-312.
[166] F. Turek, R.K. Chakrabarti, R. Lange, R. Geike, W. Flock, On the experimental study and scale-up of three-phase catalytic reactors: Hydrogenation of glucose on nickel catalyst, Chem. Eng. Sci., 38 (1983) 275-283.
[167] J. Wisnlak, R. Simon, Hydrogenation of Glucose, Fructose, and Their Mixtures, Ind. Eng. Chem. Prod. Res. Dev., 18 (1979) 50-57.
[168] G.D. Menez, O.C. Sandall, Gas Absorption Accompanied by First-Order Chemical Reaction in Turbulent Liquids, Industrial & Engineering Chemistry Fundamentals, 13 (1974) 72-76.
[169] E. Crezee, B.W. Hoffer, R.J. Berger, M. Makkee, F. Kapteijn, J.A. Moulijn, Three-phase hydrogenation of d-glucose over a carbon supported ruthenium catalyst—mass transfer and kinetics, Appl. Catal., A, 251 (2003) 1-17.
[170] D.K. Mishra, A.A. Dabbawala, J.J. Park, S.H. Jhung, J.S. Hwang, Selective hydrogenation of d-glucose to d-sorbitol over HY zeolite supported ruthenium nanoparticles catalysts, Catal. Today, 232 (2014) 99-107.
[171] H. Singh, A. Rai, R. Yadav, A.K. Sinha, Glucose hydrogenation to sorbitol over unsupported mesoporous Ni/NiO catalyst, Mol. Catal., 451 (2018) 186-191.
[172] V.J. Ipatieff, Ber. dtsh. chem. Ges., (1912) 3218.
[173] P. Gallezot, P.J. Cerino, B. Blanc, G. Flèche, P. Fuertes, Glucose hydrogenation on promoted raney-nickel catalysts, J. Catal., 146 (1994) 93-102.
[174] K. Van Gorp, E. Boerman, C.V. Cavenaghi, P.H. Berben, Catalytic hydrogenation of fine chemicals: Sorbitol production, Catal. Today, 52 (1999) 349-361.

[175] M.J. Ahmed, A.A. Khadom, A.A.H. Kadhum, Optimization hydrogenation process of D-glucose to D-sorbitol over Raney nickel catalyst, European Journal of Scientific Research, 30 (2009) 294-304.
[176] B. García, J. Moreno, G. Morales, J.A. Melero, J. Iglesias, Production of Sorbitol via Catalytic Transfer Hydrogenation of Glucose, Applied Sciences, 10 (2020) 1843.
[177] L. Hui, L. Hexing, W. Weijiang, D. Jing-Fa, Excellent Activity of Ultrafine Co-B Amorphous Alloy Catalyst in Glucose Hydrogenation, Chem. Lett., 28 (1999) 629-630.
[178] H. Li, H. Li, M. Wang, Glucose hydrogenation over promoted Co-B amorphous alloy catalysts, Appl. Catal., A, 207 (2001) 129-137.
[179] H. Li, W. Wang, J. Fa Deng, Glucose Hydrogenation to Sorbitol over a Skeletal Ni-P Amorphous Alloy Catalyst (Raney Ni-P), J. Catal., 191 (2000) 257-260.
[180] H. Li, H. Li, J.F. Deng, Glucose hydrogenation over Ni-B/SiO_2 amorphous alloy catalyst and the promoting effect of metal dopants, Catal. Today, 74 (2002) 53-63.
[181] B. Kusserow, S. Schimpf, P. Claus, Hydrogenation of Glucose to Sorbitol over Nickel and Ruthenium Catalysts, Adv. Synth. Catal., 345 (2003) 289-299.
[182] R. Geyer, P. Kraak, A. Pachulski, R. Schödel, New catalysts for the hydrogenation of glucose to sorbitol, Chemie-Ingenieur-Technik, 84 (2012) 513-516.
[183] Z. Li, Y. Liu, L. Liao, S. Wu, Catalytic conversion of glucose into sorbitol over Ni/Cu/Al/Fe catalysts derived from hydrotalcite precursors, Journal of Biobased Materials and Bioenergy, 10 (2016) 397-402.
[184] B. Zada, L. Yan, Y. Fu, Effective conversion of cellobiose and glucose to sorbitol using non-noble bimetallic NiCo/HZSM-5 catalyst, Sci. China: Chem, (2018).
[185] H.S. Luo, H.B. Guo, H.X. Li, M.H. Wang, Y.P. Xu, A novel ultrafine Ru-B amorphous alloy catalyst for glucose hydrogenation to sorbitol, Chin. Chem. Lett., 13 (2002) 1221-1224.
[186] B.W. Hoffer, E. Crezee, P.R.M. Mooijman, A.D. van Langeveld, F. Kapteijn, J.A. Moulijn, Carbon supported Ru catalysts as promising alternative for Raney-type Ni in the selective hydrogenation of d-glucose, Catal. Today, 79-80 (2003) 35-41.
[187] J. Pan, J. Li, C. Wang, Z. Yang, Multi-wall carbon nanotubes supported ruthenium for glucose hydrogenation to sorbitol, React. Kinet. Catal. Lett., 90 (2007) 233-242.
[188] J. Liu, X.S. Zhao, Glucose hydrogenation over Ru nanoparticles embedded in templated porous carbon, in: Studies in Surface Science and Catalysis, 2008, pp. 1315-1318.
[189] X. Guo, X. Wang, J. Guan, X. Chen, Z. Qin, X. Mu, M. Xian, Selective hydrogenation of D-glucose to D-sorbitol over Ru/ZSM-5 catalysts, Cuihua Xuebao, 35 (2014) 733-740.
[190] A.A. Dabbawala, D.K. Mishra, J.S. Hwang, Selective hydrogenation of D-glucose using amine functionalized nanoporous polymer supported Ru nanoparticles based catalyst, Catal. Today, 265 (2016) 163-173.

[191] A. Romero, A. Nieto-Márquez, E. Alonso, Bimetallic Ru:Ni/MCM-48 catalysts for the effective hydrogenation of D-glucose into sorbitol, Appl. Catal., A, 529 (2017) 49-59.
[192] L.M. Sanz-Moral, A. Aho, N. Kumar, K. Eränen, M. Peurla, J. Peltonen, D.Y. Murzin, T. Salmi, Synthesis and Characterization Ru–C/SiO2 Aerogel Catalysts for Sugar Hydrogenation Reactions, Catal. Lett., (2018).
[193] S. Esposito, B. Silvestri, V. Russo, B. Bonelli, M. Manzoli, F.A. Deorsola, A. Vergara, A. Aronne, M. Di Serio, Self-Activating Catalyst for Glucose Hydrogenation in the Aqueous Phase under Mild Conditions, ACS Catal., 9 (2019) 3426-3436.
[194] M.Y. Byun, D.-W. Park, M.S. Lee, Effect of sodium propionate as a stabilizer on the catalytic activity of Pt/C catalysts for d-glucose hydrogenation, Catal. Today, (2019).
[195] P.M. de Souza, L. Silvester, A.G.M. da Silva, C.G. Fernandes, T.S. Rodrigues, S. Paul, P.H.C. Camargo, R. Wojcieszak, Exploiting the Synergetic Behavior of PtPd Bimetallic Catalysts in the Selective Hydrogenation of Glucose and Furfural, Catalysts, 9 (2019) 132.
[196] A. Irchenko, Y. Khakimor, M. Abidova, Use of alloy catalysts for continuous hydrogenation of glucose to sorbitol, Uzb Khim Zh, 3 (1990) 66-68.
[197] R. Azimbekovs, A. Ivchenko, Semi-continuous hydrogenation of glucose, Uzb. Khim. Zh, 4 (1985) 73.
[198] P.J. Cerino, G. Fleche, P. Gallezot, J.P. Salome, Activity and Stability of Promoted Raney-Nickel Catalysts in Glucose Hydrogenation, in: M. Guisnet, J. Barrault, C. Bouchoule, D. Duprez, G. Pérot, R. Maurel, C. Montassier (Eds.) Studies in Surface Science and Catalysis, Elsevier, 1991, pp. 231-236.
[199] R.L. Hadley, Hydrogenation catalyst, in, Google Patents, 1960.
[200] T. Akira, K. Tadashi, S. Takashi, I. Yoshihisa, A. Satoshi, O. Tsutomu, H. Tadao, An Improved Asymmetrically-Modified Nickel Catalyst Prepared from Ultrasonicated Raney Nickel, Bulletin of the Chemical Society of Japan, 67 (1994) 2473-2477.
[201] A. Chen, H. Xu, Y. Yue, W. Hua, W. Shen, Z. Gao, Hydrogenation of methyl benzoate to benzaldehyde over manganese oxide catalysts prepared from Mg/Mn/Al hydrotalcite-like compounds, Appl. Catal., A, 274 (2004) 101-109.
[202] S. Carlier, J. Gripekoven, M. Philippo, S. Hermans, Ru on N-doped carbon supports for the direct hydrogenation of cellobiose into sorbitol, Appl. Catal., B, 282 (2021) 119515.
[203] A. Guerrero-Ruiz, P. Badenes, I. Rodríguez-Ramos, Study of some factors affecting the Ru and Pt dispersions over high surface area graphite-supported catalysts, Appl. Catal., A, 173 (1998) 313-321.
[204] E. Auer, A. Freund, J. Pietsch, T. Tacke, Carbons as supports for industrial precious metal catalysts, Appl. Catal., A, 173 (1998) 259-271.
[205] Y. Shen, Y. Lei, S. Shen, Z. Pan, Study on the activity of Ru/C catalyst prepared with ruthenium acetate as precursor for hydrogenation of glucose to produce sorbierite, Precious Met, 30 (2009) 40.
[206] M. Diao, M. Zhang, W. Li, K. Tao, Novel ruthenium catalyst for glucose hydrogenation, J. Mol. Catal, 21 (2007) 289.

[207] H. Guo, H. Li, Y. Xu, M. Wang, Liquid phase glucose hydrogenation over Cr-promoted Ru–B amorphous alloy catalysts, Materials Letters, 57 (2002) 392-398.
[208] Daily Metal Spot Prices, in, showtheplanet inc., 2022.
[209] P.A. Lazaridis, S. Karakoulia, A. Delimitis, S.M. Coman, V.I. Parvulescu, K.S. Triantafyllidis, d-Glucose hydrogenation/hydrogenolysis reactions on noble metal (Ru, Pt)/activated carbon supported catalysts, Catal. Today, 257 (2015) 281-290.
[210] B. Zada, L. Yan, Y. Fu, Effective conversion of cellobiose and glucose to sorbitol using non-noble bimetallic NiCo/HZSM-5 catalyst, Sci. China: Chem, 61 (2018) 1167-1174.
[211] I. Group, Sorbitol Market: Global Industry Trends, Share, Size, Growth, Opportunity & Forecast 2021-2026, in, 2021, pp. 133.
[212] D.L. Klass, Biomass for renewable energy, fuels, and chemicals, Elsevier, 1998.
[213] G.W. Huber, S. Iborra, A. Corma, Synthesis of Transportation Fuels from Biomass: Chemistry, Catalysts, and Engineering, Chem. Rev., 106 (2006) 4044-4098.
[214] L.-t. Fan, M.M. Gharpuray, Y.-H. Lee, Cellulose hydrolysis, Springer Science & Business Media, 2012.
[215] P.L. Dhepe, M. Ohashi, S. Inagaki, M. Ichikawa, A. Fukuoka, Hydrolysis of sugars catalyzed by water-tolerant sulfonated mesoporous silicas, Catal. Lett., 102 (2005) 163-169.
[216] F.B. Bizhanov, D.V. Sokol'skii, N.I. Popov, N.Y. Malkhina, A.M. Khisametdinov, Kinet. Katal., 10 (1969) 655-660.
[217] Y. Fu, L. Ding, M.L. Singleton, H. Idrissi, S. Hermans, Synergistic effects altering reaction pathways: The case of glucose hydrogenation over Fe-Ni catalysts, Appl. Catal., B, 288 (2021) 119997.
[218] M. Crespo-Quesada, S. Yoon, M. Jin, A. Prestianni, R. Cortese, F. Cárdenas-Lizana, D. Duca, A. Weidenkaff, L. Kiwi-Minsker, Shape-Dependence of Pd Nanocrystal Carburization during Acetylene Hydrogenation, J. Phys. Chem. C, 119 (2015) 1101-1107.
[219] J. Kibsgaard, C. Tsai, K. Chan, J.D. Benck, J.K. Nørskov, F. Abild-Pedersen, T.F. Jaramillo, Designing an improved transition metal phosphide catalyst for hydrogen evolution using experimental and theoretical trends, Energy Environ. Sci., 8 (2015) 3022-3029.
[220] B. Liu, N. Huang, Y. Wang, X. Lan, T. Wang, Promotion of Inorganic Phosphorus on Rh Catalysts in Styrene Hydroformylation: Geometric and Electronic Effects, ACS Catal., 11 (2021) 1787-1796.
[221] H. Li, W. Wang, H. Li, J.-F. Deng, Crystallization Deactivation of Ni–P/SiO2 Amorphous Catalystand the Stabilizing Effect of Silica Support on the Ni–P Amorphous Structure, J. Catal., 194 (2000) 211-221.
[222] K. An, S. Alayoglu, T. Ewers, G.A. Somorjai, Colloid chemistry of nanocatalysts: A molecular view, J. Colloid Interface Sci., 373 (2012) 1-13.
[223] Z. Xia, W. Wen, Synthesis of Nickel Nanowires with Tunable Characteristics, Nanomaterials, 6 (2016) 19.
[224] A.P. LaGrow, B. Ingham, S. Cheong, G.V.M. Williams, C. Dotzler, M.F. Toney, D.A. Jefferson, E.C. Corbos, P.T. Bishop, J. Cookson, R.D. Tilley,

Synthesis, Alignment, and Magnetic Properties of Monodisperse Nickel Nanocubes, J. Am. Chem. Soc., 134 (2012) 855-858.
[225] S. Carenco, C. Boissière, L. Nicole, C. Sanchez, P. Le Floch, N. Mézailles, Controlled Design of Size-Tunable Monodisperse Nickel Nanoparticles, Chem. Matter., 22 (2010) 1340-1349.
[226] S.L. Cumberland, K.M. Hanif, A. Javier, G.A. Khitrov, G.F. Strouse, S.M. Woessner, C.S. Yun, Inorganic Clusters as Single-Source Precursors for Preparation of CdSe, ZnSe, and CdSe/ZnS Nanomaterials, Chem. Matter., 14 (2002) 1576-1584.
[227] J. Tuoriniemi, A.-C.J.H. Johnsson, J.P. Holmberg, S. Gustafsson, J.A. Gallego-Urrea, E. Olsson, J.B.C. Pettersson, M. Hassellöv, Intermethod comparison of the particle size distributions of colloidal silica nanoparticles, Sci. Technol. Adv. Mater., 15 (2014) 035009.
[228] H. Lee, Utilization of shape-controlled nanoparticles as catalysts with enhanced activity and selectivity, RSC Adv., 4 (2014) 41017-41027.
[229] S.J. Parikh, K.W. Goyne, A.J. Margenot, F.N.D. Mukome, F.J. Calderón, Chapter One - Soil Chemical Insights Provided through Vibrational Spectroscopy, in: D.L. Sparks (Ed.) Advances in Agronomy, Academic Press, 2014, pp. 1-148.
[230] C. Mui, J.H. Han, G.T. Wang, C.B. Musgrave, S.F. Bent, Proton Transfer Reactions on Semiconductor Surfaces, J. Am. Chem. Soc., 124 (2002) 4027-4038.
[231] C.J. Pouchert, Aldrich library of FT-IR spectra, 2nd ed., Aldrich, Milwaukee, WI, 1997.
[232] A.M.A. da Costa, C.F.G.C. Geraldes, J.J.C. Teixeira-Dias, A Raman spectroscopic study of molecular interaction in long-chain primary amines systems, J. Raman Spectrosc., 13 (1982) 56-62.
[233] I.H. Campbell, P.M. Fauchet, The effects of microcrystal size and shape on the one phonon Raman spectra of crystalline semiconductors, Solid State Commun., 58 (1986) 739-741.
[234] R.E. Dietz, G.I. Parisot, A.E. Meixner, Infrared Absorption and Raman Scattering by Two-Magnon Processes in NiO, Phys. Rev. B, 4 (1971) 2302-2310.
[235] H. Richter, Z.P. Wang, L. Ley, The one phonon Raman spectrum in microcrystalline silicon, Solid State Commun., 39 (1981) 625-629.
[236] G. Gouadec, P. Colomban, Raman Spectroscopy of nanomaterials: How spectra relate to disorder, particle size and mechanical properties, Prog. Cryst. Growth Charact. Mater., 53 (2007) 1-56.
[237] L. Qiu, F. Liu, L. Zhao, W. Yang, J. Yao, Evidence of a Unique Electron Donor−Acceptor Property for Platinum Nanoparticles as Studied by XPS, Langmuir, 22 (2006) 4480-4482.
[238] M. Shimizu, Y. Tsushima, S. Arai, Electrochemical Na-Insertion/Extraction Property of Ni-Coated Black Phosphorus Prepared by an Electroless Deposition Method, ACS Omega, 2 (2017) 4306-4315.
[239] M.T. Edmonds, A. Tadich, A. Carvalho, A. Ziletti, K.M. O'Donnell, S.P. Koenig, D.F. Coker, B. Özyilmaz, A.H.C. Neto, M.S. Fuhrer, Creating a Stable Oxide at the Surface of Black Phosphorus, ACS Appl. Mater. Interfaces, 7 (2015) 14557-14562.

[240] W. Luo, D.Y. Zemlyanov, C.A. Milligan, Y. Du, L. Yang, Y. Wu, P.D. Ye, Surface chemistry of black phosphorus under a controlled oxidative environment, Nanotechnology, 27 (2016) 434002.
[241] A. Ziletti, A. Carvalho, D.K. Campbell, D.F. Coker, A.H. Castro Neto, Oxygen Defects in Phosphorene, Phys. Rev. Lett., 114 (2015) 046801.
[242] A.W. Adamson, A.P. Gast, Physical Chemistry of Surfaces, 6 ed., Wiley, 1997.
[243] M.C. Biesinger, B.P. Payne, A.P. Grosvenor, L.W.M. Lau, A.R. Gerson, R.S.C. Smart, Resolving surface chemical states in XPS analysis of first row transition metals, oxides and hydroxides: Cr, Mn, Fe, Co and Ni, Appl. Surf. Sci., 257 (2011) 2717-2730.
[244] V.K. LaMer, R.H. Dinegar, Theory, Production and Mechanism of Formation of Monodispersed Hydrosols, J. Am. Chem. Soc., 72 (1950) 4847-4854.
[245] T.O. Ely, C. Amiens, B. Chaudret, E. Snoeck, M. Verelst, M. Respaud, J.-M. Broto, Synthesis of Nickel Nanoparticles. Influence of Aggregation Induced by Modification of Poly(vinylpyrrolidone) Chain Length on Their Magnetic Properties, Chem. Matter., 11 (1999) 526-529.
[246] M.A. Watzky, R.G. Finke, Transition Metal Nanocluster Formation Kinetic and Mechanistic Studies. A New Mechanism When Hydrogen Is the Reductant: Slow, Continuous Nucleation and Fast Autocatalytic Surface Growth, J. Am. Chem. Soc., 119 (1997) 10382-10400.
[247] S. Arrhenius, Über die Dissociationswärme und den Einfluss der Temperatur auf den Dissociationsgrad der Elektrolyte, Zeitschrift für Physikalische Chemie, 4U (1889) 96-116.
[248] D.K. Mishra, A.A. Dabbawala, J.J. Park, S.H. Jhung, J.-S. Hwang, Selective hydrogenation of d-glucose to d-sorbitol over HY zeolite supported ruthenium nanoparticles catalysts, Catal. Today, 232 (2014) 99-107.
[249] L. Vitos, A.V. Ruban, H.L. Skriver, J. Kollár, The surface energy of metals, Surface Science, 411 (1998) 186-202.
[250] H. Cheng, N. Yang, X. Liu, Q. Yun, M.H. Goh, B. Chen, X. Qi, Q. Lu, X. Chen, W. Liu, L. Gu, H. Zhang, Aging amorphous/crystalline heterophase PdCu nanosheets for catalytic reactions, Natl. Sci. Rev., 6 (2019) 955-961.
[251] R.D.L. Smith, M.S. Prévot, R.D. Fagan, Z. Zhang, P.A. Sedach, M.K.J. Siu, S. Trudel, C.P. Berlinguette, Photochemical Route for Accessing Amorphous Metal Oxide Materials for Water Oxidation Catalysis, Science, 340 (2013) 60-63.
[252] G. Wu, X. Zheng, P. Cui, H. Jiang, X. Wang, Y. Qu, W. Chen, Y. Lin, H. Li, X. Han, Y. Hu, P. Liu, Q. Zhang, J. Ge, Y. Yao, R. Sun, Y. Wu, L. Gu, X. Hong, Y. Li, A general synthesis approach for amorphous noble metal nanosheets, Nat. Commun., 10 (2019) 4855.
[253] T. Liu, A. Li, C. Wang, W. Zhou, S. Liu, L. Guo, Interfacial Electron Transfer of Ni2P–NiP2 Polymorphs Inducing Enhanced Electrochemical Properties, Adv. Mater., 30 (2018) 1803590.
[254] Sorbitol Market Size, Share and Global Trend By Type, Application, and Geography Forecast 2019-2026, in: Sorbitol Market, Fortune Business Insights, 2019, pp. 135.

[255] J. So, Y. Chung, D.S. Sholl, C. Sievers, In-situ ATR-IR study of surface reaction during aqueous phase reforming of glycerol, sorbitol and glucose over Pt/γ-Al2O3, Mol. Catal., 475 (2019) 110423.
[256] B.R. Cuenya, S.-H. Baeck, T.F. Jaramillo, E.W. McFarland, Size- and Support-Dependent Electronic and Catalytic Properties of Au0/Au3+ Nanoparticles Synthesized from Block Copolymer Micelles, J. Am. Chem. Soc., 125 (2003) 12928-12934.
[257] T. Ishida, N. Kinoshita, H. Okatsu, T. Akita, T. Takei, M. Haruta, Influence of the support and the size of gold clusters on catalytic activity for glucose oxidation, Angew. Chem., Int. Ed., 47 (2008) 9265-9268.
[258] M. Haruta, S. Tsubota, T. Kobayashi, H. Kageyama, M.J. Genet, B. Delmon, Low-Temperature Oxidation of CO over Gold Supported on TiO2, α-Fe2O3, and Co3O4, J. Catal., 144 (1993) 175-192.
[259] N. Meyer, D. Pirson, M. Devillers, S. Hermans, Particle size effects in selective oxidation of lactose with Pd/h-BN catalysts, Appl. Catal., A, 467 (2013) 463-473.
[260] F. Mederos-Henry, J. Mahin, B.P. Pichon, M.M. Dîrtu, Y. Garcia, A. Delcorte, C. Bailly, I. Huynen, S. Hermans, Highly Efficient Wideband Microwave Absorbers Based on Zero-Valent Fe@γ-Fe2O3 and Fe/Co/Ni Carbon-Protected Alloy Nanoparticles Supported on Reduced Graphene Oxide, Nanomaterials, 9 (2019) 1196.
[261] J.M. Ting, R.Y. Lin, Effect of particle size distribution on sintering, Journal of Materials Science, 30 (1995) 2382-2389.
[262] C. Su, B.Y. Hong, C.M. Tseng, Sol–gel preparation and photocatalysis of titanium dioxide, Catal. Today, 96 (2004) 119-126.
[263] K.E.J. Lehtinen, M.R. Zachariah, Energy accumulation in nanoparticle collision and coalescence processes, Journal of Aerosol Science, 33 (2002) 357-368.
[264] C. Vriamont, T. Haynes, E. McCague-Murphy, F. Pennetreau, O. Riant, S. Hermans, Covalently and non-covalently immobilized clusters onto nanocarbons as catalysts precursors for cinnamaldehyde selective hydrogenation, J. Catal., 329 (2015) 389-400.
[265] C.F. Holder, R.E. Schaak, Tutorial on Powder X-ray Diffraction for Characterizing Nanoscale Materials, ACS Nano, 13 (2019) 7359-7365.
[266] K.S.W. Sing, Reporting physisorption data for gas/solid systems with special reference to the determination of surface area and porosity (Recommendations 1984), Pure and Applied Chemistry, 57 (1985) 603-619.
[267] J.A. Konvalinka, P.H. Van Oeffelt, J.J.F. Scholten, Temperature programmed desorption of hydrogen from nickel catalysts, Applied Catalysis, 1 (1981) 141-158.
[268] K. Christmann, O. Schober, G. Ertl, M. Neumann, Adsorption of hydrogen on nickel single crystal surfaces, The Journal of Chemical Physics, 60 (1974) 4528-4540.
[269] A.G. Boudjahem, S. Monteverdi, M. Mercy, M.M. Bettahar, Study of nickel catalysts supported on silica of low surface area and prepared by reduction of nickel acetate in aqueous hydrazine, J. Catal., 221 (2004) 325-334.

[270] Y. Cesteros, P. Salagre, F. Medina, J.E. Sueiras, Synthesis and characterization of several Ni/NiAl2O4 catalysts active for the 1,2,4-trichlorobenzene hydrodechlorination, Appl. Catal., B, 25 (2000) 213-227.
[271] A.-G. Boudjahem, S. Monteverdi, M. Mercy, M.M. Bettahar, Nanonickel Particles Supported on Silica. Morphology Effects on Their Surface and Hydrogenating Properties, Catal. Lett., 97 (2004) 177-183.
[272] S. Dekura, H. Kobayashi, R. Ikeda, M. Maesato, H. Yoshino, M. Ohba, T. Ishimoto, S. Kawaguchi, Y. Kubota, S. Yoshioka, S. Matsumura, T. Sugiyama, H. Kitagawa, The Electronic State of Hydrogen in the α Phase of the Hydrogen-Storage Material PdH(D)x: Does a Chemical Bond Between Palladium and Hydrogen Exist?, Angew. Chem., Int. Ed., 57 (2018) 9823-9827.
[273] S. Velu, S.K. Gangwal, Synthesis of alumina supported nickel nanoparticle catalysts and evaluation of nickel metal dispersions by temperature programmed desorption, Solid State Ionics, 177 (2006) 803-811.
[274] J.M. Los, L.B. Simpson, K. Wiesner, The Kinetics of Mutarotation of D-Glucose with Consideration of an Intermediate Free-aldehyde Form, J. Am. Chem. Soc., 78 (1956) 1564-1568.
[275] Z.Q. Li, C.J. Lu, Z.P. Xia, Y. Zhou, Z. Luo, X-ray diffraction patterns of graphite and turbostratic carbon, Carbon, 45 (2007) 1686-1695.
[276] J.K. Kesavan, I. Luisetto, S. Tuti, C. Meneghini, G. Iucci, C. Battocchio, S. Mobilio, S. Casciardi, R. Sisto, Nickel supported on YSZ: The effect of Ni particle size on the catalytic activity for CO2 methanation, Journal of CO2 Utilization, 23 (2018) 200-211.
[277] J. Gao, C. Jia, M. Zhang, F. Gu, G. Xu, F. Su, Effect of nickel nanoparticle size in Ni/α-Al2O3 on CO methanation reaction for the production of synthetic natural gas, Catal. Sci. Technol., 3 (2013) 2009-2015.
[278] M. Silveira, R. Jonas, The biotechnological production of sorbitol, Appl. Microbiol. Biotechnol., 59 (2002) 400-408.
[279] P. Brahme, M. Pai, G. Narsimhan, Hydrogenation of glucose to polyhydric, Brit Chem Eng, 9 (1964) 684-687.
[280] G. Schmid, Large clusters and colloids. Metals in the embryonic state, Chem. Rev., 92 (1992) 1709-1727.
[281] S. Van Den Bosch, T. Renders, S. Kennis, S.F. Koelewijn, G. Van Den Bossche, T. Vangeel, A. Deneyer, D. Depuydt, C.M. Courtin, J.M. Thevelein, W. Schutyser, B.F. Sels, Integrating lignin valorization and bio-ethanol production: On the role of Ni-Al2O3 catalyst pellets during lignin-first fractionation, Green Chem., 19 (2017) 3313-3326.
[282] A. Negoi, K. Triantafyllidis, V.I. Parvulescu, S.M. Coman, The hydrolytic hydrogenation of cellulose to sorbitol over M (Ru, Ir, Pd, Rh)-BEA-zeolite catalysts, Catal. Today, 223 (2014) 122-128.
[283] J. Court, J.P. Damon, J. Masson, P. Wierzchowski, Hydrogenation of glucose with bimetallic catalysts (NiM) of Raney type, in: Studies in Surface Science and Catalysis, 1988, pp. 189-196.
[284] A. Fukuoka, P.L. Dhepe, Catalytic conversion of cellulose into sugar alcohols, Angew. Chem., Int. Ed., 45 (2006) 5161-5163.
[285] F.M. Mederos-Henry, J.; Pichon, B.P.; Dîrtu, M.M.; Garcia, Y.; Delcorte, A.; Bailly, C.; Huynen, I.; Hermans, S., Highly Efficient Wideband Microwave Absorbers Based on Zero-Valent Fe@γ-Fe_2O_3 and Fe/Co/Ni Carbon-

Protected Alloy Nanoparticles Supported on Reduced Graphene Oxide, Nanomaterials, 9 (2019) 1196.
[286] K. Hadjiivanov, M. Mihaylov, D. Klissurski, P. Stefanov, N. Abadjieva, E. Vassileva, L. Mintchev, Characterization of Ni/SiO_2 Catalysts Prepared by Successive Deposition and Reduction of Ni^{2+} Ions, J. Catal., 185 (1999) 314-323.
[287] M. Liang, W. Kang, K. Xie, Comparison of reduction behavior of Fe2O3, ZnO and ZnFe2O4 by TPR technique, Journal of Natural Gas Chemistry, 18 (2009) 110-113.
[288] V. Mazzieri, F. Coloma-Pascual, A. Arcoya, P.C. L'Argentière, Fı, x, N.S. goli, XPS, FTIR and TPR characterization of Ru/Al2O3 catalysts, Appl. Surf. Sci., 210 (2003) 222-230.
[289] I.V. Vernyhora, V.A. Tatarenko, S.M. Bokoch, Thermodynamics of f.c.c.-Ni–Fe Alloys in a Static Applied Magnetic Field, ISRN Thermodynamics, 2012 (2012) 917836.
[290] A. Lutts, P.M. Gielen, The Order-Disorder Transformation in $FeNi_3$, Phys. Status Solidi B, 41 (1970) K81-K84.
[291] F.U. Hillebrecht, J.C. Fuggle, P.A. Bennett, Z. Zołnierek, C. Freiburg, Electronic structure of Ni and Pd alloys. II. X-ray photoelectron core-level spectra, Phys. Rev. B, 27 (1983) 2179-2193.
[292] R.W. Nagorski, J.P. Richard, Mechanistic Imperatives for Aldose−Ketose Isomerization in Water: Specific, General Base- and Metal Ion-Catalyzed Isomerization of Glyceraldehyde with Proton and Hydride Transfer, J. Am. Chem. Soc., 123 (2001) 794-802.
[293] R. Bermejo-Deval, M. Orazov, R. Gounder, S.-J. Hwang, M.E. Davis, Active Sites in Sn-Beta for Glucose Isomerization to Fructose and Epimerization to Mannose, ACS Catal., 4 (2014) 2288-2297.
[294] M. Moliner, Y. Román-Leshkov, M.E. Davis, Tin-containing zeolites are highly active catalysts for the isomerization of glucose in water, Proc. Natl. Acad. Sci., 107 (2010) 6164-6168.
[295] S. Xu, L. Zhang, K. Xiao, H. Xia, Isomerization of glucose into fructose by environmentally friendly Fe/β zeolite catalysts, Carbohydr. Res., 446-447 (2017) 48-51.
[296] C.H. Bartholomew, Catalyst Deactivation and Regeneration, in, 2003.
[297] I.W.C.E. Arends, R.A. Sheldon, Activities and stabilities of heterogeneous catalysts in selective liquid phase oxidations: recent developments, Appl. Catal., A, 212 (2001) 175-187.
[298] C.H. Bartholomew, Mechanisms of catalyst deactivation, Appl. Catal., A, 212 (2001) 17-60.
[299] J.A. Moulijn, A.E. van Diepen, F. Kapteijn, Catalyst deactivation: is it predictable?: What to do?, Appl. Catal., A, 212 (2001) 3-16.
[300] P.O. Thevenin, A.G. Ersson, H.M.J. Kušar, P.G. Menon, S.G. Järås, Deactivation of high temperature combustion catalysts, Appl. Catal., A, 212 (2001) 189-197.
[301] П. Николайчук, The potential - pH diagram for Ni - H2O system, 2015.
[302] C.W. Cuss, C.N. Glover, M.B. Javed, A. Nagel, W. Shotyk, Geochemical and biological controls on the ecological relevance of total, dissolved, and colloidal forms of trace elements in large boreal rivers: review and case studies, Environmental Reviews, 28 (2020) 138-163.

[303] P. Gogoi, N. Kanna, P. Begum, R.C. Deka, S. C. V. V, T. Raja, Controlling and Stabilization of Ru Nanoparticles by Tuning the Nitrogen Content of the Support for Enhanced H2 Production through Aqueous-Phase Reforming of Glycerol, ACS Catal., 10 (2020) 2489-2507.
[304] W. Shi, B. Zhang, Y. Lin, Q. Wang, Q. Zhang, D.S. Su, Enhanced Chemoselective Hydrogenation through Tuning the Interaction between Pt Nanoparticles and Carbon Supports: Insights from Identical Location Transmission Electron Microscopy and X-ray Photoelectron Spectroscopy, ACS Catal., 6 (2016) 7844-7854.
[305] C.P. Rao, K. Geetha, M.S.S. Raghavan, Fe(III) complexes of d-glucose and d-fructose, Biometals, 7 (1994) 25-29.
[306] R.P. Bandwar, M.S. Srinivasa Raghavan, C.P. Rao, Transition metal-saccharide chemistry: d-glucose complexes of Mn(II), Co(II), Ni(II), Cu(II) and Zn(II), Biometals, 8 (1995) 19-24.

Lu Bai, Sina Ghiassinejad, Jérémy Brassinne, Yang Fu, Jiande Wang, Hui Yang, Alexandru Vlad, Andrea Minoia, Roberto Lazzaroni, Jean-François Gohy. High Salt-Content Plasticized Flame-Retardant Polymer Electrolytes [J]. *ACS Appl. Mater. Interfaces*. 13 (2021). 44844-44859.

Yang Fu, Lipeng Ding, Michael L Singleton, Hosni Idrissi, Sophie Hermans. Synergistic effects altering reaction pathways: the case of glucose hydrogenation over Fe-Ni catalysts [J], *Appl. Catal., B.* 288 (2021): 119997.

Cuilian Liu, Eduard O. Bohylev, Yang Fu, David A Poole, Koen Robeyns, Charles-André Fustin, Yann Garcia, Joost NH Reek, Michael Singleton. Balancing Ligand Flexibility Versus Rigidity for the Step-Wise Self-Assembly of M12L24 Via M6L12 Metal-Organic Cages [J]. *Chem. – Eur. J.* 26 (2020): 11960-11965.

Debobrata. Sheet, Abhijit. Bera, Yang Fu, Antonin Desmecht, Olivier Riant, Sophie Hermans. Carbon-Nanotube-Appended PAMAM Dendrimers Bearing Iron(II) α-Keto Acid Complexes: Catalytic Non-Heme Oxygenase Models [J]. *Chem. – Eur. J.* 25 (2019): 9191-9196.

Yang Fu, François Devred, Beniot Pichon, Michael L. Singleton, Sophie Hermans, Facets-dependent activity of Ni catalysts in glucose hydrogenation. *J. Catal.* submitted.

Yang Fu, François Devred, Pierre Eloy, Tommy Haynes, Michael L. Singleton, Sophie Hermans. The effect of Ni particle size and carbon support on catalytic activity for glucose hydrogenation reaction. *Chem. Eng. J.* submitted.